Iron-sulfur, carbon and Molybdenum biogeochemistry in methane seep sediments off the Krishna-Godavari basin

A THESIS SUBMITTED IN PARTIAL FULFILLMENT FOR THE DEGREE OF DOCTOR OF PHILOSOPHY

In

MARINE SCIENCE

GOA UNIVERSITY



By

PILLUTLA SAI PAVAN KUMAR

(CSIR-NATIONAL INSTITUTE OF OCEANOGRAPHY, DONA PAULA GOA, INDIA)

SCHOOL OF EARTH, OCEAN AND ATMOSPHERIC SCIENCES GOA UNIVERSITY, TALEIGAO, GOA

November 2025

DECLARATION

I, Pillutla Sai Pavan Kumar, the candidate hereby declare that this thesis represents work which has been carried out by me and that it has not been submitted, either in part or full, to any other University or Institution for the award of any research degree.

Place: Taleigao Plateau. Pillutla Sai Pavan Kumar

Date: 19-11-2025 Name of the candidate

CERTIFICATE

I/We hereby certify that the work was carried out under my supervision and may be placed for evaluation.

This is to certify that the thesis entitled "**Iron-sulfur, carbon and Molybdenum biogeochemistry in methane seep sediments off the Krishna-Godavari basin**" submitted for the award of the degree of Doctor of Philosophy in Marine Sciences is the bonafide work of Mr. Pillutla Sai Pavan Kumar, carried out under my supervision.
The thesis and any part thereof have not been previously submitted for any other degree or diploma in any university or institute.

Dr. Aninda Mazumdar

(Research Supervisor)

Chief Scientist

CSIR –NIO, Goa, India

Acknowledgment

First and foremost, I express my deepest gratitude to God for granting me the strength, perseverance, and opportunity to undertake and complete this research journey. The path has been long and challenging, and it is by His grace that I have reached this milestone. I am profoundly thankful to my research supervisor, **Dr. Aninda Mazumdar**, for his unwavering support, insightful guidance, and constant encouragement throughout my doctoral studies. His expertise and mentorship have been instrumental in shaping the direction and depth of this work. I also extend my sincere gratitude to Dr. Aditya Peketi for his invaluable support with laboratory procedures, instrument troubleshooting, and manuscript refinement. I am equally thankful to Dr. Subhasree Mishra, Dr. Aniruddha Mitra, and Dr. Swati Verma for their thoughtful suggestions and constructive inputs during the writing phase of this work. I am grateful to the members of my Research Advisory Committee Prof. V. M. Matta, Dr. Siby Kurian, and Assistant Professor Nicole Ann Fae Sequeira for their constructive feedback and for encouraging me to broaden my scientific perspective. Special thanks to Dr. Ben and Dr. John Cantle from Nu Plasma Instruments, and Xi Chen from Nanjing University, China, for their support in establishing the double-spike calibration in our lab. I am grateful to Dr. Pawan Dewangan and Dr. Sriram Gullapalli, whose support during onboard operations was invaluable. Although my research is rooted in geochemistry, their contributions provided essential context that supported the broader interpretation of shale tectonism within the scope of this thesis. I also extend my thanks to Maria Ana Desa for her assistance in preparing the graphical representations featured in my published paper, which enhanced the clarity and impact of the work. I also wish to acknowledge Dr. Surya Prakash Lankalaplli for his insightful guidance and technical inputs toward establishing the Mo-speciation protocol. His support has been instrumental in refining a critical aspect of this study, and I deeply appreciate his encouragement throughout this phase of my academic journey.

I acknowledge the financial support provided by the Science and Engineering Research Board, Department of Science and Technology, Government of India (Grant No. GAP3352), and the Ministry of Earth Sciences (Project GAP2303), which made this research possible.

My heartfelt appreciation goes to the technical staff at CSIR-NIO Mrs. Supriya Karapurkar, Mrs. Anita Garg, Mr. Nikhil Mohan, and Mr. Robin for their consistent assistance in the laboratory. I also thank Satish Dixit and Priyesh Patil from Thermo Fisher Scientific for their

support with IRMS and ICP-MS troubleshooting. I would like to thank Mr. Thavapandian and Mr. Rohit from the HRM division for their institutional support, which facilitated various aspects of this research journey.I am grateful to my senior colleagues Dr. Samiksha S Volvaiker, Pulavarthi Nagendra, Brahmanand N. Sawant, Dr. Svetlana Fernandes, Dr. Rhean De Silva, and Ayusmati S. Manaskanya for sharing their knowledge and experiences. To my dear friends and fellow researchers Dr. Pankaj Prasad, Sagar Pujari, Diksha shetty, Anjali Zatale, Kalyani Sivan, Mohd Sadique, Ankita Ghosh, Surya Reddy, Dr. Vasanasetti Trinadha Rao, D. Murali Krishnam Raju, Sohan Pal Meena, and Pavas Kumar thank you for the companionship, countless conversations, and memorable moments that enriched the past six years.

I also extend my sincere thanks to Dr. Satish Mohan for his constant encouragement and moral support during my doctoral journey. I would also like to express my heartfelt gratitude to Gutha Pullarao Sir and Sunitha Madam, whose encouragement during my academic journey inspired me to pursue a Ph.D. Their belief in my potential and sincere wishes have remained a source of motivation throughout this endeavour.

This thesis is dedicated to my parents, in recognition of their enduring encouragement and unconditional love.

Table of contents

List of Figures

List of tables

Contents

Abstract 16

Chapter 1 Introduction 18

1.1. Methane Seeps and Hydrate Dynamics on Continental Margins 18

1.1.1 Methane cold seeps 18

1.1.2 Methane hydrate dynamics 22

1. 2. Iron-Sulfur geochemistry at cold seeps 24

1.2.2 Microbial Sulfate Reduction 24

1.2.2.(i) Assimilatory sulfate reduction: 24

1.2.2.(ii) Dissimilatory sulfate reduction process (DSR) 25

1.2.2.(iii). Sulfate reduction fuelled by Anaerobic Oxidation of Methane (SD-AOM) 27

1.3 Sulfide Oxidation and Disproportionation 29

1.4. Sulfide Trapping 29

1.4.1. Pyritization 29

1.4.1.i) Polysulfide pathway 30

1.4.1.ii) H_2S pathway 30

1.4.1.iii) Iron-loss pathway 30

1.4.2. Sulfurization of organic matter 30

1.5. Cold seep carbonate geochemistry 31

1.6. Molybdenum geochemistry 31

1.7 Aim and scope of the study 33

1.8 Overview of the thesis 33

Chapter 2 Geology 35

2.1 Regional setting 35

2.2 Stratigraphy 35

2.3 Sediment supply and catchments. 36

2.4 Seabed morphology and slope systems. 36

2.5 Mass-transport deposits (MTDs) and sub-bottom expression. 36

2.6 Shale tectonism, growth structures, and plumbing. 37

2.7 Gas hydrates, cold seeps, and ecosystems. 38

Chapter 3 Methodology 40

3.1 Core collection and sub-sampling 40

3.1.1 Radiocarbon dating 40

3.2 Headspace methane sampling: 41
3.3 Pore fluid extraction: 41
3.4 Pore fluid analysis 41
3.4.1. Determination of headspace methane abundance and isotopic composition 41
3.4.1.1 GC-IRMS: Working Principle 41
3.4.2 Determination of sulfate in pore water samples 47
3.4.2.1 Ion Chromatograph: Working Principle 47
3.4.2.2 Procedure 48
3.4.3 Determination of dissolved hydrogen sulfide in pore water samples 49
3.4.4 Determination of pore water sulfur isotopic composition 49
3.4.5 Quantification of total inorganic carbon (TIC): 51
3.4.6 Determination of total organic carbon (TOC) and total nitrogen (TN) 53
3.4.7 Determination of carbon isotopic ratio of organic carbon ($\delta^{13}C_{TOC}$) 53
3.4.8 Analytical Protocol for Sulfur Speciation in Sediments 54
3.4.9 Procedure for total reactive iron (Fe_{TR})extraction and degree of pyritization (DOP) Calculation 56
3.4.10 Inductively Coupled Plasma Mass Spectrometry (ICP-MS) 57
3.4.11 General description of multi collector inductively coupled plasma mass spectrometry (MC-ICP-MS) 61
3.4.12 Molybdenum speciation and phase-specific isotope ratio measurements 72
Chapter 4 Sediment pore fluid chemistry 74
4.1 Introduction 74
4.2 Results 75
4.3 Discussion 77
4.3.1 AOM and SMTZ 77
4.3.2. Non-steady sulfate profile: hydrate degassing and SD-AOM 77
4.3.3. Non-steady state of H_2S 78
4.4. Conclusion: 79
Chapter 5 Biogeochemical Reconstruction of Authigenic Carbonate Deposits at Methane Seep Site off Krishna-Godavari (K-G) Basin, Bay of Bengal 80
5.1 Abstract 80
5.2. Introduction 81
5.3 Sampling and Analytical Protocol 83
5.3.2 Optical Microscopy and SEM-EDS 83
5.3.3 Micro-FTIR Spectroscopy 84
5.3.4. X-Ray Diffractometry 84
5.3.5 Carbon and Oxygen Stable Isotope Ratio Measurements 85
5.3.6 Major and Trace Element Analyses 85

5.4 Results 85
5.4.1 Carbonate Morphology 85
5.4.2 Carbonate Mineralogy 86
5.4.3 Carbonate Petrography and SEM-EDS 87
5.4.4 Micro-FTIR 89
5.4.5 Isotope Ratios and Trace-REE Composition 92
5.5 Discussion 98
5.5.1 Authigenic Carbonate Precipitation Pathways 98
5.5.2 Evidence of Methanotrophic Biomass 100
5.5.3 Carbon Source and Carbonate Formation Environment 100
5.5.4 Redox Variability in Carbonate Formation Environment 101
5.5.5 Sr Distribution in Carbonates 103
5.5.6 Conceptual Model 104
5.6 Conclusion 105
Chapter 6. Iron-sulfur-carbon systematics of cold seep sediments 107
6.1 Introduction 107
6.2 Results 108
6.2.1. Sedimentary sulfur contents and isotope ratios 108
6.2.2. Fe-speciation 109
6.2.3. Sedimentary organic 111
6.3. Discussion 112
6.3.1 Sulfidization process at the cold seep region 112
6.3.2 Fe-Speciation 113
6.3.3 Implications of AOM from sulfur isotope ratios 115
6.4. Conclusion: 117
Chapter 7. Molybdenum sequestration and SMTZ dynamics in cold Seep Sediments 118
7.1 Introduction 118
7.2 Results of bulk metal contents of Al, Mn, Fe, Mo, and U 119
7.2.1. i) Aluminium 119
7.2.1. ii)Manganese 120
7.2.1. iii) Iron 120
7.2.1.iv) Molybdenum 120
7.2.1.v) Uranium 120
7.2.2 Molybdenum isotope ratio 120
7.2.3 Molybdenum speciation 123
7.3 Discussion 124
7.3.1. MoEZs as tracer for sulfidic pore waters 124

7.3.2. SMTZ migration and H_2S dynamics on MoEZs 126
5.3 MoEZ as a proxy for episodic reactivation of fluid pathways 127
7.3.4 Molybdenum speciation 128
7.4. Conclusion 131
Chapter 8 Conclusion 133
8.1 Summary of Key Findings 133
8.2 Non-steady state SO_4^{2-}-H_2S system 133
8.3 Authigenic Carbonates and Diagenetic Conditions 133
8.4. Fe-S-C systematics 134
8.5. MoEZ tracer for shale tectonics 134
8.7. Mo-speciation 134
8.8 Scope of the future work 135
Appendix 136
References 173

List of Tables

Table 3.1. Location and recovery details of sediment cores collected during the SSD045 expedition 136
Table 3. 2. Radiocarbon Dating and Sedimentation Rates of Core SSD045/4/G4 136
Table 4. 1 . Pore fluid geochemistry data of cold seep core SSD045/4/G4. 137
Table 5. 1. Locations of spade cores and the corresponding water depths.....139
Table 5. 2. Mineralogical, isotope ratio data and TOC content of HMC-tubes and arg-crust samples from SSD045/4 (methane seep sites off K-G basin**)** 139
Table 5. 3. Major, and trace element composition of the HMC-tubes and arg-crust samples 141
Table 5. 4. REE composition of the HMC-tubes and arg-crust samples.....143
Table 6. 1. Reactive iron minerals in sediments and their sulfidization half-lives. 115
Table 6. 2**.** Bulk sediment elemental compositions and isotope ratios of SSD045/4/G4 core. 147
Table 6. 3. Bulk sediment elemental compositions and isotope ratios of SSD045/13/G1 core. 154
Table 7. 1. Major and trace element geochemical data of cold seep core SSD045/4/G4..159
Table 7. 2. Major and trace element geochemical data of non-cold seep core SSD045/13/G1 166
Table 7. 3. Molybdenum speciation data and isotope ratios of Mo associated with Fe-oxide and pyrite phases from the cold seep core SSD045/4/G4. 171

List of Figures:

Fig. 1. 1. Schematic illustration of a cold-seep ecosystem showing methane flux, CH_4 ebullition, chemosynthetic fauna (clams, mussels, and tubeworms), and methane-hydrate deposits. Redrawn and adapted from "A diagram of a typical cold-seep community of organisms," Science Learning Hub, University of Waikato. 19
Fig. 1. 2. Schematic representation showing the ebullition of methane (CH_4) from dissociating methane-hydrate deposits and the associated enrichment of hydrogen sulfide (H_2S) in near-seabed sediments within a cold-seep environment. The depicted reactions represent key biogeochemical pathways 1) sulfate-driven anaerobic oxidation of methane (SD-AOM) generating bicarbonate (HCO_3^-) and sulfide (HS^-); (2) precipitation of

authigenic carbonate ($CaCO_3$); and (3) formation of Fe-sulfide minerals (FeS, FeS_2) through reaction between dissolved Fe^{2+} and HS^-. 19
Fig. 1. 3. (a) Aggregation of Bathymodiolus sp. (indicated as Bm) within black sulfidic sediments collected using spade cores from cold-seep sites; (b, c) Calyptogena sp. exhibiting distinct shell growth laminae; (d) *Conchocele* sp. shell with preserved soft tissue; (e) Acharax sp. shell with soft body intact; (f) Bivalve shell representing the family Pectinidae; (g) Limpet shell retaining soft tissue; (h) Limpet shell attached to Bathymodiolus sp.; (i) Gastropod shell of the family Provannidae showing soft body (foot); (j) Gastropod shell of the family Neritidae with preserved soft tissue; (k) Tube structure of *Sclerolinum* sp.; (l) Polychaete worm belonging to the family *Glyceridae*; (m) Mantle cavity of *Bathymodiolus* sp. containing the commensal polychaete *Branchipolynoe seepensis*; (n, o) Dorsal views of squat lobsters from the families Galatheidae and *Munidopsidae*; (p) Brittle star of the family *Amphiodia*; (q) Goose barnacle of the genus *Neolepas* attached to Bathymodiolus shell; (r) Enlarged view of *Neolepas* sp. showing the capitulum (adopted from Mazumdar et al. (2019). 20
Fig. 1. 4. a) Global distribution of cold seeps and gas hydrates, including the location of the present study site, compiled from Aguilar Pérez et al. (2024), Ruppel and Waite (2020), DFO (2018), Sauer et al. (2021), Syrbu et al. (2024); Syrbu et al. (2022). (b) Regional map showing the cold seep site (SSD-045; red filled star) from Pillutla et al. (2024)..... 22
Fig. 1. 5. Images (a-c) depict natural gas hydrates recovered from cold-seep sites in the K-G Basin, eastern offshore India. 23
Fig. 1. 6. Diagram illustrating the temperature and pressure conditions governing the methane hydrate stability zone following Eymold et al. (2021)..... 23
Fig. 1. 7.Schematic representation of the assimilatory sulfate reduction via the APS pathway 25
Fig. 1. 8. Schematic of assimilatory sulfate reduction via the 3′-phosphoadenosine-5′-phosphosulfate (PAPS) pathway 25
Fig. 1. 9. Dissimilatory sulfate reduction pathway involving PPi hydrolysis by pyrophosphatase 26
Fig. 2. 1. (a) Bathymetric map of the Krishna–Godavari (K-G) offshore basin showing the locations of active cold-seep sites. The toe-thrust region (solid rectangle) and diapiric mounds (dashed rectangle), where gas flares have been identified, are highlighted on the map. The inset in (a) marks the study area. (b) and (c) show representative water-column

(WC) images depicting gas flares rising from the seabed to depths of up to ~700 m below sea level (mbsl) (image adopted from Mazumdar et al. (2019).....37
Fig. 2. 2. a) Detailed seafloor morphology map of the toe-thrust region showing high-resolution air-gun seismic profiles (P1, P2), sub-bottom profiler (SBP) data displaying primary high-frequency (PHF) and secondary low-frequency (SLF) components, locations of gas flares (dots), regional faults (dashed lines), and the NE-SW-trending fault system (F1 to F6) enclosed within a dotted rectangular box. The two mutually perpendicular seismic profiles P1 (NW-SE oriented) and P2 (WSW-ENE oriented) are highlighted. (b) Bathymetric surface rendered along seismic profile P2 showing the major fault system (F1 to F6) and their subsurface extensions (solid lines) as imaged in seismic data, along with a regional fault (dashed line). (c) Bathymetric surface along profile P1 highlighting regional faults (dashed lines) and normal vertical faults (dashed lines on the seismic section). A subsurface chimney-like structure (solid lines), coinciding with water-column gas flares, is also marked. Subsurface horizons (H7 to H11, solid lines), a probable bottom simulating reflector (BSR; dashed line between two-way travel time 2.7-2.8 s), and a regional toe-thrust fault between CDPs 4400 and 4500 (dashed line) are indicated. (d) Low-frequency SBP data (SLF) delineate shallow faults (F1 to F6), whereas the high-frequency SBP data (PHF) reveal gas flares within the water column from trace numbers 165 to 240 (adopted from Dewangan et al. (2021).....39
Fig. 3. 1 Location Map showing the cold seep and non-seep core (Reference core) locations from the Krishna-Godavari basin east coast of India BoB refers to Bay of Bengal.....40
Fig. 3. 2**.** Schematic diagram of the gas chromatograph system 43
Fig. 3. 3**.** A gas chromatograph interfaced with an isotope ratio mass spectrometer. 44
Fig. 3.4 Block diagram demonstrating the fundamental working principle of a mass spectrometer. (a) Isotopic variants of gas molecules are first ionized through electron impact within the ion source. These ions are then accelerated by a strong electric potential and directed into a magnetic field, where they are separated according to their mass-to-charge ratios due to the influence of the Lorentz force. The ions, following curved paths based on their mass, are detected individually by Faraday cups positioned at the end of the flight path. (b) The Lorentz force is illustrated as follows: a positively charged particle (charge q^+, mass m) moves with velocity v on a flat surface within a magnetic field B that is perpendicular to the motion. The force F, acting at right angles to both the velocity and magnetic field, compels the particle into a circular trajectory with radius r. 46

Fig. 3. 5.(a) Schematic illustration of the Metrohm Basic IC 883 Plus ion chromatograph used for the determination of sulfate ions (Metrohm, India). b) Metrohm Basic IC 883 Plus 49
Fig. 3. 6. (a) Schematic illustration of the elemental analyzer, showing the fundamental working principle, including sample combustion, gas separation, and detection. (b) Photograph of the Thermo EA 1112 elemental analyzer used in this study..... 50
Fig. 3. 7**.** a) Schematic representation of the coulometer illustrating its working principle. b) Carbon coulometer. 53
Fig. 3. 8.(a) Diagram of the sulfur extraction apparatus highlighting the H_2S transfer pathway, and (b) setup used for sequential AVS and CRS extraction. 55
Fig. 3. 9.Schematic representation of the principal components of an inductively coupled plasma mass spectrometer (ICP-MS). 58
Fig. 3. 10. Inductively coupled plasma mass spectrometer (ICP-MS) facility at the CSIR-National Institute of Oceanography (CSIR-NIO), Goa. 58
Fig. 3. 11.Multi collector inductively coupled plasma mass spectrometer (MC-ICP-MS) facility at the CSIR-National Institute of Oceanography (CSIR-NIO), Goa..... 63
Fig. 3. 12. Schematic representation of Double spike calibration adopted from Klaver and Coath (2019)..... 66
Fig. 3. 13. Schematic four-isotope diagram illustrating the calibration of a double spike. Solid arrows represent mass-fractionation trajectories, whereas straight line denote mixing lines. Instrumental mass fractionation shifts the measured compositions of the reference material (*n*) and the double spike (*t*) from their true values (*N* and *T*). After applying a first-order IMF correction, the true reference composition (*N*) is obtained. Mixtures (M_k) prepared between *N* and *T* define the N-T mixing line, whose intersection with the mass-fractionation line *t-T* yields the calibrated spike composition. Alternatively, a compositionally distinct reference materi**l** (*E*) and its mixtures can be used to generate a second mixing line (E-T), from which the spike composition can be determined at the intersection of the N-T and E-T lines without requiring measurement of the pure spike. Following a complete mathematical framework for solving the exponential DS equation using matrix algebra combined with an iterative Newton-Raphson scheme provided by Rudge et al. (2009) data was deconvoluted for the Mo isotopic ratio determination. 69
Fig. 3. 14. Conceptual schematic illustrating the double-spike technique in four-isotope space. The natural sample (N) and the double-spike solution (T) lie at distinct positions in

isotope-ratio space and define a mixing array. A mixture (M) formed by combining the sample with the spike plots along this mixing line according to the spike-sample proportion (k). During MC-ICP-MS analysis, instrumental mass fractionation shifts the measured compositions of both the unspiked sample (n) and the mixture (m) along characteristic IMF trajectories. Because the isotopic composition of the spike is known, simultaneous measurement of n and m enables determination of the IMF parameters and reconstruction of the true isotopic composition of the natural sample. 70
Fig. 4. 1. Pore-water and isotopic profiles from cold-seep core SSD045/4/G4. a) Pore-water sulfate and methane concentration profiles; b) Carbon isotopic composition of headspace methane ($\delta^{13}C_{CH4}$); c) Pore-water chloride and chloride-normalized sulfate (×100); d) Pore-water hydrogen sulfide concentration; e) Sulfur isotopic composition of pore-water sulfate and hydrogen sulfide ($\delta^{34}S_{SO42-}$, $\delta^{34}S_{H2S}$). Light blue shading marks sulfate-driven AOM (SD-AOM) pockets; orange shading marks the present SMTZ SD-AOM pocket (modified from Peketi et al., 2022). Blue dashed line indicates the upward migration of H_2S generated at SMTZ. Dashed dark red line represents the seawater SO_4^{2-}/Cl^- ratio. 76
Fig. 5. 1.Morphology of HMC-tubes and arg-crusts. (a) HMC chimneys showing variable diameters (1.2-2.4 cm) and gas flow conduit (gfc); (b) Lateral (wall to center) growth of the carbonate HMC-tube. Numbers 1-5 indicate progressive growth layers in the chimney; (c and d) HMC-bioturbation tube fragments of variable diameter (0.25 -1.7 cm) and lengths (note the tapering ends); (e and f) HMC-bioturbation tubes with gas voids (gv) (inset in figure e) and botryoidal aragonite lining in the gas void (g). HMC-tubes packed with rounded calcareous pelloids; (h) HMC-bioturbation tubes with bifurcation and tapering end structures; (i-k) The black muddy sediment in the seep regions has hollow tubes of variable diameter (0.3-2.3 cm) and length. Inset shows tubular methane hydrate recovered from the gas conduits; (l and m) Cavernous aragonitic crusts with botryoidal aragonite (bAr) lining the cavity walls. The crust is mixed with chemosynthetic shell (sh) fragments and microcrystalline aragonite cement (mArc); (m) represents the magnified image of the botryoidal lining in figure l. 87
Fig. 5. 2.Optical and scanning microscopic imaging of HMC-tubes and aragonite crusts. (a) Micritic HMC (mHMC) with detrital quartz and clay as the non-calcareous component in HMC-tube; (b and c) HMC-tube with pelloids showing presence of gas flow conduits (gfc, white arrows) and void (gv, white arrows) filed or lined with acicular aragonite and radial crystals; (d) SEM image of acicular aragonite (acArg) filling up the gas void in HMC matrix;

(e) Back scattered image of pyrite framboids (Pyr) in the tubular HMC-matrix; (f-j) Pelloids (plt) of HMC filling up the bioturbation tubes. The intra-pelloidal space and gas voids are filled with radial calcite cement and acicular aragonite. The pelloids range in size from 400 to 2000 microns and do not show any internal structures except the presence of detrital grains including clay and organic matter. Figure j represents the magnified image of the pelloids shown in figure i; (k-l) The arg-crust shows the presence of shell fragments (sh) and cavities with microcrystalline aragonite (mcArg = acicular aragonite) and botryoidal aragonite (bAr = botryoidal aragonite). 88
Fig. 5. 3 SEM-EDS data showing cavity filling aragonite in HMC matrix (HMC-tube). The qualitative chemical composition of spots 1, 5, and 6 showed significant Mg, Al, and Si contents along with Ca, whereas aragonite crystals within the cavities (spots 2, 3, 4) showed a significant amount of Sr and negligible presence of Mg, Al, and Si. 89
Fig. 5. 4. The micro-FTIR absorption spectroscopic data of calcite matrix and cavity filling aragonite in HMC-tube samples. The color bands represent different wavenumber ranges (ν1to ν4) for carbonate minerals. Comprising cavity-filling acicular aragonite crystals and the HMC matrix. 90
Fig. 5. 5. Representative FTIR absorption spectra (ν4 band) of HMC-tubes showing the presence of minor dolomite (Dlm) in the calcite matrix 91
Fig. 5. 6. Representative FTIR absorption spectra (□3 band) of acicular cavity filling aragonite and calcite matrix in HMC-tubes. The peak deconvolution shows possible presence of unidentified phases along with aragonite in the cavity fill. Aragonite is also present in the micrite calcite matrix for HMC-13, 22. 92
Fig. 5. 7. Representative FTIR absorption spectra (ν3 band) of acicular cavity filling aragonite and calcite matrix in HMC-tubes. The peak deconvolution shows possible presence of unidentified phases along with aragonite in the cavity fill. Aragonite is also present in the micrite calcite matrix for HMC-27, 31. 92
Fig. 5. 8. (a) Scatter plot showing carbon and oxygen isotope ratios of HMC-tubes and arg-crust samples from SSD045/4 methane seep site. Arg (cal) and HMC (cal) are the calculated $\delta^{18}O$ values of the HMCs and Arg-crust samples in equilibrium with the ambient seawater (3.6°C at a water depth of 1,753 m) and corrected for crystal lattice substitution of Mg. The oxygen isotope ratio of the ambient deep seawater of the Bay of Bengal is adapted from Sengupta et al. (2013). (b) Scatter plot showing variations in HMC-tubes and arg-crust samples using molar ratios of Mg/Ca (mmol/mol) and Sr/Ca (mmol/mol). (c) Scatter plot

between the percentage of aragonite in HMC and Sr/Ca (mmol/mol) molar ratios. (d) Scatter plot showing the variation in HMC-tubes and arg-crust samples using Mg/Ca (mmol/mol) with Ba/Ca (mmol/mol).....94
Fig. 5. 9. Major element (Fe, Mn, Al) and total REE concentrations in HMC-tubes and arg-crust samples from cold seep site SSD045/4 from Krishna-Godavari basin (Bay of Bengal). Leaching of the dry carbonate sample powder was carried out using 5% supra pure acetic acid (Honeywell). a. Scatter plot between ΣREE (ppm) and Al (wt%); b. Scatter plot between ΣREE (ppm) and Mn (wt%); c. Scatter plot between ΣREE (ppm) and Fe (wt%). 95
Fig. 5. 10. (a) PAAS-normalized REE distribution pattern of HMC-tubes. Seawater data of BoB deep waters (black dotted line) is from Yu et al. (2017). (b) $PAAS_{normalized}$ REE distribution pattern of arg-crust. Seawater data of BoB deep waters (black dotted line) is from Yu et al. (2017); (c) Scatter plot showing variation of ΣLREE/ΣHREE ratio with Ce_{anm} in HMC-tubes and arg-crust. (d) (Ce/Ce*) versus (Pr/Pr*) diagram after Bau and Dulski (1996) and Shields and Stille (2001) Shields and Stille (2001). Field I: no anomaly; field IIa: positive La anomaly produces an apparent negative Ce anomaly; field IIb: a negative La anomaly causes an apparent positive Ce anomaly; field IIIa: real positive Ce anomaly; field IIIb: real negative Ce anomaly; field IV: positive La anomaly disguises a positive Ce anomaly. 96
Fig. 5. 11. Major elements (Mn, Fe, and Al) and Ce concentrations of HMC-tubes and arg crust samples from the cold seep site SSD045/4 from Krishna-Godavari basin (Bay of Bengal). a. Scatter plot between Mn (wt%) and Ce (ppm) from HMC-tubes and arg-crust samples. b. Scatter plot between Fe (wt%) and Ce (ppm) from HMC-tubes and arg-crust samples c. Scatter plot between Ba concentrations (ppm) and Eu_{anom} from HMC-21 tubes and arg-crust samples. 97
Fig. 5. 12. REE concentrations and ratios in HMC-tubes and arg-crust samples from cold seep site SSD045/4 from Krishna-Godavari basin (Bay of Bengal). a. Scatter plot between ΣLREE/ΣHREE ratios and ΣHREE (ppm), b. Scatter plot between ΣLREE/ΣHREE ratios and ΣLREE (ppm). 97
Fig. 5.13. A conceptual depositional model showing the formation of aragonite crusts and tubular HMCs at high (advective) and low (diffusive) methane flux scenarios.....105
Fig. 6. 1. a) Concentration profile of chromium-reducible sulfur (CRS, in wt%) from cold seep core SSD045/4/G4. b) Sulfur isotopic composition of CRS ($\delta^{34}S_{CRS}$) from the same core. The double-headed blue arrow represents the current sulfate-methane transition zone

(SMTZ) from Peketi et al. (2022). The shaded region indicates depleted CRS isotope ratios; the white shaded region corresponds to paleo-SMTZs recorded throughout the core. (Note: Shading in panel A is based on $\delta^{34}S_{CRS}$ profile). c) CRS concentration profile (in wt%) from non-seep core SSD045/13/G1. d) Sulfur isotopic composition of CRS ($\delta^{34}S_{CRS}$) from non-seep core SSD045/13/G1. 109
Fig. 6. 2.Concentration profile of the dithionite extractable iron (Fe_D) and oxalate extractable (Fe_{OX}) in the cold seep core (a) and non-seep core (b). DOP values for cold seep (c) and non-seep core (d). Total reactive iron (Fe_{TR}) concentrations from cold seep (e) and non-seep core (f). 111
Fig. 6. 3. a) Concentration profile of total organic carbon in wt% from cold seep core (SSD045/4/G4). c) Concentration profile of total organic carbon in wt% from non-seep core (SSD045/13/G1). d) Carbon isotopic composition of organic carbon ($\delta^{13}C_{org}$) from cold seep core (SSD045/13/G1). 112
Fig. 6. 4. a) Cross plot between TOC (wt%) and CRS wt% from cold seep core. b) Cross plot between TOC (wt%) and CRS wt% from non-cold seep core. 115
Fig. 7. 1. (a) Downcore variations in (a) molybdenum enrichment factors (MoEF), (b) $\delta^{34}S_{CRS}$ of chromium-reducible sulfur, and (c) Mo-isotope ratios (δ98Mo) for core SSD045/4/G4. Light-blue shaded intervals mark molybdenum-enrichment zones (MoEZs) and white shaded intervals correspond to the minor MoEZs and paleo-SMTZs. Red triangles show measured radiocarbon dates. Intrapolated ages are included within the light blue-shaded MoEZs. Pink, light yellow shades, and a dotted black line, respectively demarcate Mo-isotopic ranges for Mn-oxides, Fe-oxides, and seawater. 121
Fig. 7. 2. Vertical profiles representing the a) Molybdenum enrichment factor (Mo_{EF}), b) Uranium enrichment factor (U_{EF}) and c) Molybdenum isotopic composition for the SSD45/13/G1(non-seep core). 122
Fig. 7. 3. (a) Scatter plot of Mo_{EF} versus U_{EF} from core cold seep core (blue circles) and non-seep core (red circles). Black dotted lines indicate the modern seawater Mo/U molar ratio (Mo/U)sw = 3.2), with reference lines for 0.1×, 0.3×, 1×, and 3× seawater fractions. Cross plots of Mo_{EF} versus (b) Mn/Al, (c) Fe/Al, and (d) δ^{98}Mo. 123
Fig. 7. 4. Conceptual model illustrating Mo-enrichment zone (MoEZ) formation and SMTZ migration driven by variable CH_4 flux a) low CH_4 flux and b) high CH_4 flux condition from over-pressured strata along fault-fracture systems in the Krishna-Godavari (K-G) Basin. SWI = Sediment-water interface, SMTZ = sulfate methane transition zone. 123

Fig. 7. 5. a) Figure illustrating the distribution of Mo among different phases in the cold seep environment. Orange arrows highlight high-resolution views of overlapping, closely spaced samples. b) Vertical profiles of phase-specific molybdenum isotopic composition ($\delta^{98}Mo$) from a cold seep core, showing Mo associated with Fe-oxides and pyrite (FeS_2) fractions 128
Fig. 7. 6. a) Cross plot Mo associated with Fe-oxide and pyrite versus total Mo. b) Cross-plot showing Fe-oxides and pyrite-associated Mo (%) from the cold seep core, with Mo contents normalized to the maximum content for each phase. b) Cross-plot between Fe-oxides associated Mo (%) and Mo associated with the residual fraction (%) in the cold seep core. 129
Fig. 7. 7. (a) Cross-plot between Mo isotope ratios of Mo-associated with Fe-oxides and pyrite (FeS_2) and b) Vertical profile showing depth-dependent variations in the isotopic offset ($\Delta\delta^{98}Mo$) between Fe-oxide-bound and pyrite-bound Mo for samples selected across multiple depth intervals. 130
Fig. 7. 8. (a) Cross-plot % of Mo associated with Fe-oxides versus Mo isotope ratios of Fe-oxides-associated Mo and b) Cross-plot % of Mo associated with Fe-oxides versus Mo isotope ratios of pyrite-associated Mo. 131

List of Abbreviations

ANME Anaerobic methane oxidizing archaea

AOM Anaerobic oxidation of methane

APS Adenosine-5'-phosphosulfate

ATP Adenosine triphosphate

AVS Acid volatile sulfur

CRS Chromium reducible sulfur

DIC Dissolved inorganic carbon

DOP Degree of pyritization

DSR Dissimilatory sulfate reduction

EA Elemental Analyzer

FeD Dithionite extractable iron

FeOX Oxalate extractable iron

FeTR Total reactive iron

GC Gas Chromatograph

IRMS Isotope ratio mass spectrometer

ICPMS Inductively coupled plasma mass spectrometry

MC-ICP-MS Multi collector inductively coupled plasma mass spectrometry

OBS Organic bound sulfur

OSR Organo-clastic sulfate reduction

CRS Chromium reducible sulfur

PAPS Adenosine-3'-phosphate-5'-phosphosulfate

PPi Pyrophosphatase

SMTZ Sulfate-methane transition zone

SRB Sulfate reducing bacteria

TC Total carbon

TCD Thermal conductivity detector

TIC Total inorganic carbon

TN Total nitrogen

TOC Total organic carbon

VCDT Vienna Canyon Diablo Troillite

SEM-EDS Scanning Electron Microscopy with Energy-Dispersive X-ray Spectroscopy

FTIR- Fourier Transform Infrared Spectroscopy

VPDB Vienna Pee Dee Belemnite

$\delta^{13}C_{CH4}$ Stable carbon isotope ratio of methane

455 $\delta^{13}C_{DIC}$ Stable carbon isotope ratio of dissolved inorganic carbon

456 $\delta^{13}C$ carbonate-carbon isotope ratio

457 $\delta^{18}O$ carbonate oxygen isotope ratio

458 $\delta^{13}C_{TOC}$ Stable sulfur isotope ratio of total organic carbon

459 $\delta^{34}HS^-$ Dissolved pore water sulfide sulfur isotope ratio

460 $\delta^{34}S_{SO4}$ Dissolved pore water sulfate sulfur isotope ratio

461 $\delta^{98}Mo$ Molybdenum isotope ratio

462 MoEF Molybdenum enrichment factor

463 UEF Uranium enrichment factor

464 arg-crust Aragonite crust

465 HMC- High magnesian calcite

466

467

468

469

470

471

472

473

474

475

476

Abstract

Methane cold seeps along continental margins are dynamic biogeochemical systems where fault-controlled fluid flow, sulfate reduction, and steep redox gradients modulate sediment chemistry. The Krishna-Godavari (K-G) Basin in the Bay of Bengal hosts several such seep provinces associated with over-pressured strata, gas hydrates, and focused fluid migration. This thesis reconstructs Late Pleistocene (<36.4 kyr BP) methane-seepage dynamics in the K-G Basin by integrating pore-fluid chemistry, authigenic carbonate geochemistry, Fe-S-C systematics, and molybdenum (Mo) enrichment and isotopic behaviour. The geological setting lies within the toe-thrust region of the K-G margin, where active faults and over-pressured sediments facilitate advective methane transport and localized seep development

A multi-proxy analytical framework was applied to porewaters, bulk sediments, and authigenic carbonates. Dissolved H_2S concentrations were measured using the Cline colorimetric method, while $\delta^{34}S_{H_2S}$ was determined by precipitating pore-water sulfide as Ag_2S followed by EA-IRMS analysis. Pore-water sulfate and chloride were quantified by ion chromatography. Methane concentrations and $\delta^{13}C_{CH4}$ were obtained using GC-IRMS. Total inorganic carbon (TIC), total organic carbon (TOC), and $\delta^{13}C_{TOC}$ were measured by coulometry and EA-IRMS. Sedimentary sulfur speciation was determined using the chromium-reducible sulfur method (CRS), and the resulting Ag_2S was analyzed for $\delta^{34}S_{CRS}$. Dithionite-leachable (Fe_D) and oxalate-leachable (Fe_{OX}) reactive-iron pools were determined by UV-visible spectrophotometry and atomic-absorption spectroscopy, respectively, and total reactive iron (Fe_{TR}) is reported as sum of Fe_D, Fe_{OX} and pyrite-Fe contents. Major (Al, Mn and Fe) and trace (Mo and U) elements, were measured by ICP-MS. A rigorously calibrated Mo double-spike MC-ICP-MS protocol, established as part of this thesis, enabled precise δ^{98}Mo measurements for bulk sediments and phase-specific extractions.

Pore-fluid profiles of sulfate, methane, chloride, hydrogen sulfide, $\delta^{13}C_{CH_4}$, and sulfur isotopes ($\delta^{34}S_{SO42-}$, $\delta^{34}S_{H_2S}$) reveal a shallow, migratory sulfate-methane transition zone (SMTZ), non-steady sulfate distributions, and strong sulfate-driven anaerobic oxidation of methane (SD-AOM). Upward-diffusing H_2S and chloride anomalies indicate hydrate dissociation and transient fluid-flow events, defining multiple SD-AOM pockets within the upper sediment column. Authigenic carbonates show mixed HMC, aragonite mineralogy, bioturbation-derived tube structures, and REE patterns reflecting changing redox and fluid-flow regimes

This study identifies multiple Mo enrichment zones (MoEZs) interspersed with low-Mo intervals, reflecting alternating redox states linked to episodic SD-AOM intensification and SMTZ migration. MoEZs consistently align with negative $\delta^{34}S_{CRS}$ excursions, demonstrating that Mo enrichment tracks sulfidic pore-water development rather than bulk pyrite accumulation. The coupled Mo_{EF}-δ^{98}Mo-$\delta^{34}S_{CRS}$ systematics record alternating phases of enhanced and diminished methane flux. Periods of high CH_4 advection are characterized by seawater-like δ^{98}Mo (+2.34‰), moderately depleted $\delta^{34}S_{CRS}$, and strong Mo-enrichment near the sediment-water interface, indicative of shallow SMTZ positions and vigorous SD-AOM generating elevated porewater H_2S. Deeper SMTZ intervals with lower δ^{98}Mo (-0.37 to +1.69‰) and strongly depleted $\delta^{34}S_{CRS}$ (-38 to -33‰) reflect subdued H_2S availability, limited Mo capture, and a greater role for Fe-Mn redox cycling.

Chronostratigraphic constraints suggest that individual MoEZs correspond to discrete methane-flux pulses lasting ~0.1 to 4.1 kyr, implying tectonically modulated, rather than steady, seepage. Episodic reactivation of deep faults and fractures associated with shale tectonics periodically enhanced sediment permeability and fluid ascent

The Mo-speciation analysis demonstrates that Fe-oxides and pyrite are the principal phases governing molybdenum sequestration in the cold-seep sediments. Mo initially associates with Fe-oxides under sub-oxic to mildly sulfidic conditions and is subsequently redistributed into the pyrite phase as sulfidization intensifies during burial diagenesis. This transfer is accompanied by systematic isotopic modification, indicating that Mo undergoes measurable fractionation during its transition from oxide-bound to sulfide-bound forms. The seawater-like isotopic composition of Fe-oxide-bound Mo implies the preferential adsorption of reduced Mo sulfur complexes (MoS_4^{2-}) onto Fe-oxide surfaces, while the isotopically enriched pyrite-bound Mo reflects later-stage incorporation under more strongly sulfidic conditions. The vertical evolution from Fe-oxide-dominated Mo to pyrite-dominated Mo thus records progressive sulfidization of the sediment column and provides a sensitive indicator of redox transitions linked to methane-driven diagenesis at the seep site.

Chapter 1 Introduction

1.1. Methane Seeps and Hydrate Dynamics on Continental Margins

1.1.1 Methane cold seeps

Methane cold seeps are widespread features along both active and passive continental margins (Fig. 1.1 & 1.4a), formed where methane (CH_4)-rich fluids ascend through the sediment column and escape across the sediment–water interface (Campbell, 2006; Ceramicola et al., 2018; Feng et al., 2018; Judd & Hovland, 2009; Levin, 2005; Pillutla et al., 2024; Suess, 2018, 2020). These seeps often occur along faults, anticlines, and salt-tectonic structures that channel methane from deep over-pressured strata toward the seabed. Fluid migration is commonly driven by tectonic compression, mineral dehydration, and destabilization of gas hydrates (Levin, 2005; Suess, 2014; Tunnicliffe et al., 2003). Methane in these systems originates from both microbial methanogenesis and thermogenic degradation of buried organic matter (Kvenvolden & Rogers, 2005; Reeburgh, 2007). At the seabed, diffusive and advective fluxes of methane and hydrogen sulfide (H_2S) sustain distinctive chemosynthetic ecosystems under low-temperature conditions (Levin, 2005; Levin et al., 2016). These habitats develop as spatially discrete patches controlled by the geometry of fluid conduits, such as fractures and seep chimneys (Hong et al., 2017). The composition and spatial organization of seep fauna are primarily determined by local CH_4 and H_2S fluxes (Portail et al., 2015), which regulate both microbial activity and faunal zonation. Persistent seepage maintains highly productive benthic communities over geological timescales.

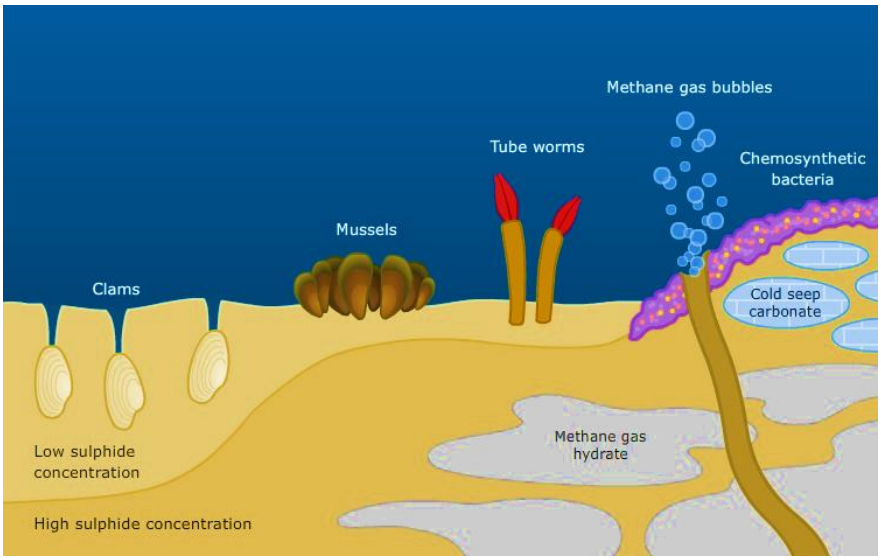


Fig. 1. 1. Schematic illustration of a cold-seep ecosystem showing methane flux, CH_4 ebullition, chemosynthetic fauna (clams, mussels, and tubeworms), and methane-hydrate deposits. Redrawn and adapted from "A diagram of a typical cold-seep community of organisms," Science Learning Hub, University of Waikato.

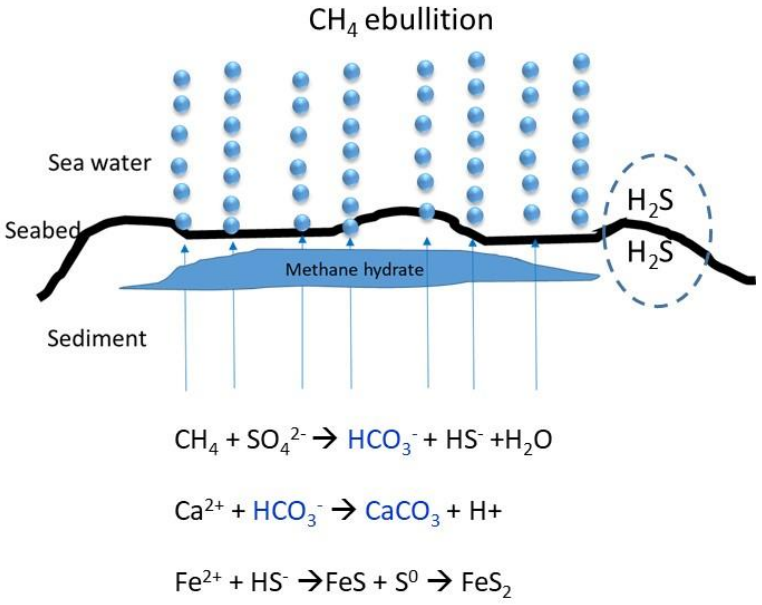


Fig. 1. 2. Schematic representation showing the ebullition of methane (CH_4) from dissociating methane-hydrate deposits and the associated enrichment of hydrogen sulfide (H_2S) in near-seabed sediments within a cold-seep environment. The depicted reactions represent key biogeochemical pathways 1) sulfate-driven anaerobic oxidation of methane (SD-AOM) generating bicarbonate (HCO_3^-) and sulfide (HS^-); (2) precipitation of authigenic carbonate ($CaCO_3$); and (3) formation of Fe-sulfide minerals (FeS, FeS_2) through reaction between dissolved Fe^{2+} and HS^-.

Cold-seep ecosystems have been documented across most continental margins, including the (Fig. 1.4a) Hikurangi Margin (New Zealand), Nankai Trough (Japan), Gulf of Mexico, Congo Angola and Nigerian margins (West Africa), Gulf of Cádiz and Nile Deep-Sea Fan (Mediterranean), Barbados Trench, South China Sea, Nordic margin, Makran margin (Pakistan), and Krishna-Godavari Basin (Bay of Bengal) (Ãstrom et al., 2020; Feng et al., 2020; Mazumdar et al., 2019; Niemann et al., 2009; Sibuet & Olu-Le Roy, 2002; Vanreusel et al., 2009). Similar environments also occur beneath polar ice shelves, such as the Larsen Ice Shelf in Antarctica. Global attention to these systems stems from their roles in modulating carbon cycling, influencing ocean chemistry, and preserving evolutionary

analogues of early life (Le Bris et al., 2016). Recent surveys in the Northern Indian Ocean reveal, for the first time, the association of Lamellibrachia tubeworms with methane-seep-related carbonate chemoherms in the Mannar Basin (within India's EEZ) (Mazumdar et al., 2021). The seep community, developed on inactive carbonate mounds, includes chemosymbiont-bearing bivalves, heterotrophic fauna, and shallow methane hydrate deposits (2-3 mbsf) at a depth of 1,644 m (pressure = 13.9 MPa, temperature = 4.95 °C). Comparable seep systems have been discovered off the K-G Basin, at water depths ranging from 900 to 1800 m, characterized by chemosynthetic assemblages and near-surface gas hydrates (Fig. 1.3).



Fig. 1. 3. (a) Aggregation of Bathymodiolus sp. (indicated as Bm) within black sulfidic sediments collected using spade cores from cold-seep sites; (b, c) Calyptogena sp. exhibiting distinct shell growth laminae; (d) *Conchocele* sp. shell with preserved soft tissue; (e) Acharax sp. shell with soft body intact; (f) Bivalve shell representing the family Pectinidae;

(g) Limpet shell retaining soft tissue; (h) Limpet shell attached to Bathymodiolus sp.; (i) Gastropod shell of the family Provannidae showing soft body (foot); (j) Gastropod shell of the family Neritidae with preserved soft tissue; (k) Tube structure of *Sclerolinum* sp.; (l) Polychaete worm belonging to the family *Glyceridae*; (m) Mantle cavity of *Bathymodiolus* sp. containing the commensal polychaete *Branchipolynoe seepensis*; (n, o) Dorsal views of squat lobsters from the families Galatheidae and *Munidopsidae*; (p) Brittle star of the family *Amphiodia*; (q) Goose barnacle of the genus *Neolepas* attached to Bathymodiolus shell; (r) Enlarged view of *Neolepas* sp. showing the capitulum (adopted from Mazumdar et al. (2019).

Animal-microbe symbioses are crucial to the productivity of cold seeps. Thiotrophic and methanotrophic endosymbionts hosted by bivalves and tubeworms, together with heterotrophic consumers, drive rapid organic carbon turnover and maintain steep chemical gradients. This dynamic coupling of biotic and abiotic processes establishes cold seeps as among the most productive and evolutionarily significant benthic ecosystems on Earth's continental margins (Eilertsen et al., 2018; Wang et al., 2025). Globally, megafaunal biomass at cold seeps exceeds that of surrounding sediments by several orders of magnitude. Dominant taxa include large bivalves (Mytilidae, Vesicomyidae, Lucinidae, Thyasiridae) and vestimentiferan tubeworms, along with pogonophorans, cladorhizid sponges, gastropods, and shrimps (Aguilar Pérez et al., 2024; Li et al., 2023). Infaunal assemblages at greater bathyal and abyssal depths show high population densities and low species diversity, dominated by dorvilleid, hesionid, and ampharetid polychaetes, nematodes, and calcareous foraminifera (Ãstrom et al., 2020; Nanajkar et al., 2022). Cold-seep ecosystems exhibit striking microhabitat heterogeneity linked to redox zonation and fluid flow. Distinct communities form within microbial mats, clam and mussel beds, and tubeworm colonies, reflecting geochemical gradients of CH_4, H_2S, and O_2 (Aguilar Pérez et al., 2024; Xu et al., 2024). Variations in seep intensity and porewater chemistry govern faunal composition, physiological adaptations, and behavioural ecology (Li et al., 2023). In turn, the activity of seep fauna including burrowing, bioirrigation, and shell accumulation modifies sediment texture and redox boundaries, generating strong feedbacks between biology and geochemistry (Nanajkar et al., 2022; Pillutla et al., 2024; Wang et al., 2025).

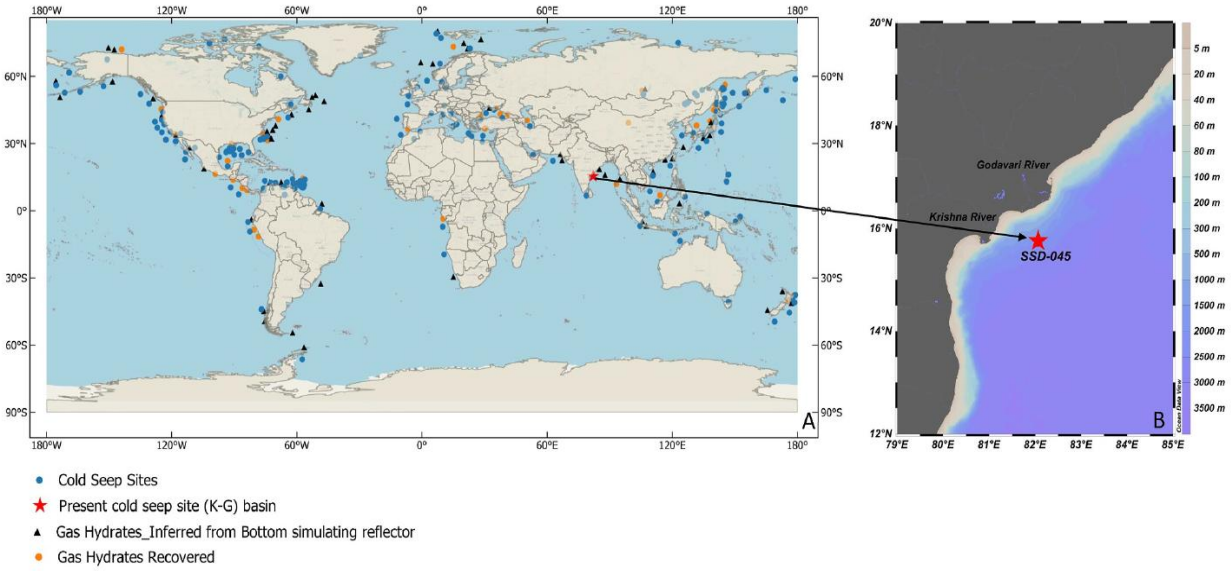


Fig. 1. 4. a) Global distribution of cold seeps and gas hydrates, including the location of the present study site, compiled from Aguilar Pérez et al. (2024), Ruppel and Waite (2020), DFO (2018), Sauer et al. (2021), Syrbu et al. (2024); Syrbu et al. (2022). (b) Regional map showing the cold seep site (SSD-045; red filled star) from Pillutla et al. (2024).

1.1.2 Methane hydrate dynamics.

Cold seeps represent seafloor outlets of methane-rich fluids where gas generated in subsurface sediments migrates upward and escapes across the sediment-water interface (Fig. 1.2 & 1.5). Biogenic methane, produced through microbial degradation of buried organic matter, accumulates in anoxic strata and ascends by diffusion or advection along faults and permeable layers (Archer et al., 2012). Within the gas-hydrate stability zone (GHSZ), part of this ascending methane becomes trapped as crystalline gas hydrates solid clathrates in which water molecules encase CH_4 without chemical bonding (Sloan & Koh, 2008). Hydrate stability (Fig. 1.6) depends on pressure-temperature conditions typical of continental slopes, where low temperature and high hydrostatic pressure prevail.



Fig. 1. 5. Images (a-c) depict natural gas hydrates recovered from cold-seep sites in the K-G Basin, eastern offshore India.

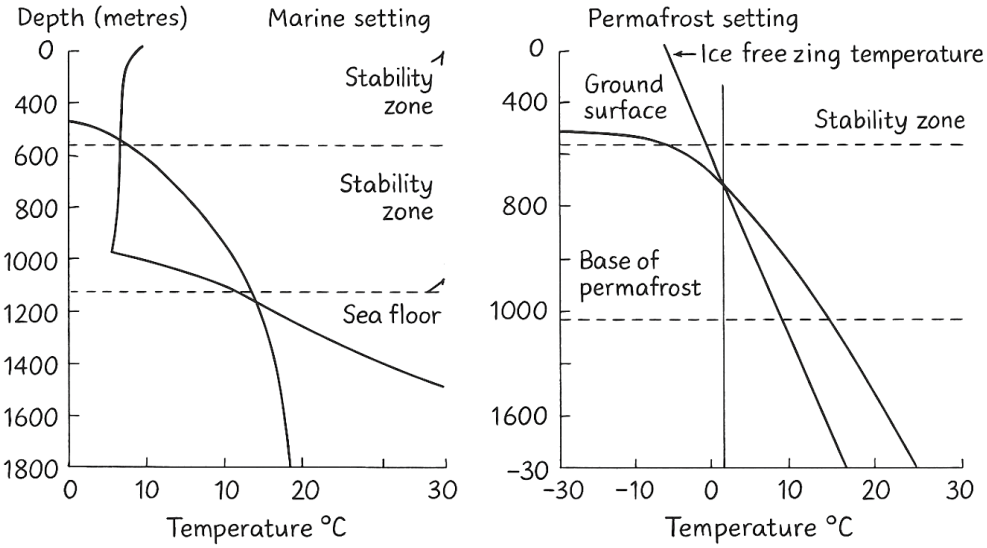


Fig. 1. 6. Diagram illustrating the temperature and pressure conditions governing the methane hydrate stability zone following Eymold et al. (2021)

The base of gas-hydrate stability (BGHS) marks the transition from hydrate to free gas and defines the lower boundary of hydrate occurrence. Acoustic impedance contrasts across this boundary produce bottom-simulating reflections (BSRs) on seismic profiles, signifying a free-gas zone that can extend tens to hundreds of metres beneath the hydrate layer (Bangs et al., 1996; Pecher et al., 1996). Focused fluid flow through fractures or faults can bypass the BGHS, forming near-surface or exposed hydrates at cold-seep sites. These conduits supply methane and sulfide-rich fluids to the seabed, establishing the geochemical foundation for seep ecosystems.

At the seafloor, anaerobic oxidation of methane (AOM) coupled to sulfate reduction converts CH_4 to bicarbonate and H_2S, (Eq. 1.10) generating steep redox gradients that support dense microbial consortia and chemosynthetic fauna (Levin, 2005; Mazumdar et al., 2019). Hydrogen sulfide sustains symbiotic bivalves, tubeworms, and microbial mats, while bicarbonate drives the precipitation of authigenic carbonates that form chemoherms and pavements characteristic of mature seep habitats (Fig. 1.3). Thus, hydrate stability, methane flux, and microbial metabolism are tightly coupled in regulating seep activity and carbonate accumulation (Eq.1.11).

Gas hydrates collectively sequester ~100 to 1000 Gt C, which is 5 to 25 % of Earth's mobile exogenic carbon reservoir (Buffett & Archer, 2004; Wallmann et al., 2012). Perturbations, such as bottom-water warming, sea-level fall, or tectonic uplift, can destabilize hydrates by shifting the BGHS upward, thereby enhancing methane seepage and fueling transient ecosystem expansion. Yet hydrate dissociation is thermodynamically buffered: the endothermic phase change and multiphase fluid diffusion delay large-scale methane release over millennial timescales (Goto et al., 2016).

1. 2. Iron-Sulfur geochemistry at cold seeps

Sulfur (S), carbon (C), and iron (Fe) are key components of marine sediment biogeochemistry at cold seeps. Through microbially mediated redox reactions, these elements drive profound transformations in pore water chemistry, control the precipitation and dissolution of mineral phases, and influence the preservation or degradation of organic matter. Marine sediments function as the ultimate sink for these elements, with their burial depending on external fluxes (e.g., riverine input, sedimentation rates, hydrothermal supply) and internal processes such as sulfate reduction, methanogenesis, and iron mineral reactivity.

1.2.2 Microbial Sulfate Reduction

Modern seawater contains ~28 mM sulfate (Rickard & Luther III, 2007) with a residence time of ~14 Myr (Walker, 1986). Riverine input from sulfide weathering, evaporite dissolution, and carbonate-associated sulfate provides the dominant flux (~10^{14} g yr^{-1}; Bottrell & Newton, 2006), supplemented by minor volcanic and hydrothermal contributions. Oxidation of pyrite is a key reaction supplying sulfate:

$$FeS_2 + 3.5O_2 + H_2O \rightarrow Fe^{2+} + 2SO_4^{2-} + 2H^+ \quad \text{(Eq. 1.1)}$$

$$FeS_2 + 14Fe^{3+}\ 8H_2O \rightarrow 15Fe^{2+} + 2SO_4^{2-} + 16H^+ \quad \text{(Eq. 1.2)}$$

Microbial sulfate reduction occurs via two pathways including assimilatory and dissimilatory sulfate reductions (organo-clastic and anaerobic oxidation of methane):

1.2.2.(i) Assimilatory sulfate reduction:

The assimilatory sulfate reduction occurs in two distinct stages. Initially, sulfate is transported into the microbial cell via specialized sulfate-binding proteins. Once inside, sulfate reacts with adenosine triphosphate (ATP) to form adenosine-5'-phosphosulfate (APS) through the APS pathway (Fig. 1.7). This reaction is catalyzed by ATP sulfurylase.

In the second stage, APS can follow two pathways: one option involves phosphorylation by ATP, converting APS into adenosine-3'-phosphate-5'-phosphosulfate via the action of APS kinase; the other pathway involves APS sulfotransferase, which transforms APS into an organic thiosulfate. This thiosulfate is subsequently reduced, producing the essential sulfur amino acid, cysteine (Zehnder A.J.B. & S.H., 1980).

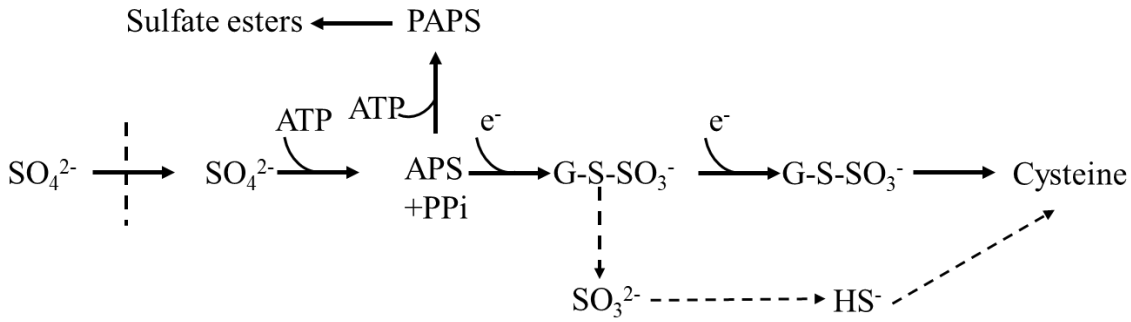


Fig. 1. 7.Schematic representation of the assimilatory sulfate reduction via the APS pathway

In the PAPS (3'-phosphoadenosine-5'-phosphosulfate) pathway, (Fig. 1.3) sulfate reduction leads to the formation of PAPS, which is then reduced to sulfite through the action of PAPS sulfotransferase.

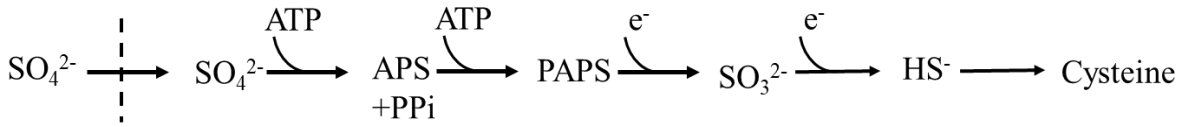


Fig. 1. 8. Schematic of assimilatory sulfate reduction via the 3′-phosphoadenosine-5′-phosphosulfate (PAPS) pathway

Finally, sulfite is reduced to hydrogen sulfide (H_2S) by assimilatory sulfite reductase. Assimilatory sulfate reduction is pivotal in generating organo-sulfur compounds that are vital for cellular metabolism and contribute to biomass production. Cysteine, an end product of this process, acts as a precursor to other sulfur metabolites like homocysteine, methionine, and various sulfur-containing proteins (Andreae, 1990).

1.2.2.(ii) Dissimilatory sulfate reduction process (DSR)

The dissimilatory sulfate reduction process is a microbial process in which sulfate dissociates, leading to the production of hydrogen sulfide (H_2S). This process, which shifts the sulfur valence from +6 to -2 (Canfield et al., 2005; Jorgensen et al., 2019; Madigan et

al., 2000; Mazumdar et al., 2014; Peketi et al., 2015), generates intermediate sulfur compounds such as sulfite (SO_3^{2-}), tetrathionate ($S_4O_6^{2-}$), thiosulfate ($S_2O_3^{2-}$), and elemental sulfur (S^o) (Jorgensen et al., 2019; Zopfi et al., 2004). The free energy yield (ΔG^o) from dissimilatory sulfate reduction is influenced by the organic electron donor used, such as fermentation byproducts like lactate, acetate, formate, and hydrogen (H_2), which are abundant in organic-rich sediments (Bruchert, 2004). This process plays a key role in the global sulfur cycle, especially in the remineralization of organic matter and the formation of pyrite (FeS_2) in sediments, accounting for 12-29% of organic matter remineralization in marine sediments (Bowles et al., 2014; Rickard & Luther III, 2007). The mechanisms of dissimilatory sulfate reduction are illustrated by equations 1.3 and 1.4.

$$SO_4^{2-} + 2CH_2O \rightarrow H_2S + 2HCO_3^- \quad \text{(Eq. 1.3)}$$

$$4H_2 + SO_4^{2-} + H^+ \rightarrow H_2S + 4H_2O \quad \text{(Eq. 1.4)}$$

Dissimilatory sulfate reduction begins with the transport of sulfate across the cell membrane (Fig. 1.9), driven by the concentration gradient and electrical potential difference. In marine environments, sulfate transport systems operate close to equilibrium, given the high sulfate concentrations in seawater (approximately 28 mM) ((Rabus et al., 2006). This initial transport is reversible (Cypionka, 1995). The next step involves the conversion of sulfate to APS through ATP sulfurylase (Eq. 1.5).

$$SO_4^{2-} + ATP + 2H^+ + H_2O \rightarrow APS + 2P_i \ (G^o = -22kJ/mol) \quad \text{(Eq. 1.5)}$$

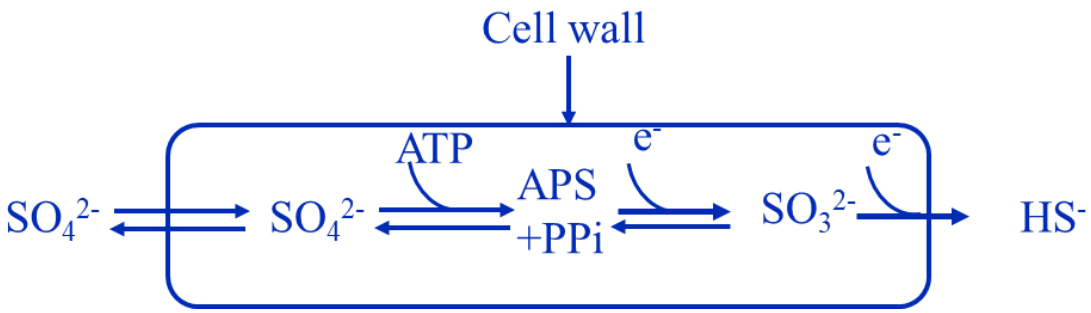


Fig. 1. 9. Dissimilatory sulfate reduction pathway involving PPi hydrolysis by pyrophosphatase

Dissimilatory sulfite reductase (DSR) catalyzes the reduction of sulfite, produced from APS, to sulfide, which is then released into the surrounding environment. This reduction involves the transfer of six electrons from sulfite to sulfide (Eq. 1.6). Some of the sulfide is preserved

as iron-sulfide minerals or incorporated into organo-sulfur compounds, while the rest may be oxidized or transformed into intermediate sulfur species such as elemental sulfur (S^o), thiosulfate ($S_2O_3^{2-}$), and polysulfides (S_x^{2-}) (Berner & Westrich, 1985; Canfield et al., 2005; Chen & Morris, 1972; Jørgensen, 2021; Kasten & Jørgensen, 2000; Thamdrup et al., 1994).

$$SO_3^{2-} + 6e^- + 8H^+ \rightarrow H_2S + 6H_2O \quad \text{(Eq. 1.6)}$$

Sulfide oxidation can occur through microbial processes (e.g., (Eckert et al., 2011; Nielsen et al., 2010; Rao et al., 2016; Raven et al., 2016) or through abiotic reactions with metal oxides such as MnO_2 and FeOOH (Berner & Westrich, 1985; Canfield et al., 2005; Chen et al., 2025; Findlay et al., 2020; Fossing & Jørgensen, 1990 a; Jorgensen et al., 2019; Sekerci et al., 2025; Thamdrup et al., 1994; Yao & Millero, 1993; Yao & Millero, 1995). The sulfur intermediates formed during sulfide oxidation can undergo disproportionation, a process where sulfur compounds like thiosulfate, sulfite, and elemental sulfur are simultaneously converted to both sulfide and sulfate without external electron donors or acceptors (Bak & Cypionka, 1987; Böttcher & Thamdrup, 2001; Canfield, 1994; Habicht et al., 1998) (Bak & Cypionka, 1987; Böttcher & Thamdrup, 2001; Canfield, 1994b; Habicht et al., 1998). Equations 1.7 to 1.9 illustrate the disproportionation of thiosulfate, sulfite, and elemental sulfur, along with their corresponding free energies (Finster, 2008).

$$S_2O_3^{2-} + H_2O \rightarrow SO_4^{2-} + HS^- + H^+ \ (\Delta G^o = -21.9 \text{ kj/mol}) \quad \text{(Eq. 1.7)}$$

$$SO_3^{2-} + H^+ \rightarrow 3SO_4^{2-} + HS^- \ (\Delta G^o = -58.9 \text{ kj/mol}) \quad \text{(Eq. 1.8)}$$

$$4S^0 + 4H_2O \rightarrow SO_4^{2-} + 3HS^- + 5H^+ \ (\Delta G^o = +10.2 \text{ kj/mol}) \quad \text{(Eq. 1.9)}$$

1.2.2.(iii). Sulfate reduction fuelled by Anaerobic Oxidation of Methane (SD-AOM)

The anaerobic oxidation of methane (AOM) in anoxic sediments results in the oxidation of more than 71% of the methane produced, preventing its release into the atmosphere and overlying water (Boetius & Wenzhofer, 2013; Gao et al., 2022; Hinrichs & Boetius, 2002; Jiang et al., 2022; Reeburgh & and Alperin, 1988; Reeburgh, 2007; Zhao et al., 2024). This process is commonly referred to as anaerobic oxidation of methane (SD-AOM). The extent of methane consumption by AOM process is strongly influenced by fluid flow rates, with slow-flowing seeps consuming up to ~80% of the methane, while high-flow seeps may consume less than 20%. Considering the presence of several tens of thousands of active cold seep systems along continental slopes globally, the potential methane flux to the ocean is estimated to be around 0.02 Gt of carbon (Boetius & Wenzhofer, 2013). In addition to

regulating methane fluxes, AOM exerts a strong influence on the global sulfur cycle. Sulfur sequestration in sediments through AOM has been estimated to be nearly twice the previously recognized global burial flux of sulfur in marine settings (Hensen et al., 2003). Accordingly, AOM at cold seep environments along continental margins constitutes a major pathway in both the marine carbon and sulfur cycles.

The oxidation of methane and sulfate reduction are believed to be linked through electron transfer between methanotrophic archaea and sulfate-reducing bacteria, mediated by extracellular cytochromes and nanowire-like structures (Boetius, 2000; Boetius & Wenzhofer, 2013; Hinrichs et al., 1999; Knittel & Boetius, 2009; Knittel et al., 2005; Lapham et al., 2024; McGlynn et al., 2015; Orphan et al., 2001; Scheller, Ermler, et al., 2017; Scheller, Yu, et al., 2017; Wegener et al., 2015; Yu et al., 2022). AOM predominantly takes place at the sulfate-methane transition zone (SMTZ) within marine sediments, which forms a distinct microenvironment where methane and sulfate diffuse to create a habitat for anaerobic methanotrophs (Knittel & Boetius, 2009). The SMTZ is usually found in the upper few meters of sediment and is influenced by factors such as the burial rate of organic carbon, depth of the methanogenesis zone, and methane and sulfate fluxes (Q. Lin et al., 2016; Mazumdar et al., 2009; Raven et al., 2016). AOM results in increased dissolved inorganic carbon (DIC) and alkalinity in pore fluids, leading to calcium carbonate precipitation, as detailed in Eq. 1.10 (Knittel & Boetius, 2009). These habitats often feature distinctive carbonate structures (Aloisi et al., 2002). The AOM process also produces distinctive stable isotope signatures in DIC and methane. Due to the preferential oxidation of the lighter ^{12}C isotope, residual methane in the SMTZ becomes enriched in ^{13}C, while DIC becomes isotopically lighter in the same zone (Knittel & Boetius, 2009). The preferential oxidation of ^{12}C occurs because of the Kinetic Isotope Effect (KIE). Molecules containing the lighter ^{12}C isotope ($^{12}CH_4$) have a higher **zero-point vibrational energy** compared to those with the heavier ^{13}C isotope ($^{13}CH_4$). This higher energy state makes the ^{12}C-H bonds less stable and easier to break during the chemical or microbial oxidation process. Consequently, ($^{12}CH_4$) reacts faster, leading to a residual methane pool that becomes progressively enriched in ^{13}C.

$$CH_4 + SO_4^{2-} \rightarrow HCO_3^- + HS^- + H_2O \quad \text{(Eq. 1.10)}$$

$$HCO_3^- + Ca^{2+} \rightarrow CaCO_3\,(arg/cal) + H^+ \quad \text{(Eq. 1.11)}$$

Anaerobic microbial activity favors the formation of characteristic authigenic minerals associated with the carbon cycle (e.g., carbonate minerals) and sulfur cycle (e.g., pyrite, elemental sulfur), thereby altering the seafloor environment (Aloisi et al., 2002; Jørgensen,

2021; Jorgensen et al., 2019; Luff et al., 2004; Nöthen & Kasten, 2011; Pillutla et al., 2024; Zhang et al., 2014). The resulting carbonate cementation creates hardgrounds that provide suitable substrates for chemosynthetic fauna such as tubeworms and seep mussels, in contrast to the otherwise unstable, mud-dominated seafloor (Bayon et al., 2009; Campbell, 2006; D. Feng et al., 2018; Marlow et al., 2021; Mazumdar et al., 2019; Mazumdar et al., 2011; Mazzini et al., 2006; L. Wang et al., 2021; Zhang et al., 2023).

1.3 Sulfide Oxidation and Disproportionation

Hydrogen sulfide produced during sulfate reduction is either oxidized back to sulfate or trapped in sediments. Oxidation may occur via microbial mediation or reaction with Mn(IV) and Fe(III) oxides, generating intermediates such as elemental sulfur (S^0), polysulfides, and thiosulfate. These intermediates can undergo disproportionation, producing both sulfate and sulfide without an external electron acceptor (Jørgensen, 2021; Jorgensen et al., 2019; Pellerin et al., 2019).

1.4. Sulfide Trapping

1.4.1. Pyritization

Pyrite (FeS_2) is the major long-term sulfur sink in sediments and an important regulator of atmospheric oxygen and seawater sulfate over geological timescales. Pyrite forms through precursor iron monosulfide phases (e.g., mackinawite, greigite) that transform via three possible pathways:

Due to kinetic barriers, pyrite does not nucleate directly but forms through intermediate iron monosulfides ($Fe_{1+x}S$) (Schoonen & Barnes, 1991 (b), 1991(a)). Hydrogen sulfide reacts with Fe^{2+} in pore waters to precipitate colloidal FeS, with mackinawite ($Fe_{1+X}S$), ordered mackinawite (Fe_9S_8), and greigite (Fe_3S_4) acting as key precursors (Liu, 2025; Mansor et al., 2025; Rickard & Luther III, 2007; Rickard & Morse, 2005; Rickard et al., 2017; Schoonen, 2004). Reactive Fe-oxides such as FeOOH and $Fe(OH)_3$ supply Fe^{2+} via reduction by HS^- (Rickard & Luther III, 2007; Theberge & Luther III, 1997). An alternative mechanism involves Fe-HS complexation and subsequent transformation to mackinawite (Rickard, 1995). The precipitation of Fe-sulfides is strongly dependent on Fe-H_2S saturation state and pH (Wilkin & Barnes, 1996). Three main pathways have been proposed for FeS_2 formation from FeS discussed in the following section.

1.4.1.i) Polysulfide pathway

FeS reacts with polysulfide species, derived from elemental sulfur or sulfur oxyanions (Berner, 1970; Luther III, 1991; Schoonen, 2004) (Berner, 1970; Luther III, 1991; Rickard et al., 2017; Schoonen, 2004), forming FeS_2. Experimental work indicates pyrite forms preferentially through polysulfide or colloidal sulfur (Wilkin & Barnes, 1996).

$$FeS + S_X^{2-} \rightarrow FeS_2 + S_{X-1}^{2-} \quad \text{(Eq. 1.12)}$$

1.4.1.ii) H_2S pathway

H_2S reacts with FeS to form $Fe(SH)_2$, which dehydrogenates to pyrite and H_2 gas (Drobner et al., 1990; Rickard et al., 2017; Thiel et al., 2019).

$$FeS + H_2S \rightarrow FeS_2 + H_2 \quad \text{(Eq. 1.13)}$$

1.4.1.iii) Iron-loss pathway

FeS is converted to FeS_2 through partial iron removal by an external electron acceptor such as O_2 (Berner, 1970; Furukawa & Barnes, 1995).

$$2FeS + 1/2O_2 + 2H^+ \rightarrow FeS_2 + Fe^{2+} + H_2O \quad \text{(Eq. 1.14)}$$

1.4.2. Sulfurization of organic matter

In addition to mineral pathways, H_2S is incorporated into organic matter, forming organosulfur compounds that contribute to sulfur storage in sediments (Brüchert, 1998; Brüchert & Pratt, 1996). These reactions enhance organic matter preservation by stabilizing labile biomolecules. Sulfurization occurs via intra- and intermolecular incorporation of sulfur, forming compounds ranging from thiophenes to high-molecular-weight cross-linked structures. Such sulfurization is particularly significant in iron-deficient environments (Vairavamurthy et al., 1994). Organic sulfur forms either directly through H_2S addition or via oxidation intermediates (Berg et al., 2014; Casagrande et al., 1979; Francois, 1987; Mossmann et al., 1991; Werne et al., 2004; Yucel et al., 2017). Polysulfides and elemental sulfur act as important sulfurizing agents during early diagenesis (Mossmann et al., 1991). Sulfur incorporation stabilizes labile organic compounds and enhances their preservation (Sinninghe Damsté et al., 1990; Sinninghe Damsté et al., 1987; Sinninghe Damsté et al., 1986). Two mechanisms operate: intramolecular sulfurization, producing low molecular weight compounds such as thianes and thiophenes, and intermolecular sulfurization, forming high molecular weight polymers via polysulfide linkages (Adam et al., 1993;

Brassell et al., 1986; Kohnen et al., 1989; Werne et al., 2004). Compared to biosynthetic organosulfur, these diagenetic compounds are more refractory and contribute to long-term organic matter preservation (Dinur et al., 1981; Werne et al., 2000).

1.5. Cold seep carbonate geochemistry

Anaerobic oxidation processes account for the generation of HCO_3^- in sediment pore fluids, which increases carbonate alkalinity and subsequently leads to the authigenic precipitation of carbonate structures like chimneys, pavements, mounds, and crusts at methane seep sites (Antler et al., 2014; Gontharet et al., 2007; Nöthen & Kasten, 2011). Authigenic carbonate deposition (Eq. 1.11) at cold seep sites (chemoherms and bioherms) includes a variety of $CaCO_3$ polymorphs such as aragonite (arg), high magnesian calcite (HMC), low magnesian calcites (LMC), dolomite, and calcareous shells. Globally, methane-derived seep carbonates sequester 2.34-5.8 Tmol C/yr in the ocean, accounting for 33%-50% of methanogenic-derived dissolved inorganic carbon (Akam et al., 2023). The formation of cold-seep carbonates is likely to alter the physical properties of sediments, such as porosity, permeability, and density, which in turn impacts the stability of gas hydrates/sediments and fluid migration (Bayon et al., 2009; Mazumdar et al., 2009). According to theoretical and experimental data on carbonate crusts, (Luff et al., 2004; Ye et al., 2019), growth rates can vary from 0.01 to 0.014 cm y^{-1} based on sedimentation rate, bioturbation activity and fluid flow velocity. Carbonate chimneys are expected to expand laterally at a rate of 0.002-0.003 cm^{-1} (L. Wang et al., 2021). Cold seep carbonates preserve information regarding the composition and flow of cold seep fluids (Aloisi et al., 2000; Bayon et al., 2009). Methane hydrate destabilization causes excess pore pressure, which breaks sediment seals and causes Authigenic seep carbonates to become brecciated (Greinert et al., 2001; Mazumdar et al., 2009).

1.6. Molybdenum geochemistry

Molybdenum (Mo) is widely used to trace sulfidic events and serves as a key tool for reconstructing sediment-water interface redox conditions (Algeo & Tribovillard, 2009) Argentino (Algeo & Tribovillard, 2009; Chen et al., 2016; Hlohowskyj, 2021; Hu et al., 2015; Jin et al., 2024; Lin et al., 2021; Miao et al., 2021; Peketiet al., 2012). Molybdenum exists in the form of molybdate (MoO_4^{2-}) in oxygenated seawater conditions. Due to its very long residence time of Mo (440 ky) compared to the sea water mixing time (~1000 yrs) Mo is uniformly distributed with ~10 µg/L in oxic water column conditions (Collier, 1985;

Smedley & Kinniburgh, 2017). Dissolved Mo is adsorbed onto Fe-Mn (oxy)hydroxides and transported to the seabed as hydrogenous Mo fraction of the marine sediments (Barling & Anbar, 2004; Goldberg et al., 2009; Kashiwabara et al., 2009; Kashiwabara et al., 2011; Tanaka et al., 2018; Wasylenki et al., 2008; Wasylenki et al., 2011). Furthermore, laboratory experiments have demonstrated Mo's strong affinity for organic matter under reducing environments and restricted basins (Algeo & Lyons, 2006; Dickson et al., 2020; Wagner et al., 2017). However, Helz and Vorlicek (2019)Helz and Vorlicek (2019) pointed out the uncertainty regarding organic matter's role in Mo enrichment, both field studies in porewater, soils, and sediments.

$$MoO_4^{2-} + H_2S \rightarrow MoO_3S^{2-} + H_2S \rightarrow MoO_2S_2^{2-} + H_2S \rightarrow MoOS_3^{2-} + H_2S \rightarrow MoS_4^{2-} \quad \text{(Eq. 1.15)}$$

Under anoxic-sulfidic pore water conditions, the accumulation of dissolved sulfide in sedimentary pore waters triggers geochemical switch, leading to the conversion of MoO_4^{2-} to thiomolybdate (MoS_4^{2-}; Eq. 1.15) (Erickson & Helz, 2000; Helz et al., 1996; Zheng et al., 2000). Thiomolybdates adsorbed/complexed with pyrite and/or organic matter authigenic enriches Mo contents in the sediments (Bostick et al., 2003; Chappaz et al., 2014; Erickson & Helz, 2000; Helz et al., 1996; Tribovillard et al., 2004; Vorlicek et al., 2018; Wagner et al., 2017; Zheng et al., 2000). Methane Seep settings characterised by excess dissolved sulfide in the pore fluids due to the intense SD-AOM process which promotes thiomolybdate formation (Eq. 1.15), resulting in a notable enrichment of Mo in associated sediments. This Mo-enrichment has earlier been used to track past-methane seepage activities (Chen et al., 2016; Cheng et al., 2015; Jin et al., 2024; Lin et al., 2021; Miao et al., 2025; Miao et al., 2024; Peketi et al., 2012).

The Mo isotope ($\delta^{98}Mo$) of sedimentary pore water, and the overlying water column Mo concentrations as well as isotope ratios has been extensively utilized for examining marine redox conditions during diagenesis (Dahl et al., 2010; Eroglu et al., 2020; Goldberg et al., 2009; McManus et al., 2006; McManus et al., 2002; Nan et al., 2023; Poulson Brucker et al., 2009; Poulson, 2006; Siebert et al., 2006). There is considerable variation in the Mo isotope composition across different sedimentary environments. Under oxic conditions, Fe-Mn (oxy)hydroxides preferentially extract light Mo isotopes from seawater, resulting in a depletion $\delta^{98}Mo$ values in the sediment (Goldberg et al., 2009). On the other hand, in anoxic-sulfide environments, especially when the level of dissolved hydrogen sulfide is greater than 11 μM ($[H_2S]aq > 11$ μM), molybdate (MoO_4^{2-}) is nearly completely transformed into

tetrathiomolybdate (MoS_4^{2-}). This compound is particle-reactive in nature, which may adsorb or complex with pyrite and/or organic material, eventually leading to the burial of Mo. This process leads to minimal fractionation of the Mo isotopic composition, resulting in $\delta^{98}Mo$ values in the sediment that are relatively elevated and similar to those found in seawater, with $\delta^{98}Mo$ = +2.34‰. (Erickson & Helz, 2000; Helz et al., 1996; Hlohowskyj, 2021; Kendall et al., 2017; Nakagawa et al., 2012) (Erickson & Helz, 2000; Hlohowskyj et al., 2021; Jia et al., 2023; Kendall et al., 2017). However, some studies have suggested that elevated Mo contents correspond to the depleted $\delta^{98}Mo$ values, which are attributed to the Fe-Mn shuttle process (Jin et al., 2024; Miao et al., 2025; Miao et al., 2024). The mechanisms governing molybdenum (Mo) sequestration and its isotopic fractionation during diagenesis remain poorly constrained. To address this gap, the present study examines the impact of diagenetic processes on Mo isotopic variability and identifies the potential sinks responsible for Mo retention in marine sediments.

1.7 Aim and scope of the study

This study aims to reconstruct paleo-methane seepage events using multiple proxies, including carbonate geochemistry, sulfur isotopes, and bulk molybdenum (Mo) concentrations and isotopic compositions from a cold seep site in the Krishna-Godavari Basin. In addition, the role of different sedimentary phases-such as carbonates, Fe-Mn oxides, organic matter, pyrite, and silicates-in the sequestration of Mo within seep sediments is systematically investigated.

The research focuses on the following objectives:

1. To decipher the role of depositional and diagenetic processes in the accumulation of Fe-sulfides, organic matter, and carbonate minerals in methane seep sediments.
2. To understand the role of Fe, S, organic matter, and carbonate minerals in sequestration and isotopic composition of Molybdenum in methane seep sediments

1.8 Overview of the thesis

This thesis is structured into eight chapters, each addressing a specific aspect of the study. Chapter 1 introduces cold seep ecosystems, outlining their global distribution, geochemical significance, and the processes governing fluid-sediment interactions. Chapter 2 describes the geological framework of the Krishna-Godavari Basin, with emphasis on tectonic evolution, sedimentation patterns, and their relevance to methane seepage activity. Chapter

3 presents the methodologies and analytical techniques employed in this work, including details of sample collection, preparation, and geochemical analyses. Chapter 4 discusses the pore-fluid chemistry of the sediments, focusing on the biogeochemical processes that operate within the sulfate-methane transition zone (SMTZ). Chapter 5 examines the morphology, petrography, mineralogy, and geochemistry of cold seep carbonates from the Krishna-Godavari Basin in order to reconstruct depositional and diagenetic pathways. Chapter 6 investigates the speciation of iron, sulfur, and carbon in sediments, highlighting their interactions and implications for diagenetic processes. Chapter 7 is dedicated to molybdenum geochemistry, combining bulk concentration and isotopic analyses with speciation studies to evaluate the mechanisms of Mo retention, isotopic fractionation, and their implications for reconstructing paleo-methane seepage events. Finally, Chapter 8 synthesizes the key findings of the thesis, discusses their broader significance, and outlines directions for future research.

Chapter 2 Geology

2.1 Regional setting

The Krishna-Godavari (K-G) Basin is a prominent pericratonic, petroliferous rift basin situated along the eastern continental margin of India, extending from Vishakhapatnam in the north to Ongole in the south and spanning water depths of ~30 to 1600 m (Dewangan et al., 2021). The basin originated during the Early Cretaceous (~130 Ma) as a result of rifting and subsequent drifting of the India-Antarctica-Australia continental block, following the breakup of the Eastern Gondwana landmass (Bastia & Nayak, 2006; Dewangan et al., 2021). The rift-related extension led to the development of northeast–southwest-trending horst and graben systems, which control the subsurface structural configuration of the basin. These structural features were later overprinted by compressional deformation along the continental slope and toe-thrust (Fig. 2.2) fault systems (Bastia, 2007; Dewangan et al., 2010; Dewangan et al., 2021). The basin receives voluminous sediment discharge from the Krishna and Godavari river systems, which deliver detritus eroded from the Deccan Plateau and the Eastern Ghats to the continental margin (Dewangan et al., 2021; Subramanian, 1993). The sediment thickness exceeds 8 km in the offshore region and gradually thins toward the shelf and onshore sectors (Dewangan et al., 2021; Prabhakar & Zutshi, 1993). During the Neogene, the collision of the Indian and Eurasian plates and subsequent uplift of the Himalayas significantly enhanced sediment supply, resulting in accelerated deltaic progradation and rapid margin loading (Dewangan et al., 2021; Krishna et al., 2016). The narrow continental shelf and high sediment influx have promoted the development of shelf-edge deltas, channel-levee systems, and mass-transport deposits (MTDs) (Dewangan et al., 2021; Forsberg et al., 2007; Ramprasad et al., 2011).

2.2 Stratigraphy

The K-G Basin preserves a thick and laterally extensive sedimentary succession ranging from the Early Cretaceous to Recent, deposited in fluvial, deltaic, and deep-marine environments (Bastia & Radhakrishna, 2012; Dewangan et al., 2021; Rao, 2001). The lower stratigraphic units comprise organic-rich shales (e.g., Raghavpuram and Chintalapalu formations), overlain by alternating sand-shale sequences of the Vadaparru and Ravva formations, and capped by Quaternary deltaic clays (Dewangan et al., 2021; Rao, 2001). High Neogene sedimentation rates led to the rapid burial of smectite-rich clays with very low permeability, resulting in the entrapment of pore fluids and the development of abnormally high formation pressures (Dewangan et al., 2021; Rao & Mani, 1993; Singha &

Chatterjee, 2014). The presence of such over-pressured, ductile shale layers has facilitated gravity-driven shale tectonism, particularly across the upper and middle slope regions (Bastia, 2006; Choudhuri et al., 2010; Dewangan et al., 2021).

2.3 Sediment supply and catchments.

Detrital input is overwhelmingly sourced from the Krishna and Godavari rivers. The Krishna catchment (~258,948 km²; 13° to 19°30′ N, 73°23′ to 80°30′ E) rises in the Western Ghats (~1337 m asl) and delivers ~67.72 × 10^6 t yr^{-1} of sediment with ~69.81 km^3 yr^{-1} discharge; major tributaries include the Bhima and Tungabhadra (Kumar et al., 2005; Ramesh & Subramanian, 1988). Approximately 80% of the basin is underlain by Archean and younger crystalline rocks, with the remainder comprising the Deccan Traps and recent sediments (Ramesh & Subramanian, 1988). The Godavari catchment (~313,147 km^2; 16° to 18° N, 75° to 83.3° E) originates near Nasik (~1600 m asl) and includes 25 tributaries (e.g., Pranahita, Indravati, Wardha, Manjeera, Sabari). Lithologies are dominated by Deccan Traps (48%) and Archean granites (39%), with Precambrian/Gondwana sediments (11%) and alluvium (2%) (Biksham & Subramanian, 1988; Peketi, 2012). Basin-wide sedimentation rates are highly variable, ~5.7 to 1024 cm kyr^{-1} (Mazumdar et al., 2015).

2.4 Seabed morphology and slope systems.

At the river mouths, a narrow continental shelf exhibits an irregular topography; the shelf break occurs near ~130 m water depth. The continental slope is steep and transitions to a marginal rise at its base (Murthy & Rao, 1990; Peketi, 2012). Numerous canyons and channels funnel slope processes; slumps and turbidity currents are significant sediment vectors that are transferred to the deep sea, with mudflows mapped to a water depth of ~1600 m (Ramana & Ramprasad, 2010; Venkatarathnam & Biscaye, 1973). Fault systems are pervasive across the basin.

2.5 Mass-transport deposits (MTDs) and sub-bottom expression.

High-resolution sub-bottom profiler (SBP) and seismic data reveal both Holocene and pre-Holocene MTDs, prominently within mid-slope mini basins. Their offshore extent is constrained by bathymetric highs mounds and sedimentary ridges interpreted as products of shale tectonism and neotectonics; overlapping truncation of MTDs against these structures supports this control (Dewangan et al., 2011). High but spatially variable sedimentation rates characterize the Holocene drape above MTDs.

2.6 Shale tectonism, growth structures, and plumbing.

Differential loading of thick Neogene sediments on under-compacted shales generated overpressure and gravity-driven shale tectonism, producing shale diapirs, mud mounds, bathymetric ridges, growth faults, and toe-thrust systems (Bastia, 2007; Choudhuri et al., 2011; Dewangan et al., 2010; Dewangan et al., 2011; Rao & Mani, 1993). These structures form a basin-scale fracture–fault network (Fig. 2.2) that serves as a subsurface plumbing system, focusing the upward migration of deep-seated fluids and gas (Dewangan et al., 2010; Dewangan et al., 2021; Dewangan et al., 2011; Pillutla et al., 2024). Geophysical indicators of active fluid flow such as acoustic voids, chimneys, and turbid layers are widely documented (Dewangan et al., 2010; Dewangan et al., 2011). The regional geothermal gradient increases with water depth from ~30 °C km^{-1} at a depth of around 900 m below sea level (mbsl) to ~51 °C km^{-1} at a depth of around 1500 mbsl, with local deviations attributed to fluid advection along faults (Dewangan et al., 2011; Peketi, 2012).

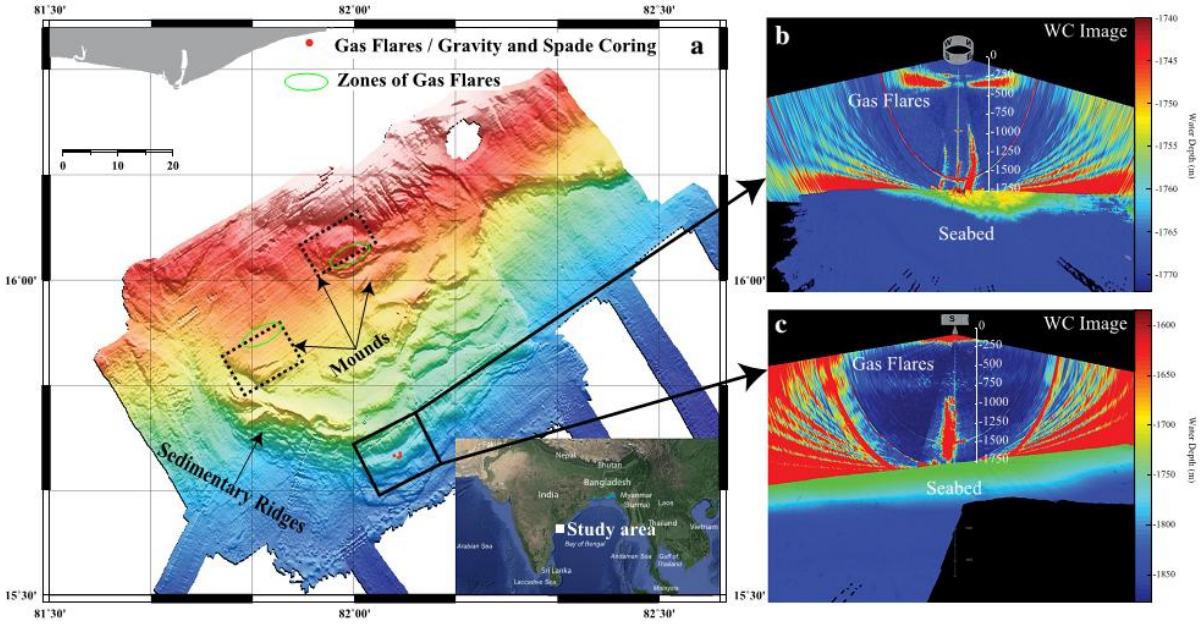


Fig. 2. 1. (a) Bathymetric map of the Krishna–Godavari (K-G) offshore basin showing the locations of active cold-seep sites. The toe-thrust region (solid rectangle) and diapiric mounds (dashed rectangle), where gas flares have been identified, are highlighted on the map. The inset in (a) marks the study area. (b) and (c) show representative water-column (WC) images depicting gas flares rising from the seabed to depths of up to ~700 m below sea level (mbsl) (image adopted from Mazumdar et al. (2019).

2.7 Gas hydrates, cold seeps, and ecosystems.

In K-G basin, methane gas hydrates are widespread in intermediate to deep-water sediments, typically within ~30 to 160 mbsf of the gas hydrate stability zone (Collett et al., 2008). Hydrate accumulations at intermediate depths are commonly concentrated in fault-fracture networks within clay-rich strata, where focused CH_4 flux promotes hydrate precipitation (Dewangan et al., 2021; Mazumdar et al., 2009; Mazumdar et al., 2012; Mazumdar et al., 2011; Pillutla et al., 2024). Recent observations report widespread active methane seepage and well-developed cold-seep ecosystems (Fig. 1.3), consistent with the shale-tectonic and (Fig. 2.2) fracture framework (Dewangan et al., 2021; Mazumdar et al., 2019). Paleo-seepage is recorded by authigenic carbonates and related geophysical facies (Joshi et al., 2014; Mazumdar et al., 2009; Mazumdar et al., 2011; Pillutla et al., 2024). Cold seep sites occur from ~900 to ~1800 m water depth (≈ 9-18 MPa; ~7.15-3.55 °C) and host chemosymbiotic bivalves (Vesicomidae, Mytilidae, Thyasiridae, Solemyidae), siboglinid polychaetes, and provannid gastropods (Mazumdar et al., 2019; Peketi et al., 2022).

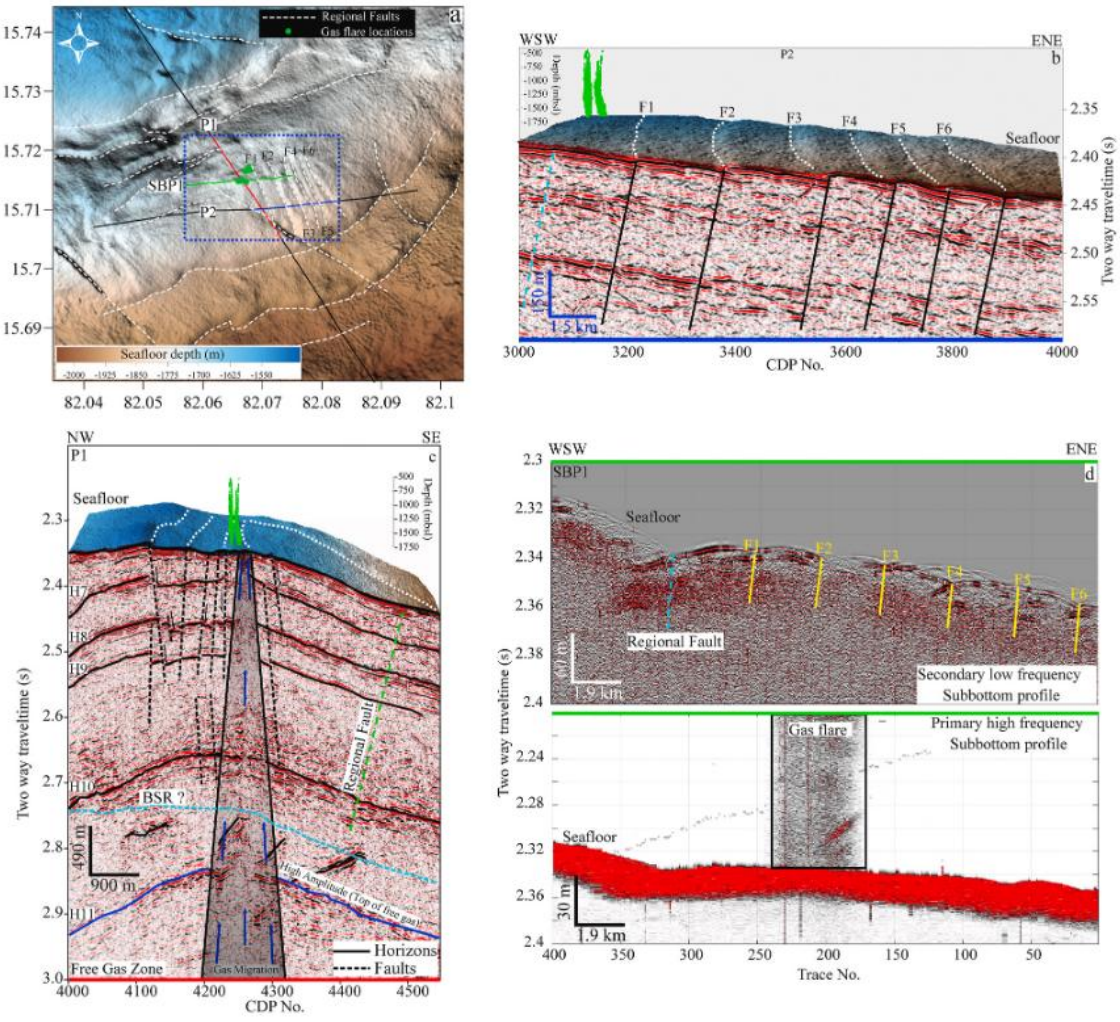


Fig. 2. 2. a) Detailed seafloor morphology map of the toe-thrust region showing high-resolution air-gun seismic profiles (P1, P2), sub-bottom profiler (SBP) data displaying primary high-frequency (PHF) and secondary low-frequency (SLF) components, locations of gas flares (dots), regional faults (dashed lines), and the NE-SW-trending fault system (F1 to F6) enclosed within a dotted rectangular box. The two mutually perpendicular seismic profiles P1 (NW-SE oriented) and P2 (WSW-ENE oriented) are highlighted. (b) Bathymetric surface rendered along seismic profile P2 showing the major fault system (F1 to F6) and their subsurface extensions (solid lines) as imaged in seismic data, along with a regional fault (dashed line). (c) Bathymetric surface along profile P1 highlighting regional faults (dashed lines) and normal vertical faults (dashed lines on the seismic section). A subsurface chimney-like structure (solid lines), coinciding with water-column gas flares, is also marked. Subsurface horizons (H7 to H11, solid lines), a probable bottom simulating reflector (BSR; dashed line between two-way travel time 2.7-2.8 s), and a regional toe-thrust fault between CDPs 4400 and 4500 (dashed line) are indicated. (d) Low-frequency SBP data (SLF) delineate shallow faults (F1 to F6), whereas the high-frequency SBP data (PHF) reveal gas flares within the water column from trace numbers 165 to 240 (adopted from Dewangan et al. (2021).

Chapter 3 Methodology

3.1 Core collection and sub-sampling

During the SSD045 expedition aboard the ORV *Sindhu Sadhana*, gravity cores were collected from a cold seep site (SSD045/St4/G4; 1760 m water depth; Fig. 3.1) and a non-seep site (SSD045/St13/G1; ~1424 m) in the Krishna-Godavari (K-G) Basin, Bay of Bengal, India. Both cores were sub-sectioned at 2 cm intervals and stored at 4 °C for shore-based analyses.

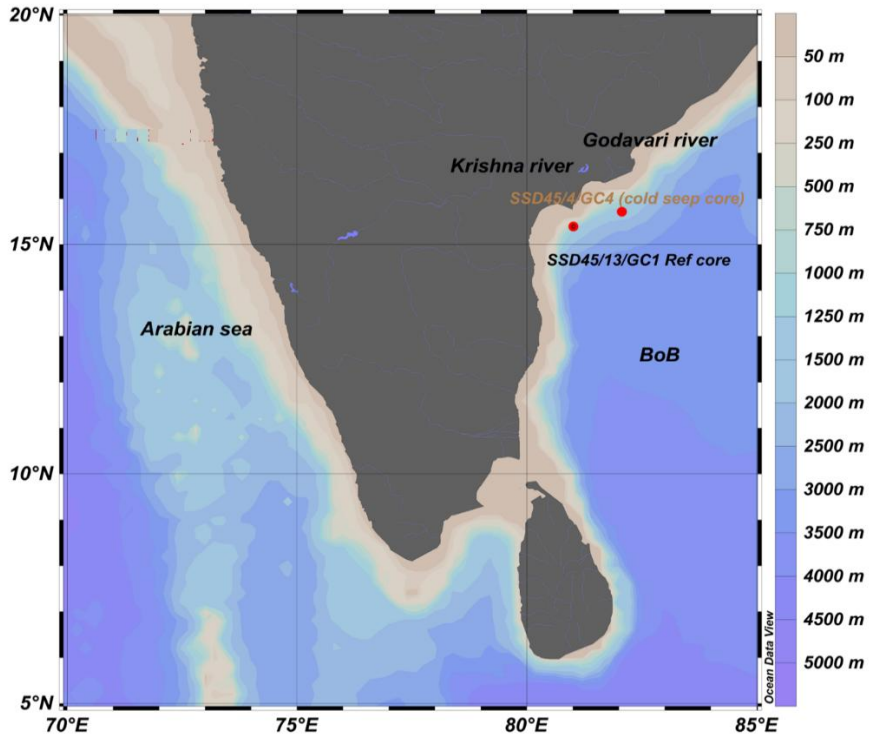


Fig. 3. 1 Location Map showing the cold seep and non-seep core (Reference core) locations from the Krishna-Godavari basin east coast of India BoB refers to Bay of Bengal.

3.1.1 Radiocarbon dating

Radiocarbon dating of the collected sediment core was conducted using Accelerator Mass Spectrometry (AMS) at the Inter-University Accelerator Centre (IUAC), New Delhi, India. Clean, well-preserved shells with open pores of planktic foraminiferal species such as *Globigerinoides ruber* and *G. sacculifer* were selected for analysis. The carbonate shells were treated with phosphoric acid (H_3PO_4) to liberate CO_2, which was subsequently reduced to graphite at 550 °C in the presence of an iron catalyst. These graphite targets were then analyzed using AMS, alongside blanks and internationally recognized radiocarbon standards, including NBS Oxalic Acid I (NIST-SRM-4990) and Oxalic Acid II (NIST-SRM-

4990C). Radiocarbon ages obtained from AMS measurements were calibrated to calendar years Before Present (yr BP) using the CALIB 8.20 software with the MARINE20 calibration curve. To estimate the approximate ages of sediment layers, the linear sedimentation rate equation was applied.

3.2 Headspace methane sampling:

An aliquot of the sediment sample was transferred into ~30 ml glass vials preloaded with 3 mL of NaN_3 to inhibit microbial activity and KOH to trap CO_2. The vials were crimped under a continuous N_2 gas flush and preserved at 4°C for shore-based analysis.

3.3 Pore fluid extraction:

Sediment samples were centrifuged in a Remi C-30 research centrifuge (REMI Laboratory Instruments, Mumbai, India) at 8000 rpm for 15 mins at 4°C. After centrifuging the samples, the supernatant was filtered through 0.22 µm PTFE syringe filters and collected into three separate glass vials for the determination of multiple pore-fluid parameters like sulfate, sulfide and trace metal analysis. The samples were stored for shore-based analysis at 4°C.

3.4 Pore fluid analysis

3.4.1. Determination of headspace methane abundance and isotopic composition

3.4.1.1 GC-IRMS: Working Principle

A gas chromatograph (Thermo-Trace GC Ultra) coupled with a Thermo-Delta V Plus Isotope Ratio Mass Spectrometer through a GC Combustion III interface was employed to analyze hydrocarbon gases (methane) in the headspace, determining both their concentrations and carbon isotopic compositions.

The concentration and carbon isotopic composition of hydrocarbon gases (specifically methane) present in the headspace were analyzed using a gas chromatograph (Thermo-Trace GC-Ultra) coupled to a Thermo-Delta V Plus Isotope Ratio Mass Spectrometer via a GC Combustion III interface. Gas chromatography enables the separation of individual gas components within a mixture based on their varying interactions with the stationary phase. These interactions are influenced by the physical and chemical characteristics of each gas. Once separated, the gases are carried by an inert carrier gas to a detector, which quantifies their concentrations. A typical gas chromatograph (GC) comprises four main components.

(i) Controls and supply of carrier gas:

The carrier gas consisted of ultra-high-purity helium (He, 99.9995% purity), acting as the mobile phase, transporting the sample or standard from the injection port through the column to the detector. It is chemically inert and does not interact with either the stationary phase or the components of the sample.

(ii) Injection port

The injection port is a heated interface that introduces the sample into the carrier gas stream of the gas chromatograph. It rapidly vaporizes the sample to form a uniform vapor plug that enters the column for separation. Precise temperature control prevents condensation and minimizes band broadening. Samples or standards were injected through the port using a gas-tight syringe, while auto samplers ensured reproducible injections in automated runs

(iii) Oven and chromatography column

Separation of the gas mixture in to individual components takes place within the chromatographic column. According to Braithwaite and Smith (2012), the component exhibiting the least interaction with the stationary phase elutes first, while the most strongly retained component elutes last. A PoraPLOT Q column was employed, featuring a length of 30 m, an internal diameter of 0.25 mm, and a film thickness of 0.25 μm. The stationary phase. The stationary phase in the PoraPLOT column consists of a porous polymer layer (e.g., divinylbenzene or styrene-divinylbenzene copolymer) coated on the inner wall of a fused silica capillary. This highly porous surface provides strong adsorption sites for volatile compounds and permanent gases, enabling effective separation based on molecular size and polarity differences.

(iv) Detector

The detector continuously monitors the effluent from the GC column and records changes in its composition as individual components elute. The signal generated is directly proportional to the concentration or amount of each component.

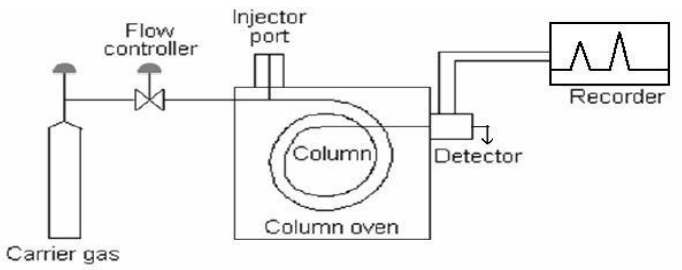


Fig. 3. 2**.** Schematic diagram of the gas chromatograph system

Commonly used detectors in gas chromatography include the flame ionization detector (FID), thermal conductivity detector (TCD), nitrogen-phosphorus detector (NPD), flame photometric detector (FPD), and electron capture detector (ECD).

The gas chromatography isotope ratio mass spectrometry (GC-IRMS) setup configured for this study utilizes the mass spectrometer itself (Thermo Delta V Plus) as the primary detector, completely bypassing these conventional gas chromatography channels. Upon physical separation of the gas sample on the PoraPLOT column, the eluted methane CH_4 peak passes directly into a high-temperature combustion furnace to be quantitatively oxidized to CO_2 gas. This oxidized gas is subsequently introduced into the ion source of the mass spectrometer, where positive ions are generated and accelerated toward earthed multi-Faraday cup collectors which are explicitly discussed in the following sections.

Mass Spectrometer Interface and Principle

In the present analysis, the effluents from the GC column were directed to a mass spectrometer for the detection of carbon isotopic ratios in headspace hydrocarbon gases. Mass spectrometry operates on the principle of separating molecules or isotopes of an element based on their mass-to-charge (m/z) ratios.



Fig. 3. 3**.** A gas chromatograph interfaced with an isotope ratio mass spectrometer.

A typical mass spectrometer comprises three main components:

(i) Ion Source

The ion source ionizes gas-phase molecules introduced from either the gas chromatograph or the elemental analyzer (EA). It contains a heated tungsten or rhenium filament that emits electrons when heated. These electrons are accelerated through a potential difference of 50 to 150 eV, providing sufficient kinetic energy to ionize the incoming sample gas molecules. The exact electron energy depends on the ionization potential and molecular mass of the target species (Hoefs, 2009). A magnetic field within the ion source confines the electrons into a focused beam that interacts with the gas molecules, resulting in the ejection of an electron and the formation of a singly charged molecular ion, as represented in Equation 3.1.

$e^- + M \rightarrow M^{*+} + 2e^-$ (M^{*+} is a radical-cation) (Eq. 3.1)

(ii) Magnetic Analyzer

A magnetic analyzer differentiates molecular ions according to their mass-to-charge (m/z) ratios. When molecular ions are accelerated and enter a magnetic field (B) oriented perpendicularly to an electric field (V), they experience a Lorentz force that bends their trajectory into a circular path. The curvature of this path is mass-dependent lighter ions are deflected more sharply, while heavier ions trace broader curves. This effect results in spatial separation of isotopes.

The Lorentz force FF acting on an ion is described by:

$$F = B \times qv \quad \text{(Eq. 3.2)}$$

This magnetic force is counterbalanced by the centripetal force required to maintain circular motion:

$$F = (mv^2)/r = Bqv \quad \text{(Eq. 3.3)}$$

The ion's velocity arises from acceleration through an electric potential VV in the ion source:

$$qV = (1/2)mv^2 \quad \text{(Eq. 3.4)}$$

Combining these expressions gives the formula for the ion’s circular path radius:

$$r = (1/B) \times \sqrt{(2mV/q)} \quad \text{(Eq. 3.5)}$$

Where:

q is the elementary charge (1.6×10^{-19} C)

B and V are set according to the instrument parameters

Since both B and V are held constant during operation, the radius r becomes directly proportional to the square root of the ion's mass. This allows for effective isotopic separation based on differences in mass-to-charge ratio.

(iv) Detector:

Ion detectors are broadly categorized into single (point) collectors, which record ion beams sequentially by mass, and multi-collector (array) systems, which measure several ion beams simultaneously along the focal plane. The mass spectrometer used in this study, the Thermo Delta V-plus, is equipped with multi-Faraday cup collectors that enable simultaneous detection of isotopic ion beams with high precision. Upon reaching an earthed metal plate, positive or negative ions are neutralized through the acceptance or donation of electrons. The resultant flow of electrons forms a little electric current that can be amplified and utilized to operate a recording device. This current is passed through a high-resistance amplifier (typically 10^{11} Ω), converting the ion current into a measurable voltage signal (recorded in millivolts mV). The software utilizes these voltage intensities to calculate the final isotope ratios. Here, the 'area under the curve' represents the integrated voltage intensity over time (volt x seconds) across the distinct mass traces ((m/z) 44, 45, and 46). This bulk integrated peak area is directly proportional to the total mass of carbon entering the source, enabling the concurrent determination of methane concentration alongside stable carbon isotope ratios ($\delta^{13}C_{CH4}$) directly through the mass spectrometer completely bypassing the need for an external flame ionization detector (FID). The Faraday cup assembly is highly favored because it is simple, robust, and exceptionally reliable when extreme, ion-counting sensitivity is not required. The multi-Faraday cup assembly is highly favored because it is simple, robust, and exceptionally reliable when extreme, ion-counting sensitivity is not required. To ensure analytical stability and prevent background gas interference, the entire detector and flight tube assembly is strictly sustained at a high vacuum of (10^{-6} to 10^{-7}) mbar throughout operation.

3.4.1.2 Procedure for headspace CH_4 gas analysis

The sediment samples taken for headspace hydrocarbon gas measurement were homogenized using a vortex mixer. The concentration and carbon isotopic composition of hydrocarbon gases in the headspace samples were analyzed using a continuous flow isotope ratio mass spectrometer (Delta V Plus, Thermo Fisher Scientific, Germany) connected to a gas chromatograph (Thermo Fisher Scientific, Germany) via a GC-C III interface. A 0.5 mL aliquot of the headspace gas was injected into the chromatographic column in splitless mode for hydrocarbon separation, with helium serving as the carrier gas. The oven temperature was programmed to 25°C for 5 minutes, then ramped from 25°C to 150°C at a rate of 15°C per minute. An external calibration line was established with five distinct gas combinations (CH_4, C_2H_6, C_3H_8, C_4H_{10}, and iso-C_5H_{12}) with concentration standards ranging from 10 to 1000 ppm. Calibration of the laboratory CO_2 tank was performed against the Natural Gas Standard-2 (NGS-2; -44.6‰). Carbon isotope ratios are reported relative to the Vienna Peedee Belemnite (VPDB) standard. The external precision for $\delta^{13}C$ is 0.07-0.09‰ (VPDB).

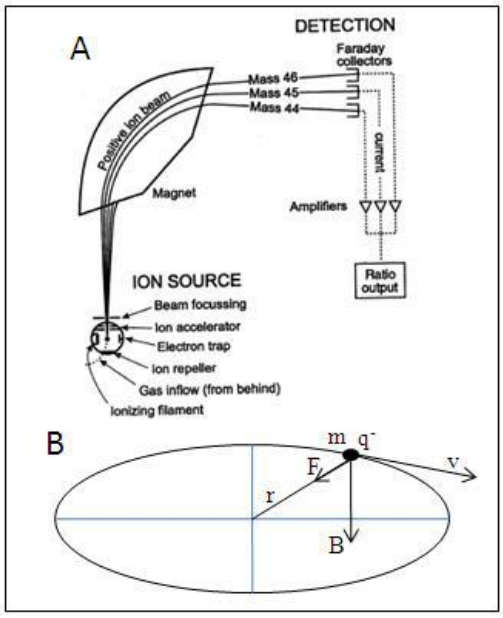


Fig. 3.4 Block diagram demonstrating the fundamental working principle of a mass spectrometer. (a) Isotopic variants of gas molecules are first ionized through electron impact within the ion source. These ions are then accelerated by a strong electric potential and directed into a magnetic field, where they are separated according to their mass-to-charge ratios due to the influence of the Lorentz force. The ions, following curved paths based on their mass, are detected individually by Faraday cups positioned at the end of the flight path. (b) The Lorentz force is illustrated as follows: a positively charged particle (charge q^+, mass

m) moves with velocity v on a flat surface within a magnetic field B that is perpendicular to the motion. The force F, acting at right angles to both the velocity and magnetic field, compels the particle into a circular trajectory with radius r.

3.4.2 Determination of sulfate in pore water samples

3.4.2.1 Ion Chromatograph: Working Principle

Sulfide-free pore water samples were analyzed for sulfate concentrations using ion chromatography. In this study, ion exchange chromatography was employed, which operates on the principle of stoichiometric interactions between ions in a solution and a solid medium featuring functional groups that facilitate ion retention through electrostatic interactions. Initially, the functional groups on the stationary phase are associated with eluent ions to maintain electrical neutrality. Upon injecting the analyte, its ions compete with the eluent ions for binding sites on the stationary phase. Cation separation utilizes sulfonic acid groups, while tetra-ammonium ion groups are used for anion separation in the stationary phase. Charged analytes in the moving solution compete with similarly charged ions from the mobile phase (eluent) for binding sites with opposite charges on the stationary phase. As the mobile phase traverses the stationary phase, ions with a greater affinity for the stationary phase are exchanged and retained. The degree of retention for analyte ions is influenced by various factors, including the characteristics and concentration of eluent ions, the nature of the functional groups, the conditions of the stationary phase, additives in the eluent, and temperature (Coskun, 2016). Effective separation of target analytes is achieved by exploiting their selective interaction with the stationary phase, following the prior removal of interfering matrix components. The time taken from the moment the sample is loaded into the system until the analyte is detected is referred to as the retention time. This parameter is essential for identifying ions as they are detected by the electrochemical detector. The pore water samples introduction onto the chromatographic column to the detector is governed by the pump system.

The eluent and sample are moved through the column and toward the detector using a pump mechanism. The sample is delivered to the analytical column through a software-controlled injector, which can alternate between fill mode, where the sample loop is loaded, and inject mode, where the sample is directed into the column for analysis. The pulsation dampener, connected between the inline filter (which prevents particulates in the analyte from entering

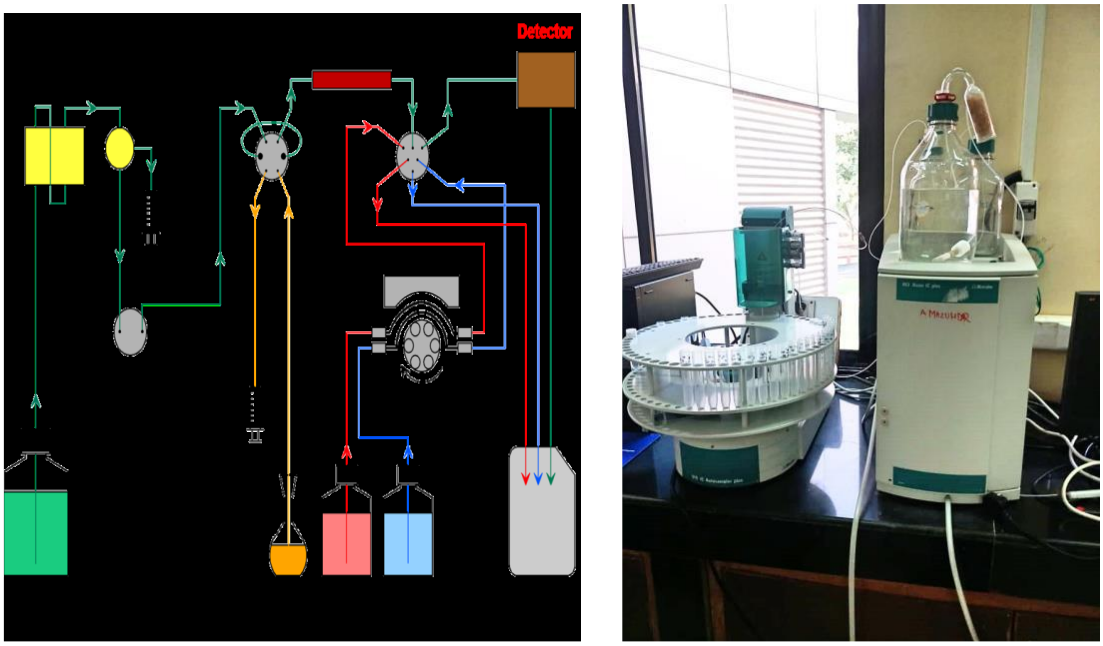
the column) and the injector, smooths the eluent flow and protects the column from pressure fluctuations. These variations can occur during the switching of valves in the system.

In ion chromatography, minimum conductivity is achieved by using a suppressor consisting of three modules. One module allows the analyte to reach the detector, another acidifies the analyte by supplying H^+ ions from dilute sulfuric acid, and the third module directs the waste to the drain. Through ion exchange, this procedure lowers the eluent's conductivity, improving the analytes' sensitivity and precision of detection.

Following chromatographic separation in the column, the eluent is directed into the conductivity detector, where changes in electrical conductivity are measured as ions elute over time. These conductivity variations correspond to the concentration of individual ions in the solution, producing distinct chromatographic peaks used for quantitative determination.

3.4.2.2 Procedure

The aliquots obtained for the ΣHS- concentration measurement were subjected to centrifugation at 7000 rpm for 10 minutes, after which the sulfide-free supernatant was used to determine sulfate concentration. Sulfate ion determination was conducted using a Metrohm ion chromatograph (Basic IC plus 883) equipped with a suppressed conductivity detector (Metrohm, IC detector 1.850.9010) and a Metrosep A Supp 5 (150/4.0) anion exchange column (Metrohm). A mixture of 1 mM $NaHCO_3$ (Merck) and 3.2 mM Na_2CO_3 (Merck) served as the eluent, while 0.2 N H_2SO_4 (Merck) was used as the suppressor regeneration fluid. Prior to analysis, samples were subjected to a 1000-fold dilution with de-ionized water, which had a conductivity of less than 0.06 µS. For quantification, a 10 ppm Fluka mixed anion standard was prepared and used for calibration. The reproducibility of the sample was determined to be ± 0.1%



A B

Fig. 3. 5.(a) Schematic illustration of the Metrohm Basic IC 883 Plus ion chromatograph used for the determination of sulfate ions (Metrohm, India). b) Metrohm Basic IC 883 Plus

3.4.3 Determination of dissolved hydrogen sulfide in pore water samples

For sulfide analysis, porewater samples were sub-sampled into two aliquots immediately after extraction. One aliquot was transferred into glass vials containing 1 M $Cd(NO_3)_2$ under a nitrogen atmosphere to prevent oxidation; dissolved hydrogen sulfide ($\Sigma HS^- = H_2S + HS^-$) was precipitated as CdS and stored for subsequent sulfur isotopic analysis. The second aliquot was used for quantitative measurements of dissolved sulfide concentrations by the spectrophotometric methylene blue method (Cline, 1969). In this method, N, N-dimethyl-p-phenylenediamine dihydrochloride reacts with H_2S in an acidic medium (HCl) in the presence of $FeCl_3$ as an oxidizing agent, producing a methylene blue complex measurable at 670 nm (Chemito Spectrascan UV-2700). Sodium sulfide nonahydrate (≥ 99.99%, Merck) was used to prepare calibration standards. Replicate analyses yielded a precision better than ±5 %, and the detection limit was below 1 µM.

3.4.4 Determination of pore water sulfur isotopic composition

3.4.4.1 Working Principle of an Elemental Analyzer Coupled to an Isotope Ratio Mass Spectrometer (EA-IRMS)

The $\delta^{34}S$ values of pore water sulfate and sulfide were measured using an EA-IRMS system (Thermo EA 1112). In this setup, the elemental analyzer introduces the sample encapsulated in tin foil into a high-temperature reactor tube. Upon sample injection, combustion is initiated and intensified by an oxygen pulse, converting the sample into a mixture of gaseous

products. These combustion gases are then directed through a chromatographic column, where they are separated into individual components. To prevent water vapor generated during combustion from interfering with chromatographic separation, a magnesium perchlorate trap is employed to remove moisture.

Detection of the separated gases is carried out by a thermal conductivity detector (TCD). The Thermo EA 1112 consists of four primary modules: (i) an autosampler for continuous sample loading, (ii) a reactor tube housed within a furnace, (iii) chromatography column for separation, and (iv) the TCD for detection. A schematic layout of the elemental analyzer is shown in Fig. 3.6. The analyzer is interfaced with the isotope ratio mass spectrometer via a ConFlo IV interface. The working principle of the mass spectrometer is described in Section 3.4.1.1.

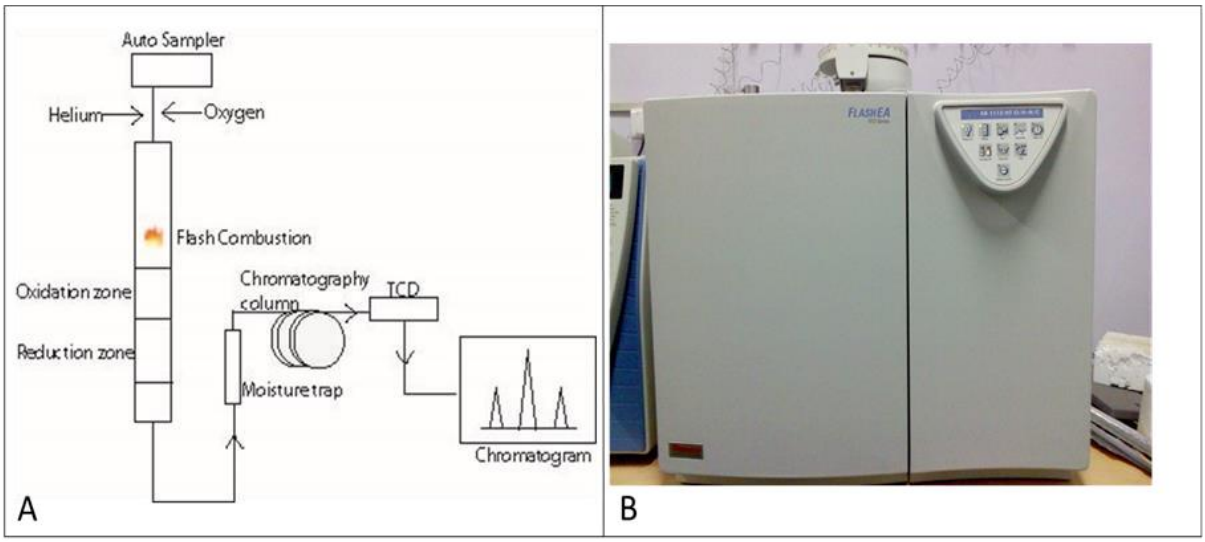


Fig. 3. 6. (a) Schematic illustration of the elemental analyzer, showing the fundamental working principle, including sample combustion, gas separation, and detection. (b) Photograph of the Thermo EA 1112 elemental analyzer used in this study.

3.4.4.2 Procedure for the determination of sulfate sulfur isotope ratio ($\delta^{34}S_{SO42-}$) of pore water sulfate

For the analysis of sulfate sulfur isotopes ($\delta^{34}S$), pore water sulfate was precipitated as barium sulfate ($BaSO_4$) by adding 1 mL of 1 M $BaCl_2$ solution. The resulting precipitate was filtered using a 0.22 µm nitrocellulose membrane filter (Millipore). Following multiple rinses with deionized water, the filter paper was transferred into 10 mL glass vials. After air-drying, the vials were placed in a Heraeus muffle furnace (Model M-110) at 550°C for one

hour to combust the nitrocellulose, which was completely oxidized to CO_2, leaving only $BaSO_4$ behind. Once cooled, the remaining precipitate was analyzed for $\delta^{34}S$ using a Thermo EA coupled with a Thermo Delta V Plus isotope ratio mass spectrometer (IRMS) via continuous flow, and connected to an elemental analyzer (Thermo EA1112). Prior to analysis, $BaSO_4$ was homogenized with V_2O_5, encapsulated in tin capsules, and combusted at 1150°C to produce SO_2 gas. Isotopic values are expressed in standard delta (δ) notation relative to the Vienna Canyon Diablo Troilite (VCDT) standard, with an analytical precision of ± 0.3‰. Calibration was performed using IAEA reference materials SO-5 ($BaSO_4$: +0.5‰ VCDT), SO-6 ($BaSO_4$: -34.1‰-VCDT), S-1 (Ag_2S: -0.3‰-VCDT), and S-2 (Ag_2S: +22.7‰-VCDT).

3.4.4.3 Procedure for determination of pore water sulfide ($\delta^{34}S_{H2S}$)

A separate aliquot of pore water was used to determine the $\delta^{34}S$ isotopic composition of dissolved sulfide. Sulfide was first precipitated as cadmium sulfide (CdS), which was then collected on a 0.22 µm nitrocellulose membrane filter. To convert CdS to silver sulfide (Ag_2S), a silver nitrate ($AgNO_3$) solution was carefully added dropwise onto the filter. The resulting Ag_2S precipitate was analyzed for its stable sulfur isotopic composition ($\delta^{34}S$) using a Thermo Delta V Plus isotope ratio mass spectrometer (IRMS) coupled with a Thermo EA1112 elemental analyzer via a continuous flow interface. Prior to combustion, Ag_2S was homogenized with vanadium pentoxide (V_2O_5), encapsulated in tin, and combusted at 1150°C to generate SO_2 gas for IRMS detection. The $\delta^{34}S$ values are reported in delta notation relative to the Vienna Canyon Diablo Troilite (VCDT) standard, with a measurement reproducibility of ± 0.3‰.

3.4.5 Quantification of total inorganic carbon (TIC):

3.4.5.1 Coulometer: Working Principle

The total inorganic carbon (TIC) concentrations in sediment samples were determined using a UIC CO_2 coulometer (Model 5014). This analytical system operates on the principle of coulometric titration, where the quantity of carbon dioxide is indirectly measured through the electrochemical generation of a titrant.

The titration cell contains a partially aqueous electrolyte comprising ethanolamine and a pH-sensitive colorimetric indicator. Carbon dioxide from the sample reacts with ethanolamine to form a titratable weak acid, which alters the solution's color. A photometric detector continuously monitors the absorbance (expressed as percent transmittance, %T) of the

solution. As the acid concentration increases, the indicator fades, leading to an increase in %T. When the %T surpasses a set threshold, a feedback loop triggers the generation of hydroxide ions (OH^-) via electrolysis at the cathode, at a rate proportional to the change in %T. Titration continues until the %T stabilizes at a predefined baseline value (typically 29%).

The total amount of electric charge passed during the titration is used to calculate the TIC content, based on Faraday's First Law of Electrolysis, which relates the amount of substance altered at an electrode to the total electric charge transferred.

The primary chemical reactions involved in the coulometric cell include:

1. Absorption of CO_2 by ethanolamine (cathode reaction):

$$CO_2 + HOCH_2CH_2NH_2 \rightarrow HOCH_2CH_2NHCOOH \quad \text{(Eq. 3.6)}$$

2. Electrochemical generation of hydroxide ions at the cathode:

$$2\ H_2O + 2\ e^- \rightarrow H_2(g) + 2\ OH^- \quad \text{(Eq. 3.7)}$$

3. Neutralization of the absorbed CO_2-acid complex by OH^-:

$$HOCH_2CH_2NHCOOH + OH^- \rightarrow HOCH_2CH_2NHCOO^- + H_2O \quad \text{(Eq. 3.8)}$$

4. Anode oxidation reaction:

$$Ag^0 \rightarrow Ag^+ + e^- \quad \text{(Eq. 3.9)}$$

3.4.5.2 Procedure

The total amount of inorganic carbon in the samples is determined using a carbon coulometer (CM5130). Approximately 15 mg of desalinated sediment was added to the reaction tube. An acid dispenser dispensed approximately 5 ml of 1N HCl into the tube. The CO_2 released from the sample upon adding acid is transported by the carrier gas (nitrogen) to the coulometric cell for measurement. The coulometric cell comprises a partly aqueous media with ethanol amine and a colorimetric indicator. Carbon dioxide combines with ethanolamine to produce a potent titratable acid that results in the fading of the indicator's color. A photodetection system observes the variation in the solution's color as a percentage of transmittance (%T). As the %T rises, the titration current is automatically initiated to electrochemically produce the base at a rate commensurate with the %T. Titration concludes when the %T attains the background value of 29%. The TIC concentration in the sample is determined according to Faraday's first law, which asserts that the quantity of substance released (or dissolved) at the electrodes of a cell is directly proportional to the amount of electricity that traverses the solution. Ultrapure calcium carbonate (Sigma-Aldrich) served

as the calibration reference for the coulometer. The standard repeatability was 12.0 ± 0.25 %.

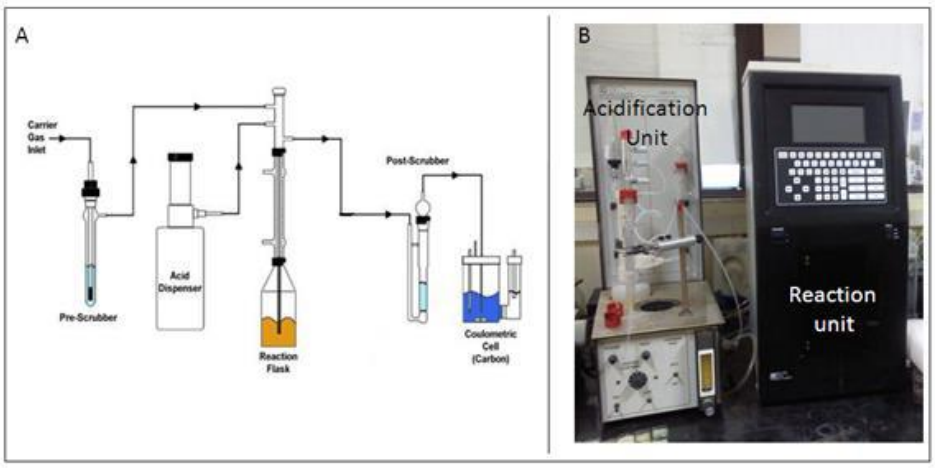


Fig. 3. 7. a) Schematic representation of the coulometer illustrating its working principle. b) Carbon coulometer.

3.4.6 Determination of total organic carbon (TOC) and total nitrogen (TN)

Sub-samples of sediment were subjected to desalination, drying, and homogenization. A sample weighing 8-10 mg was encapsulated in a tin capsule and inserted into the reactor tube of the elemental analyzer using an autosampler. The operational principle of EA is detailed in section 3.4.4.1. Samples were incinerated with a surge of oxygen at 1050°C. Flash combustion due to the exothermic oxidation of Sn to SnO elevated the reactor tube temperature to approximately 1500°C for a brief duration. The carbon and nitrogen in the sample were transformed into CO_2 and NO_x. NO_x was converted to N_2 in the reduction section of the reactor tube. CO_2 and N_2 were subsequently isolated from additional gaseous contaminants using a chromatography column at 60°C. A thermal conductivity detector (TCD) was employed to quantify the segregated CO_2 and N_2. 2,4-Dinitrophenylhydrazine (2,4-DNP). Total organic carbon was determined by deducting total inorganic carbon from total carbon. The reproducibility of total carbon (TC) in the NIST-SRM1944 sediment standard was determined to be 4.4 ± 0.2 %, whereas total nitrogen (TN) in the MAG-1 sediment standard was measured at 0.24 ± 0.03 %.

3.4.7 Determination of carbon isotopic ratio of organic carbon ($\delta^{13}C_{TOC}$)

$\delta^{13}C_{TOC}$ was quantified using an elemental analyzer (Thermo EA 1112) linked to a Delta V Plus isotope ratio mass spectrometer using a continuous flow system (ConFlo IV). The operational principles of EA and IRMS are detailed in sections 3.4.4.1 and 3.4.1.1,

respectively. Approximately 2 mg of decarbonated sediment was enclosed in a tin capsule and incinerated in the reactor. The ratios of carbon isotopes in CO_2 are repeatedly analyzed. Isotopic compositions are reported in mil (‰) deviations from the VPDB (Vienna PeeDee Belemnite) and are provided in standard δ notation.

3.4.8 Analytical Protocol for Sulfur Speciation in Sediments

3.4.8.1 Extraction and determination of acid volatile sulfur (AVS) and chromium reducible sulfur (CRS)

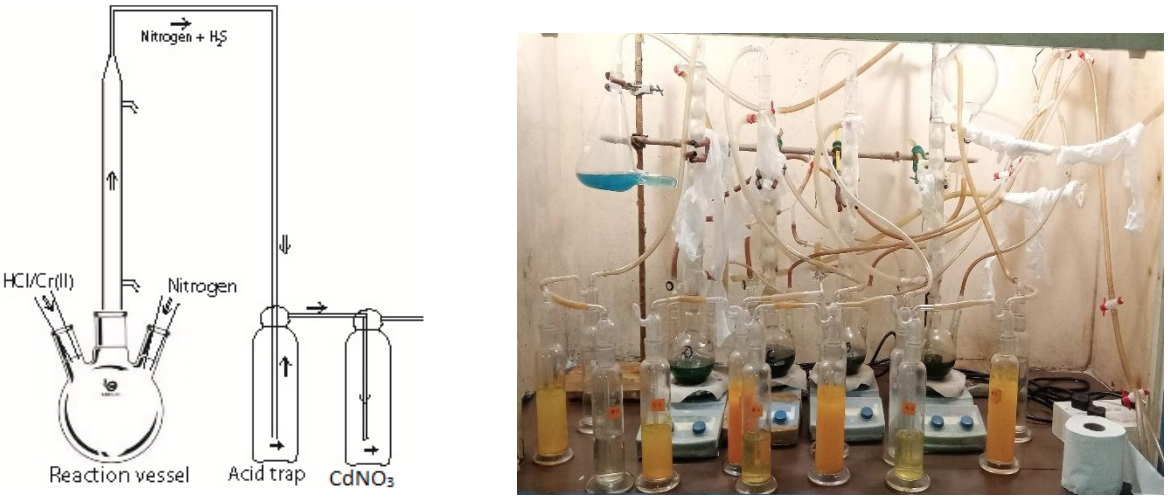
Sequential extraction of acid-volatile sulfur (AVS) and chromium-reducible sulfur (CRS) was performed using custom-built sulfide extraction units (Fig. 3.10). AVS was isolated by boiling sediment samples in 50 mL of cold 6N hydrochloric acid under anoxic conditions. Oxygen-free conditions were ensured by continuously purging the reaction vessels (round-bottom flasks) with high-purity nitrogen gas, following the procedure described by (Chanton & Martens, 1985). Under these conditions, acid-labile iron sulfides (e.g., FeS) were converted to hydrogen sulfide (H_2S), as represented by Equation 3.10. Once AVS extraction was complete, a chromium (II) chloride ($Cr^{+2}Cl_2$) solution was introduced into the reaction flask under a nitrogen atmosphere. The $CrCl_2$ solution was prepared in-house by reducing a 1 M $CrCl_3$ solution in 6N HCl with zinc granules. Throughout the procedure, the system remained anoxic due to continuous nitrogen flushing. Boiling the sediment now free of monosulfides in $CrCl_2$ solution led to the reduction of iron disulfides (e.g., FeS_2), releasing additional H_2S according to Equation 3.11 (Canfield et al., 1986). The H_2S evolved during both AVS and CRS extraction steps was carried by nitrogen gas into separate gas-washing bottles containing cadmium nitrate ($Cd(NO_3)_2$) solution. Here, H_2S was trapped and precipitated as cadmium sulfide (CdS), as shown in Equation 3.12. Distinct collection bottles were used for AVS derived and CRS derived H_2S to prevent cross-contamination. Subsequently, the CdS precipitate was converted to silver sulfide (Ag_2S) via reaction with silver nitrate (Eq. 3.13). The Ag_2S was then boiled, filtered, thoroughly washed, dried, and weighed to determine sulfur content gravimetrically.

$$FeS + HCl \rightarrow H_2S \quad \text{(Eq. 3.10)}$$

$$4HCl\ (con.) + Cr^{2+}Cl_3 + FeS_2 \rightarrow FeCl_3 + Cr^{3+}Cl_3 + 2H_2S\ (\uparrow) \quad \text{(Eq. 3.11)}$$

$$H_2S + Cd(NO_3)_2 \rightarrow CdS + 2HNO_3 \quad \text{(Eq. 3.12)}$$

$$CdS + 2AgNO_3 \rightarrow Cd(NO_3)_2 + Ag_2S \quad \text{(Eq. 3.13)}$$



A **B**

Fig. 3. 8.(a) Diagram of the sulfur extraction apparatus highlighting the H_2S transfer pathway, and (b) setup used for sequential AVS and CRS extraction.

3.4.8.2 Extraction of organic bound sulfur

For the determination of organic bound sulfur (OBS), the sediment residue free from AVS + CRS was combusted at 850°C for two hours by mixing a specific amount of the sediment residue with Eschka's mixture (a 2:1 weight ratio of MgO to Na_2CO_3, Merck, analytical grade). Eschka's mixture effectively oxidizes and solubilizes all sulfur, particularly OBS, remaining in the residue treated with Cr(II) (Tuttle & Goldhaber, 1986). Following combustion, sulfate was recovered by dissolving the residue in hot water, and subsequently precipitated as $BaSO_4$ by adding 20 ml of a 10% $BaCl_2$ solution. The solution was adjusted to an acidic pH before the addition of $BaCl_2$ to prevent the precipitation of carbonates. The barium sulfate suspension was boiled for one hour and maintained at approximately 90°C overnight to facilitate the coarsening and purification of the barium sulfate crystals. The barium sulfate precipitate underwent filtration, was thoroughly washed with distilled water, dried, and subsequently weighed to quantify the OBS.

3.4.8.3 Measurement of Stable Sulfur Isotopes ($\delta^{34}S$) in Extracted Sulfur Phases

A Thermo Delta-V-plus isotope ratio mass spectrometer with a continuous flow system and connected to an elemental analyzer (Thermo EA1112) was used to determine the stable sulfur isotopic composition of the extracted sulfur species. Sections 3.4.4.1 and 3.4.1.1 provide the working principles for EA and IRMS, respectively. A mixture of the $Ag_2S/BaSO_4$ precipitate and V_2O_5 was combusted at 1150°C to yield SO_2. All results are

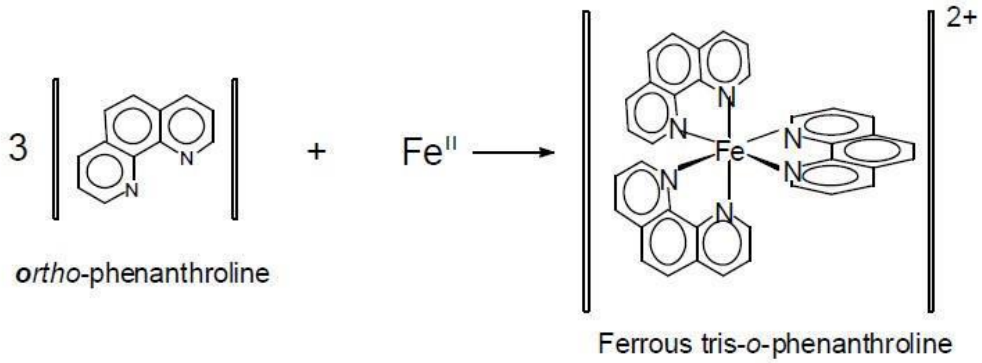
provided in conventional delta notation ($\delta^{34}S$) as per mil deviations from the VCDT (Vienna Canyon Diablo Troilite). Sample repeatability was ± 0.3‰.

3.4.9 Procedure for total reactive iron (Fe_{TR})extraction and degree of pyritization (DOP) Calculation

3.4.9.1 Dithionite extractable iron

The dithionite-leachable iron (Fe_D) in the sediment, predominantly derived from highly reactive iron oxides (ferrihydrite, lepidocrocite, goethite, and hematite), was extracted using a buffered sodium dithionite solution, as per the methodologies of Mehra and Jackson (1960), and Canfield (1989). The samples were agitated with 20 ml of dithionite solution for two hours. The two-hour extraction duration was systematically established by quantifying the Fe removed from a test sample at 30-minute intervals over a span of 7 hours. The results are illustrated in Figure 3.12. The Fe_D content did not exhibit a substantial increase after 120 minutes. A Chemito spectrophotometer (Spectroscan UV 2700) was used to measure the extracted iron by ferrozine-complexometry. An orange-red complex, ferrous tris-o-phenanthroline $[(C_{12}H_8N_2)_3Fe]^{2+}$, is formed when 1, 10-phenanthroline interacts with Fe^{2+} ions in ferrozine complexometry (Eq. 3.10). In the pH range of 2 to 9, the color remains constant and its intensity is unaffected by activity. The addition of hydroxyl amine hydrochloride reduces any Fe^{3+} ions in the sample to Fe^{2+} (Eq. 3.14, (Vogel & Bassett, 1987). Absorbance was quantified using a Chemito spectrophotometer (Spectroscan UV 2700) at a wavelength of 515 nm. Using analytical-grade ferrous ammonium sulfate (Merck), calibration standards were made.

$$2Fe^{3+} + 2NH_2OH + 2OH^- \rightarrow 2Fe^{2+} + N_2 + 4H_2O \qquad \text{(Eq. 3.14)}$$



3.4.9.2 Oxalate extractable Iron:

The magnetite-bound iron (Fe_{OX}) was extracted from the Fe_D-free residual sediment by leaching it for 6 hours with 0.2 M ammonium oxalate buffer (3.2 pH), following (Poulton

& Canfield, 2005). The samples were subjected to centrifugation at 7000 rpm for 15 minutes, and iron concentrations in the supernatant leachate were quantified using an atomic absorption spectrophotometer (Agilent: 200 Series AA). The repeatability for both the standard and sample of Fe was 0.3%. The Fluka AAS iron standard was used to prepare the calibration line.

3.4.9.3 Computation of Fe_{TR} and DOP:

The total ferrous iron (Fe_{TR}) is determined by adding the ferrous extractable (Fe_D), ferrous leachable (Fe_{OX}), and pyrite iron (Fe_{CRS}) components, as shown in Eq. 3.15. Fe_{CRS} is derived from the stoichiometry of FeS_2 within CRS compositions.

$$Fe_{TR} = Fe_D + Fe_{CRS} + Fe_{OX} \quad \text{(Eq.3.15)}$$

The degree of pyritization is determined as follows:

$$DOP = Fe_{CRS}/Fe_{TR} \quad \text{(Eq.3.16)}$$

Fe_{CRS} denotes pyritized iron, while Fe_D signifies current reactive iron (Leventhal & Taylor, 1990).

3.4.10 Inductively Coupled Plasma Mass Spectrometry (ICP-MS)

Inductively Coupled Plasma Mass Spectrometry (ICP-MS) is a highly sensitive technique widely employed for trace element quantification and isotopic studies. It is extensively applied in disciplines such as geochemistry, environmental science, materials research, and biological studies. The technique combines an inductively coupled plasma source, which efficiently ionizes elements in a sample, with a mass spectrometer, which separates ions based on their mass-to-charge (m/z) ratios. Owing to its exceptionally high sensitivity, wide linear dynamic range, and multi-element detection capability, since its introduction in the early 1980s, ICP-MS has rapidly become a key technique in analytical sciences, with the first commercial instruments appearing in 1983 and subsequently being adopted widely across laboratories. Geochemical laboratories were among the earliest adopters because of the ability of ICP-MS to detect rare earth elements (REEs) and other trace metals at ultra-trace concentrations levels often unattainable by conventional techniques.

One of the unique advantages of ICP-MS is its ability to detect concentrations as low as 10^{-15} g/g (ppq levels) for isotopes free from interferences. This outstanding detection power arises from the efficiency of the plasma in generating ions and the precision of the mass analyzer in filtering and quantifying them. In ICP-MS, the inductively coupled plasma ionizes the sample, producing positively charged ions that are subsequently directed into the

mass spectrometer for separation and detection. This allows the technique to perform both sensitive multi-element quantification and accurate isotopic ratio measurements, making it highly versatile for applications in research and applied sciences.

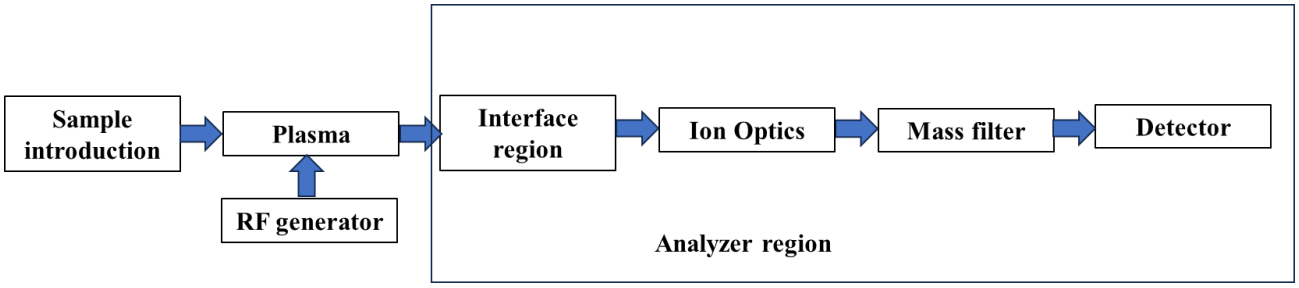


Fig. 3. 9.Schematic representation of the principal components of an inductively coupled plasma mass spectrometer (ICP-MS).



Fig. 3. 10. Inductively coupled plasma mass spectrometer (ICP-MS) facility at the CSIR-National Institute of Oceanography (CSIR-NIO), Goa.

Major Components of ICP-MS are as follows

3.10.1. Sample Introduction System

The sample introduction system delivers analyte solutions from the container to the plasma torch. It consists of:

- Peristaltic Pump: Transfers liquid at controlled rates (0.2-2.5 mL/min, adjustable in small increments).
- Nebulizer: Aerosolizes the liquid sample into a fine mist of droplets.
- Spray Chamber: Removes larger droplets, ensuring only fine aerosols reach the plasma. A peltier-cooled cyclonic chamber is often used to improve performance.
- Torch Injector: Directs the aerosol into the central channel of the plasma.

3.10.2. Inductively Coupled Plasma

The ICP is the ionization source of the instrument. It is produced by passing argon gas through a quartz torch and applying a radio-frequency electromagnetic field generated by an induction coil.

- Plasma temperatures range from 6000-10,000 K, allowing efficient atomization and ionization of sample constituents.
- The plasma consists primarily of singly charged positive ions (M^+), with very few negative ions. Elements that preferentially form negative ions (e.g., halogens) are difficult to detect.
- A combination of argon gas flows ensures the plasma is confined within the quartz torch and separated from the walls.

Within the plasma, the processes of desolvation, vaporization, atomization, and ionization take place in sequence. The aerosol introduced into the central channel undergoes solvent evaporation, dissociation of molecules, and finally ionization of atoms. At the prevailing temperatures, most atoms lose an electron to form singly charged ions.

3.10.3. Interface Region

The interface serves as the transition zone, guiding ions from the atmospheric-pressure plasma into the high-vacuum environment of the mass spectrometer. This transfer is facilitated by two metallic cones, known as the sample and skimmer cones, commonly manufactured from nickel or copper. For analyses involving aggressive matrices such as HF,

platinum-tipped cones are often employed. Because of their close proximity to the hot plasma, the cones are generally water-cooled to prevent thermal damage.

3.10.4. Mass Spectrometer

Once within the vacuum system, ions are sorted according to their mass-to-charge (m/z) ratio. The quadrupole mass analyzer is the most commonly adopted configuration in ICP-MS. It consists of four parallel rods supplied with oscillating radiofrequency and direct current potentials in opposing phases. Only ions with a stable trajectory at a particular m/z value can pass through to the detector, while others are deflected. The quadrupole's ability to scan rapidly across a broad mass range enables fast and efficient multi-element measurements.

3.10.5. Detector

The transmitted ions are measured using an electron multiplier detector, which amplifies the signal through a cascade of dynodes coated with an active film. Each ion striking the detector surface releases electrons, which multiply through successive dynodes to produce a measurable current. The output signal is directly proportional to the ion concentration in the sample.

3.10.6. Ion Optics and Collision/Reaction Cell

Electrostatic lenses (ion optics) focus and steer ions into the quadrupole. To reduce interferences, a collision/reaction cell (commonly helium-filled) is employed. Two main operational modes are:

- Collision Cell Technology (CCT): Polyatomic ions undergo more frequent collisions and are discriminated against analyte ions.
- Kinetic Energy Discrimination (KED): Uses small energy barriers to filter out interfering polyatomic species while transmitting analyte ions.

3.10.7. Analytical Workflow of ICP-MS

The overall steps in ICP-MS analysis are as follows:

1. Generation of a fine aerosol from the sample solution.
2. Desolvation, vaporization, atomization, and ionization within the plasma.
3. Extraction of ions into the mass spectrometer via the interface.

4. Separation of ions based on their m/z ratio using the quadrupole.
5. Detection of ions and quantification with reference to calibration standards.

3.4.10.8 Interferences in ICP-MS

ICP-MS measurements are affected by several types of interferences:

- Spectral Interferences: Caused by polyatomic ions such as ArO^+, $ArCl^+$, or ArN^+, formed from plasma, solvent, or acid species.
- Isobaric Overlaps: When isotopes of different elements have the same nominal mass (e.g., ^{58}Fe and ^{58}Ni).
- Matrix Effects: High concentrations of major elements can suppress or enhance analyte signals.

Approaches to minimize interferences include applying mathematical corrections, employing internal standards, and utilizing collision or reaction cells. Internal standards such as rhodium (Rh) are preferred because they are mono-isotopic, chemically stable, and less prone to contamination

3.4.10.9. Geochemical Analysis of Major and Trace Elements:

Freeze-dried grounded organic matter-free sediment sample around 50 mg was taken into an acid-cleaned Savillex PTFE vial. The samples were digested as per Peketi et al., (2020) in brief digestion was followed by using HNO_3: HF and HNO_3: HCl acid mixtures in a closed condition at 120ºC for 24 hours. Addition of the subsequent acid mixture is proceeded by the evaporating the sample to semi-dryness. Finally, after completing the digestion procedure samples were dissolved into a 2% HNO_3 medium and stored for ICP-MS analysis. Thus, digested samples were spiked with ^{103}Rh for the determination of Al, Mn, Fe, and Mo concentrations using an in-house Quadrupole ICP-MS (Thermo Scientific iCAPQ). The accuracy of the analysis is monitored by analyzing marine sediment standard MAG-I, and USGS Basalt standard BCR-2 and the precision is better than <3% (Peketiet al., 2020).

3.4.11 General description of multi collector inductively coupled plasma mass spectrometry (MC-ICP-MS)

The Nu-Plasma MC-ICP-MS instrument is double-focused (electrostatic analyzer and magnetic sector analyzer, in Nier-Johnson geometry), equipped with 12 faraday detectors, and features variable zoom optics for beam focusing (Belshaw et al., 1998)Belshaw et al.,

1998). Mass spectrometry is fundamentally based on the behavior of ions that are accelerated through a potential into a magnetic field. The deflection of the ion's trajectory through the field is governed by its mass-to-charge ratio (M/Z). The accelerated and deflected ions strike the detectors, which measure the ion count per unit time as current. The voltage is measured by passing the current through a resistor with a specific resistivity of $10^{-11}\Omega$, which generates the voltage (V = I * R).

There are two main ways in which mass spectrometers vary: first, in the method by which ions are produced at the sample-input end, and second, in the method by which the mass and quantity of ions are determined. For elements with low to intermediate ionization potentials, techniques like thermal ionization (TIMS) or gas sources are suitable/can be employed. On the other hand, elements with high ionization potentials necessitate a higher energy approach like plasma. Mo can be ionized through thermal processes; however, its elevated first ionization potential of 684 kJ/mol indicates that it is particularly appropriate for ionization via ICP. At the ionization temperature, 98% of molybdenum is ionized (Houk, 1986). This aspect considers the user's intention to quantify either element or isotope abundances or to evaluate element or isotope ratios. For the most accurate isotope ratios, it is recommended to use an instrument with multiple detectors, while a single detector is more suitable for element abundances. This pertains to challenges associated with magnet hysteresis when examining a broad mass spectrum. MC-ICP-MS will be the primary focus of this discussion, as most of the current research has concentrated on measuring high-precision and accurate isotope ratios. Instruments that use inductively coupled plasma (ICP) to generate ions often employ argon gas, which serves as both the carrier gas and the "source" gas. Using a radio-frequency generator (set at 27 MHz), a time-varying electrical current is circulated through a cylindrical (induction) coil wound around a quartz flame. This creates fluctuating magnetic fields in the gas. A spark plug initiates the initial electron interactions within the magnetic field. Ionization of argon atoms results in the formation of a plasma, characterized by temperatures ranging from 6000 to 10000 K. Samples are introduced in aerosol form, and ionization occurs indiscriminately within the plasma. The generated ions exhibit a spectrum of kinetic energies, thereby requiring the implementation of an electrostatic filter (Albarède & Beard, 2004). The Plasma Laboratory is equipped with multiple devices designed for the introduction of samples. The two nebulizers utilized for Mo work, ESI Apex and CETAC Aridus, function based on the identical principle of desolvation. Before each analytical session, a liquid sample of approximately 40 µl/min is introduced into the instrument and

analyzed. The solvent evaporates as the liquid sample moves through a heated chamber or membrane. The residual solute is introduced into the torch through a continuous flow of sampling gas.



Fig. 3. 11.Multi collector inductively coupled plasma mass spectrometer (MC-ICP-MS) facility at the CSIR-National Institute of Oceanography (CSIR-NIO), Goa.

3.4.11.1 Instrumental Mass Bias

Mass bias, also termed instrumental fractionation, arises due to the unequal transmission of ions of different masses through the ICP-MS system. Heavier isotopes are often transmitted preferentially, introducing systematic deviations in measured isotope ratios (Wombacher & Rehkämper, 2003). This effect is mainly produced in the plasma–interface region rather than the mass analyzer itself (Albarède & Beard, 2004). Factors such as the geometry of sampler and skimmer cones, torch position, and matrix composition can strongly influence the extent of fractionation.

In ICP-MS, the magnitude of mass bias is larger than in thermal ionization mass spectrometry (TIMS), although it remains relatively stable during a given analytical session (Wombacher & Rehkämper, 2003). To correct for this effect, several mathematical models are commonly used, including linear, power, and exponential laws. Among these, the exponential law provides the most accurate description of mass fractionation behavior in

plasma-based systems and is widely adopted in isotope geochemistry (Albarède & Beard, 2004; Urey, 1947).

Mass bias corrections may also be affected by matrix interferences, which can be classified into:

- Spectral effects, such as isobaric overlaps (e.g., ^{96}Zr on ^{96}Mo), oxide/nitride molecular ions (e.g., $^{84}Kr^{16}O$ on ^{100}Mo), or doubly charged species (e.g., $^{190}Os^{2+}$ on ^{95}Mo).
- Non-spectral effects, where additional matrix elements modify ion transmission and instrument sensitivity, thereby influencing the magnitude of mass bias (Albarède & Beard, 2004).

Correction Strategies for Mass Fractionation

Accurate isotope ratio measurements require correction for instrumental mass bias. This is particularly important for heavier elements, where natural isotopic variations are relatively small—for example, $\delta^{98}Mo$ varies by only ~5‰ in natural samples compared with ~60‰ for $\delta^{7}Li$ (Urey, 1947). Several approaches are employed to achieve this correction, including internal normalization, sample–standard bracketing, and double-spike methods (Lu et al., 2023; J.F. Rudge et al., 2009; Siebert et al., 2001; Skierszkan et al., 2015; Wombacher & Rehkämper, 2003; Zhang et al., 2018).

3.4.11.2 Double-Spike Technique

The double-spike approach is one of the most robust strategies for correcting instrumental mass bias. It is applicable to elements with four or more stable isotopes and involves the addition of two isotopically enriched tracers of known composition to the sample (Compston & Oversby, 1969; Dodson, 1963; Dodson, 1970; Hofmann, 1971; Lu et al., 2023; Russell et al., 1978; Siebert et al., 2001; Skierszkan et al., 2015; Zhang et al., 2018). Because both the spike and the sample undergo identical fractionation during measurement, the true isotopic composition can be retrieved after deconvolution (Galer, 1999; Johnson & Beard, 1999).

For successful application, careful sample purification and minimization of analytical blanks are essential. Quantitative yield is less critical, but memory effects and incomplete equilibration between spike and sample can reduce accuracy (Albarède & Beard, 2004). To ensure reliability, the spike must be equilibrated with the sample prior to any chemical processing so that subsequent fractionation affects both equally (Johnson & Beard, 1999).

Although the mathematical treatment of double-spike data can be complex often requiring iterative or matrix-based inversion methods (Rudge et al., 2009; Siebert et al., 2001; Skierszkan et al., 2015; Zhang et al., 2018). It provides one of the most accurate means of correcting for mass bias, especially when high precision is required for heavy stable isotope systems.

3.4.11.2.i) Mo Isotope Mass Bias Correction Using Double Spike

Precise and accurate metal isotope measurements, such as δ^{98}Mo, require correction for both instrumental mass bias and laboratory-induced fractionation, particularly during sample digestion and chromatographic separation. While standard-sample bracketing (SSB) is commonly used, it assumes full recovery and consistent mass bias behavior across standards and samples assumptions that may not hold in the presence of matrix effects or incomplete recovery.

To overcome these limitations, this study adopted a double spike (DS) technique using a calibrated mixture enriched in ^{97}Mo and ^{100}Mo. The spike was added to samples prior to chemical purification, enabling internal correction of mass bias and eliminating the need for quantitative recovery. During MC-ICP-MS analysis, the deviations from expected spike-sample isotope ratios were used to correct for fractionation using a matrix inversion approach (Lu et al., 2023; Rudge et al., 2009; Siebert, 2001; Skierszkan et al., 2015; Zhang et al., 2018). This internally-referenced method provides robust and reliable correction for both instrumental and procedural fractionation, and is especially advantageous in complex matrices where quantitative yields are challenging.

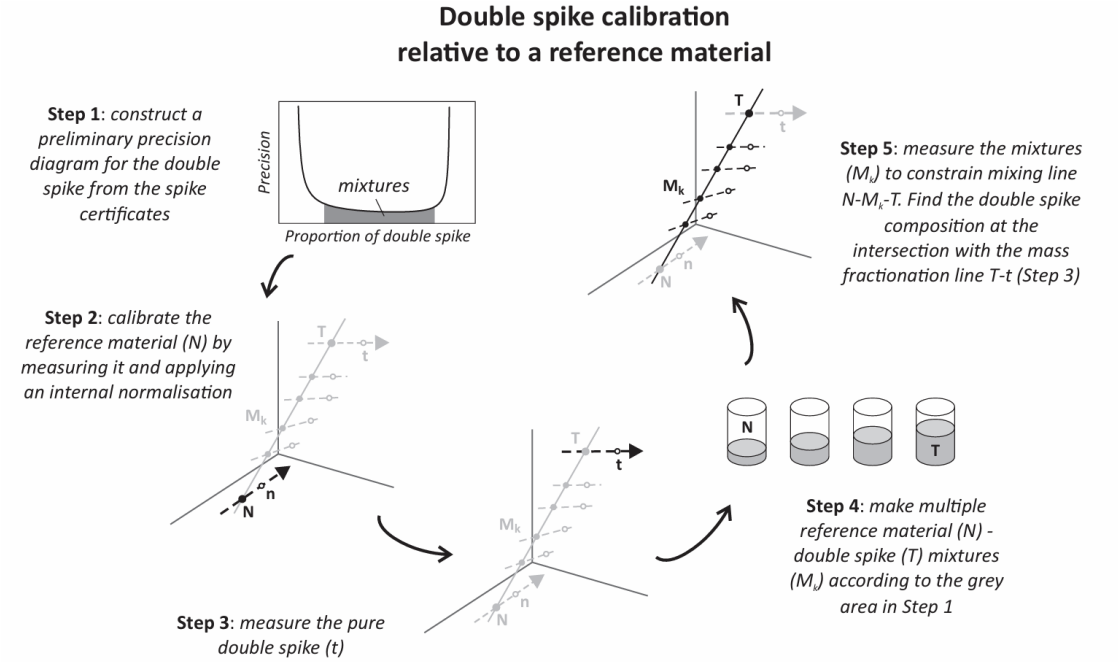


Fig. 3. 12. Schematic representation of Double spike calibration adopted from Klaver and Coath (2019)

3.4.11.2. ii) Workflow Equations for Calibration and Validation

The full calibration/validation procedure shown in Figure 1.3 can be summarised as follows:

a. **Pre-calibration of the reference material**

Measure the unspiked reference material, and correct it using either internal normalisation or an external dopant to obtain a nearly unbiased estimate of R_i. Equation (3.21) is used here with $N_i \equiv R_i$.

b. **Construction of reference-spike mixtures**

Prepare several mixtures with known $k_j$and apply equations (3.18) and (3.19) to solve for the spike composition T_i. At this stage the same inversion machinery (equation 3.23) is effectively applied, but with the roles of "sample" and "spike" swapped: the reference acts as the known endmember, and the pure spike measurement is treated as the unknown.

c. **Primary spike calibration**

Perform a least-squares optimisation over all mixtures to obtain the best-fitting set of $T_i$values and their covariance. These calibrated spike ratios are then fixed for all subsequent double-spike inversions.

d. **Validation using a quality-control material**

A second solution (quality-control material, QCM) of composition Q_i is mixed with the spike over a range of k and processed through the standard DS inversion using equations (3.21) - (3.23) and the calibrated T_i. If the calibration is accurate and blank corrections are under control, the retrieved Q_i values should be independent of k within uncertainty. Any systematic trend of δ or ratio with k would indicate a bias in spike calibration, blank subtraction, or reference composition.

Mathematically, this means that for all QC mixtures j,

$$N_{i,j}^{(\mathrm{QCM})} \approx Q_i \text{ for all } k_j, \qquad \text{(Eq. 3.17)}$$

within the propagated uncertainty from σ_α and the measurement noise. Demonstrating this k-independence is a crucial validation step for any double-spike method.

3.4.11.2.iii). Double Spike Calibration Protocol for Mo Isotope Analysis

Double-spike calibration was performed following the procedure of Siebert et al. (2001). To achieve accurate molybdenum isotope measurements and resolve both instrumental and procedural fractionation effects, a two-step calibration protocol was implemented for the ^{97}Mo-^{100}Mo double spike. This approach ensures robust internal normalization and high reproducibility across varying sample matrices.

Step 1: Primary Calibration Using Pd-Doped Reference Solutions

The initial calibration step involved correcting instrumental mass bias by doping both the double spike and the NIST-3134 Mo standard (lot No. 130418) with palladium. The ^{104}Pd/^{102}Pd ratio (10.922) was used as an internal reference to establish the ^{100}Mo/^{97}Mo ratio in both solutions. To minimize uncertainty:

- Identical measurement routines and parameters were applied to spike and standard.
- Both solutions were prepared in the same matrix to eliminate matrix effects.
- The spike was formulated to match the natural ^{100}Mo/^{97}Mo ratio, ensuring comparable signal intensities.

This step yielded a precise relative ^{100}Mo/^{97}Mo ratio for the spike, anchored to the standard, and served as the foundation for subsequent internal normalization.

Step 2: Internal Normalization of Remaining Isotope Ratios

Following Pd-corrected calibration, all other Mo isotope ratios (e.g., ^{98}Mo/^{97}Mo, ^{96}Mo/^{97}Mo, etc.) were determined in pure Mo runs. These ratios were internally normalized using the previously

established $^{100}Mo/^{97}Mo$ ratio. This strategy avoids reliance on external doping elements and ensures consistency across all isotopic ratios.

Step 3: Validation via Spike–Standard Mixing Series

To verify calibration accuracy, mixtures of spike and standard at varying proportions were analyzed under identical conditions. The results confirmed that the calibration remained stable across a wide range of spike-to-sample ratios. This flexibility allows for reliable quantification even when sample Mo concentrations are uncertain or variable. In addition, BCR-2 and Nod-P1 were included in every analytical session, providing a continuous monitor of long-term reproducibility. Across all sessions, these standards yielded $\delta^{98}Mo$ values with a reproducibility consistently better than 0.06‰ (2SE), demonstrating excellent stability of the analytical system and further validating the robustness of the double-spike approach.

3.4.11.2 iv) Equations Underlying Double-Spike Calibration

Calibration of the double spike fixes the values of T_i in the same exponential fractionation framework. A reference material with composition R_i (after a first-order IMF correction) is mixed with the spike in a series of mixtures with known spike fractions k_j (index j for each mixture). For each mixture, the true mixture composition is

$$M_{i,j} = k_j\, T_i + (1 - k_j)\, R_i. \qquad \text{(Eq. 3.18)}$$

The measured ratios $m_{i,j}$ are again related to $M_{i,j}$ through an exponential IMF parameter β_j:

$$M_{i,j} = m_{i,j}\, e^{-\beta_j P_i}. \qquad \text{(Eq. 3.19)}$$

For a given trial spike composition T_i, each mixture satisfies equations (3.18) and (3.19). In four-isotope space, all mixtures fall along a straight mixing line connecting the reference point R and the (unknown) spike point T. The calibrated spike composition corresponds to the point T that gives the best joint fit to all mixtures, i.e. minimises the residuals between the observed $m_{i,j}$ and those predicted from equations (3.18 to 3.19). Geometrically, this is the intersection between the spike's IMF trajectory and the reference–spike mixing line, as depicted in Figure 3.13. Because the geometry is controlled mainly by the direction of the mixing line, using multiple mixtures with different k_j values significantly increase the robustness and precision of the spike calibration.

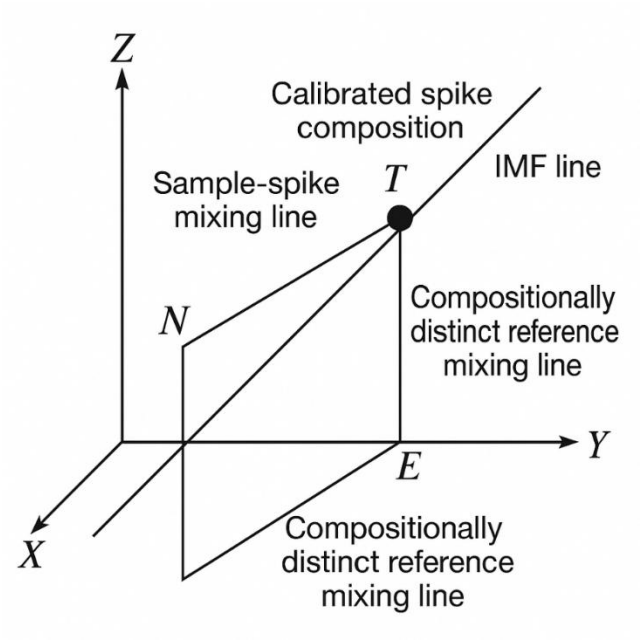


Fig. 3. 13. Schematic four-isotope diagram illustrating the calibration of a double spike. Solid arrows represent mass-fractionation trajectories, whereas straight line denote mixing lines. Instrumental mass fractionation shifts the measured compositions of the reference material (n) and the double spike (t) from their true values (N and T). After applying a first-order IMF correction, the true reference composition (N) is obtained. Mixtures (M_k) prepared between N and T define the N-T mixing line, whose intersection with the mass-fractionation line t-T yields the calibrated spike composition. Alternatively, a compositionally distinct reference materi**l** (E) and its mixtures can be used to generate a second mixing line (E-T), from which the spike composition can be determined at the intersection of the N-T and E-T lines without requiring measurement of the pure spike. Following a complete mathematical framework for solving the exponential DS equation using matrix algebra combined with an iterative Newton-Raphson scheme provided by Rudge et al. (2009) data was deconvoluted for the Mo isotopic ratio determination.

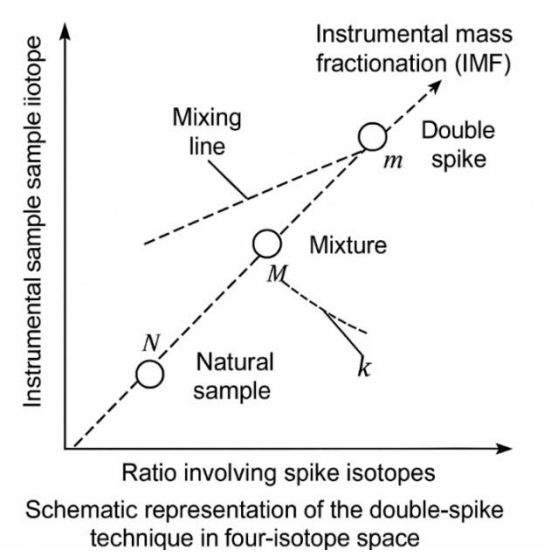
3.4.11.2.v). Principles of the Double-Spike Technique and Core Equations

In isotope-ratio measurements, the isotope ratios recorded by the mass spectrometer differ from the true isotope composition due to instrumental mass fractionation (IMF). For an element with at least four isotopes, the IMF can be described by an exponential law. For a given isotope ratio i (for example, $^{98}Mo/^{95}Mo$), the relationship between the **true** ratio $N_i$and the **measured** ratio $n_i$of an unspiked sample is

$$N_i = n_i\, e^{-\alpha P_i} \qquad \text{(Eq. 3.20)}$$

where $\alpha$is the mass-fractionation parameter for the sample and P is the natural logarithm of the exact mass ratio of the two isotopes used in ratio i. The value of $\alpha$is the same for all ratios of that element in a single measurement; only $P_i$changes from ratio to ratio.

$$P_i = \ln\ (\frac{m_{\text{heavy},i}}{m_{\text{light},i}})$$



Schematic representation of the double-spike technique in four-isotope space

Fig. 3. 14. Conceptual schematic illustrating the double-spike technique in four-isotope space. The natural sample (N) and the double-spike solution (T) lie at distinct positions in isotope-ratio space and define a mixing array. A mixture (M) formed by combining the sample with the spike plots along this mixing line according to the spike-sample proportion (k). During MC-ICP-MS analysis, instrumental mass fractionation shifts the measured compositions of both the unspiked sample (n) and the mixture (m) along characteristic IMF trajectories. Because the isotopic composition of the spike is known, simultaneous measurement of n and m enables determination of the IMF parameters and reconstruction of the true isotopic composition of the natural sample.

In the double-spike approach, a tracer solution Tenriched in two isotopes is mixed with the natural sample. The true isotope ratios of the mixture are denoted M_i, and the measured ratios are m_i. The IMF affecting the mixture is described by a second fractionation parameter β:

$$M_i \ = \ m_i\, e^{-\beta P_i}. \qquad \text{(Eq. 3.21)}$$

The composition of the true mixture is a linear combination of the true spike and true sample compositions. If $k$is the mole fraction of spike in the mixture (so $1 - k$is the contribution of the natural sample), then

$$M_i \ = \ k\, T_i + (1 - k)\, N_i. \qquad \text{(Eq. 3.22)}$$

Substituting equations (3.17) and (3.18) into (3.19) gives the double-spike equation:

$$k\,T_i + (1-k)\,n_i\,e^{-\alpha P_i} - m_i\,e^{-\beta P_i} = 0. \qquad \text{Eq. (3.23)}$$

For an element with four isotopes, we can write equation (3.20) for three independent ratios (e.g. $^{98}Mo/^{95}Mo$, $^{97}Mo/^{95}Mo$, $^{100}Mo/^{95}Mo$). This yields three nonlinear equations in the three unknowns α, $\beta$and k. Solving this system (the "double-spike inversion") provides (i) the IMF experienced by the sample (α), (ii) the IMF acting on the mixture (β), and (iii) the spike-sample mixing proportion k. The true sample composition $N_i$then follows from equation (Eq. 3.20). This geometric relationship between sample, spike, mixture and IMF trajectories is illustrated schematically in Figure 3.12.

When the goal is to express mass-dependent fractionation relative to a reference material, it is convenient to convert αinto delta notation. If the reference material defines $\delta = 0$ and we are interested in ratio i, the isotopic offset of the sample can be written as

$$\delta_i X = \exp(-\alpha P_i) - 1 \;\approx\; -\alpha P_i \qquad \text{(Eq. 3.24)}$$

where the approximation holds for small fractionations. In practice, this δ value is usually reported in per mil (‰) by multiplying by 1000.

3.4.11.3. Mo-isotope analysis

For Mo-isotopic analysis, an adequate amount of double spike (^{97}Mo and ^{100}Mo) was added to the sediment sample before digestion (Lu et al., 2023; John F Rudge et al., 2009; Siebert, 2001; Skierszkan et al., 2015) and digested using HNO_3: HF: HCl as mentioned earlier (Peketi et al., 2020). Following the Pearce et al. (2009) Mo column separation protocol, digested samples were dissolved into 1M HF + 0.5M HCl medium and loaded onto the Bio-Rad AG1X-8 resin 200-400 mesh. Molybdenum was eluted using 3N HNO_3 medium. Eluted Mo aliquots were evaporated to semi-dryness and finally brought into 2% HNO_3 + 0.1% HF medium for Mo isotope ratio analysis using an in-house MC-ICP-MS, (Nu Plasma-III, NP-III) coupled with Desolvation Solvation Nebulizer System (DSN-100) with a flow rate 2.8ml/min and N_2 at 3ml/min in low-resolution mode. The sample concentrations range from 40 to 50 ng/ml and monitored ^{98}Mo mass. Measurements were carried out on an average of 4 blocks of 20 cycles with an integration time of 10s. The Mo isotopes were reported with respect to the NIST-3134, with an offset of +0.25‰ (Nägler et al., 2014). Accuracy was monitored by measuring the standards BCR-2, Nod-P-1 (BCR-2, $\delta^{98}Mo$ = +0.21 ± 0.8‰, Nod-P-1 $\delta^{98}Mo$ = -0.66 ± 0.7‰ (J. Li et al., 2016).

$$\delta^{98}Mo = [(^{98}Mo/^{95}Mo)_{sample}/(^{98}Mo/^{95}Mo)_{NIST\text{-}3134})]\text{-}1*1000+0.25 \qquad \text{(Eq. 3.25)}$$

3.4.12 Molybdenum speciation and phase-specific isotope ratio measurements

To investigate the phase-specific partitioning of molybdenum (Mo) and assess the effectiveness of the extraction protocol, a six-step sequential extraction procedure was applied to selected sediment intervals from the cold seep core SSD045/4/G4. Approximately 0.5 g of finely powdered sediment was weighed into 50 mL polypropylene centrifuge tubes and subjected to the following extractions:

- F1 (Carbonate phase): Sediment was treated with a sodium acetate buffer (pH 5.0) and shaken for 16 hours to release Mo loosely adsorbed onto mineral surfaces and associated with carbonates (Solongo et al., 2018).
- F2 (Mn-oxide-bound phase): The residue was leached with 0.1 M hydroxylamine hydrochloride (pH 2.0) for 16 hours to mobilize Mo associated with Mn-oxides (Chao, 1972; Prakash et al., 2012).
- F3 (Fe-oxide -bound phase): A buffered ammonium oxalate solution (pH 3.0) was used for 6 hours to extract Mo associated with amorphous and crystalline Fe Mn-oxides (Prakash et al., 2012)
- F4 (Organic-bound phase): The residue was treated with 0.1 M sodium pyrophosphate (pH 10.0) to extract Mo bound to humic substances (Bascomb, 1968).
- F5 (Sulfide-bound phase): Extraction of sulfide-associated Mo was achieved by leaching with 3 N HNO_3 for 4 hours (Huerta-Diaz & Morse, 1990; Teimouri et al., 2022).
- F6 (Detrital phase): The final residue was combusted at 550 °C and digested using a mixture of concentrated HNO_3-HCl-HF at 140 °C to recover detrital Mo.

Each leaching step was carried out using a mechanical shaker under ambient conditions. Following centrifugation, the supernatant was separated, and the residue was rinsed with deionized water four times before proceeding to the next step. Leachates were evaporated and subsequently digested using concentrated HNO_3 (where applicable) for complete dissolution. Each leachate was then reconstituted in 2% HNO_3 prior to analysis.

To assess extraction efficiency and validate analytical results, a recovery test was conducted. Approximately 50 mg of sediment, pre-combusted at 550 °C to remove organic matter, was fully digested using a mixture of HNO_3-HCl-HF at 140 °C for 24 hours in Teflon digestion vessels. The digests were semi-evaporated and reconstituted in 2% HNO_3 for ICP-MS analysis. Recovery was calculated by comparing the sum of Mo from the six extracted fractions with the total Mo in the bulk digests.

Molybdenum analysis was performed using an in-house Thermo iCAPQ quadrupole ICP-MS. Replicate measurements and blank extractions confirmed that both accuracy and precision were better than ± 5% (RSD) (except for residual phase), ensuring reliability of the sequential leaching data.

Chapter 4 Sediment pore fluid chemistry

4.1 Introduction

Tightly coupled biogeochemical processes shape the chemical composition of marine sediment pore fluids. Organic matter delivered to the seafloor undergoes successive remineralization, primarily driven by microbial respiration under sub-oxic to anoxic conditions. Sulfate is the principal terminal electron acceptor in anoxic marine sediments and accounts for a substantial fraction of organic matter degradation (Beulig, Roy, Glombitza, et al., 2018; Canfield, 1989 b; Jørgensen, 1982; Jorgensen et al., 2019; Kristensen, 2000). The rate of sulfate reduction is influenced by several factors, including the reactivity of organic matter, ambient temperature, types of bacterial communities, sedimentation rates, and sulfate availability (Canfield, 2006; Goldhaber & Kaplan, 1975; Patrick Meister et al., 2013; Westrich & Berner, 1988). Organo-clastic sulfate reduction is commonly described by Equation 4.1.

$$2\ CH_2O + SO_4^{2-} \rightarrow 2\ HCO_3^- + HS^- \qquad \text{(Eq. 4.1)}$$

In addition to organo-clastic sulfate reduction, sulfate is consumed via anaerobic oxidation of methane (AOM), a microbially mediated process involving consortia of anaerobic methanotrophic archaea (ANME) and sulfate-reducing bacteria represented in equation 4.2 (Boetius, 2000; Hinrichs et al., 1999; Hoehler et al., 1994; Knittel & Boetius, 2009; Lapham et al., 2024; Milucka et al., 2012; Wegener et al., 2015; Zhou et al., 2025) and may involve multiple cooperative metabolic strategies (Beulig et al., 2019; Milucka et al., 2012; Moran et al., 2008; Scheller et al., 2016; Wegener et al., 2015; Zhou et al., 2025). AOM occurs predominantly within the sulfate-methane transition zone (SMTZ), a narrow redox boundary where upward-diffusing methane from deeper sediments encounters downward-diffusing sulfate (Beulig, Roy, McGlynn, et al., 2018; Hong et al., 2013; Jorgensen et al., 2019; Malinverno & Pohlman, 2011; Mazumdar, A Peketi, et al., 2012; Reeburgh, 2007; Sultan et al., 2016). Sulfate reduction via AOM pathway can be represented by the stoichiometric equation below.

$$CH_4 + SO_4^{2-} \rightarrow HCO_3^- + HS^- + H_2O \qquad \text{(Eq. 4.2)}$$

This redox coupling produces hydrogen sulfide and bicarbonate (Eq. 4.2), which can precipitate as authigenic iron sulfides and carbonate minerals, thereby influencing the overall diagenetic mineral inventory (Antler et al., 2014; Li et al., 2018; Pillutla et al., 2024;

Rickard & Luther III, 2007; Schoonen, 2004; Ussler III & Paull, 2008). The depth of the SMTZ is further governed by the balance between sulfate supply, methane flux, and sediment permeability, as well as by factors such as sediment thickness, porewater composition, and alterations linked to late-stage methanogenesis. SMTZ depth may also fluctuate over time, displaying substantial variation across geological periods. Because it reflects depositional stability, methane flux intensity, and the extent of the methanic zone, reconstructing both present and past SMTZ positions is of considerable importance for geological interpretations (Argentino et al., 2020; Borowski et al., 2013; Graves et al., 2017; Mazumdar et al., 2009; Mazumdar et al., 2012; Sundby et al., 2021). In cold seep environments, where methane fluxes are elevated, AOM serves as a primary sink, oxidizing more than 90% of the upward methane flux (Hinrichs & Boetius, 2002; Reeburgh, 2007). Under suitable pressure-temperature conditions, residual methane may form gas hydrates, further modifying the pore water chemical signature and the stability of the AOM process (Kvenvolden, 1993; Sloan, 1998).

4.2 Results

The porewater SO_4^{2-}, CH_4, H_2S concentrations, and $\delta^{13}C_{CH4}$ profiles are presented in figure 4.1. The concentration data are replotted from Peketi et al. (2022) for reference when interpreting other porewater parameters. Sulfate (SO_4^{2-}) concentrations (Fig. 4.1) decline from approximately 28 mM at the sediment-water interface to about 23 mM at 380 cm below the seafloor (cmbsf). Within this interval, sulfate exhibits noticeable fluctuations, although the overall gradient remains gentle, at approximately 0.01 mM/cm. Between 380 and 580 cmbsf, sulfate levels drop sharply from 23 mM to 1.7 mM, with a steeper average gradient of 0.1 mM/cm. The SO_4^{2-} concentration profile shows substantial heterogeneity instead of a smooth gradient commonly observed in diffusion-dominated systems. Methane concentrations (Fig. 4.1) in the headspace begin to rise significantly below 310 cmbsf and show pronounced variability. The C_1/C_2 hydrocarbon ratio ranges from 1065 to 3772 (Table 4.1). The sulfate-methane transition zone (SMTZ) is marked (orange-shaded) in Fig. 4.1. The chloride concentrations (Fig. 4.1c) fluctuate between 353.1 and 582.4 mM relative marine average of 550 mM. Sulfate/Chloride (SO_4^{2-}/Cl^-) ratio (Fig. 4.1c) ranged from 0.1 to 5.6 which are multiplied by 100.

The $\delta^{13}C$ values of headspace methane (Table 4.1; Fig. 4.1b) vary between -94.7‰ and -56.7‰, with the most depleted signatures found within the SMTZ. Notably, a trend toward ^{13}C-enrichment is observed both above and below SMTZ (Fig. 4.1b). Dissolved hydrogen

sulfide concentrations span from 40 to 9030 µM (Table 4.1), with the highest value (9030 µM) recorded at 471 cmbsf within the SMTZ (Fig. 4.1d).

The ratios of sulfate sulfur isotopes range from +22.2‰ to +78.8‰ VCDT (Fig.4.1e). The $\delta^{34}S_{SO42-}$ value at the core top is +22.2‰, which increases to +27.8‰ at 20 cm, then decreases to +24.7‰ at 40 cm. At a depth of 60 cm, $\delta^{34}S_{SO42-}$ measures +27.4‰, rising to +32.9‰ at 120 cm before decreasing to +27.3‰ at 140 cm. Between 160 cm and 300 cm, $\delta^{34}S_{SO42-}$ fluctuates between +27.6‰ and +27.1‰. Notably, at 310 cm, $\delta^{34}S_{SO42-}$ rises sharply from +29.1‰ to a maximum of +78.8‰ at 471 cm, then stabilizes at +76.3‰ at 480 cm. Isotope ratios below 480 cm could not be measured due to lower sulfate concentrations. The hydrogen sulfide isotope ratio ($\delta^{34}S_{H_2S}$) ranges from -27.8‰ to +16.5‰ VCDT (Fig. 4.1e). At 5 cm, the $\delta^{34}H_2S$ value is -27.8‰, increasing to -15.7‰ at 20 cm and decreasing to -24.5‰ at 40 cm. Below 40 cm, the $\delta^{34}S_{H_2S}$ values rise progressively, reaching -17.2‰ at 160 cm. A significant decrease follows, with $\delta^{34}S_{H_2S}$ attaining a minimum of -26.1‰ at 240 cm. From 260 cm, $\delta^{34}S_{H_2S}$ rises from -25.9‰, reaching a peak of +16.2‰ at 520 cm, before decreasing slightly to +14.5‰ at 600 cm.

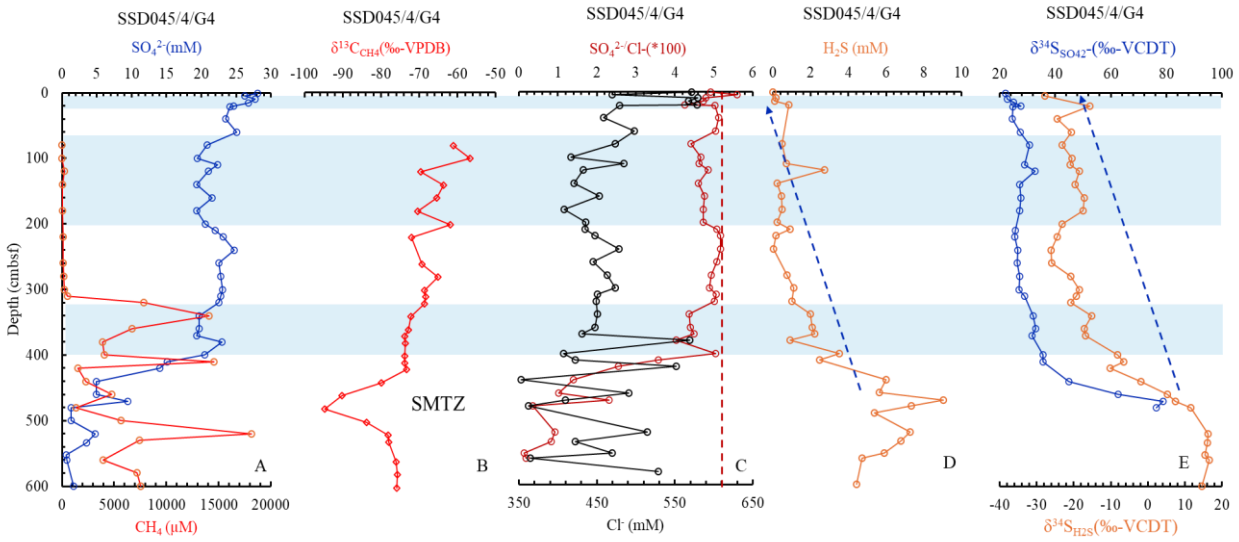


Fig. 4. 1. Pore-water and isotopic profiles from cold-seep core SSD045/4/G4. a) Pore-water sulfate and methane concentration profiles; b) Carbon isotopic composition of headspace methane ($\delta^{13}C_{CH4}$); c) Pore-water chloride and chloride-normalized sulfate (×100); d) Pore-water hydrogen sulfide concentration; e) Sulfur isotopic composition of pore-water sulfate and hydrogen sulfide ($\delta^{34}S_{SO42-}$, $\delta^{34}S_{H2S}$). Light blue shading marks sulfate-driven AOM (SD-AOM) pockets; orange shading marks the present SMTZ SD-AOM pocket

(modified from Peketi et al., 2022). Blue dashed line indicates the upward migration of H_2S generated at SMTZ. Dashed dark red line represents the seawater SO_4^{2-}/Cl^- ratio.

4.3 Discussion

4.3.1 AOM and SMTZ

The non-steady-state pore water sulfate concentration profile shows contrasting overall gradients 0.01 mM/cm and 0.1 mM/ cm above and below 380 cmbsf respectively (Fig. 4.1a). The sharp drop in the sulfate concentrations within 380 to 480 cmbsf may be attributed to AOM caused by high methane flux (Borowski et al., 1996; Borowski et al., 1999). The persistence of methane in and above the SMTZ (Fig. 4.1a) suggests a greater upward flux of methane across the SMTZ than what could be consumed via AOM. The SMTZ, which is shaped by AOM, is demarcated by the well-defined zone of ^{13}C-depleted CH_4. Within the SMTZ, $\delta^{13}C_{CH4}$ value drops to -94.7‰, which may be attributed to the kinetic isotope fractionation effect involving preferential consumption of ^{12}C during microbial oxidation of methane (Alperin et al., 1988; Mazumdar, et al., 2009; Xiao et al., 2017). Low $\delta^{13}C_{CH4}$ values (-78.2 to -75.8‰) below SMTZ may be attributed to microbial methanogenesis involving reduction of CO_2 by the hydrogentrophic pathway (Galimov, 2006; Whiticar, 1999; Whiticar et al., 1986). The high C1/C2 ratio, varying between 1065 and 3772, also indicates a microbial origin of the hydrocarbon gases (Whiticar, 1999; Whiticar et al., 1986). Biogenic methane from the K-G basin was earlier reported by Mazumdar et al. (2009); Mazumdar et al. (2019); Mazumdar et al. (2012). The observed ^{13}C-enrichment in carbon isotope ratios of methane above SMTZ and towards the core top (Fig. 4.1b) may be attributed to the diffusion of ^{13}C-enriched residual methane from the SMTZ kinetic isotope fractionation effect involving preferential consumption of ^{12}C during microbial oxidation of methane (Alperin et al., 1988; Mazumdar et al., 2009; Xiao et al., 2017).

4.3.2. Non-steady sulfate profile: hydrate degassing and SD-AOM

The Chloride concentration profile shows significant fluctuation which is dominated by values less than that of ambient sea water (550 mM). The low values indicate fresh water dilution attributed to the thawing of gas hydrate during core recovery (Bohrmann et al., 2002; Greinert et al., 2001; Hesse & Harrison, 1981; Mazumdar et al., 2012; Tomaru et al., 2006) which may significantly lower the porewater sulfate concentrations. On the other hand, hydrate formation may cause dehydration and subsequent sulfate concentration enrichment. Chloride normalization of porewater sulfate eliminates the influence of physical

dilution or concentration effects, enabling the identification of true sulfate depletion related to microbial sulfate reduction. Deviations from the conservative seawater (SO_4^{2-}/Cl^- *100) ratios (5.2) (Fig. 4.1c) indicate in situ biogeochemical consumption associated with SD-AOM within the SMTZ. The post normalization profile (Fig. 4.1c) clearly shows a non-steady pattern due to sulfate reduction (light blue shades). The marked fluctuation in this ratio above the SMTZ indicates variable extent of sulfate reduction creating a non-steady state profile. The Cl^- anomaly observed in the porewaters indicates heterogeneous distribution of methane hydrates in the micro fractures indicating flow methane across the SMTZ. The presence of methane is probably responsible for the development of isolated pockets of SD-AOM at multiple depths above the SMTZ. The enrichment of sulfur isotopes (+25.7 to +32.9‰ and +26.5 to +35.7‰) in the residual sulfate within these anomalous zones further supports active SD-AOM processes. These zones are demarcated in the figure 4.1 represents multiples micro zones within the sedimentary column.

4.3.3. Non-steady state of H_2S

Hydrogen sulfide produced within the SMTZ by SD-AOM diffuses outwards due to the concentration gradients (Fig. 4.1d). Preferential utilization of ^{32}S during sulfate reduction enriches the residual sulfate and the resulting sulfide in ^{34}S under diffusion-limited, semi-closed conditions. Because of differing diffusion coefficients of $H_2{}^{32}S$ and $H_2{}^{34}S$, the upward flux induces isotopic fractionation (Donahue et al., 2008; Jorgensen, 1979; Jørgensen et al., 2004; Jorgensen et al., 2019), resulting in ^{34}S-enriched H_2S near the SMTZ. The highest H_2S concentration (9032 µM) occurs within the SMTZ, where sulfate-dependent AOM (SD-AOM) is the dominant source of sulfide in cold-seep sediments. The $\delta^{34}S_{H_2S}$ value of +16.2‰ is recorded within the SMTZ, with a maximum of +16.5‰ at its lower boundary, while the shallower and deeper intervals show distinctly lower values (-27.8 to -15.7‰ and -20.9 to -17.1‰, respectively SD-AOM pockets Fig 4.1). The gradual decrease in $\delta^{34}S_{H_2S}$ above the SMTZ suggests isotopic differentiation governed by diffusion process. Interestingly, anomalous sulfate depletion above SMTZ (SD-AOM pockets) also corresponds to elevated H_2S concentrations (214 to 2737 µM and 755 to 2194 µM) as well as ^{34}S enriched H_2S. The elevated H_2S concentrations above the SMTZ reveals micro-zones of active AOM, producing non-steady state H_2S in a fracture-dominated system possibly due to the presence of methane hydrate dissociation within the sedimentary column. The inverse relationship between the SO_4^{2-}/Cl^- and $\delta^{34}S_{H_2S}$ profiles indicates that sulfate depletion corresponds to enhanced AOM-related sulfide production above the SMTZ. These dynamic,

non-steady state H_2S enrichments, coupled with elevated $\delta^{34}S_{H_2S}$ values, suggest the presence of shallow methane hydrates within fault-controlled fluid pathways.

4.4. Conclusion:

Porewater sulfate analysis reveals a non-steady-state profile with contrasting gradients of 0.01 mM/cm and 0.1 mM/cm above and below 380 cmbsf, respectively, driven by intense anaerobic oxidation of methane (AOM). The location of the current sulfate-methane transition zone (SMTZ) is uniquely demarcated by a sharp decrease in $\delta^{13}C\text{-}CH_4$ value down to -94.7‰, reflecting strong kinetic isotope fractionation during microbial methane consumption. Downcore chloride anomalies tracking below ambient seawater values (550 mM) reveal localized freshwater dilution from recovery-induced gas hydrate dissolution across sediment micro-fractures. Normalizing porewater sulfate against chloride concentrations effectively eliminates these physical overprints, isolating a highly fluctuating, non-steady-state SO_4^{2-}/Cl^- ratio above the SMTZ. This spatial trend further corroborated by enriched residual sulfate stable isotope compositions (up to +35.7‰) reveals the development of isolated pockets of active, fluid-flow-driven sulfate-dependent AOM (SD-AOM) at multiple depths within the shallow column. In alignment with these fracture-hosted SD-AOM pockets, elevated hydrogen sulfide concentrations (up to 2,737 μM) and distinct ^{34}S-enrichments in H_2S match the secondary zones of sulfate depletion. Ultimately, these overlapping non-steady-state ionic fluxes, diagnostic $\delta^{13}C\text{-}CH_4$ drops, and localized $\delta^{34}S\text{-}H_2S$ anomalies confirm that advective methane transport through fault-controlled pathways sustains active micro-zones of shallow gas hydrates well above the primary SMTZ baseline.

Published paper G-cubed, Volume25, Issue10; October 2024

Chapter 5 Biogeochemical Reconstruction of Authigenic Carbonate Deposits at Methane Seep Site off Krishna-Godavari (K-G) Basin, Bay of Bengal

S. P. K. Pillutla[1,2], A. Peketi[1,3], A. Mazumdar[1,3], Mohd. Sadique[1,2], K. Sivan[1,3], Anjali Zatale[1,3], S. Mishra[1], and Swati Verma[1]

[1]Gas Hydrate Research Group, CSIR - National Institute of Oceanography, Dona Paula, Goa, India, [2]**School of Earth, Ocean, and Atmospheric Sciences, Goa University, Taleigao, Goa, India**, [3]Academy of Scientific and Innovative Research (AcSIR), Ghaziabad, India

5.1 Abstract

Active and relic marine methane-seep sites are widely distributed globally and are distinguished by distinctive geology, biogeochemistry, and ecosystems. The discovery of methane-seep sites in the Krishna-Godavari (K-G) basin has created exciting new opportunities for methane - seep research in the Bay of Bengal. In this study, we document the occurrence of authigenic carbonates, including micro-crystalline aragonite crust (arg-crusts) admixed with chemosynthetic shells and high-magnesium carbonate tubular structures (HMC-tube), from the methane-seep site SSD045/4 in the K-G basin. The $\delta^{13}C$ values of HMC-tubes (-54.5 to -46.2‰) and arg-crusts (-57.6 to -34.8‰) indicate biogenic methane as the likely carbon source. Enhanced porewater alkalinity driving carbonate precipitation may be attributed to microbial - mediated SO_4^{2-}-AOM processes. Additionally, $\delta^{13}C$ values (-35.2 $\pm$ 8‰) of the residual organic matter within the carbonates suggest a contribution of methanotrophic bacterial biomass. The $\delta^{18}O_{carb}$ values of HMC and aragonite indicate methane hydrate degassing and crystallization pathways, respectively. Pelloid-filled burrows suggest the reworking of shallow HMC deposit by burrowing organisms, whereas the polyphase cementations (aragonite and HMC) within burrows indicate early and burial diagenetic pathways. The wide range in ΣLREE/ΣHREE ratios and Ce_{anom} values in arg-crusts reflect micro-spatial variations in redox conditions, likely due to cementation occurring in both open and closed diagenetic systems. In contrast, more constrained Ce_{anom} values and ΣLREE/ΣHREE ratios in HMC tubes suggest persistent sulfidic conditions. Overall, these findings provide insights into the pathways of carbonate formation at the K-G basin methane-seep site, highlighting the complex interplay of microbial processes, fluid dynamics, and diagenetic alterations.

5.2. Introduction

Active and relic methane-seep sites (Bernardino et al., 2012; Cordes et al., 2010; Foucher et al., 2009; Kravchishina et al., 2021; Lawal et al., 2023; Levin, 2005; Levin et al., 2016; Mazumdar et al., 2021; Mazumdar et al., 2019; Paull et al., 1984; Peketi et al., 2022; Wang et al., 2023) are extensively reported from marine sediments around the world (Fig. 1.1a) from both passive and active continental margins (Suess, 2018). Marine cold seep sites are characterized by the emission of CH_4 across the sediment-water interface and enrichment of H_2S (Levin, 2005; Levin et al., 2016), which fuels the proliferation of a unique ecosystem consisting of chemosynthetic organisms and a wide variety of heterotrophs including molluscs and crustaceans. The ecosystem may thrive on mud volcanoes, pockmarks, carbonate mounds, and crusts/chimneys (Bayon et al., 2013; Bayon et al., 2009; Bohrmann et al., 2002; Campbell, 2006; J. Feng et al., 2018; Gontharet et al., 2007; Lawal et al., 2023; Marlow et al., 2021; Mazumdar et al., 2021; Mazumdar et al., 2019; Mazumdar et al., 2011; Mazzini et al., 2006; J. Wang et al., 2021; Weidlich et al., 2023; Wirsig et al., 2012; Xu et al., 2018; Zhang et al., 2023). The formation of carbonate deposits including carbonate mounds, pavements, crusts and chimneys at methane seep sites is attributed to the anaerobic oxidation of CH_4 (AOM) coupled with the reduction of dissolved SO_4^{2-} (SR) (Eq. 1.10 and 1.11) in the interstitial waters, which leads to the generation of enhanced porewater carbonate alkalinity (Antler et al., 2014; Gontharet et al., 2007; Nöthen & Kasten, 2011). This microbially mediated reaction (Eq. 1.10) is carried out by a consortium of methane-oxidizing archaea (ANME) and sulfate-reducing bacteria (Boetius, 2000; Hinrichs et al., 1999; Knittel et al., 2005; Orphan et al., 2001; Yu et al., 2022) at the sulfate methane transition zone (SMTZ). The depth of SMTZ below the seabed depends on vertical methane and sulfate flux, bioturbation, and microbial community structure (Hong et al., 2014; Y. Hu et al., 2017; Komada et al., 2016; Q. Lin et al., 2016; Marlow et al., 2021; Niewöhner et al., 1998). Sulfate-AOM also results in the buildup of H_2S in the porewaters (Eq. 1.10) which supports the chemosynthetic ecosystem at methane seep sites. H_2S may be partitioned into Fe-sulfides (Eq. 1.12 and 1.13) and organic bound sulfur (Canfield et al., 2005; Jørgensen & Kasten, 2006; Raven et al., 2016). The excess H_2S seeping out at the sediment - water interface may partially or completely oxidized to S^0, SO_4^{2-}, $S_2O_3^{2-}$ (or other intermediate oxidized species) by sulfide oxidizing bacteria using oxygen and/or nitrate as terminal electron acceptors (Canfield et al., 2005; Findlay et al., 2019; Jørgensen & Kasten, 2006; Raven et al., 2016). The authigenic carbonate deposition (Eq. 2) at the cold seep sites

(combination of chemoherms and bioherms) comprise various polymorphs of $CaCO_3$ including aragonite (arg), high magnesian calcite (HMC), low magnesian calcites (LMC), dolomite, and calcareous shells. At a global scale, methane derived seep carbonates are responsible for the sequestration of 2.34 – 5.8 Tmol carbon yr^{-1} in the modern ocean and 33% – 50% of methanogenic dissolved inorganic carbon (Akam et al., 2023). The formation of cold-seep carbonates may change the porosity, density, and permeability of the medium, which in turn affects the fluid migration and gas hydrates/sediment stability (Bayon et al., 2009; Mazumdar, P. Dewangan, et al., 2009). Experimental and modeling results (Luff et al., 2004; Ye et al., 2019) on carbonate crusts suggest variable growth rates ranging from 0.01 to 0.014 cm y^{-1} depending on fluid flow velocity, sedimentation rate, and bioturbation activity. Whereas, the carbonate chimneys are estimated to grow laterally at a rate of 0.002 – 0.003 cm y^{-1} (L. Wang et al., 2021). Cold seep carbonates preserve the information about the composition and flux of cold seep fluids (Aloisi et al., 2000; Bayon et al., 2009). Authigenic seep carbonates are often brecciated due to the breaking of sediment seals through excess pore pressure triggered by methane hydrate destabilization (Greinert et al., 2001; Mazumdar et al., 2009). Discovery of paleo-methane seepage events (Mazumdar et al., 2009; Peketi et al., 2012) and active seep-sites (Dewangan et al., 2021; Mazumdar et al., 2019; Peketi et al., 2022) in the Krishna-Godavari basin, off east coast of India (western Bay of Bengal) opened up the window for investigating modern and past seepage activities methane hydrate/gas plumbing system and cold-seep ecosystems. Sediment fluid chemistry analyses from the present study site (SSD045/4) by Peketi et al. (2022) reveal the depth of present SMTZ within ~460-500 cmbsf. The ΣHS^- concentration increases sharply to a value of 9 mM within this zone. Authigenic carbonates recovered from the surface sediments (in spade cores) from this site are archives of the past seepage activities and SMTZ oscillations. A recent study (Dewangan et al., 2021) reported 22 gas flares (ranging in water depth from 630 to 1,960 m) in the water column in and around the study area. Seabed sampling from the gas flare regions shows the presence of shallow gas hydrates within 2-4 mbsf. The distribution of gas flares tends to align with the toe - thrust zones and shale diapiric mounds. The cold seep sites comprise characteristic chemosynthetic symbionts bearing bivalves (*Bathymodiolus*, *Acharax*, *Thyasiridae*), polychetes (*Sclerolinum*), and heterotrophs including gastropods, squat lobsters, goose barnacles, and brittle stars (Mazumdar et al., 2019; Peketi et al., 2022). In the present study, we have analyzed morphology, petrography, mineralogy and geochemical characteristics of these authigenic carbonates to reconstruct the

depositional and diagenetic pathways. A depositional model has also been proposed for the study sites emphasizing the significant role of burrowing activities on carbonate morphology.

5.3 Sampling and Analytical Protocol

5.3.1 Sampling

The cold seep expedition (SSD-045) in the K-G basin (Fig. 1.1b) was conducted on board *ORV Sindhu Sadhana* from the 12 January to the 6 February 2018. The characteristics of the seep sites, including multi-beam echo sounder based water-column imaging, CTD and sound velocity profiling (SVP), and assemblages of chemosynthetic/heterotrophic organisms, are provided in Dewangan et al. (2021) Mazumdar et al. (2019). Sediment samples were collected using a gravity corer with a PVC liner (ID: 10 cm) and a spade-corer (48 cm (L) × 48 cm (B) × 44 cm (H)). Sediment pore-water/gas extraction and preservation for subsequent onshore analyses were carried out onboard following standard protocols (Mazumdar et al., 2019; Mazumdar et al., 2012; Mazumdar et al., 2014). Authigenic carbonates (tubes and crusts) were recovered in closely spaced spade cores (Table 5.1) at sampling station SSD045/4 (water depths: ~1,750 m). Authigenic carbonates and hard shells were cleaned ultrasonically in distilled water, dried in an oven at 40°C, and stored in plastic bags for chemical analyses. In the present study, a suite of analytical techniques were employed to gain comprehensive insights into the composition and origins of the carbonate samples. Optical microscopic analysis was conducted for textural characterization with mineralogical association. Scanning Electron Microscopy with Energy Dispersive X-ray Analysis (SEM-EDX) was utilized to investigate high-resolution textural features and a qualitative assessment of elemental contents. Micro Fourier Transform Infrared (μ-FTIR) spectroscopy offered valuable information regarding the mineralogical analyses and distribution. X-Ray diffractometry was used for the relative quantification of carbonate contents. To evaluate the carbonate formation pathways, an isotope ratio mass spectrometer coupled with a gas bench facility was employed. Additionally, Inductively Coupled Plasma Mass Spectrometry (ICP-MS) was used to determine the major, trace, and rare earth element (REE) contents in carbonate samples.

5.3.2 Optical Microscopy and SEM‐EDS

Textural analyses and photomicrography of the carbonate thin sections were carried out using Nikon (LV100) and Leica (EZ4D) optical microscopes. SEM-Energy‐dispersive X-

ray Spectrometer EDS (Model: Quanta FEG 250) analyses of gold - coated polished thin sections were carried out on representative carbonate samples for qualitative chemical analysis at BITS Pilani (KK Birla campus) Goa, India and CSIR-National Institute of Oceanography Goa India.

5.3.3 Micro - FTIR Spectroscopy

Micro-Fourier transform infrared spectroscopy (μ-FTIRS) was carried out on polished thin sections of selected carbonate samples. Micro-FTIRS include focussed mineralogical analyses of textural elements in the thin section instead of bulk sample powder FTIRS. The micro-FTIRS technique can collect IR signals at high spatial resolution (the beam size can be as small as 5 μm), and has the potential for the characterization of compositionally complex samples (Chen et al., 2015; Rathore et al., 2023). In the present study, an AIM-8800 Shimadzu infrared microscope was used for the analyses using reflectance mode. The IR microscope (ceramic IR source) was equipped with a Cassegrain reflecting objective (15X) and a mercury-cadmium-telluride (MCT) detector to record the spectra. The detector reservoir was filled with liquid nitrogen before taking measurements. The room temperature was maintained at ~25°C and humidity of 30% – 50% or less for proper functioning of the μ-FTIR system. Background corrections related to ambient conditions like temperature, humidity, CO_2, and other vapours were applied to reduce spectral noise and improve peak resolution. Following background correction, the sample was brought to focus, and the analytical area was demarcated. All the analyses were carried out within the midinfrared band (~650 – 4,000 cm^{-1}). FTIR spectral analyses were carried out at a resolution of 4 cm^{-1} and consisted of 100 scans (Liu et al., 2013). The IR absorption spectra were further analyzed using the Origin multipeak fitting module. Coupling of SEM-EDS and μ-FTIR data help in better understanding of the mineralogical and textural association in the carbonate specimens.

5.3.4. X - Ray Diffractometry

Mineralogical identification of carbonate samples was carried out using a Rigaku (Ultima IV) X - ray (CuKα radiation; λ = 1.5418 Å) diffractometer adjusted at 40 kV and 20 mA with a scan speed of 1°/min. Peak positions and d - spacings were corrected using quartz 011 (4.255 Å) and 100 (3.343 Å) peaks as references. Relative quantification of MgCO3 (mol %) and HMC/aragonite (%) was carried out as follows (Goldsmith et al., 1961; Hardy & Tucker, 1988; Milliman et al., 1974).

5.3.5 Carbon and Oxygen Stable Isotope Ratio Measurements

Carbon and oxygen stable isotope ratio measurements of carbonate samples were carried out using a Thermo-Finnigan Delta V-Plus isotope ratio mass spectrometer attached to Gas Bench II in continuous flow mode NBS-18, 19, and Carrara marble were used as standards. The external precision was typically calculated from 0.07 to 0.09‰ VPDB for $\delta^{13}C$ and 0.0 -0.12‰ VPDB for $\delta^{18}O$. Total organic carbon (TOC wt%) contents in carbonate samples were obtained by decarbonating ~1g of carbonate powder with 0.5 N HCl. The insoluble residue (IR) was subjected to TOC content and $\delta^{13}C_{TOC}$ measurements using an Elemental analyzer (Thermo Flash EA 2000) and IRMS (Thermo Delta Plus) coupled with EA (Thermo EA1112) respectively. The analytical precision of the instrument was monitored using the International Atomic Energy Agency (IAEA) standard CH - 3 cellulose ($\delta^{13}C$ value = -24.7‰). A routine precision of ±0.1‰ (1σ) was obtained for $\delta^{13}C_{org}$ analysis. The $\delta^{13}C_{org}$ values were reported against VPDB.

5.3.6 Major and Trace Element Analyses

Major elements (Al, Ca, Mg, Fe, Mn), trace elements (Ba, Sr), and REEs + Y concentrations in the 5% supra-pure acetic acid-soluble carbonate fraction were measured using an in-house ICP - MS (Thermo iCAPQ; Peketi et al., 2020). Approximately, 50 mg of bulk carbonate powder was leached with 5% supra-pure acetic acid (Honeywell) for 2 hr on a rotary shaker following Hu et al. (2014). After 2 hr of leaching, the suspension was centrifuged, and the leachate was evaporated to semi-dryness in an acid-cleaned Teflon beaker and subsequently dissolved in 2% ultrapure HNO_3 (Merck) spiked with 10 ppb Rh for ICP-MS analysis. The acid blank for the measured elements was below the detection limit. JDO-1 and JLS-1 carbonate standards were used for quality control. The RSD for major/trace elements and REE + Y were <5%.

5.4 Results

5.4.1 Carbonate Morphology

At the K-G basin methane-seep site (SSD - 045/4), clusters of light gray colored carbonate tubes along with fragments of carbonate crusts were recovered within the top 5 cm of closely spaced spade cores. Tubular carbonate (Fig. 5.1a - 5.1h) is the dominant morphological type. The chimneys (hollow cylindrical) are characterized by lateral (wall-to center) growth layers (Fig. 5.1a and 5.1b) and diameter ranging from 1.2 to 2.4 cm. Unlike the chimneys, other

tubular structures (Fig. 5.1c - 5.1h) are tapering at one end and occasionally bifurcate (Figure 5.1h). The tubular structures (Figures 5.1c - 5.1h) are partially to completely filled with calcareous pelloids (plt) and micritic carbonate. Occasionally, the tubes show the presence of gas flow conduits (gfc) and gas voids (gv) lined with botryoidal aragonite (bAr: Fig. 5.1e and 5.1f). The black mudstones in the seep region show the presence of tubular gas flow conduits of variable diameter and length (Fig. 5.1i - 5.1k). The gas flow tubes show bent/tortuous paths with diameters ranging from 0.3 to 2.3 cm. Cylindrical - shaped tubular methane hydrate is observed in some tubular holes (inset in Fig. 5.1k).

Aragonite carbonate crusts (Fig. 5.1l and 5.1m) recovered at the study site are cavernous with botryoidal aragonite lining the cavity walls. The crust is admixed with shell fragments of chemosynthetic organisms (Fig. 5.1l and 5.1m) and microcrystalline aragonite cement (mArc). In brief, the authigenic carbonates reported here comprise aragonite crusts cemented with shells of chemosynthetic organisms and tubular high magnesian carbonates with variable internal features.

5.4.2 Carbonate Mineralogy

A total of 44 carbonate samples were analyzed for the relative concentrations of HMC/aragonite and $MgCO_3$ (mole %) content in HMCs (Table 5.2). The content of HMC and aragonite in tubular carbonates ranges from 81 to 100 wt% and 0 to 18 wt%, respectively, while arg - crusts have >99% aragonite. Owing to higher counting error in case of very low peak areas, LMC was not taken into account for the calculation of contents. The mole percentage of MgCO3 in HMCs ranges from 13.4 to 17.9 (average: 15.3 ± 1%; Table 5.2). The insoluble residue (IR%) contents after 5% acetic acid treatment range from 5.2% to 17.7% (Avg:12.4% ± 3.6) in the HMC tubes, whereas the IR% in the arg - crust samples are below detection level. In brief, the relative percentages of aragonite and HMC help in distinguishing the depositional conditions of the authigenic carbonate, including the variable redox regimes of the ambient sediment pore fluid.

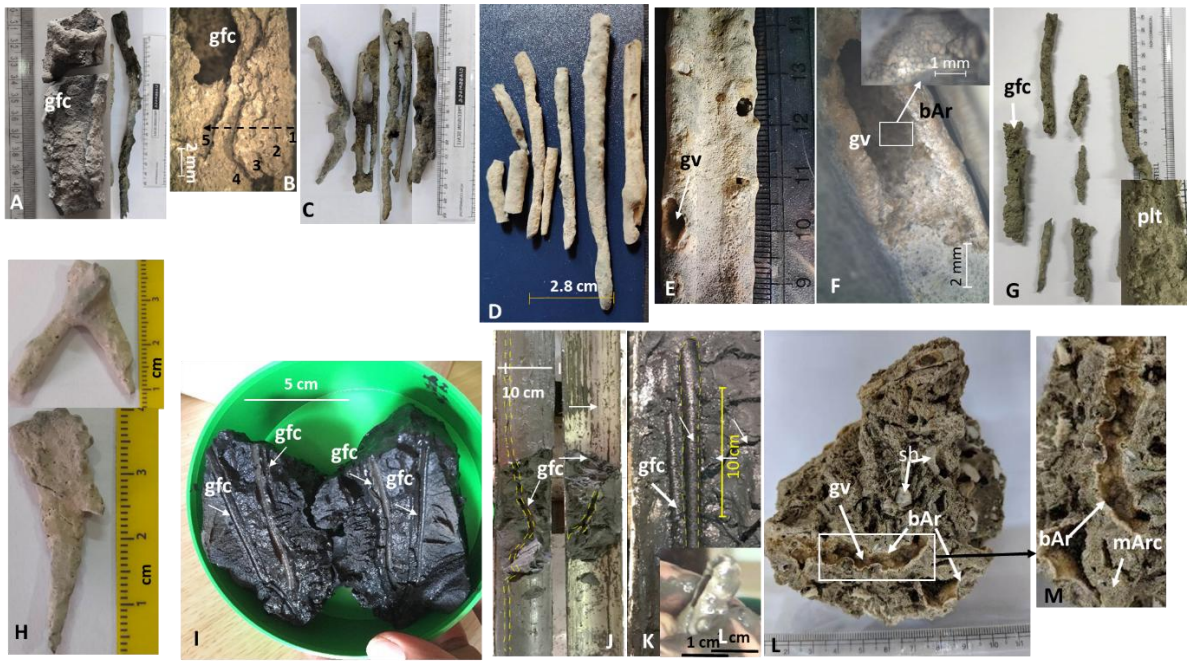


Fig. 5. 1.Morphology of HMC-tubes and arg-crusts. (a) HMC chimneys showing variable diameters (1.2-2.4 cm) and gas flow conduit (gfc); (b) Lateral (wall to center) growth of the carbonate HMC-tube. Numbers 1-5 indicate progressive growth layers in the chimney; (c and d) HMC-bioturbation tube fragments of variable diameter (0.25 -1.7 cm) and lengths (note the tapering ends); (e and f) HMC-bioturbation tubes with gas voids (gv) (inset in figure e) and botryoidal aragonite lining in the gas void (g). HMC-tubes packed with rounded calcareous pelloids; (h) HMC-bioturbation tubes with bifurcation and tapering end structures; (i-k) The black muddy sediment in the seep regions has hollow tubes of variable diameter (0.3-2.3 cm) and length. Inset shows tubular methane hydrate recovered from the gas conduits; (l and m) Cavernous aragonitic crusts with botryoidal aragonite (bAr) lining the cavity walls. The crust is mixed with chemosynthetic shell (sh) fragments and microcrystalline aragonite cement (mArc); (m) represents the magnified image of the botryoidal lining in figure l.

5.4.3 Carbonate Petrography and SEM - EDS

Optical microscopic studies of carbonate tubes reveal the presence of micritic HMC (mHMC) with detrital siliclastic grains and organic particulates as the non - calcareous component (Fig. 5.2a). Calcareous foraminifera shells are ubiquitous in HMC tubes. The micritic matrix shows the presence of acicular aragonite (acArg) filled cavities and gas flow conduits (gfc) (Fig. 5.2b - 5.2d). Clusters of pyrite framboids (Pyr) and isolated pyrite

crystals observed in most of the HMC tubes (Fig. 2e) indicate sulfidic porewater derived from SO_4^{2-}-AOM. The HMC tubes are often filled with pelloids (plt) ranging from 300 to 3,000 microns in diameter (Fig. 5.2f- 5.2j). The pelloids do not show any internal structures except the presence of detrital grains, clay, and organic matter in variable contents. The inter-pelloidal space is filled with micritic HMC and radial/acicular late-stage cement (Fig. 5.2f-5.2j), which often partially replaces the pelloids. The voids in the pelloid-filled tubes are lined/filled with acicular aragonite (Fig. 5.2f, 5.2h, and 5.2i). The arg-crust samples show the presence of shell (sh) fragments (Fig. 5.2k) and microcrystalline cement (mArc). The cavities are lined with botryoidal aragonite (Fig. 5.2l). The qualitative EDS data (Fig. 5.3) of the HMC - tubes show distinctly high Mg, Al, Si, and faint Sr contents in the HMC phase, whereas the aragonite-filled cavities show high Sr and non - detectable Mg, Al, and Si contents. In the present data the SEM - EDS data helps in distinguishing the pockets of aragonite within the HMC-matrix.

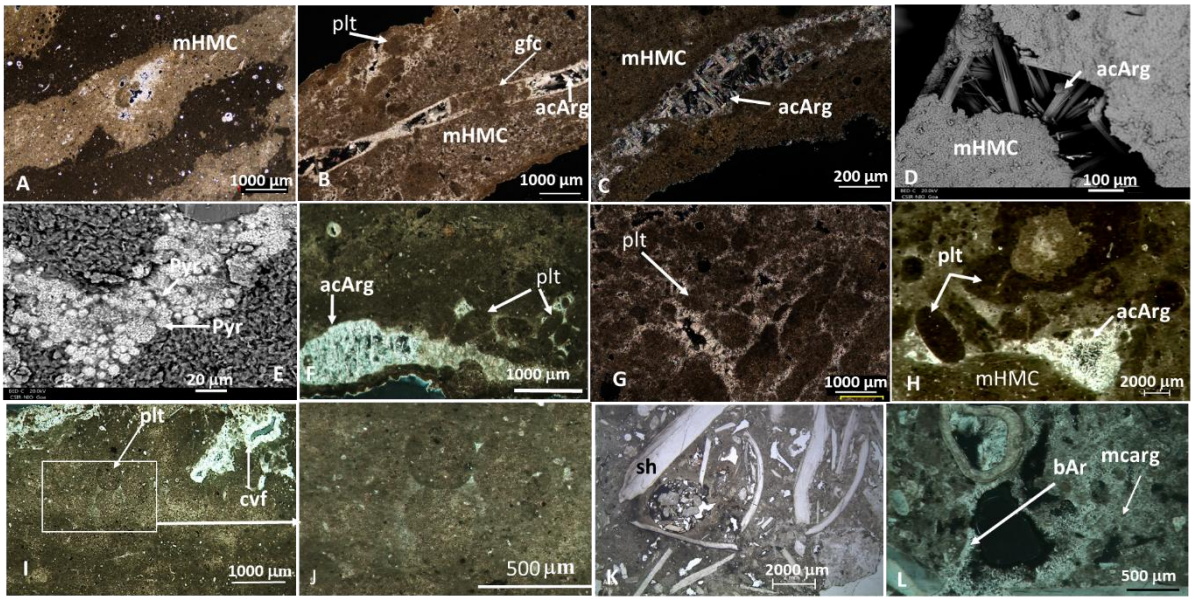


Fig. 5. 2.Optical and scanning microscopic imaging of HMC-tubes and aragonite crusts. (a) Micritic HMC (mHMC) with detrital quartz and clay as the non-calcareous component in HMC-tube; (b and c) HMC-tube with pelloids showing presence of gas flow conduits (gfc, white arrows) and void (gv, white arrows) filed or lined with acicular aragonite and radial crystals; (d) SEM image of acicular aragonite (acArg) filling up the gas void in HMC matrix; (e) Back scattered image of pyrite framboids (Pyr) in the tubular HMC-matrix; (f-j) Pelloids (plt) of HMC filling up the bioturbation tubes. The intra-pelloidal space and gas voids are filled with radial calcite cement and acicular aragonite. The pelloids range in size from 400

to 2000 microns and do not show any internal structures except the presence of detrital grains including clay and organic matter. Figure j represents the magnified image of the pelloids shown in figure i; (k-l) The arg-crust shows the presence of shell fragments (sh) and cavities with microcrystalline aragonite (mcArg = acicular aragonite) and botryoidal aragonite (bAr = botryoidal aragonite).

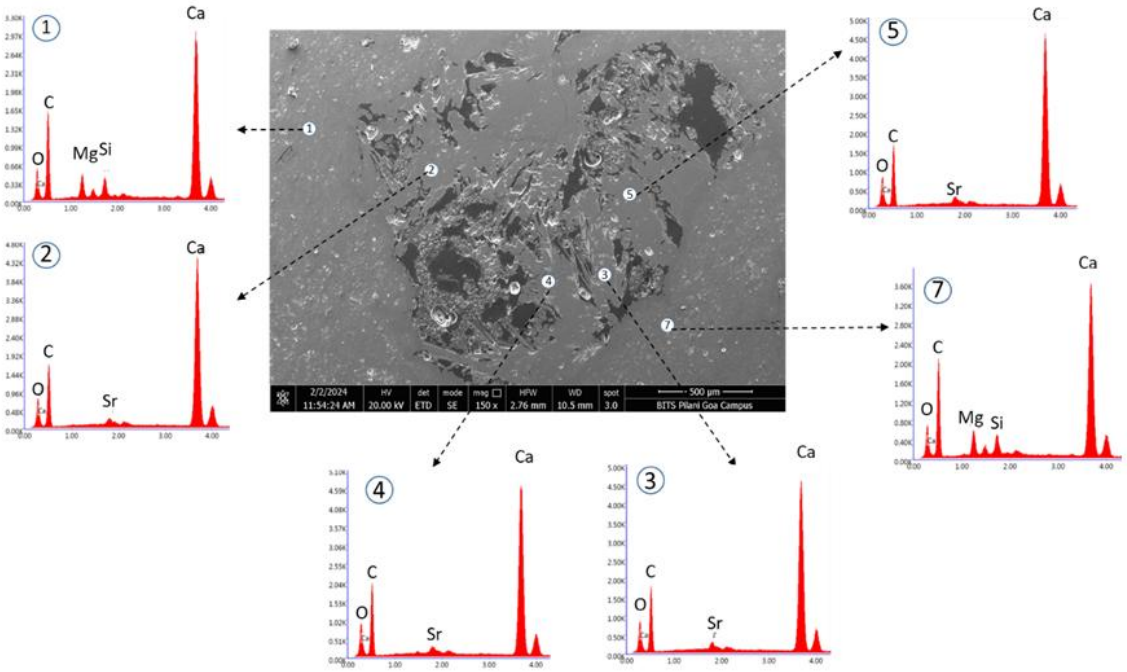
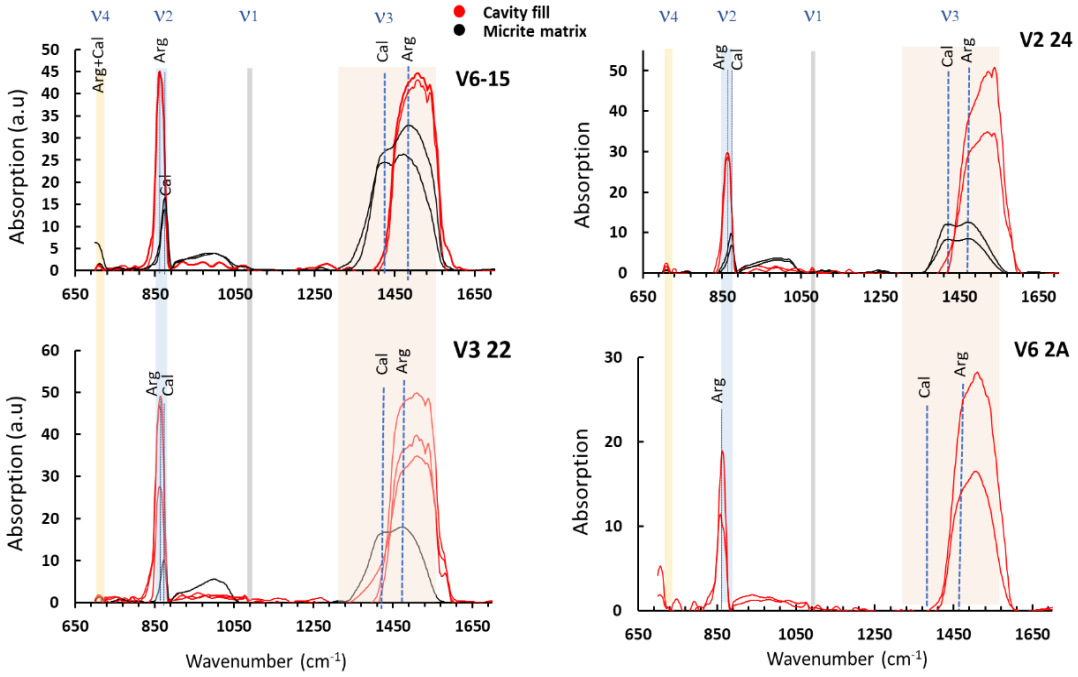


Fig. 5. 3 SEM-EDS data showing cavity filling aragonite in HMC matrix (HMC-tube). The qualitative chemical composition of spots 1, 5, and 6 showed significant Mg, Al, and Si contents along with Ca, whereas aragonite crystals within the cavities (spots 2, 3, 4) showed a significant amount of Sr and negligible presence of Mg, Al, and Si.

5.4.4 Micro - FTIR

The micro-FTIR spectroscopic analyses (in the aragonite-bearing HMC-tubes) were carried out in two distinct textural components, including cavity-filling acicular crystals and the HMC matrix. Various CO_3^{2-} mid-IR absorption bands across the wave numbers 1,085 cm^{-1} (ν1: C = O symmetrical stretching), 850 – 890 cm^{-1} (ν2: C = O bending beyond the plane), 1,300 – 1,560 cm^{-1} (ν3: C = O asymmetrical stretching) and 700-750 cm^{-1} (ν4: C = O bending in the plane) are demarcated in Fig. 5.4. The HMC matrix shows the presence of both calcite and aragonite characterized by their absorption wave numbers close to 1,420 and 1,475 cm^{-1} as well as 856 and 876 cm^{-1} respectively. The ν4 absorption band shows the distinct

presence of minor dolomite (~725 – 730 cm^{-1}) (Fig. 5.5). The cavity fillings within the HMC matrix show the presence of aragonite crystals and the absence of calcite. One notable observation is the widening of the cavity-filling aragonite peak in the ν3 band.



Deconvolution of the peak shows the presence of additional peaks ranging from 1,484 to 1,541 cm^{-1} which are not assigned to specific inorganic or organic phases (Fig. 5.6 and 5.7).

Fig. 5. 4. The micro-FTIR absorption spectroscopic data of calcite matrix and cavity filling aragonite in HMC-tube samples. The color bands represent different wavenumber ranges (ν1to ν4) for carbonate minerals. Comprising cavity-filling acicular aragonite crystals and the HMC matrix.

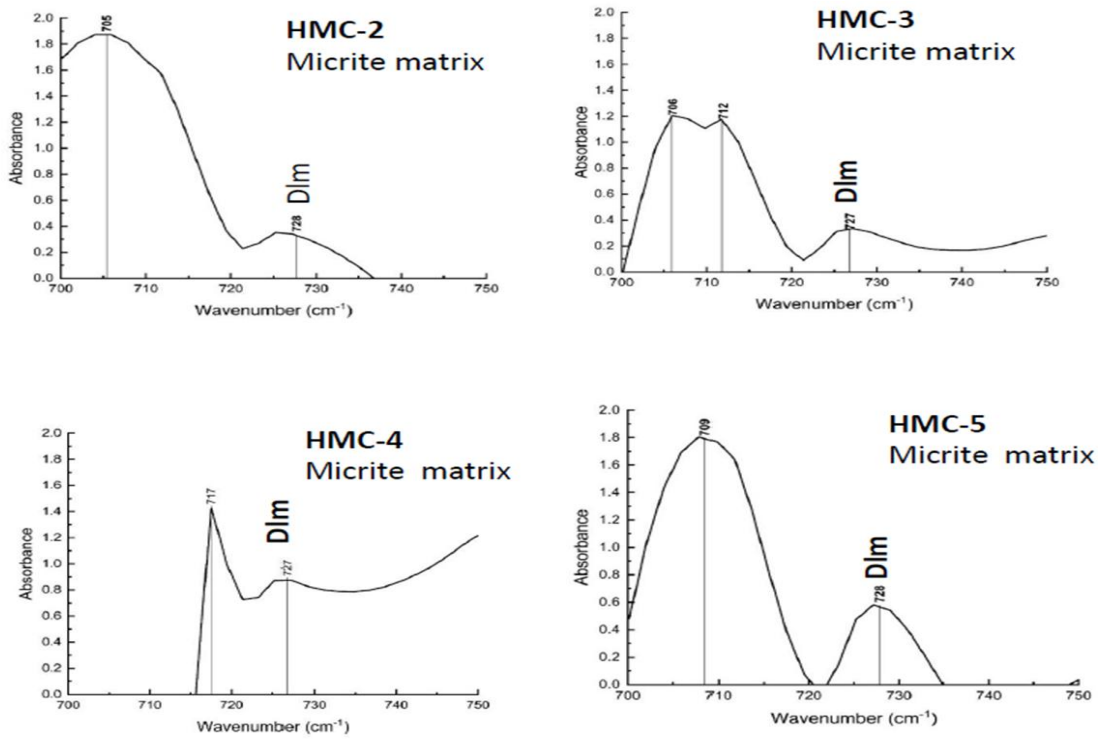


Fig. 5. 5. Representative FTIR absorption spectra (ν4 band) of HMC-tubes showing the presence of minor dolomite (Dlm) in the calcite matrix

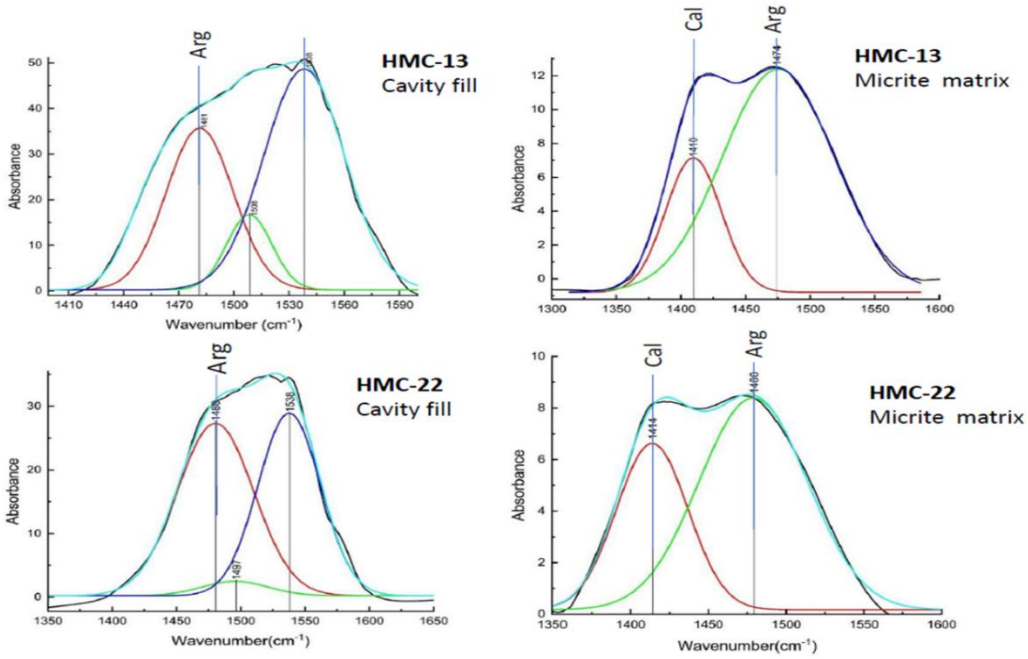


Fig. 5. 6. Representative FTIR absorption spectra (v3 band) of acicular cavity filling aragonite and calcite matrix in HMC-tubes. The peak deconvolution shows possible presence of unidentified phases along with aragonite in the cavity fill. Aragonite is also present in the micrite calcite matrix for HMC-13, 22.

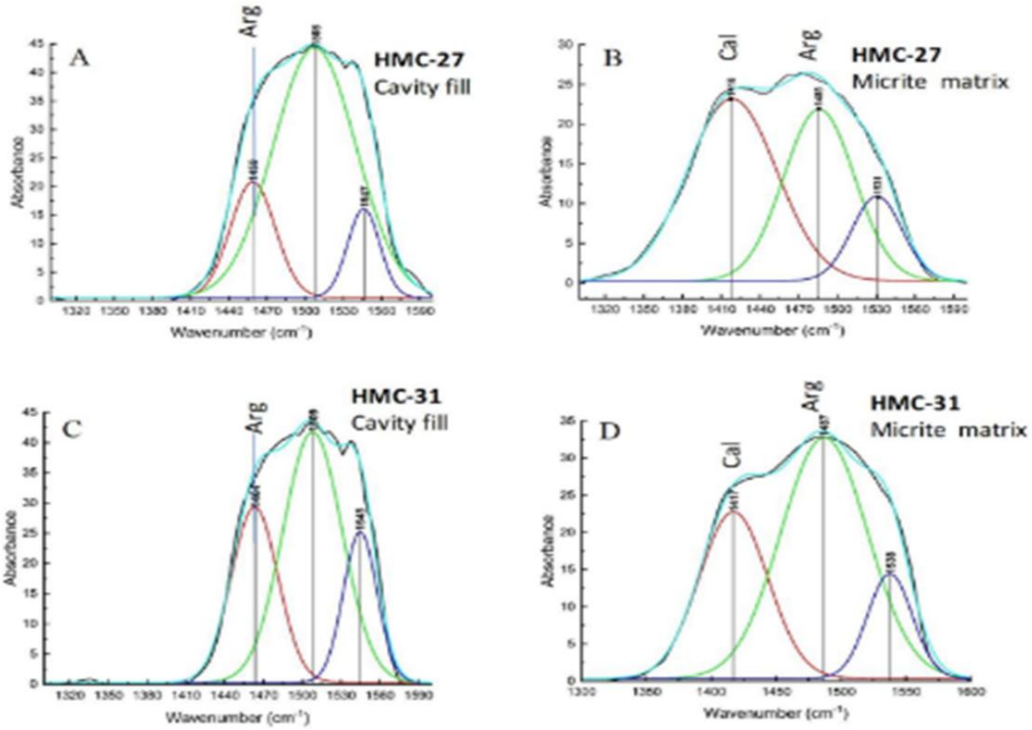
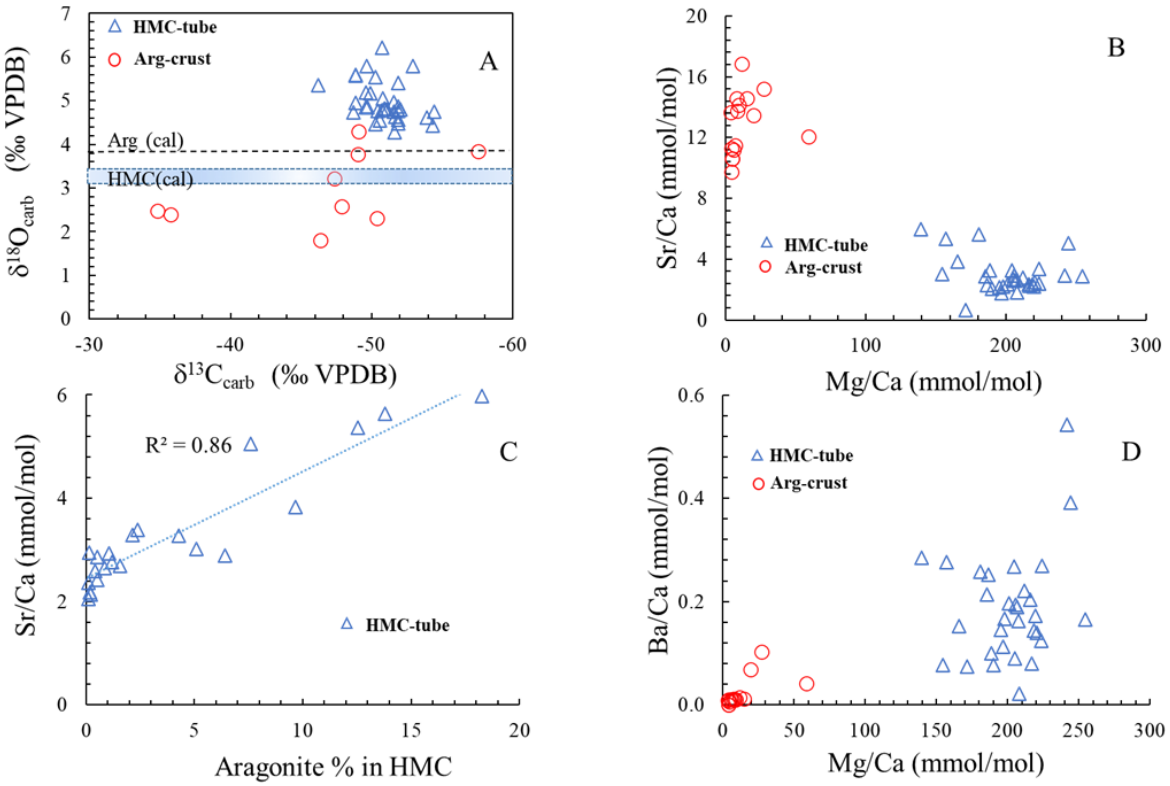


Fig. 5. 7. Representative FTIR absorption spectra (v3 band) of acicular cavity filling aragonite and calcite matrix in HMC-tubes. The peak deconvolution shows possible presence of unidentified phases along with aragonite in the cavity fill. Aragonite is also present in the micrite calcite matrix for HMC-27, 31.

5.4.5 Isotope Ratios and Trace - REE Composition

Carbon ($\delta^{13}C$) and oxygen ($\delta^{18}O$) isotope ratios of HMC - tubes range from -54.5 to -46.2‰ and +4.3 to +6.2‰ (VPDB), respectively, whereas $\delta^{13}C$ and $\delta^{18}O$ values of arg - crusts range from -57.6 to -34.8‰ and +1.8 to +4.3‰ respectively (Fig. 5.8a and Table 5.2). The TOC contents (Table 5.2) in the HMC tubes range from 0.17% to 0.77% (Avg.: 0.44 ± 0.1%) and the $\delta^{13}C_{TOC}$ ranges from -54.8 to -20‰ (Avg:-35.2 ± 8‰). The average sediment $\delta^{13}C_{TOC}$ (Table 5.2) from the carbonate sampling sites ranges from -20.4 to -19.4‰ (Avg: -20.0 ± 0.33‰). The trace, major and REE concentration data (46 numbers) are presented in Tables 5.3 and 5.4, respectively. Aluminium concentrations in 5% acetic acid leachate range from 0.002% to 0.09% in arg - crust and 0.03%-0.1% in HMC-tubes (Table 5.3). Mg/Ca

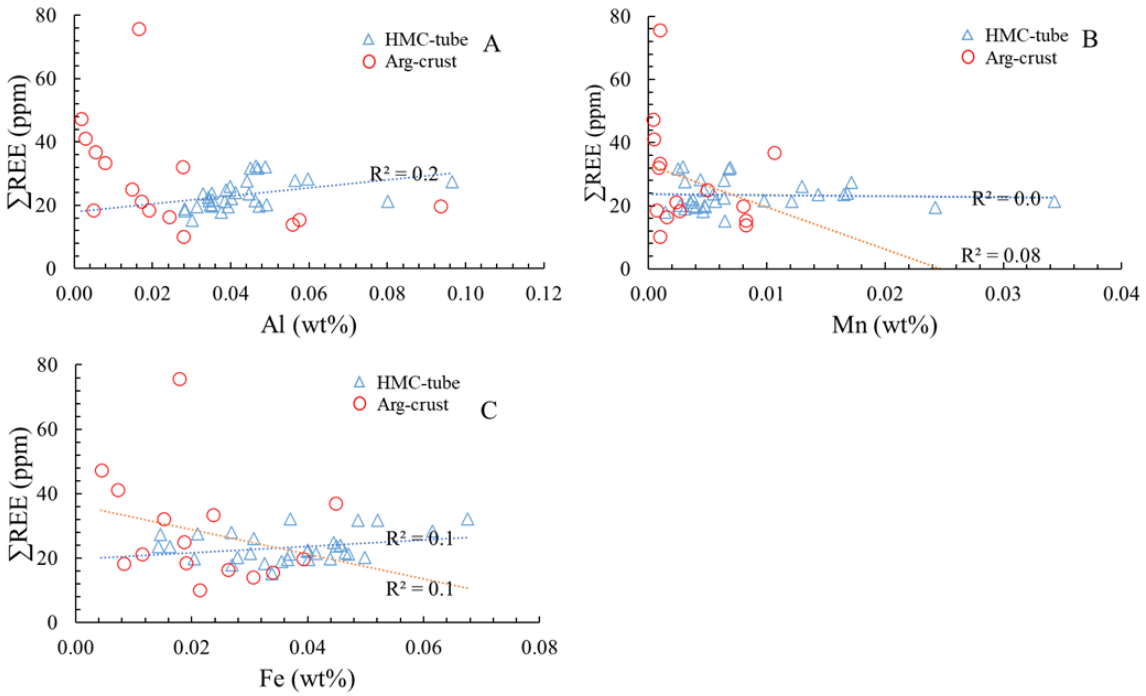
molar ratios range from 139.5 to 254.5 mmol/mol and 3.5 – 58.8 mmol/mol in HMC - tubes and arg-crusts, respectively. Manganese concentrations range from 0.001 to 0.03 (wt%) in HMC-tubes and 0.004 to 0.01 (wt%) in arg - crusts, whereas the Fe concentrations range from 0.01 to 0.07 (wt%) in HMC-tubes and 0.004 to 0.045 (wt%) in arg - crusts. Barium concentrations in HMC-tubes and arg - crusts ranged from 20 to 469 ppm and bd to 110 ppm, respectively. Strontium concentrations in HMC tubes and arg - crusts range from 378 to 3,707 ppm and 6,777-10,312 ppm, respectively. Sr/Ca and Ba/Ca molar ratios (mmol/mol) are plotted against Mg/Ca molar ratios in Fig. 5.8b and 5.8d. In Fig. 5.8c, Sr/Ca molar ratios were plotted against aragonite percentage in HMC showing a positive correlation of ($R^2 = 0.86$). The total REE concentrations ranged from 15.2 to 32.3 ppm (Avg: 23.4 ± 5 ppm) in HMC - tubes and 10.2 to 75.7 ppm (Avg.: 28.4 ± 18 ppm) in arg-crusts. The total REE concentration did not show any correlation with the Al, Mn, and Fe concentrations (Fig. 5.9), suggesting an insignificant contribution of REEs from the leaching of detrital constituents. The HMC-tubes and arg-crusts show distinct PAAS-normalized REE distribution patterns (Fig. 5.10a and 5.10b). The PAAS-normalized MREE and HREE values are distinctly higher than the LREE values in HMC-tubes, whereas PAAS-normalized LREE values are higher than that of MREE and HREE values in the arg-crusts. The ΣLREE/ΣHREE ratios vary from 7.8 to 15.7 in HMC-tubes and 19.7 to 184.8 in arg - crusts (Fig. 5.10c). The Bay of Bengal Sea water REE distribution pattern is plotted in Fig. 5.10a and 5.10b for reference. The Y/Ho molar ratios of HMC - tubes (55.6 – 63.8) are slightly higher than that of arg-crusts (46-61.4). The calculated Ce anomaly values ($Ce_{PAAS}/(0.5xLa_{PAAS} + 0.5x\ Pr_{PAAS})$) and Pr anomaly values ($Pr_{PAAS}/(0.5xCe_{PAAS} + 0.5xNd_{PAAS})$) show the presence of true positive Ce anomaly (Fig. 5.10d) for most of the HMC-tubes and arg-crusts (Bau & Dulski, 1996). The arg-crusts show a significantly greater spread in Ce_{anm} values (1.0-1.5) compared to that of HMC-tubes (1.3-1.5) (Fig. 5.10c). The Ce concentrations do not show any correlation with Fe and Mn concentrations (Fig. 5.12a and 5.12b). The Ba versus Eu plot (Fig. 5.12c) shows a positive correlation for both carbonate types.



2547

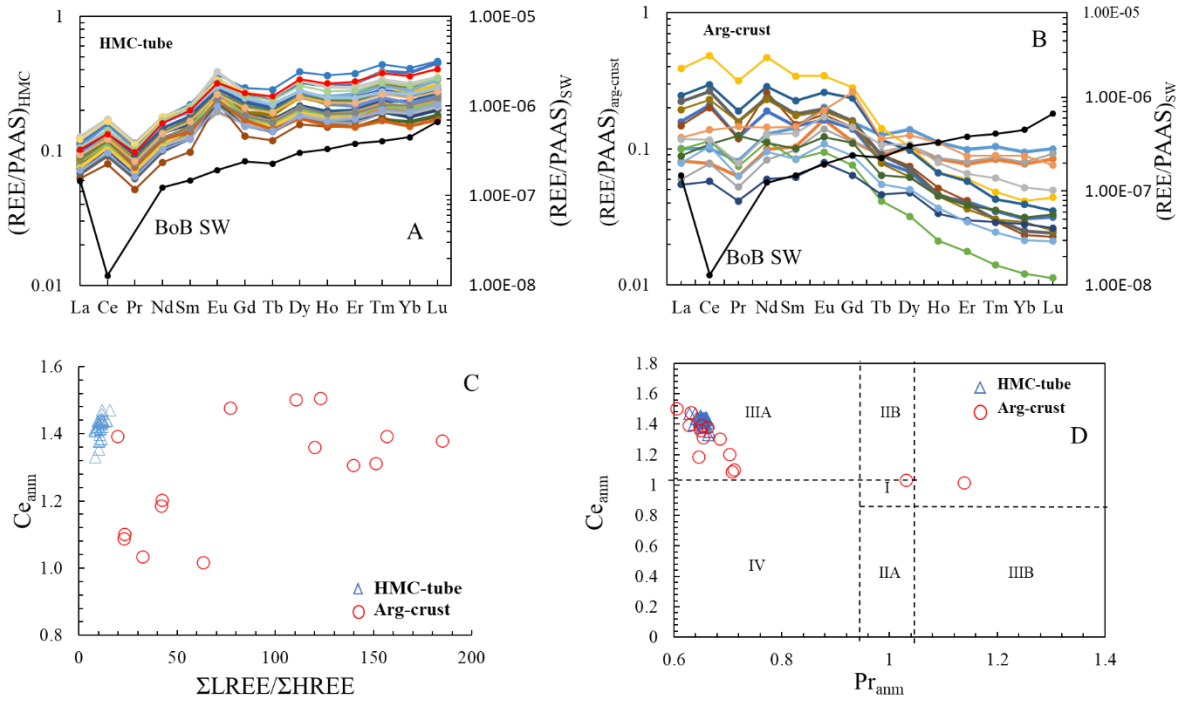
2548 Fig. 5. 8. (a) Scatter plot showing carbon and oxygen isotope ratios of HMC-tubes and arg-
2549 crust samples from SSD045/4 methane seep site. Arg (cal) and HMC (cal) are the calculated
2550 $\delta^{18}O$ values of the HMCs and Arg-crust samples in equilibrium with the ambient seawater
2551 (3.6°C at a water depth of 1,753 m) and corrected for crystal lattice substitution of Mg. The
2552 oxygen isotope ratio of the ambient deep seawater of the Bay of Bengal is adapted from
2553 Sengupta et al. (2013). (b) Scatter plot showing variations in HMC-tubes and arg-crust
2554 samples using molar ratios of Mg/Ca (mmol/mol) and Sr/Ca (mmol/mol). (c) Scatter plot
2555 between the percentage of aragonite in HMC and Sr/Ca (mmol/mol) molar ratios. (d) Scatter

2556 plot showing the variation in HMC-tubes and arg-crust samples using Mg/Ca (mmol/mol)
2557 with Ba/Ca (mmol/mol).



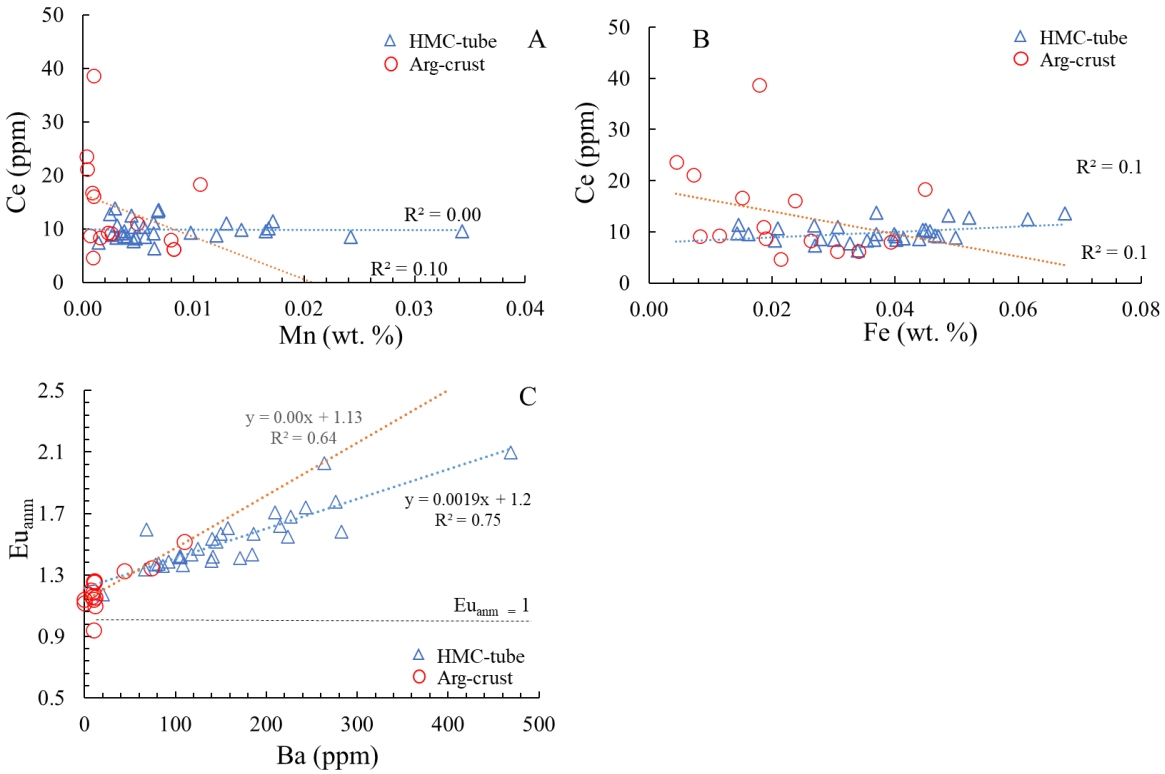
2558

2559 Fig. 5. 9. Major element (Fe, Mn, Al) and total REE concentrations in HMC-tubes and arg-
2560 crust samples from cold seep site SSD045/4 from Krishna-Godavari basin (Bay of Bengal).
2561 Leaching of the dry carbonate sample powder was carried out using 5% supra pure acetic
2562 acid (Honeywell). a. Scatter plot between ΣREE (ppm) and Al (wt%); b. Scatter plot between
2563 ΣREE (ppm) and Mn (wt%); c. Scatter plot between ΣREE (ppm) and Fe (wt%).



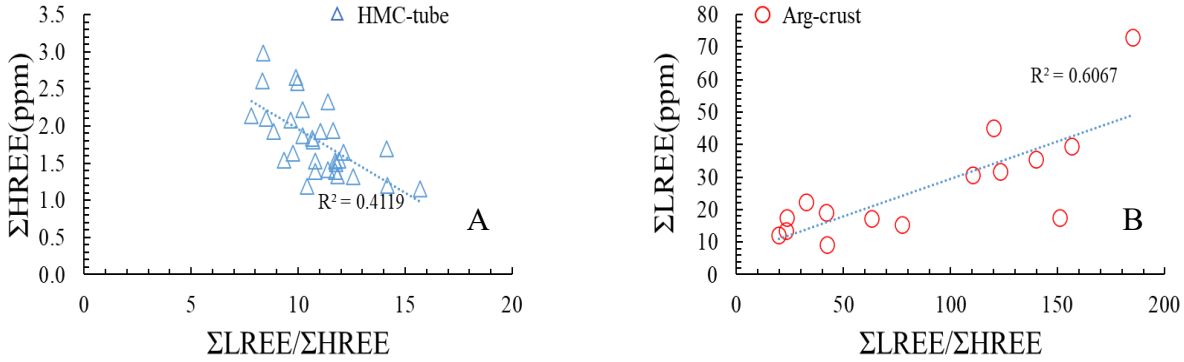
2564

2565 Fig. 5. 10. (a) PAAS-normalized REE distribution pattern of HMC-tubes. Seawater data of
2566 BoB deep waters (black dotted line) is from Yu et al. (2017). (b) $PAAS_{normalized}$ REE
2567 distribution pattern of arg-crust. Seawater data of BoB deep waters (black dotted line) is
2568 from Yu et al. (2017); (c) Scatter plot showing variation of ΣLREE/ΣHREE ratio with Ce_{anm}
2569 in HMC-tubes and arg-crust. (d) (Ce/Ce*) versus (Pr/Pr*) diagram after Bau and Dulski
2570 (1996) and Shields and Stille (2001) Shields and Stille (2001). Field I: no anomaly; field IIa:
2571 positive La anomaly produces an apparent negative Ce anomaly; field IIb: a negative La
2572 anomaly causes an apparent positive Ce anomaly; field IIIa: real positive Ce anomaly; field
2573 IIIb: real negative Ce anomaly; field IV: positive La anomaly disguises a positive Ce
2574 anomaly.



2575

2576 Fig. 5. 11. Major elements (Mn, Fe, and Al) and Ce concentrations of HMC-tubes and arg
2577 crust samples from the cold seep site SSD045/4 from Krishna-Godavari basin (Bay of
2578 Bengal). a. Scatter plot between Mn (wt%) and Ce (ppm) from HMC-tubes and arg-crust
2579 samples. b. Scatter plot between Fe (wt%) and Ce (ppm) from HMC-tubes and arg-crust
2580 samples c. Scatter plot between Ba concentrations (ppm) and Eu_{anom} from HMC-21 tubes
2581 and arg-crust samples.



2582

2583 Fig. 5. 12. REE concentrations and ratios in HMC-tubes and arg-crust samples from cold
2584 seep site SSD045/4 from Krishna-Godavari basin (Bay of Bengal). a. Scatter plot between
2585 ΣLREE/ΣHREE ratios and ΣHREE (ppm), b. Scatter plot between ΣLREE/ΣHREE ratios
2586 and ΣLREE (ppm).

5.5 Discussion

5.5.1 Authigenic Carbonate Precipitation Pathways

Aragonite and HMC precipitate across contrasting geochemical milieus (Aloisi et al., 2000; Bohrmann et al., 2002; Crémière, Lepland, Chand, Sahy, Kirsimäe, et al., 2016; Gontharet et al., 2007; Peckmann & Thiel, 2004; Pierre & Fouquet, 2007; Zhang et al., 2023) . In cold seep environments, aragonite precipitation (via SO_4^{2-}-AOM: Equations 1.10 and 1.11) and growth rates are generally favored over HMC at high methane fluxes (Luff & Wallmann, 2003), oversaturation of HCO_3^- , high porewater SO_4^{2-} and low phosphate concentrations near the seafloor (Aloisi et al., 2000; Boon et al., 2020; Bots et al., 2011; Cremiere et al., 2013; De Choudens-Sanchez & Gonzalez, 2009; Greinert et al., 2001; Nöthen & Kasten, 2011; Peckmann et al., 2001; Ruban et al., 2022; Savard et al., 1996; Weidlich et al., 2023). In the present study, occurrences of intact and broken shells of seabed - dwelling chemosynthetic bivalves (including *Calyptogena*, *Bathymodiolus* and *Acharax*) admixed with the arg-crusts (Figures 5.3k and 5.3l) (Mazumdar et al., 2019) suggest near seabed genesis of highly porous arg-crusts (Cremiere et al., 2013; Greinert et al., 2001; Roberts & Feng, 2013; Ruban et al., 2022; Wang et al., 2022). Aragonite precipitation is expected to be stabilized during times of high methane flux and near seabed SMTZ (Magalhães et al., 2012). The porous and permeable crust likely resulted in downward advective SO_4^{2-} flux facilitating aragonite crystallization. High bicarbonate concentrations responsible for aragonite precipitation may be attributed to SO_4^{2-}-AOM; the absence of pyrite in the arg-crust is possibly due to post-depositional oxidation of any FeS/FeS_2 precipitated due to the circulation of oxygenated seawater through the porous permeable crust close to the sediment-water interface. Large vugs in the sample lined with botryoidal/isopachous aragonite (Figures 5.2l and 5.2m) suggest its formation in association with methane hydrate (Bohrmann et al., 1998; Bohrmann et al., 2002; Greinert et al., 2001). The absence of terrigenous impurities as insoluble residues in the arg-crusts further supports the methane hydrate - aragonite association (Bohrmann et al., 2002) at the sea bed (Fig. 5.13). The seabed (water depth of 1,753 m and 3.6°C) at the study site is well within the methane hydrate stability zone (Fig. 5.13). Tubular - HMCs are common in many modern (Bayon et al., 2013; Joshi et al., 2014; Liang et al., 2022; Mazumdar et al., 2009; Mazumdar et al., 2011; Stakes et al., 1999; Sun et al., 2020b; Wirsig et al., 2012) and ancient (Campbell, 2006; Oppo et al., 2015) cold seep sites worldwide. In contrast to aragonite, HMC

precipitation is hindered by high porewater SO_4^{2-} concentrations above the SMTZ since incorporation of SO_4^{2-} into the calcite lattice may cause an anisotropic change in the calcite unit cell parameters leading to instability and decreased precipitation rate (Boon et al., 2020; Busenberg & Plummer, 1985; Kontrec et al., 2004) whereas, H_2S diffusing across the SMTZ absorbs on the growing surface of Ca-Mg carbonates and decreases the energy of Mg^{2+} dehydration, thus facilitating HMC precipitation (Goetschl et al., 2019; Joseph et al., 2013; Shen et al., 2014; Smrzka et al., 2021; Zhang et al., 2012; Zhang et al., 2013). Hence, low SO_4^{2-} concentrations and H_2S enrichment at SMTZ augment the precipitation of Mg-rich carbonates including dolomite in methane seep sediments. The HMC-tubes recorded in our study site may be attributed to carbonate precipitation within the gas flow conduits (chimney) and reworking of unconsolidated HMC mud (Figures 5.2a - 5.2k and 5.14) made by benthic organisms (Blouet et al., 2021; Crémière, Lepland, Chand, Sahy, Condon, et al., 2016; Crémière, Lepland, Chand, Sahy, Kirsimäe, et al., 2016; Foucher et al., 2009; Liang et al., 2022; Xu et al., 2018; Zwicker et al., 2015). Tubular methane hydrate recorded within gas flow conduits (Fig. 5.1k) further supports the methane flow in the study area. The annular/chimney-like HMC tubes (Fig. 5.1a) show a wall-to-center growth pattern (Fig. 5.1b) indicating episodic intensification of methane flux through the gas flow conduits (Jin et al., 2021; Wirsig et al., 2012). The ubiquitous occurrences of pyrite in the HMC tubes (Fig. 5.2e) indicate that the carbonate cementation occurred under sulfidic conditions attributed to SO_4^{2-}-AOM (Eq. 1.10 and 1.12) (Bayon et al., 2007; Liang et al., 2022; Lu et al., 2018; Peckmann et al., 2001; Peckmann & Thiel, 2004; Yao et al., 2021). The presence of minor dolomite in the HMC chimney structure (Fig. 5.5) is reported in our micro-FTIR study. The chimneys probably formed within the gas flow conduits recorded in the black muddy sediments, as evident from the comparable shape and diameter of the HMC chimneys (1.2-2.4 cm) and gas flow conduits (0.3-2.3 cm) respectively. The absence of aragonite in the chimneys suggests a lack of seawater SO_4^{2-} circulation. The frequent occurrences of HMC-tubes with carbonate pelloids (Fig. 5.2f-5.2j) may be attributed to bioturbation activity and fecal pellet production (Gontharet et al., 2007; Mazumdar et al., 2009; Mazumdar et al., 2011; Sun et al., 2020b; Xu et al., 2018; Zwicker et al., 2015) by the benthic organisms. Burrowing bivalves including *Calyptogena* sp., *Acharax* sp., *Thysiridae* sp., and polychetes, etc. are known to exist at the K-G basin cold seep sites (Mazumdar et al., 2019; Peketi et al., 2022). These organisms obtain H_2S/CH_4 by extending their tensile foot into the sediments (Childress & Girguis, 2011; Levin, 2005; Seike et al., 2012) to carry out their metabolic

activities. Based on the extent of penetration capacity, the benthic organisms may create shallow to deep burrows (up to 30-50 cm) into the sediments (Dufour & Felbeck, 2003; Sun et al., 2020a; Zwicker et al., 2015) Sun et al., 2020; Zwicker et al., 2015). High magnesian calcite pelloids including fecal pellets (Mazumdar et al., 2011; Teichert et al., 2005; Vanneste et al., 2012) in the HMC-tubes may be attributed to the reworking of shallow unconsolidated HMC precipitated near the sediment-water interface (Fig. 5.13). Precipitation of HMC close to the sediment-water interface indicates shallow SMTZ in a low (diffusion) dominated diagenetic regime in contrast to the dominantly high (advective) flow pathway in aragonite crust formation. The cavities/annular and inter-pelloidal spaces within the burrows show the presence of acicular aragonite (Fig. 5.2g - 5.2j) and HMC cementation as evident from EDS (Fig. 5.3) and FTIR (Fig. 5.4) data. The aragonite precipitation within the HMC tubes may be attributed to the percolation of SO_4^{2-}-rich seawater into the burrows facilitating aragonite crystallization (Bots et al., 2011; Cuesta Mayorga et al., 2019; Fernández-Díaz et al., 2010; Gong et al., 2018; Roberts et al., 2010) during the burrowing phase. The HMC cementation may be attributed to post - burial SO_4^{2-} reduction, H_2S build - up, and precipitation of HMC-cement/pyrite SO_4^{2-} flux (Fig. 5.13), earlier modeled in Zwicker et al. (2015).

5.5.2 Evidence of Methanotrophic Biomass

Highly depleted carbon isotope ratios of the organic matter in the HMC tubes suggest a variable contribution of methanotrophic input. The TOC contents and $\delta^{13}C_{TOC}$ values in the HMC tubes ranged from 0.17% to 0.77% and -54.8 to -20.0‰ (Avg: -35.2 ± 8‰ VPDB), respectively, compared to the ambient clastic sediments with an average $\delta^{13}C_{TOC}$ of -20 ± 0.3‰ (Table 5.2). The spread in $\delta^{13}C_{TOC}$ values of the HMC tubes may be attributed to the variable contribution and preservation of the chemosynthetic biomass (Yao et al., 2021). The TOC content and the $\delta^{13}C_{TOC}$ values in the arg-crust could not be determined in the present study.

5.5.3 Carbon Source and Carbonate Formation Environment

The $\delta^{13}C_{carb}$ values of HMC-tubes, and arg-crusts (Fig. 5.8a) suggest biogenic methane as the carbon source (Chuang et al., 2019; Grossman & Ku, 1986; Mazumdar et al., 2009; Peketiet al., 2012; Ussler III & Paull, 2008) The calculated $\delta^{18}O$ values (Grossman & Ku, 1986) of the HMC-tubes in equilibrium with the present deep-sea water (water depth of 1,753 m and 3.6°C) and corrected for crystal lattice substitution of Mg (Kim & O'Neil, 1997;

Tarutani et al., 1969) are consistently lower than the measured $\delta^{18}O$ values (Fig. 5.8a). The positive $\Delta\delta^{18}O$ ($\delta^{18}O_{measured}$-$\delta^{18}O_{calculated}$) values (+1.0 to +2.9‰) indicate ^{18}O enrichment of interstitial waters likely due to hydrate destabilization/degassing, which results in freshening of pore water (Bohrmann et al., 2002; Greinert et al., 2001; Hesse & Harrison, 1981; Naehr et al., 2007; Tomaru et al., 2006; Yao et al., 2021). On the other hand, methane hydrate crystallization results in preferential trapping of ^{18}O in the clathrate structure leading to ^{16}O enrichment in the residual porewater and exclusion of salts, which leads to enhanced chlorinity (Tomaru et al., 2006; Ussler & Paull, 1995). The calculated $\delta^{18}O$ values of arg-crusts in equilibrium with the ambient seawater are consistently higher than the measured $\delta^{18}O_{arg}$ values (Fig. 5.8a). The low $\Delta\delta^{18}O_{values}$ (-1.8 to +0.7‰) possibly suggest a lowering of porewater $\delta^{18}O_{values}$ due to methane hydrate crystallization. Lower measured values compared to the calculated $\delta^{18}O_{arg}$ values in cold seep carbonates from the northern South China Sea (Liang et al., 2022) have been attributed to hydrate stabilization and lowering of porewater $\delta^{18}O$ values. ^{16}O enriched aragonite associated with methane hydrate has been termed as clathrite by Teichert et al. (2005a) attributed to the trapping of ^{18}O in coexisting methane hydrate (Joseph et al., 2013). Co-occurrence of methane hydrate and aragonite at and above sediment-water interface has been demonstrated by Bohrmann et al. (2002) and Greinert et al. (2001).

5.5.4 Redox Variability in Carbonate Formation Environment

The authigenic carbonate phases are likely to inherit the pore water REE characteristics (Smrzka et al., 2019) since no significant fractionation is expected during REE incorporation into the carbonate minerals. Both the carbonate types in our study do not resemble the deep seawater REE pattern Bay of Bengal; (Yu et al., 2017), which may be attributed to porewater REE complexation and redox processes during carbonate precipitation (Deng et al., 2017; Sholkovitz et al., 1994; Sholkovitz et al., 1992). The PAAS normalized REE distribution pattern (Fig. 5.11a and 5.11b) and ΣLREE/ΣHREE ratios (Fig. 5.10c) are distinct for HMC-tube and arg-crust samples. Diagenetic remobilization of REE-bearing particulates has strong control over the distribution and concentration of REEs in reducing sedimentary pore waters (Elderfield & Sholkovitz, 1987; Haley et al., 2004; Himmler et al., 2013; Sholkovitz et al., 1992; Smrzka et al., 2019). In contrast to LREEs and MREEs, which have a stronger affinity toward particulates including Fe-Mn (oxy)hydroxides and humic matter, the HREEs form stronger carbonate complexes in seawater or sediment pore waters (Deng

et al., 2017; Himmler et al., 2013; Luo & Byrne, 2004; Ohta & Kawabe, 2001; Sholkovitz et al., 1994). At high porewater alkalinity, $[HREE](CO_3)_2^-$ complexes (Equations 5.1 and 5.2) have enhanced stability (Luo & Byrne, 2004).

$$REE^{3+} + HCO_3^- \rightarrow REECO_3^+ + H^+ \quad \text{(Eq. 5.1)}$$

$$REE^{3+} + 2HCO_3^- \rightarrow REE(CO3)_2^- + 2H^+ \quad \text{(Eq. 5.2)}$$

The stability of $REE(CO_3)_2^-$ increases steadily from LREE to HREE in alkaline solutions (Ohta & Kawabe, 2001). At methane seep sites, the AOM-driven (Equation 1.10) carbonate alkalinity of sediment porewater shows a marked increase with depth below the seabed (Krause et al., 2014; Liu et al., 2020; Nöthen & Kasten, 2011; Pop Ristova et al., 2012) leading to enhanced $[REE](CO_3)_2^-$ complexation (Himmler et al., 2013; Kim et al., 2012; Yang et al., 2017). The distinct HREE enrichment in HMC tubes in the present study may be attributed to the enhanced carbonate alkalinity. Relative enrichment of HREE and MREE over LREE in HMCs has previously been reported from the cold seep carbonates (Rongemaille et al., 2011; Sun et al., 2020b). In contrast, the arg-crusts show a distinctly broad REE concentration range and ΣLREE/ΣHREE ratios (Fig. 5.10c). The broad range of ΣLREE/ΣHREE ratios in aragonite crusts is also observed in high-resolution laser-ablation analysis (Himmler et al., 2013; Zwicker et al., 2018) of different types of aragonites (microcrystalline, cryptocrystalline and botryoidal), which show markedly variable REE distribution patterns including the LREE enriched and HREE depleted patterns which is observed in our study as well (Fig. 5.10b). The ΣLREE/ΣHREE ratios of the arg-crust show a good positive correlation ($R^2 = 0.61$: Fig. 5.12) with ΣLREE suggesting LREE enrichment in porewater due to reductive dissolution of Fe-Mn (Sholkovitz et al., 1992) and LREE incorporation into aragonite crystal lattice. Based on the Ce_{anm} versus Pr_{anm} diagram (Bau & Dulski, 1996), all the carbonate samples (excluding two arg-crust samples) show true positive Ce anomalies (Fig. 5.10d). The arg-crust samples show a significantly larger spread in Ce_{anm} (1.0-1.5) values compared to HMCs (1.33-1.43). The absence of correlation between Ce concentrations and Fe & Mn concentrations (Fig. 5.11a and 5.11b) indicates that the 5% acetic acid leachate has no significant contribution from the Fe/Mn phases, which are known to hold the bulk of the LREEs including Ce in the marine sediments. Therefore, the positive Ce anomaly (Fig. 5.11c) in the carbonate minerals may be attributed to the enhanced Ce concentrations in the pore waters from which the carbonates precipitated.

Enhanced Ce concentrations in the pore waters may be a result of the dissolution of Fe-Mn (oxy)hydroxides under reducing/sulfidic conditions. The observed large spread in ΣLREE/ΣHREE ratios and Ce_{anm} values (Fig. 5.11c) in the arg-crusts may be attributed to a broad micro-spatial variation in redox conditions owing to cementation in open to close diagenetic systems and evolution of pore fluid composition in the course of early diagenesis (Crémière, Lepland, Chand, Sahy, Condon, et al., 2016; Crémière, Lepland, Chand, Sahy, Kirsimäe, et al., 2016; Himmler et al., 2010; Himmler et al., 2013; Zwicker et al., 2018). On the other hand, the constrained Ce_{anm} and ΣLREE/ΣHREE ratios in HMC-tubes may be attributed to persistent sulfidic conditions and limited redox variability. All the carbonate samples barring one show a positive Eu-anomaly ($Eu_{anm} > 1$). A strong positive correlation (Fig. 5.11c) of Eu_{anm} with Ba concentrations may be attributed to the influence of BaO production during ICP MS analysis (Zhu & Itoh, 2021). Ba/Ca molar ratios are significantly lower in arg-crusts when compared to that of HMC-tubes (Fig. 5.11d). Due to the larger ionic radii of Ba^{2+} (1.47 Å), the incorporation of Ba^{2+} is relatively favorable (Mavromatis et al., 2018) in aragonite lattice over calcite since the ionic radii of Ca^{2+} in aragonite and calcite are 1.18 Å and 1 Å, respectively. Low concentrations of Ba^{2+} in arg-crust samples may be attributed to the precipitation of $BaSO_4$ phase (Eq. 5.3) above SMTZ, which is unlikely to dissolve in 5% acetic acid solution used in the present study. Dissolution of $BaSO_4$ (bio-barite/diagenetic barite) within the SO_4^{2-} depleted zone below SMTZ results in diffusion of Ba^{2+} across SMTZ where it re-precipitates as $BaSO_4$ (Dickens, 2001; Fischer et al., 2013; Torres et al., 1996 a). In contrast, the observed high Ba concentrations in HMC tubes may be attributed to the precipitation of the $BaCO_3$ (Witherite) (LÜ et al., 2003; Pi et al., 2014) mineral phase (Eq. 5.4) below the SMTZ due to high alkalinity.

$$Ba^{2+} + SO_4^{2-} \leftrightarrow BaSO_4 \quad \text{(Eq. 5.3)}$$

$$Ba^{2+} + HCO_3^{-} \leftrightarrow BaCO_3 + H^{+} \quad \text{(Eq. 5.4)}$$

5.5.5 Sr Distribution in Carbonates

Sr/Ca molar ratios in arg-crust samples are significantly greater than that of HMC-tubes (Fig. 5.8b). The preferential incorporation of Sr into aragonite over calcite may be attributed to the larger Sr^{2+} ionic radii (Shannon ionic radii = 1.31 Å) which is compatible with the aragonite crystal lattice in which Ca^{2+} ion (Shannon ionic radii = 1.18 Å) is in nine coordination state (Sunagawa et al., 2007). In contrast, the 6-coordination state of Ca^{2+} (ionic radii = 1 Å) in calcite is unfavourable for Sr^{2+} substitution because of its larger ionic radii.

On the other hand, Ca^{2+} may preferably be substituted by smaller cations such as Mg^{2+} (Shannon ionic radii = 0.72 Å). Incorporation of Mg^{2+} ions may cause strain on the calcite lattice, which may be relieved by the inclusion of a minor content of Sr^{2+} (Mucci & Morse, 1983). The positive correlation between the Sr/Ca molar ratio and aragonite percentage in HMC-tubes (Fig. 5.8c) shows Sr contribution from aragonite crystallization within the cavities and inter-pelloidal spaces of HMC tubes. Strontium enrichment in the cavity filling aragonite in HMC is further supported by the EDS data (Fig. 5.3).

5.5.6 Conceptual Model

A conceptual depositional model (Fig. 5.13) for the authigenic carbonate formation at the K-G basin methane seep site has been developed by collating the physical and geochemical observations within a framework of existing concepts (Bayon et al., 2009; Crémière, Lepland, Chand, Sahy, Condon, et al., 2016; Crémière, Lepland, Chand, Sahy, Kirsimäe, et al., 2016; Foucher et al., 2009; Liang et al., 2022; Luff & Wallmann, 2003). The model attempts to contrast the depositional regime of aragonite-crust and tubular HMCs at the study site. Previous studies from K-G basin have proposed the influence of both advective (fracture controlled) and diffusive methane flow pathways on sediment biogeochemistry. Here we propose two scenarios, a high CH_4 flow system (advective flow) and a low flow system (diffusive flux), to model the authigenic carbonate formation. In scenario-i, the build-up of aragonite crust associated with methane hydrate formation across the sediment-water interface is attributed to the high methane flow regime and presence of SO_4^{2-} ions in the pore fluid. The fault/fracture systems in the high flow regime are considered to be cut across the seabed and provide conduits for CH_4 seepage. HMC chimneys (Fig. 1.1a and 1.1b) probably formed in high methane flow conditions below SMTZ. In scenario-ii, the fault/fracture system presumably is subsurface and does not cut across the sediment-water interface. The argillaceous unconsolidated HMC micritic layer is formed at the sediment-water interface under diffusive methane flux conditions. Subsequent reworking of the HMC layers at the sediment-water interface by benthic biota produced the pelloids filling up the tubular burrows. The model also suggests multiphase cementation of the inter-pelloidal pores and cavities by aragonite and HMC during early and post - burial diagenesis respectively.

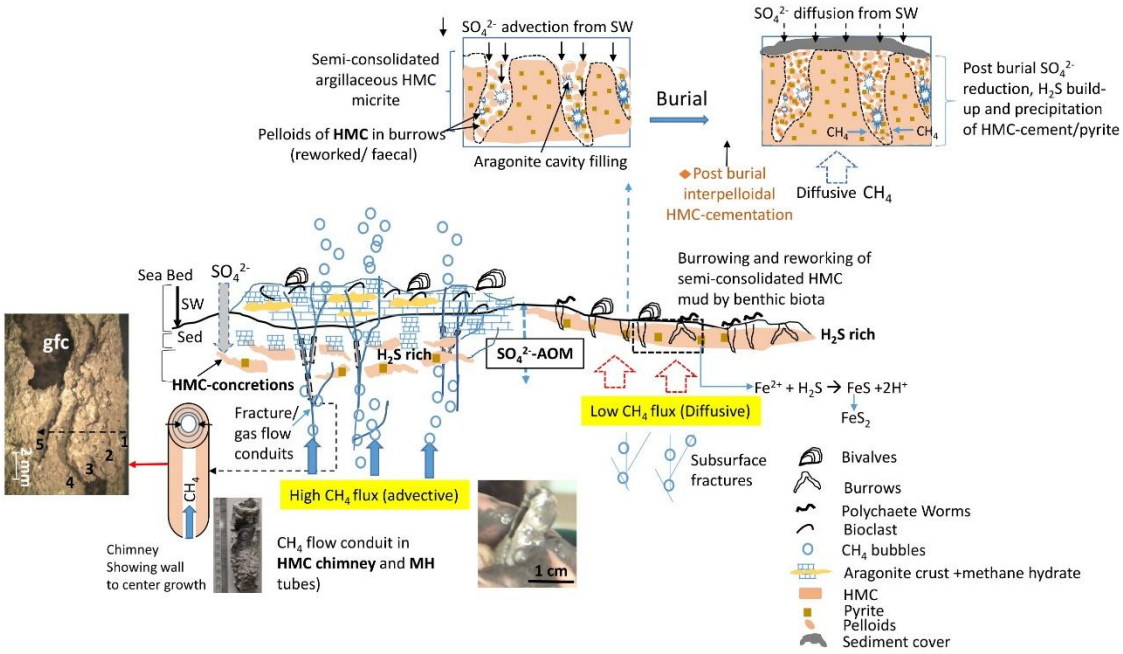


Fig. 5.13. A conceptual depositional model showing the formation of aragonite crusts and tubular HMCs at high (advective) and low (diffusive) methane flux scenarios.

5.6 Conclusion

Here we report the mineralogy and geochemistry of authigenic carbonates in spade cores recovered from a cold seep site (SSD045/4) off the Krishna - Godavari basin (western Bay of Bengal). An attempt has been made to reconstruct the formational pathways of the carbonate minerals. The authigenic carbonate minerals at the study site comprise tubular HMCs and fragments of porous arg-crusts admixed with chemosynthetic bivalve shells. The carbonate mineral precipitation at the seep sites may be attributed to enhanced bicarbonate alkalinity fueled by SO_4^{2-}-AOM in the sediment interstitial water. The $\delta^{13}C$ values of the carbonates suggest biogenic methane as the dominant carbon source. Positive $\Delta\delta^{18}O_{meas-calc}$ values (+1.0 to + 2.9‰) of the HMC-tubes indicate ^{18}O enrichment of interstitial water likely due to methane hydrate destabilization/degassing. In contrast, the low $\Delta\delta^{18}O_{meas-calc}$ values (-1.8 to +0.7‰) of arg-crusts possibly suggest a lowering of porewater $\delta^{18}O$ values due to methane hydrate crystallization. Aragonite crusts are admixtures of chemosynthetic shells, microcrystalline aragonite cement and botryoidal aragonite lining the cavities. This type of crust formation is favored by vigorous methane flow sustained by the deep fault/fracture system of the K-G basin. The arg-crust formation happened close to the sediment-water interface and interlayered with methane hydrate. At our study site, the HMC-tubes occur as chimneys and bioturbation structures filled with pelloids and micrite-

microsparitic carbonate. The chimneys probably formed within the gas flow tubes recorded in the black muddy sediments. The absence of aragonite in the chimneys suggests a lack of seawater SO_4^{2-} circulation. High magnesian carbonate pelloids of various shapes and sizes may be attributed to the reworking of shallow semi-consolidated HMC layers by burrowing benthic biota and fecal pellet production. The presence of acicular aragonite and HMC cement within the gas conduits/cavities and inter pelloidal space inside the burrows suggest multiple cementation episodes during burial. The PAAS normalized REE distribution patterns of HMC tubes show distinct HREE enrichment with relatively lower ΣLREE/ΣHREE ratios which may be attributed to the enhanced carbonate alkalinity and $REE(CO_3)_2^-$complexation and reductive remobilization of LREEs from particulate Fe-Mn (oxy)hydroxides. On the other hand, the arg-crusts show a relative enrichment of LREEs and a distinctly broad REE concentration range. The large spread in ΣLREE/ΣHREE ratios Ce_{anm} values in the arg-crusts may be attributed to a broad micro-spatial variation in redox conditions owing to cementation in open to close diagenetic systems and evolution of pore fluid composition in the course of early diagenesis. On the other hand, constrained Ce_{anm} and ΣLREE/ΣHREE ratios in HMC-tubes may be attributed to dominant sulfidic conditions within and below SMTZ. The ubiquitous presence of pyrite and minor dolomite in HMCs supports persistent sulfidic conditions. Contrasting Ba/Ca ratios in HMC and aragonite additionally suggest contrasting redox regimes for the two carbonate phases. Based on our petrographic observations and geochemical analyses of cold seep carbonates recovered from the K-G basin cold seep sites, we propose a generalized model explaining the contrasting depositional/diagenetic conditions responsible for the formation/distribution of aragonite crust and high-magnesium calcite.

Chapter 6. Iron-sulfur-carbon systematics of cold seep sediments

6.1 Introduction

At methane cold seeps, sulfate reduction coupled with anaerobic oxidation of methane (SD-AOM), is the key process, which is mediated by a consortium of sulfate-reducing bacteria (SRB) and methanotrophic archaea (ANME) (Boetius, 2000; Knittel & Boetius, 2009; Knittel & Boetius, 2010; Lapham et al., 2024; Orphan et al., 2001; Wegener et al., 2015). SD-AOM predominantly occurs in a redox zone known as the sulfate-methane transition zone (SMTZ), where downward diffusing sulfate interacts with ascending methane and drops to background levels. Increased concentrations of bicarbonate ions and hydrogen sulfide in the sediment pore waters of cold seep sediments are attributed to the SD-AOM processes within the SMTZ (Boetius & Wenzhofer, 2013; Jørgensen et al., 2004; Jorgensen et al., 2019; Nöthen & Kasten, 2011; Pellerin et al., 2018). The depth of the SMTZ is governed by the balance between sulfate supply, methane flux, and sediment permeability, as well as by factors such as sediment thickness, porewater composition, and alterations linked to late stage methanogenesis. Because it reflects depositional stability, methane flux intensity, and the extent of the methanic zone, reconstructing both present and past SMTZ positions is of considerable importance for geological interpretations (Argentino et al., 2020; Borowski et al., 2013; Graves et al., 2017; Mazumdar et al., 2009; Sundby et al., 2021).

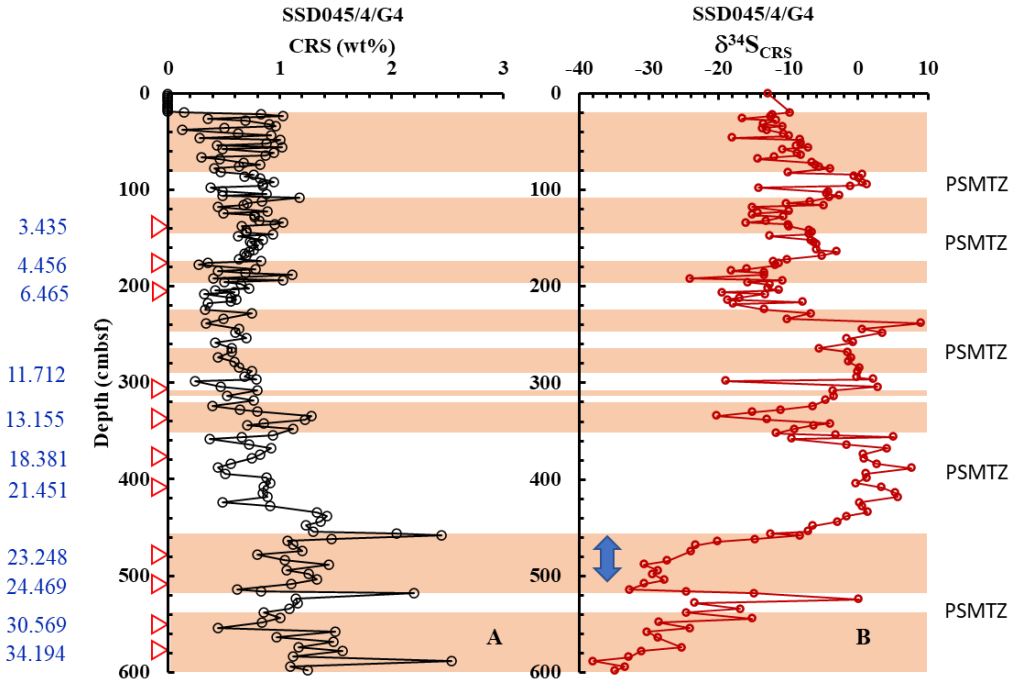
A portion of the H_2S generated through SD-AOM can be scavenged from pore waters via Fe-sulfidization forming mackinawite (FeS) or greigite (Fe_3S_4), which are eventually buried as pyrite in marine sediments, organic matter sulfurization, or oxidation at the sediment-water interface, producing intermediate sulfur species such as sulfoxy anions ($S_2O_3^{2-}$, SO_3^{2-}, $S_4O_6^{2-}$), elemental sulfur (S^0), and polysulfides (S_x^{2-}) (Cremiere et al., 2017; Jørgensen & Kasten, 2006; Jorgensen et al., 2019; Raven et al., 2016; Rickard & Luther III, 2007; Schoonen, 2004; Werne et al., 2003). Enhanced pyrite contents are often observed within or below the SMTZ, which accounts for the extensive paleo-seepage activity at the corresponding depth intervals (Q. Lin et al., 2016). In this study we reconstruct the paleo-SMTZs using the Pyrite-S ($\delta^{34}S_{CRS}$) isotope ratios and Fe-speciation data from the cold seep core (SSD045/4/G4).

6.2 Results

6.2.1. Sedimentary sulfur contents and isotope ratios

Sedimentary sulfur contents were analysed for cores collected from the cold-seep (SSD045/4/G4) and non-seep (SSD045/13/G1) regions. As part of the geochemical analyses, acid-volatile sulfur (AVS) contents were measured, but AVS was below the detection limit in both cores; therefore, only chromium-reducible sulfur (CRS) contents is reported (Fig. 6.1a). In the cold-seep core, CRS concentrations were below detection level in the upper 20 cm (Table 6.2). Between 20 cm and 428 cm depth, CRS values fluctuated between 0.5 wt% and 1.0 wt%, whereas below 428 cm they increased progressively, ranging from 0.5 wt% to 2.5 wt%. In contrast, the non-seep core exhibited markedly lower CRS contents, varying between 0.001 wt% and 0.03 wt% (average ≈ 0.01 wt%), which are an order of magnitude lower than those in the cold-seep sediments (Table 6.3).

The $\delta^{34}S_{CRS}$ values (Fig. 6.1b) range from -38.0 to +9.0‰ (VCDT), with an average of -10.4‰. The most ^{34}S-depleted value (-38.0‰) occurs at 588 cm, whereas at the near-surface depth of 0.5 cm $\delta^{34}S_{CRS}$, is -12.9‰. In the $\delta^{34}S_{CRS}$ profile, pink-shaded intervals denote the sediment–water interface, while the intervening white bands mark paleo-SMTZs preserved



throughout the cold-seep core. At the non-seep site (SSD-045/13/G1), $\delta^{34}S_{CRS}$ values (Fig. 6.1d) varying between -44.6 and -6.6‰ (VCDT).

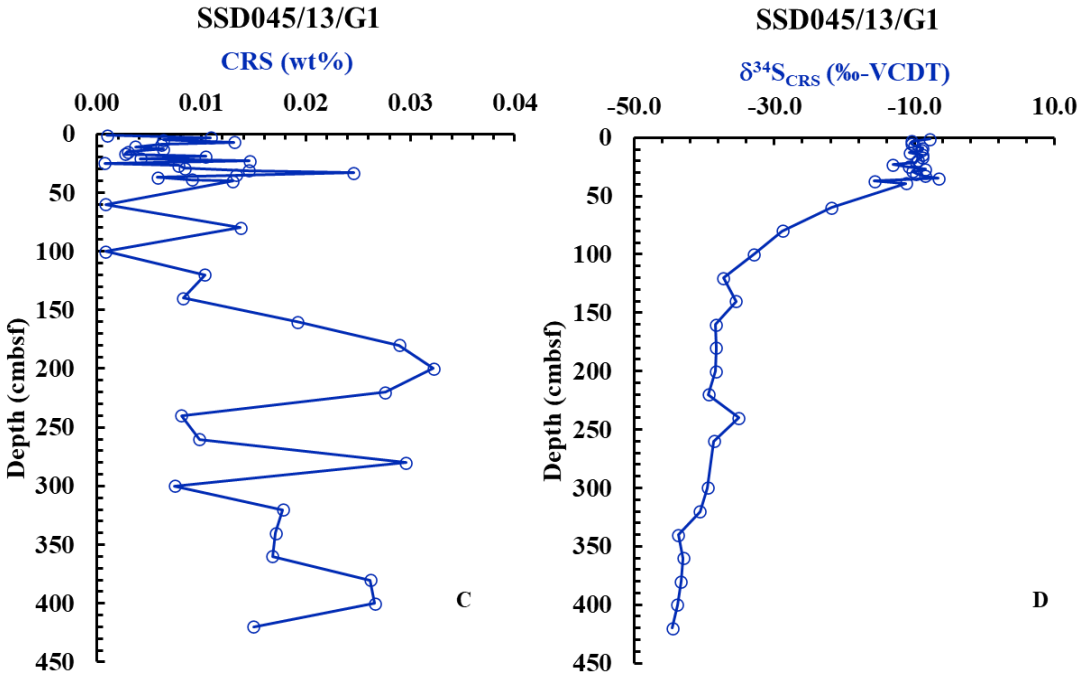
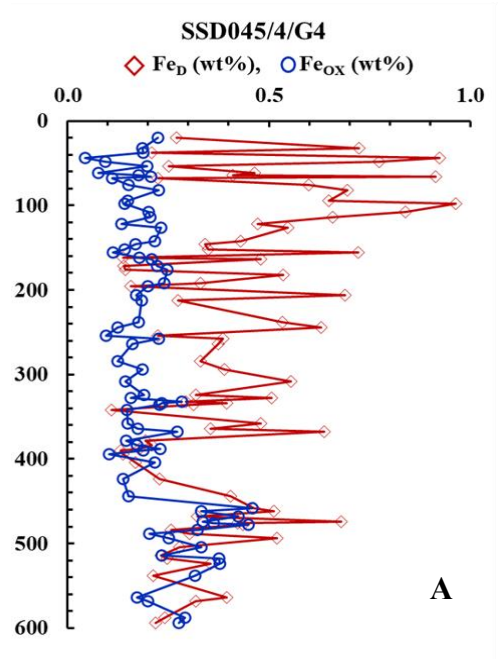
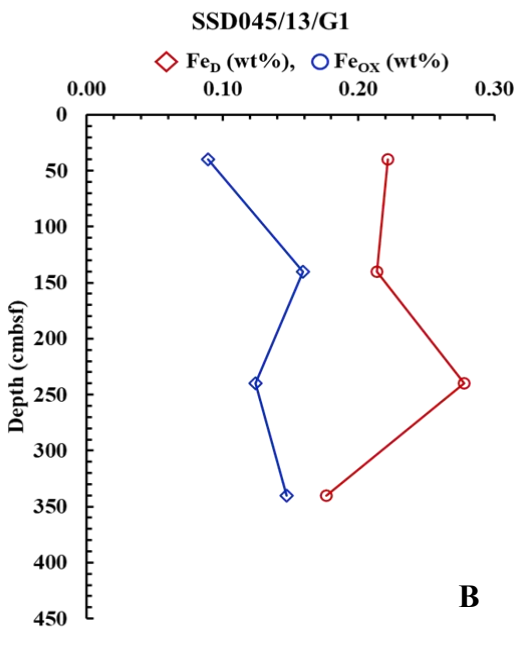


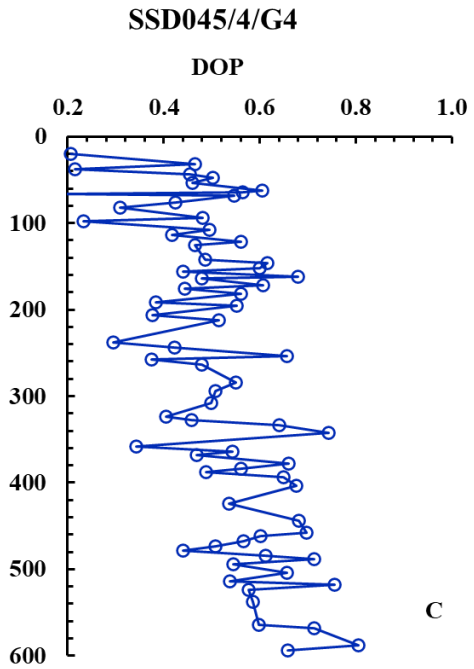
Fig. 6. 1. a) Concentration profile of chromium-reducible sulfur (CRS, in wt%) from cold seep core SSD045/4/G4. b) Sulfur isotopic composition of CRS ($\delta^{34}S_{CRS}$) from the same core. The double-headed blue arrow represents the current sulfate-methane transition zone (SMTZ) from Peketi et al. (2022). The shaded region indicates depleted CRS isotope ratios; the white shaded region corresponds to paleo-SMTZs recorded throughout the core. (Note: Shading in panel A is based on $\delta^{34}S_{CRS}$ profile). c) CRS concentration profile (in wt%) from non-seep core SSD045/13/G1. d) Sulfur isotopic composition of CRS ($\delta^{34}S_{CRS}$) from non-seep core SSD045/13/G1.

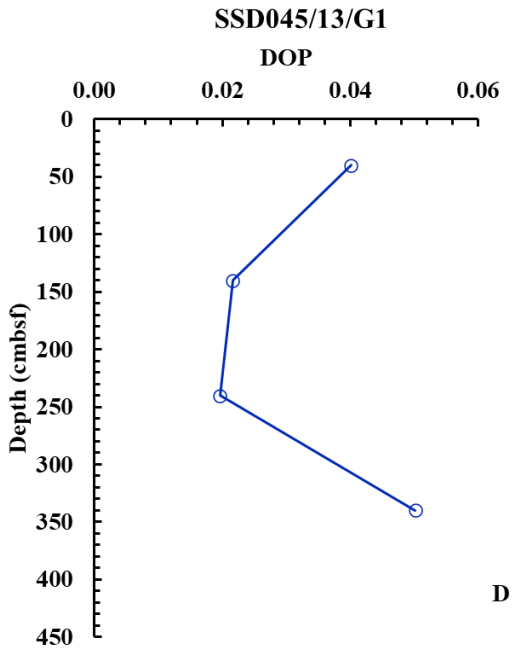
6.2.2. Fe-speciation

In the cold-seep (SSD045/4/G4) and non-seep (SSD045/13/G1) cores, the distribution of different iron phases shows distinct contrasts (Fig. 6.2). In the cold-seep core (Fig. 6.2a), the dithionite leachable iron (Fe_D) ranges from 0.11 to 0.96 wt% (Table 6.2), while the corresponding oxalate leachable iron (Fe_{OX}) varies between 0.04 and 0.46 wt%. The non-seep site (Fig. 6.2b), Fe_D ranges from 0.09 to 0.16 wt%, and Fe_{OX} from 0.18 to 0.28 wt% (Table 6.3). The total reactive iron (Fe_{TR}) ranges from 0.32 to 3.05 wt% in the cold-seep sediments (Fig. 6.2e) and from 0.27 to 0.41 wt% in the non-seep core (Fig. 6.2f).









2922

2923

2924

2925

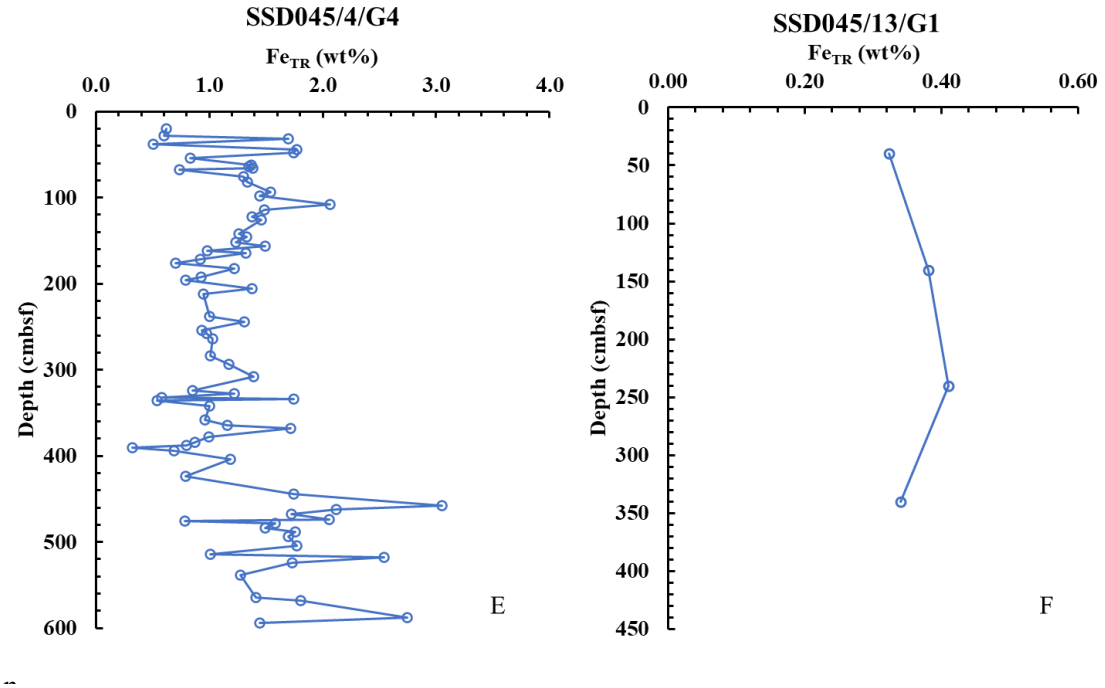


Fig. 6. 2.Concentration profile of the dithionite extractable iron (Fe_D) and oxalate extractable (Fe_{OX}) in the cold seep core (a) and non-seep core (b). DOP values for cold seep (c) and non-seep core (d). Total reactive iron (Fe_{TR}) concentrations from cold seep (e) and non-seep core (f).

6.2.3. Sedimentary organic

Total organic carbon content varies from 0.87 to 2.50 wt% (Table 6.2) and 0.7 to 2.4 wt% (Table 6.3) for cold seep core (Fig. 6.3 a and b) and non-seep core (Fig. 6.3c and d) respectively. The molar ratios of TOC/TN vary from 8.9 to 25.4.

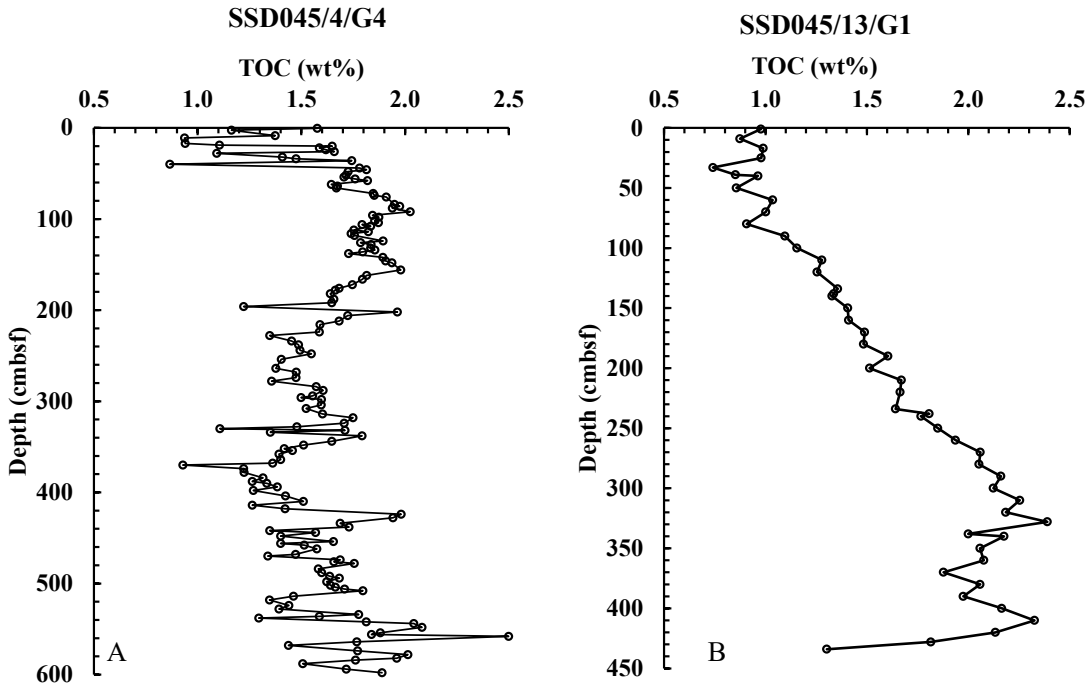


Fig. 6. 3. a) Concentration profile of total organic carbon in wt% from cold seep core (SSD045/4/G4). c) Concentration profile of total organic carbon in wt% from non-seep core (SSD045/13/G1). d) Carbon isotopic composition of organic carbon ($\delta^{13}C_{org}$) from cold seep core (SSD045/13/G1).

6.3. Discussion

6.3.1 Sulfidization process at the cold seep region

In the present study, the cold-seep core (SSD045/4/G4) exhibits markedly elevated CRS contents approximately two orders of magnitude higher than those observed in the non-seep core (SSD045/13/G1). From the surface to 434 cm depth, CRS concentrations remain below 1.0 wt% with minor fluctuations. Below 434 cm, CRS contents increase notably, ranging from 1.5 wt% to 2.5 wt%, with the maximum value recorded at 588 cm. In marine sedimentary environments, sulfide mineral precipitation is typically characterized by microbially mediated sulfur cycling processes, primarily organo-clastic sulfate reduction (OSR) and sulfate-driven anaerobic oxidation of methane (SD-AOM) (Bazzaro et al., 2020; Borowski et al., 2013; Gong et al., 2018; C. Y. Hu et al., 2017; Jørgensen et al., 2004; Q. Lin et al., 2016; Peckmann & Thiel, 2004; Sun et al., 2024). Hydrogen sulfide generated by

these pathways reacts with reactive iron (Eq. 1.13) to precipitating metastable Fe-sulfides such as mackinawite (FeS) and greigite (Fe_3S_4), that ultimately transformed and preserved as pyrite (FeS_2) (Butler et al., 2004; Fernandes et al., 2020; Liu, 2025; Mazumdar et al., 2012; Neretin et al., 2004; Peketiet al., 2012; Rickard et al., 2017). At methane-rich cold seep settings, intensified methane flux enhances the SD-AOM rate, thereby promoting the authigenic precipitation of Fe-bearing sulfide minerals (FeS, FeS_2) within the sulfate-methane transition zone (SMTZ) (Arvidson et al., 2004; Formolo et al., 2004; Jørgensen, 2021; Jørgensen et al., 2004; N. Li et al., 2016; Lim et al., 2011; Neretin et al., 2004; Peketi et al., 2015; Peketiet al., 2012; Wehrmann et al., 2015).

Consequently, in methane-rich marine systems, AOM serves as the principal driver of pyrite formation. The elevated CRS contents observed in the cold-seep core are thus attributed to enhanced SD-AOM activity. Furthermore, the absence of a significant correlation between CRS and TOC (Fig. 6.5) supports the interpretation that pyrite enrichment is primarily controlled by methane-driven sulfidic diagenesis rather than by organic-matter degradation alone. Net CRS content depends on multiple factors including content and reactivity of total iron content, H_2S exposure time and H_2S concentrations.

6.3.2 Fe-Speciation

Reactive iron minerals in marine sediments can be classified based on their sulfidization half-lives into highly, moderately, and poorly reactive phases (Canfield et al., 1992). Highly reactive phases such as ferrihydrite, lepidocrocite, goethite, and hematite have short half-lives of ~2.8 hours to 31 days (Table 6.1) and are generally extracted using the dithionite method (Fe_D). Moderately reactive phases, including magnetite and reactive silicates, exhibit half-lives on the order of 105-230 years and correspond to oxalate-extractable iron (Fe_{OX}). Poorly reactive phases, such as sheet silicates and other aluminosilicates, possess half-lives exceeding 8.4×10^4 years. In marine sediments, dithionite-extractable Fe(oxy)hydroxides typically supply 75–85% of the reactive iron available for pyrite formation (Raiswell & Canfield, 2012).

In the cold-seep core, elevated Fe_D contents near the surface suggest the availability of reactive iron for sulfidization. Below 424 cm, Fe_D concentrations decrease markedly, plausibly due to progressive consumption of reactive iron during pyritization consistent with the concurrent increase in CRS contents at this depth interval. The enhanced CRS values are attributed to intensified SD-AOM activity, as indicated by the absence of a significant correlation between TOC and CRS (Fig. 6.5). In contrast, the non-seep core (SSD-

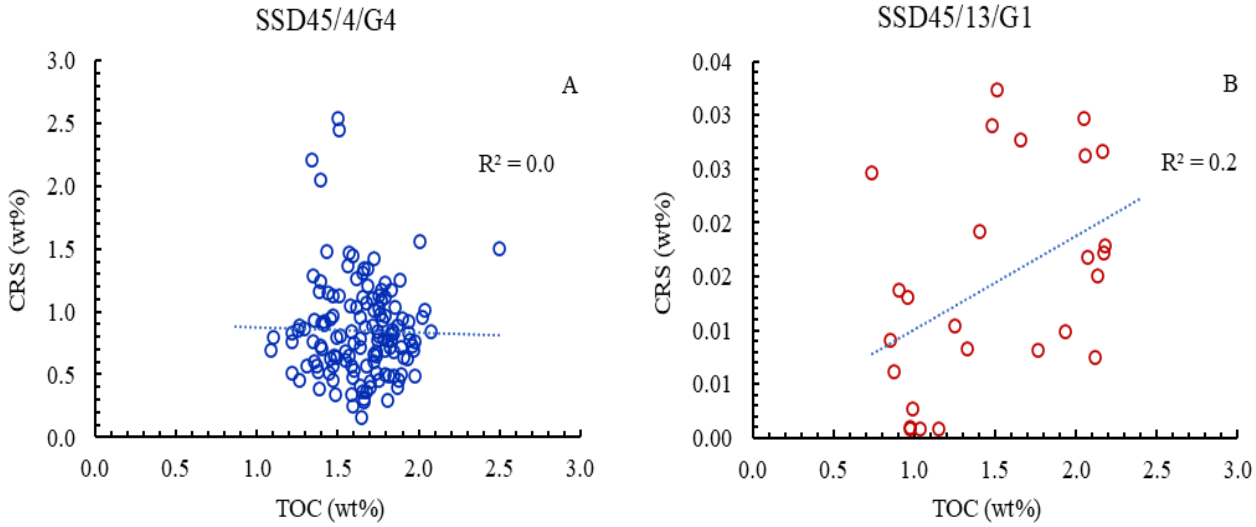
045/13/G1) shows minimal correlation between these parameters (R^2 = 0.2), suggesting negligible sulfide generation through sulfate reduction.

The total organic carbon to total sulfur ratio (TOC/TS) has long been used as a diagnostic proxy to distinguish marine from freshwater depositional settings (Berner & Raiswell, 1984). Marine siliciclastic sediments underlying oxygenated, normal-salinity water columns typically show a linear relationship between organic carbon and sulfide sulfur, with an average TOC/TS ratio of 2.8 ± 0.8 (Berner, 1982; Lim et al., 2011; Morse & Berner, 1995; Raiswell & Canfield, 2012). Lower ratios generally indicate euxinic or oxygen-depleted conditions, whereas higher ratios are characteristic of freshwater settings (Fig. 6.6). The degree of pyritization (DOP), originally proposed by Berner (1970), quantifies the extent to which reactive iron is converted into pyrite and serves as a proxy for bottom-water redox conditions. DOP is controlled by both the availability of dissolved sulfide in pore waters and the abundance of reactive iron phases within sediments (Raiswell & Berner, 1985; Raiswell & Canfield, 2012; Roychoudhury et al., 2003). Values approaching unity generally indicate iron limitation during pyritization (Berner, 1970; Dean & Arthur, 1989). Based on shale calibrations, DOP < 0.45 reflects deposition under oxic waters, 0.46–0.75 corresponds to dysoxic to hypoxic conditions, and > 0.75 indicates euxinic environments (Raiswell et al., 1988; Raiswell & Canfield, 2012). In the cold-seep core, DOP values range from 0.21 to 0.81, showing a downcore increase that suggests enhanced pyritization with depth. This trend likely reflects greater H_2S availability generated through SD-AOM, corroborated by the corresponding decrease in Fe^D contents. Conversely, the non-seep core exhibits very low DOP values (0.02-0.05), implying deposition under oxic conditions with minimal influence from sulfate reduction processes.

Iron mineral	Half-life with respect to sulfidization
Ferrihydrite	2.8 hours
Lepidocrocite	< 3 days
Goethite	11.5 days
Haematite	31 days
Magnetite	105 years
'Reactive' silicates	230 years
Sheet silicates	84000 years
Poorly reactive silicates	2-4 X 10^6 years

3008

3009 Table 6. 1. Reactive iron minerals in sediments and their sulfidization half-lives.



30

3011 Fig. 6. 4. a) Cross plot between TOC (wt%) and CRS wt% from cold seep core. b) Cross
3012 plot between TOC (wt%) and CRS wt% from non-cold seep core.

3013 *6.3.3 Implications of AOM from sulfur isotope ratios*

3014 Pyrite sulfur isotope ratios ($\delta^{34}S_{CRS}$) are widely used to reconstruct the position of the paleo-
3015 SMTZ within sedimentary sequences (Borowski et al., 2013; Q. Lin et al., 2016; Mazumdar
3016 et al., 2012; Peketi et al., 2012; Sun et al., 2024). The $\delta^{34}S$ values of pyrite reliably record
3017 the isotopic composition of dissolved sulfide because pyrite formation induces only
3018 negligible sulfur isotopic fractionation (Price & Shieh, 1979). In methane-seep

environments, sulfate reduction is predominantly fuelled by the anaerobic oxidation of methane (AOM), which occurs along a distinct redox boundary known as the SMTZ. Sulfate methane transition zone is commonly characterized by pronounced ^{34}S enrichment of CRS relative to near-surface sediments (Borowski et al., 2013; Jorgensen et al., 2019; Pellerin et al., 2018). This enrichment reflects pyrite formation from ^{34}S-enriched sulfide produced by microbial sulfate reduction coupled to AOM at SMTZ. Preferential consumption of ^{32}S during microbial sulfate reduction under diffusion-limited, semi-closed conditions progressively enriches the residual sulfate pool and the produced sulfide in ^{34}S; because FeS_2 precipitation imparts negligible fractionation, the FeS_2 that is buried in sediments retains the isotopic signature of the dissolved sulfide (Jorgensen et al., 2019; Z. Lin, X. Sun, J. Peckmann, et al., 2016; Sun et al., 2024). Hydrogen sulfide generated within the SMTZ through SD-AOM diffuses upward toward the sediment-water interface due to a concentration gradient (Fig. 4.3b). Owing to the differential diffusion coefficients of $H_2{}^{32}S$ and $H_2{}^{34}S$, upward flux induces a significant sulfur-isotope fractionation (Donahue et al., 2008; Jorgensen, 1979; Jorgensen et al., 2004; Jorgensen et al., 2019), resulting in significantly ^{34}S-depleted S-isotope ratios ($\delta^{34}S_{CRS}$) near the seabed. Microbial disproportionation of intermediate sulfur species (S^0, SO_3^{2-}, $S_2O_3^{2-}$) further enhances ^{34}S depletion near the sediment surface (Pellerin et al., 2019; Pellerin et al., 2018; Sivan et al., 2025), accentuated by bioturbation/bioirrigation. In the studied cold seep (SSD045/4/G4) core, pyrite-S ($\delta^{34}S_{CRS}$) values range from -38.0 to +9.0‰ VCDT. The orange zones marked in the figure 6.1b indicates an upward diffusion of the SMTZ generated H_2S and precipitating at or close to the sediment-water interface. Whereas the white zone delineated in the figure 6.1b represents the paleo-SMTZ's recorded throughout the evolution of the sedimentary package. The $\delta^{34}S_{CRS}$ profile demonstrates an overall upward-increasing trend, indicating progressive shoaling of the sulfate-methane transition zone (SMTZ) associated with intensification of methane flux through time. Alternating ^{34}S-enriched (white) and ^{34}S-depleted (orange) intervals demarcate successive redox fronts formed during different stages of methane seepage (Fig. 6.1b). Below approximately 450 cmbsf, highly depleted $\delta^{34}S_{CRS}$ values reflect reduced methane flux and the consequent deepening of the SMTZ. Above this depth, enhanced anaerobic oxidation of methane (AOM) activity promoted upward migration of ^{34}S-enriched sulfide toward the sediment-water interface, resulting in the precipitation of authigenic pyrite with moderately enriched $\delta^{34}S_{CRS}$ values (Borowski et al., 2013; Jørgensen et al., 2004; Q. Lin et al., 2016; Z. Lin, X. Sun, Y. Lu, et al., 2016; Z. Lin,

X. Sun, J. Peckmann, et al., 2016). At present, the active SMTZ (Peketi et al., 2022) occurs below ~450 cmbsf, consistent with a relative decline in CH_4 flux.

6.4. Conclusion:

Sulfate reduction coupled with anaerobic oxidation of methane enriches pore water H_2S. A major fraction of this H_2S reacts with reactive Fe-oxide minerals to form meta stable Fe-S species that are ultimately buried as pyrite. Since the precipitation of H_2S as pyrite involves negligible fractionation pyrite-S isotope ratios ($\delta^{34}S_{CRS}$) record fluctuations in the paleo-SMTZ. The moderately enriched $\delta^{34}S_{CRS}$ values observed above 450 cmbsf, attributed to the progressive shallowing of the paleo-SMTZ towards the sub-surface driven by episodic intensifications of advective methane flux over time. Conversely, highly depleted $\delta^{34}S_{CRS}$ values, below 450 cmbsf, are attributed to the deepening of the SMTZ due to the waning of the methane flux. The multiple moderately enriched pyrite-S isotope ratios reflect the shallowing of SMTZ linked to the methane intensification with the evolution of sedimentary-package. Ultimately, these alternating isotope trends confirm a highly non-steady-state depositional regime, in which successive redox fronts were continuously reshaped by fluctuating fluid-flow dynamics throughout the evolution of the sedimentary package.

Chapter 7. Molybdenum sequestration and SMTZ dynamics in cold Seep Sediments

7.1 Introduction

Molybdenum (Mo) concentrations and isotope ratios are widely used to reconstruct paleo-sulfidic conditions and to assess redox states at or near the sediment-water interface (Algeo & Tribovillard, 2009; Chen et al., 2016; Hlohowskyj, 2021; Hu et al., 2015; Jin et al., 2024; Lin et al., 2021; Miao et al., 2021; Peketi et al., 2012). At methane cold seeps, the anaerobic oxidation of methane (AOM) is a key biogeochemical process that governs the sedimentary redox conditions. AOM generated H_2S in pore fluids promotes the authigenic enrichment of redox-sensitive elements, such as molybdenum (Mo) in the sedimentary environments. Sedimentary Mo is sourced from seawater, where it is homogeneously distributed as tetrahedrally coordinated dissolved molybdate (MoO_4^{2-}) species. Owing to its long residence time (~0.4 million years), Mo behaves conservatively and is homogeneously distributed throughout the water column, resulting in a uniform concentration of 110 nM (Collier, 1985; Miller et al., 2011; Smedley & Kinniburgh, 2017) and isotopic composition of $\delta^{98}Mo = +2.34 \pm 0.1‰$ (2SD), relative to the NIST-3134 standard (Goldberg et al., 2013; Nakagawa et al., 2012) Goldberg et al., 2013; Nakagawa et al., 2012). Under oxygenated water column conditions, Fe-Mn (oxy)hydroxides preferentially scavenge the lighter Mo isotopes by adsorbing dissolved molybdate (MoO_4^{2-}) onto reactive particle surfaces, thereby facilitating Mo removal from the water column to the sediments (Barling & Anbar, 2004; Goldberg et al., 2009; Kashiwabara et al., 2009; Tanaka et al., 2018; Wasylenki et al., 2008; Wasylenki et al., 2011) Adsorption onto Mn-(oxy)hydroxides transforms molybdate from tetrahedral to octahedral coordination, generating a relatively large isotopic fractionation between dissolved Mo and Mn (oxy)hydroxides ($\Delta\delta^{98}Mo_{\text{solution-Mn (oxy)hydroxides}} \approx +2.7$ to +3.2‰) (Barling & Anbar, 2004; Kashiwabara et al., 2011; Siebert et al., 2003; Tossell, 2005). In contrast, Mo uptake by Fe-(oxy)hydroxides produces smaller and more variable fractionations ($\Delta\delta^{98}Mo_{\text{solution-Fe-oxides}} \approx +0.83$ to +2.19‰), with the magnitude controlled by Fe-oxide mineralogy and crystallinity; experimentally, fractionation increases from magnetite to ferrihydrite, goethite, and finally hematite (Goldberg et al., 2009; Kashiwabara et al., 2011). Collectively, these adsorption processes leave the residual seawater enriched in heavy Mo isotopes relative to continental and particulate inputs, accounting for the observed offset between dissolved-phase and solid-phase $\delta^{98}Mo$ (Barling & Anbar, 2004; Bertine & Turekian, 1973; Goldberg et al., 2009).

$MoO_4^{2-} + H_2S \rightarrow MoO_3S^{2-} + H_2S \rightarrow MoO_2S_2^{2-} + H_2S \rightarrow MoOS_3^{2-} + H_2S \rightarrow MoS_4^{2-}$ (Eq. 7.1)

Under anoxic-sulfidic conditions, dissolved H_2S in the water column or pore waters progressively converts molybdate to oxy-thiomolybdate intermediates and ultimately to tetrathiomolybdate as H_2S increases ($MoO_{4-x}S_x^{2-}$, x = 1 to 4; Eq. 7.1) (Dahl et al., 2010; Dahl et al., 2013; Erickson & Helz, 2000; Helz et al., 1996). Each step of this sulfidation sequence can produce a measurable Mo isotope fractionation (Dahl et al., 2010; Nägler et al., 2011; Tossell, 2005). Above an empirical threshold near 11 µM H_2S, conversion to tetrathiomolybdate (MoS_4^{2-}) becomes effectively quantitative, resulting in the efficient removal Mo to sulfidic sediments (Erickson & Helz, 2000). Thiomolybdate species are particle-reactive and are scavenged from the water column by protonated particle surfaces, either by incorporation into authigenic Fe-Mo sulfide phases or by adsorption onto sulfurized organic matter, thereby retaining Mo in the sediments (Bostick et al., 2003; Chappaz et al., 2014; Erickson & Helz, 2000; Helz et al., 1996; Tribovillard et al., 2004; Vorlicek et al., 2018; Wagner et al., 2017; Zheng et al., 2000).

Methane Seep settings characterised by excess dissolved sulfide in the pore fluids due to the intense SD-AOM process which promotes thiomolybdate formation (Eq. 1.15), resulting in a notable enrichment of Mo in associated sediments. This Mo-enrichment has earlier been used to track past-methane seepage activities (Chen et al., 2016; Cheng et al., 2015; Jin et al., 2024; Lin et al., 2021; Miao et al., 2025; Miao et al., 2024; Peketi et al., 2012)

In the present study, we carried out a detailed assessment of Mo bulk geochemistry to reconstruct paleo-sulfidic conditions at the sediment-water interface, and Mo speciation analysis to demarcate the influence of diagenetic processes on Mo sequestration in cold-seep sediments. In order to assess these paleo-sulfidic conditions, we further analyzed a suite of trace metals including Al, Mn, Fe, Mo, and U (see Section 3.4.10.9 for detailed methodology) whose distributions provide insights into particle-reactive behavior, redox conditions, and diagenetic overprinting. Accordingly, Mo and U concentrations were normalized to Al to calculate enrichment factors relative to PAAS whereas Fe and Mn contents were examined to evaluate the role of particle-adsorption mechanisms.

7.2 Results of bulk metal contents of Al, Mn, Fe, Mo, and U

7.2.1. i) Aluminium

In the cold seep core, aluminium contents range from 6.4 to 10.2 wt%, with an average value of 8.0 wt% (Table 7.1). The Al contents in the non-seep core range from 8.8 to 11.6 wt%, with an average of 10.5 wt% (Table 7.2).

7.2.1. ii)Manganese

In the current study, the sediment core analysis reveals that Mn contents vary between 331.5 and 859.1 ppm, (Table 7.1). Al-normalised Mn (Mn/Al) ranges from 37.7 to 112.9 (ppm/wt%) for the cold seep core (Table 7.1). Manganese contents from the non-seep core (SSD045/13/G1) varied from 321.3 to 690.9 ppm (Table 7.2). Mn/Al from the non-seep region varied from 28.5 to 71.3 (Table 7.2) with an average of 42.5 (ppm/wt%).

7.2.1. iii) Iron

The analysis of the cold seep core reveals that iron contents range from 4.4 wt% to 9.2 wt%, (Table 7.1). The analysis of the non-seep region reveals that Fe contents vary from 7.3 to 9.6 wt%, with an average of 8.5 wt% (Table 7.2). Fe/Al ratios range from 0.7 to 1.0 wt%

7.2.1.iv) Molybdenum

The molybdenum contents from the cold seep core and non-seep core range from 1.0 to 17.4 ppm, 0.9 to 1.9 ppm respectively (Table 7.1). Molybdenum enrichment factor (Mo_{EF}) was calculated using $Mo_{EF} = [(Mo/Al)_{sample}/(Mo/Al)_{PAAS}]$. Mo_{EF} for cold seep core and non-seep core range from 0.8 to 14.5 and 0.6 to 1.1 (Table 7.2; Fig. 7.2a) respectively. The Mo-enrichment zones (MoEZs) in the cold seep core were marked in blue shaded regions these are accompanied by the *Calyptogena* shell fragments (Fig. 7.1a).

7.2.1.v) Uranium

The uranium contents observed in the cold seep and non-seep cores range from 1.8 to 6.5 ppm, and 1.4 to 2.4 ppm respectively (Table 7.1). Uranium enrichment factor (U_{EF}) was calculated using $U_{EF} = [(U/Al)_{sample}/(U/Al)_{PAAS}]$. U_{EF} for the cold seep and non-seep cores range from 0.6 to 2.6 and 0.5 to 0.7 (Table 7.2; Fig. 7.2b) respectively.

7.2.2 Molybdenum isotope ratio

The molybdenum isotope ratios ($\delta^{98}Mo$) in sediments from the cold-seep site range from -0.37 to +2.62‰ (Table 7.1). The $\delta^{98}Mo$ profile from the cold-seep core exhibits values approximating modern seawater (~+2.34‰) at several depth intervals above 360 cm, whereas specific horizons display noticeable offsets from the seawater composition (Fig. 7.1c). Below 360 cm, however, the $\delta^{98}Mo$ values deviate significantly from the seawater

signature. In contrast, sediments from the non-seep site yield δ^{98}Mo values ranging from +0.05 to +1.37‰ (Table 7.2). These values fall within the range typical of molybdenum adsorbed onto Fe-(oxy)hydroxides and/or particulate-bound Mo, consistent with deposition under sub-oxic to weakly reducing conditions.

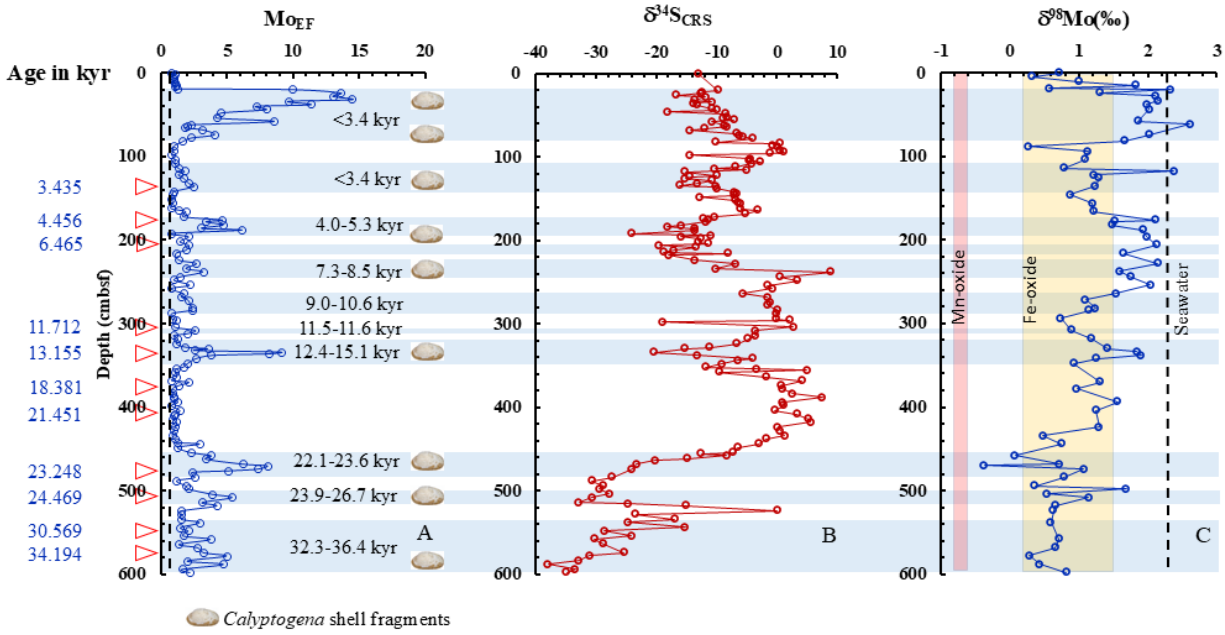
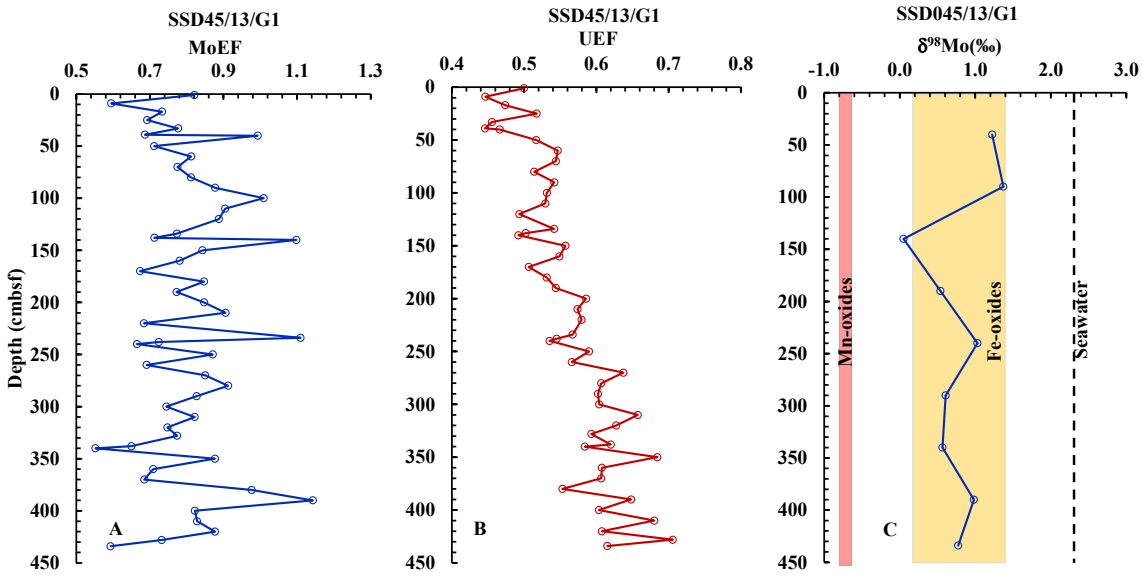
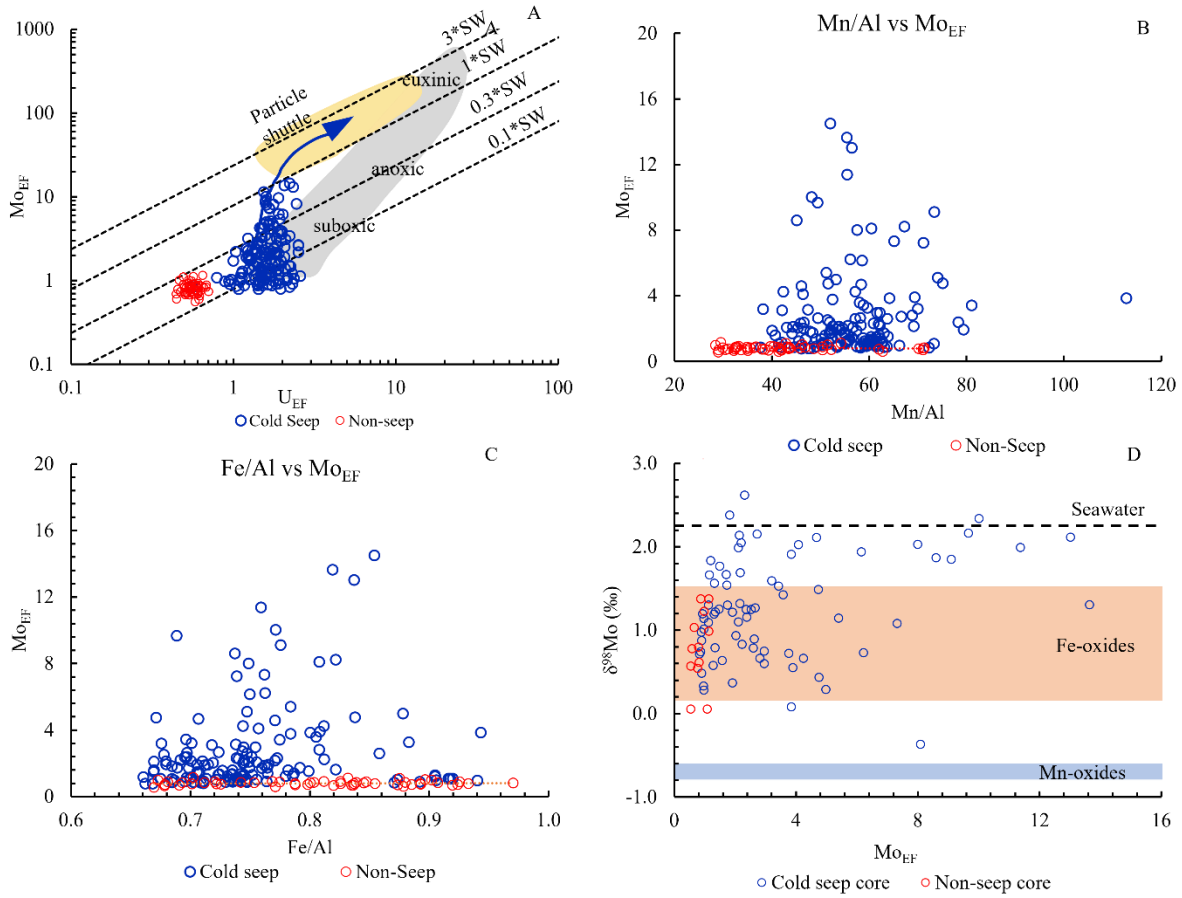


Fig. 7. 1. (a) Downcore variations in (a) molybdenum enrichment factors (MoEF), (b) $\delta^{34}S_{CRS}$ of chromium-reducible sulfur, and (c) Mo-isotope ratios (δ98Mo) for core SSD045/4/G4. Light-blue shaded intervals mark molybdenum-enrichment zones (MoEZs) and white shaded intervals correspond to the minor MoEZs and paleo-SMTZs. Red triangles show measured radiocarbon dates. Intrapolated ages are included within the light blue-shaded MoEZs. Pink, light yellow shades, and a dotted black line, respectively demarcate Mo-isotopic ranges for Mn-oxides, Fe-oxides, and seawater.



3191 Fig. 7. 2. Vertical profiles representing the a) Molybdenum enrichment factor (Mo_{EF}), b)
3192 Uranium enrichment factor (U_{EF}) and c) Molybdenum isotopic composition for the
3193 SSD45/13/G1(non-seep core).



3194

Fig. 7. 3. (a) Scatter plot of Mo_{EF} versus U_{EF} from core cold seep core (blue circles) and non-seep core (red circles). Black dotted lines indicate the modern seawater Mo/U molar ratio (Mo/U)sw = 3.2), with reference lines for 0.1×, 0.3×, 1×, and 3× seawater fractions. Cross plots of Mo_{EF} versus (b) Mn/Al, (c) Fe/Al, and (d) δ^{98}Mo.

7.2.3 Molybdenum speciation

The results of molybdenum (Mo) speciation for the cold-seep core (Fig. 7.4) are summarized in Table 7.3. Sediment samples from the cold-seep site below detection limit for Mo associated with the Mn-oxides fraction, plausibly due to the loss of Mn associated Mo into sedimentary porewaters under reducing conditions. The carbonate-associated Mo fraction ranges from 0.04 to 0.5 ppm, whereas the Fe-oxide bound Mo varies between 0.3 and 10.2 ppm. The humic-bound fraction contributes 0.07 to 1.0 ppm, the sulfide (pyrite)-bound fraction 0.1 to 5.4 ppm, and the residual fraction 0.3 to 2.7 ppm (Fig. 7.4a). Isotopically, the Fe-oxide-bound Mo exhibits δ^{98}Mo values between +0.28 and +2.39‰, while the pyrite-bound fraction shows a broader range from +0.02 to +3.03‰ (Fig. 7.4b).

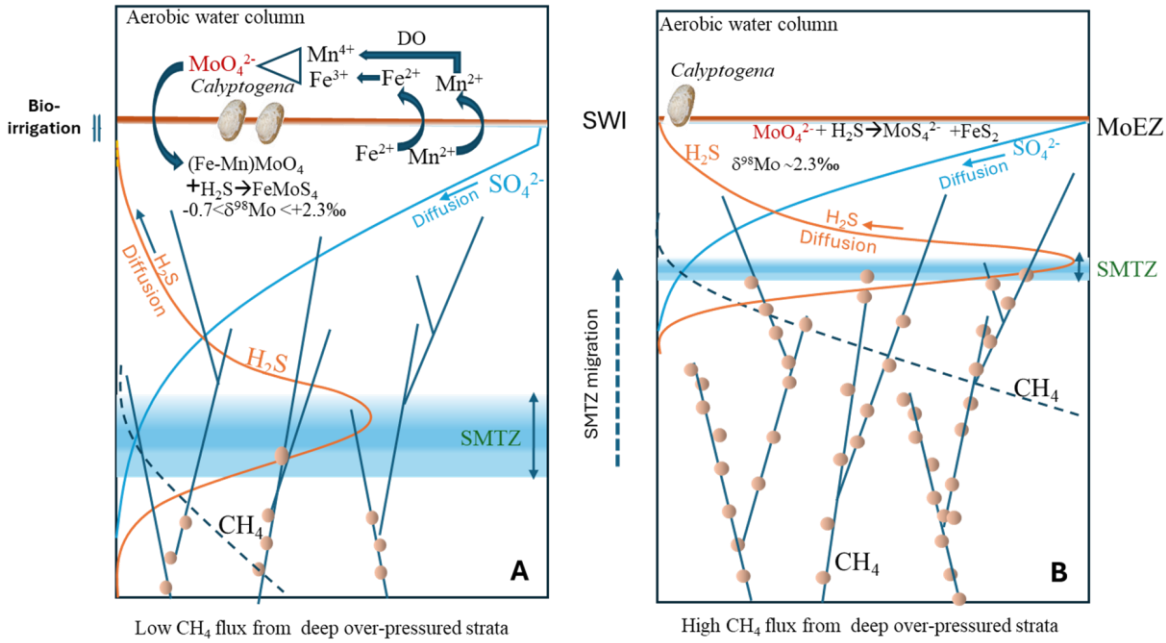


Fig. 7. 4. Conceptual model illustrating Mo-enrichment zone (MoEZ) formation and SMTZ migration driven by variable CH_4 flux a) low CH_4 flux and b) high CH_4 flux condition from over-pressured strata along fault-fracture systems in the Krishna-Godavari (K-G) Basin. SWI = Sediment-water interface, SMTZ = sulfate methane transition zone.

7.3 Discussion

7.3.1. MoEZs as tracer for sulfidic pore waters

The Mo_{EF} profile in core SSD045/4/G4 from the K-G Basin cold seep site records multiple episodes of pronounced MoEZs, delineated by light blue shades in figure 7.1a, interspersed with intervals of none (~1) to moderate enrichments, indicating a dynamic sediment redox history over the past 36.4 kyr whereas the core from non-seep location the Mo_{EF} are close to background values (Fig, 7.1b). Molybdenum enrichment in sulfidic sediments involves the progressive removal of dissolved molybdate (MoO_4^{2-}) from seawater and porewaters and its conversion into particle-reactive thiomolybdate species (MoS_4^{2-}), which are ultimately sequestered through adsorption onto Fe-sulfides and sulfurized organic matter (Bostick et al., 2003; Helz et al., 1996; Tribovillard et al., 2004; Vorlicek et al., 2018). Evidence for past sulfidic porewaters near the sediment-water interface is additionally supported by remnants of thiotrophic (H_2S-dependent) chemosynthetic *Calyptogena* clam shells (Sahling et al., 2002) within the MoEZs (Fig. 7.6). The past record of H_2S enrichments in the porewaters, along with a recent report (Pillutla et al., 2024) of aragonite and high-magnesium calcites ($\delta^{13}C_{carb}$ ranging from -57.6 to -34.8‰ VPDB) from the study site, may be linked to the SD-AOM process (Eq. 1.10) occurring in the sediments.

Mo-enrichment in sediments may occur through multiple pathways, including variations in sediment redox state, particulate shuttle dynamics, and water-column euxinia (Algeo & Tribovillard, 2009; Jin et al., 2024; Qin et al., 2023; Scott & Lyons, 2012). Given the contrasting sequestration/enrichment pathways of Mo and U, the Mo_{EF}/U_{EF} ratio can be effectively used to trace depositional and early diagenetic processes (Algeo & Tribovillard, 2009; Jin et al., 2024). In contrast to sulfidic porewater conditions responsible for Mo enrichment, U enrichment is favoured under sub-oxic conditions near the Fe^{3+}/Fe^{2+} redox boundary. In the present study, Mo_{EF}/U_{EF} ratios (Fig. 7.3a) follow the trajectory expected for a particulate shuttle process; however, the data points plot outside the canonical shuttle field defined by Algeo and Tribovillard (2009). The particulate shuttle mechanism involves the upward advective flux of reduced sediment porewaters containing dissolved Fe^{2+}, Mn^{2+}, and colloidal particulates into the overlying water column, where rapid oxidation forms Fe-Mn (oxy)hydroxide nanoparticles. These particles exhibit large reactive surface areas that effectively adsorb MoO_4^{2-} and subsequently settle back to the seabed, enriching the sedimentary Mo pool (Kashiwabara et al., 2011; Miao et al., 2025; Tanaka et al., 2018).

Methane ebullition across the sediment-water interface can intensify this process by enhancing porewater advection and increasing the flux of dissolved and colloidal phases (Jin et al., 2024; Miao et al., 2025). However, the magnitude of Mo-enrichment through this pathway depends critically on both methane flux intensity and the abundance of highly reactive Fe-Mn (oxy)hydroxide phases in the sediment (Fig. 7.3b & c). In the absence of strong methane-driven advection, Mo enrichment may be more limited and driven by the direct diffusion and adsorption of MoO_4^{2-} from bottom waters into H_2S-rich porewater, coupled with localized redox cycling of Fe and Mn across the sediment-water interface (Eroglu et al., 2020). A lack of correlation between Mo_{EF} and Fe/Al, Mn/Al, and <20 ppm Mo contents (Fig. 3) supports the role of H_2S-rich porewaters as the driving factor for Mo enrichment, rather than the involvement of the particle-shuttle pathway and water-column euxinia (Scott & Lyons, 2012). Since different enrichment pathways impart characteristic isotopic signatures, the molybdenum isotope composition ($\delta^{98}Mo$) serves as a sensitive tool to distinguish among these processes and evaluate the relative contributions of distinct Mo sources (Hlohowskyj, 2021; Kendall et al., 2017).

In this study, $\delta^{98}Mo$ values range from -0.37 to +2.62‰, exhibiting substantial variability with an overall trend of isotopic enrichment toward the sediment surface (Fig. 7.1c). The absence of a significant correlation between $\delta^{98}Mo$ and Mo-enrichment factors (Mo_{EF}; Fig. 7.3d) suggests that multiple, coexisting mechanisms influence both Mo accumulation and isotopic fractionation. One dominant mechanism involves the direct scavenging of seawater-derived molybdate (MoO_4^{2-}) as thiomolybdate (MoS_4^{2-}) via reaction with free H_2S at or above the sediment-water interface. Under such conditions, $\delta^{98}Mo$ values tend to approximate that of ambient seawater ($\delta^{98}Mo_{SW} \approx +2.3‰$), provided that H_2S concentrations are sufficiently sustained to drive quantitative Mo drawdown (Erickson & Helz, 2000; Poulson Brucker et al., 2009). In contrast, Mo associated with Fe-Mn (oxy)hydroxide cycling, particularly under sub-oxic to mildly sulfidic conditions, can exhibit lower $\delta^{98}Mo$ values due to partial isotope fractionation during adsorption and remobilization (Scholz et al., 2017), as reflected in the depleted isotope ratios relative to seawater Mo (Fig. 7.1c). The relative dominance and persistence of these two pathways-sulfidic Mo capture versus Fe-Mn redox cycling-ultimately govern both the extent of MoEZs and the isotopic composition preserved in sediments (Fig. 7.4). This $\delta^{98}Mo$ profile exhibits an upward Mo-isotopic enrichment trend (Fig. 7.1c), showing multiple depth zones that archive dominantly $\delta^{98}Mo_{SW}$ contributions interspersed with depleted Mo-isotope ratios, demarcating a variable degree of mixed pathways. The seawater-like Mo-

isotope ratios likely reflect enhanced H_2S flux at or above the sediment-water interface, resulting from intensified SD-AOM activity driven by elevated CH_4 flux and the upward migration (shallowing) of the SMTZ. High H_2S events at or above sediment-water interfaces are recorded during time windows ranging from recent to 3.4 ky and 4 to 10.6 ky BP, except for intermittent spikes. In contrast, before 10.6 ky, an incremental lowering of $\delta^{98}Mo$ may be attributed to the waning of H_2S flux towards the sediment-water interface.

7.3.2. SMTZ migration and H_2S dynamics on MoEZs

Sulfate methane transition zone (SMTZ) is commonly characterized by pronounced ^{34}S enrichment of CRS relative to near-surface sediments (Borowski et al., 2013; Jorgensen et al., 2019; Pellerin et al., 2018). This enrichment reflects pyrite formation from ^{34}S-enriched sulfide produced by microbial sulfate reduction coupled to AOM at SMTZ. Preferential utilization of ^{32}S during sulfate reduction progressively enriches residual sulfate and the resulting sulfide in ^{34}S under diffusion-limited, semi-closed system conditions, with negligible fractionation during FeS_2 precipitation (Jorgensen et al., 2019; Z. Lin, X. Sun, J. Peckmann, et al., 2016; Sun et al., 2024). Hydrogen sulfide generated within the SMTZ through SD-AOM diffuses upward toward the sediment-water interface due to a concentration gradient (Fig. 7.4). Owing to the differential diffusion coefficients of $H_2{}^{32}S$ and $H_2{}^{34}S$, upward flux induces a significant sulfur-isotope fractionation (Donahue et al., 2008; Jorgensen, 1979; Jorgensen et al., 2004; Jorgensen et al., 2019), resulting in significantly ^{34}S-depleted S-isotope ratios ($\delta^{34}S_{CRS}$) near the seabed. Microbial disproportionation of intermediate sulfur species (S^0, SO_3^{2-}, $S_2O_3^{2-}$) further enhances ^{34}S-depletion near the sediment surface (Pellerin et al., 2019; Pellerin et al., 2018; Pellerin et al., 2015; Sivan et al., 2025), accentuated by bioturbation/bioirrigation. Alternating zones of ^{34}S-enrichment (white zone; Fig. 7.1b) and ^{34}S depletion (light-blue zones; Fig. 7.1b) in the $\delta^{34}S_{CRS}$ profile demarcate successive redox fronts. The ^{34}S-enriched white zones represent paleo-SMTZ horizons, whereas the ^{34}S-depleted light blue zones record sulfidization near the sediment-water interface. The coupled $\delta^{34}S_{CRS}$-Mo_{EF} profiles (Fig. 7.1) reveal a correspondence between MoEZs and low $\delta^{34}S_{CRS}$ values, indicating preferential Mo sequestration in transiently sulfidic microenvironments near the seabed rather than within the deeper SMTZ, despite locally elevated H_2S concentrations (Fig. 7.4). Low $\delta^{98}Mo$ values (-0.37 to +1.69‰) corresponding to MoEZs below 450 cmbsf, coupled with highly depleted $\delta^{34}S_{CRS}$ values (-32.7 to -38‰), signify the presence of a deeper paleo-SMTZ, reduced H_2S flux to the sediment surface, and a dominant Fe-Mn redox cycling-controlled Mo sequestration pathway (Fig. 7.4a). In contrast, $\delta^{98}Mo$ values associated with MoEZs above 450 cmbsf approach

seawater-like signatures and are accompanied by moderately depleted $\delta^{34}S_{CRS}$ values (-24.1 to -4.0‰), consistent with enhanced H_2S flux near the sediment-water interface due to upward migration and shoaling of the paleo-SMTZ (Fig. 7.4b).

5.3 MoEZ as a proxy for episodic reactivation of fluid pathways

The correspondence of MoEZs with variations in $\delta^{98}Mo$ and $\delta^{34}S_{CRS}$ signatures provides compelling evidence for the episodic intensification of SD-AOM and the associated migration of the SMTZ during the depositional evolution of the sedimentary succession over the past ~36.4 kyr BP (Fig. 7.1). These coupled redox and isotopic fluctuations reflect variable methane flux regimes, which were likely modulated by changes in subsurface fluid migration pathways along deep-seated fault and fracture networks within the K-G Basin seep field (Dewangan et al., 2021; Joshi et al., 2014; Mandal et al., 2014; Mazumdar et al., 2009; Peketiet al., 2012). Episodic passive tectonic reactivation of these faults likely governed the permeability architecture of the basin, intermittently enhancing the upward migration of methane- and fluid-rich phases from deeper gas-charged strata through the overlying sediment column (Fig. 7.4). Such tectonically controlled fluid-gas transport processes regulated the temporal evolution of the SMTZ. Chronostratigraphic constraints allow the demarcation of individual Mo enrichment episodes, each reflecting short-lived (0.1- 4.1 kyr) methane flux events associated with passive tectonic activities. These events collectively record a pattern of recurrent hydrocarbon migration and redox dynamics within the sediment column. The physico-chemical feedbacks responsible for generating these episodic MoEZs, are schematically illustrated in Figure 7.4.

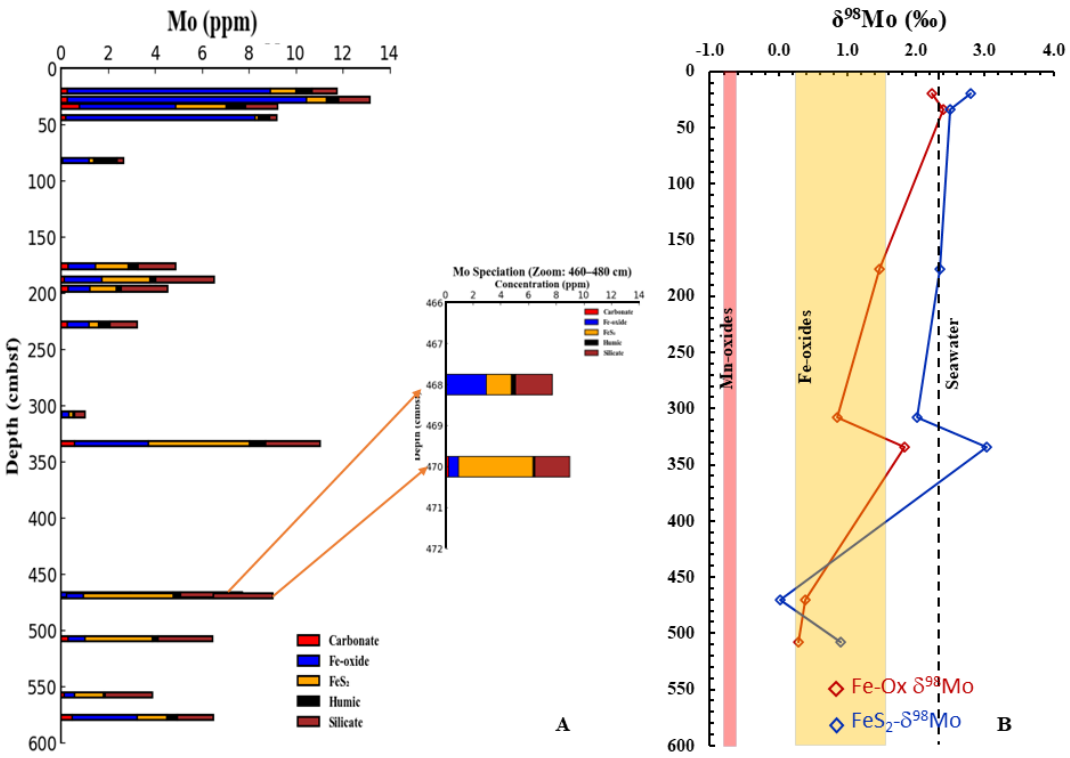


Fig. 7. 5. a) Figure illustrating the distribution of Mo among different phases in the cold seep environment. Orange arrows highlight high-resolution views of overlapping, closely spaced samples. b) Vertical profiles of phase-specific molybdenum isotopic composition (δ^{98}Mo) from a cold seep core, showing Mo associated with Fe-oxides and pyrite (FeS_2) fractions

7.3.4 Molybdenum speciation

A detailed sequential leaching analysis of Mo from carbonates, Mn-Fe-oxides, organic matter, sulfide, and silicate phases, was conducted on selected samples from the cold seep core SSD045/4/G4 (Fig. 7.5). Speciation analysis reveals that both the Fe-oxide phases and sulfide phase (pyrite) are likely to play a key role in the sequestration of Mo in the cold seep sediments followed by the residual phases comprising refractory organic matter and silicate fractions. A significant correlation of $R^2 = 0.90$ observed between the scatter plot (Fig. 7.6a) of total Mo contents and Mo associated with Fe-oxides and pyrite phases further corroborates Fe-oxide and Fe-sulfide as the dominant phase sequestering Mo. The scatter plot between the % of Mo associated with the Fe-oxides and pyrite phases (Fig. 7.6b) shows a negative slope with an $R^2 = 0.48$, which is attributed to the redistribution of Fe-oxide-associated Mo to the pyrite phase during diagenesis. This further underscore the dynamic repartitioning of Mo during burial diagenesis in which pyritization of Fe-oxides redistributes the Mo from Fe-oxide to Fe-sulfide phase. Although mineralogical data are not available in this study, previous work by Xu et al.

(2006) demonstrated the effectiveness of goethite in Mo adsorption, which may have implications for the observed Mo partitioning. However, this redistribution is unlikely to change the total Mo contents (Eroglu et al., 2021).

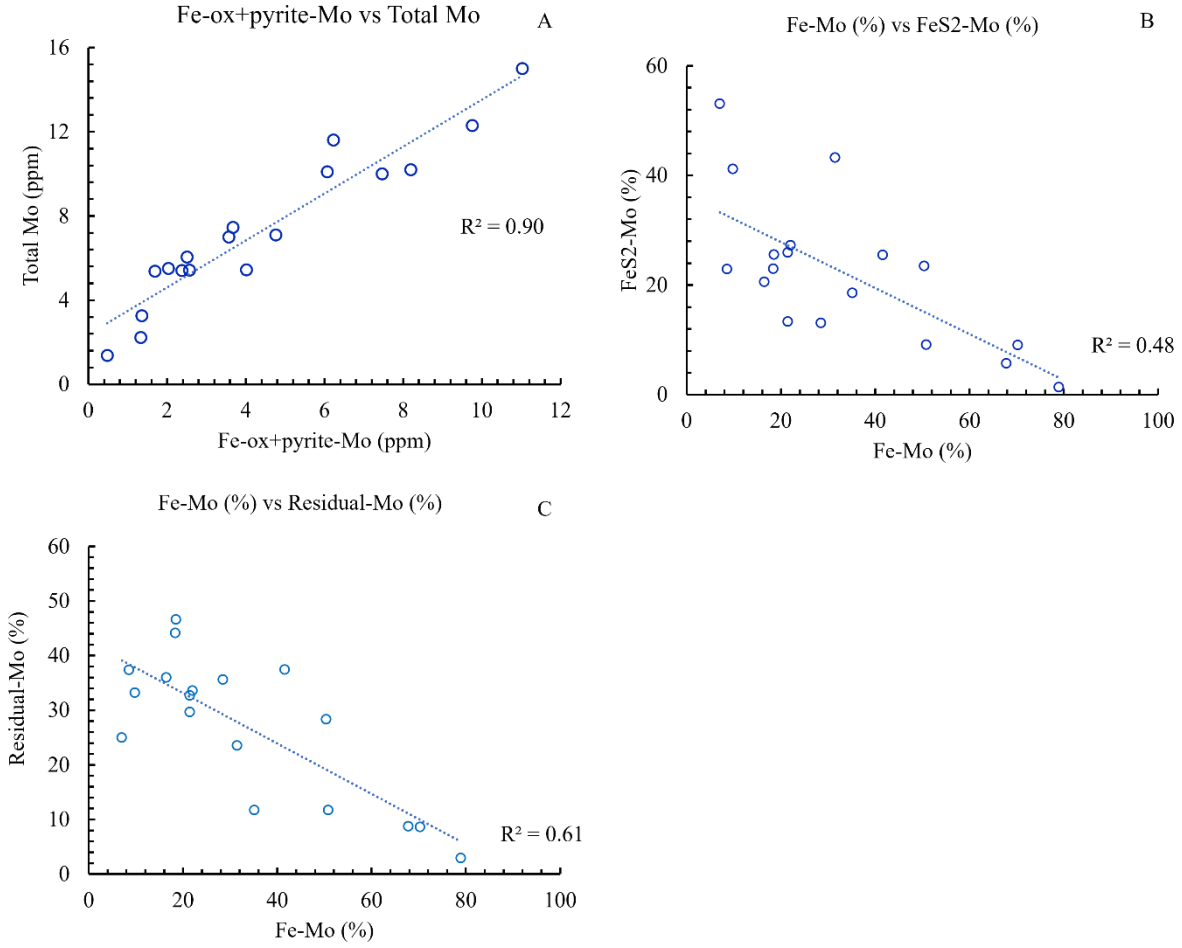


Fig. 7. 6. a) Cross plot Mo associated with Fe-oxide and pyrite versus total Mo. b) Cross-plot showing Fe-oxides and pyrite-associated Mo (%) from the cold seep core, with Mo contents normalized to the maximum content for each phase. b) Cross-plot between Fe-oxides associated Mo (%) and Mo associated with the residual fraction (%) in the cold seep core.

Phase-specific Mo isotope measurements were performed on Fe-oxide and FeS_2 fractions of the speciation samples**.** Interestingly, the Fe-oxide-associated Mo exhibits a δ^{98}Mo value (+2.23 to +2.39‰) similar to that of seawater, which contrasts with previously reported observations like Goldberg et al. (2009). In comparison, Mo-bound to the pyrite phase is relatively enriched (+2.02 to +3.03‰). The plot of $\delta^{98}Mo_{FeS2}$ and $\delta^{98}Mo_{Fe\text{-}ox}$ has an $R^2 = 0.73$ (Fig. 7.7a) coupled with $\Delta\delta^{98}Mo_{FeS2\text{-}Feox}$ of -0.37 to 1.20 shows possibility of Mo isotopic fractionation during Mo partitioning during redistribution (Fig. 7.7b). The proportion of Mo

associated with Fe-oxides phases (Fig. 7.8a) exhibits a strong positive correlation with $\delta^{98}Mo$ values of the Fe-oxides fraction ($R^2 = 0.68$), suggesting that increasing Mo accumulation is associated with isotopically heavier signatures, likely due to the preferential sorption of ^{98}Mo during authigenic Fe-oxides formation. A Significant positive correlation (Fig. 7.8b) is also observed between % Fe-oxides-bound Mo and $\delta^{98}Mo$ values of pyrite (FeS_2) with $R^2 = 0.58$ further corroborates the redistribution of Fe-oxides associated Mo into the pyrite phase during diagenesis.

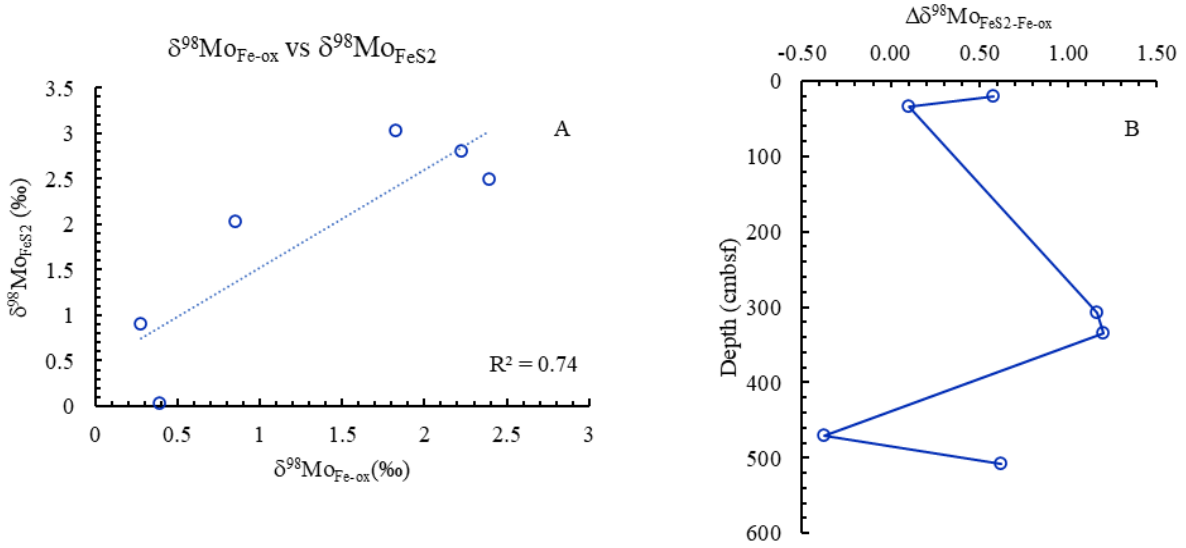


Fig. 7. 7. (a) Cross-plot between Mo isotope ratios of Mo-associated with Fe-oxides and pyrite (FeS_2) and b) Vertical profile showing depth-dependent variations in the isotopic offset ($\Delta\delta^{98}Mo$) between Fe-oxide-bound and pyrite-bound Mo for samples selected across multiple depth intervals.

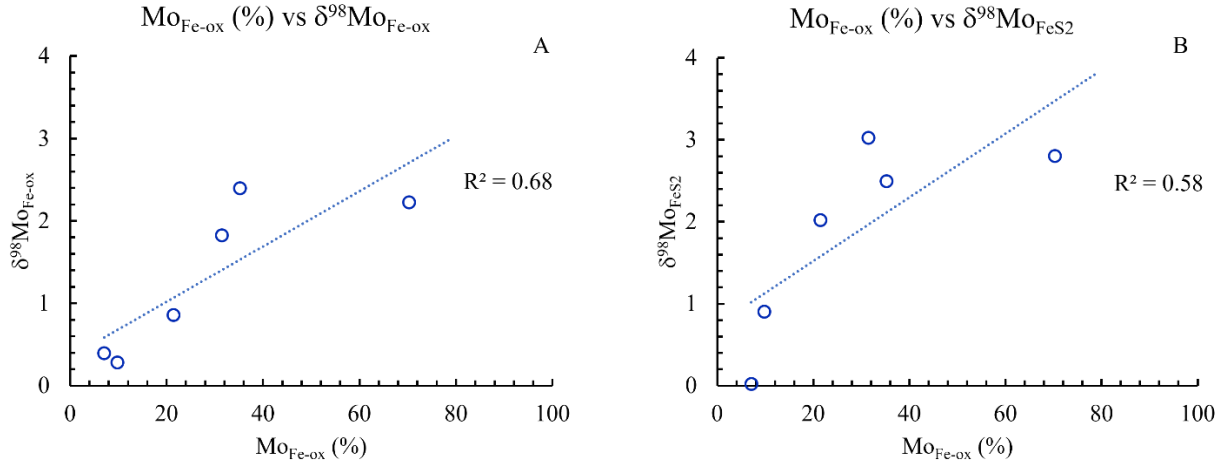


Fig. 7. 8. (a) Cross-plot % of Mo associated with Fe-oxides versus Mo isotope ratios of Fe-oxides-associated Mo and b) Cross-plot % of Mo associated with Fe-oxides versus Mo isotope ratios of pyrite-associated Mo.

The speciation study has brought to light two major observations:

1. Seawater like δ^{98}Mo values for Fe-oxide is completely in contrast to the known experimental observation which suggests lower (0.2 to 1.5‰) as shown in figures 7.5b. Seawater like δ^{98}Mo values are normally attributed MoS_4^{2-} formation at the sulfidic bottom water or sediment-water interface. It appears that this MoS_4^{2-} species is preferentially adsorbed to the Fe-oxide phase forming a complex. Our observation is also supported by Xu et al. (2006) which suggest preferential complexation of MoS_4^{2-} with goethite through inner sphere sulfur complexes.
2. The vertical speciation analyses (Fig. 7.7b) clearly shows a drastic drop in Fe-oxide bound Mo and increase in FeS_2 bound Mo with depth. This observation coupled to a positive correlation of δ^{98}Mo-FeS_2 and δ^{98}Mo-Fe-oxide (Fig. 7.7a) suggests sulfidization Fe-oxides during burial and associated portioning of Mo from oxide to sulfide mineral phase. However, this partitioning possibly involves certain amount Mo isotopic fraction.

7.4. Conclusion

The K-G Basin cold-seep record (<36.4 kyr) tracks episodic methane pulses lasting between 0.1 and 4.1 kyr, where fluctuating advective fluxes drove dynamic redox changes and established distinct Molybdenum Enrichment Zones (MoEZs). Heavy, seawater-like δ^{98}Mo signatures (+2.34‰) coupled with moderately depleted $\delta^{34}S_{CRS}$ values mark elevated methane fluxes that shoaled the SMTZ and generated intense porewater H_2S. Conversely, depleted δ^{98}Mo values (-0.37 to +1.69‰) and highly negative $\delta^{34}S_{CRS}$metrics (-38 to -20‰) register a waning methane flux, resulting in a deeper SMTZ dominated by Fe-Mn oxyhydroxide redox controls.

Phase-specific Mo speciation reveals that the Fe-oxide fraction exhibits anomalously heavy, seawater-like δ^{98}Mo values (+2.23 to +2.38‰), which reflects the direct adsorption of tetrathiomolybdate (MoS_4^{2-}) formed at a sulfidic sediment-water interface onto highly reactive iron phases via inner-sphere sulfur complexation. Downcore profiles display a concurrent drop

in Fe-bound Mo alongside an increase in pyrite-bound Mo, supported by positive isotopic correlations between both matrices. This vertical trend captures the progressive sulfidization of iron oxides during burial, which drives the continuous chemical redistribution and isotopic fractionation of Mo from oxide to sulfide mineral phases during early diagenesis.

Chapter 8 Conclusion

8.1 Summary of Key Findings

This study presents a multi-proxy geochemical investigation of cold seep sediments from the Krishna-Godavari (K-G) basin, with a focus on understanding the interplay between methane flux, redox dynamics, and trace metal behaviour. Through integrated analyses of porewater chemistry, isotopic compositions, sediment mineralogy, and trace element distributions, we reconstructed the biogeochemical processes governing cold seep evolution and identified multiple paleo-seepage events preserved in the sedimentary archive.

8.2 Non-steady state SO_4^{2-}-H_2S system

Methane seep sediments from the K-G Basin record non-steady-state redox conditions driven by sulfate-dependent anaerobic oxidation of methane (SD-AOM). $\delta^{13}C$ enrichment of methane and elevated $\delta^{34}S_{SO42-}$ values indicate microbial oxidation and sulfate reduction. Pronounced chloride depletion signals hydrate dissociation, while multiple SO_4^{2-}/Cl^- anomalies above the SMTZ reflect active micro-zones of SD-AOM. High H_2S concentrations (up to 9032 μM) and $\delta^{34}S_{H_2S}$ enrichment confirm in situ sulfide generation and upward diffusion through fractures. Collectively, the data reveal dynamic methane-sulfur coupling and transient AOM processes in fracture-controlled, hydrate-influenced cold-seep sediments of the K-G Basin.

8.3 Authigenic Carbonates and Diagenetic Conditions

Petrographic and geochemical analyses revealed two distinct carbonate phases high magnesium calcite (HMC) tubes and aragonite crusts formed under contrasting redox and depositional conditions. HMC tubes reflect sulfidic environments within gas conduits, while aragonite crusts formed near the sediment-water interface under vigorous methane flow. Oxygen isotope data suggest both hydrate dissociation and crystallization processes influenced carbonate formation. The contrasting characteristics of authigenic carbonates in the cold seep core reflect variable methane flux regimes. High-magnesium calcite (HMC) pelloids, often associated with high methane flux zones, formed under persistent sulfidic conditions and show evidence of bioturbation and reworking. In contrast, aragonite crusts, linked to relatively lower flux conditions near the sediment–water interface, exhibit broader geochemical variability. These mineralogical differences underscore the influence of methane seep intensity on carbonate precipitation pathways and diagenetic evolution in cold seep environments. The contrasting formation mechanisms of HMC tubes and aragonite crusts underscore the

complexity of carbonate precipitation in cold seep environments and highlight the role of tectonically driven fluid migration in shaping sedimentary mineralogy.

8.4. Fe-S-C systematics

The cold-seep core (SSD045/4/G4) from the K-G Basin shows CRS contents up to 2.5 wt%, nearly two orders of magnitude higher than the non-seep core, indicating intense pyritization driven by sulfate-dependent anaerobic oxidation of methane (SD-AOM). High surface Fe_D reflects abundant reactive iron, which decreases with depth as it is consumed during pyrite formation. The lack of correlation between CRS and TOC confirms methane-driven sulfidic diagenesis. Downcore DOP increase (0.21 to 0.81) signals enhanced H_2S availability, whereas the non-seep core's low DOP (0.02 to 0.05) reflects oxic, non-seep deposition with minimal sulfate reduction.

8.5. MoEZ tracer for shale tectonics

The K-G Basin cold-seep record (<36.4 kyr) reveals multiple Mo-enrichment zones (MoEZs) reflecting episodic methane flux and dynamic redox conditions driven by sulfate-dependent anaerobic oxidation of methane (SD-AOM). Coupled MoEF-δ^{98}Mo-$\delta^{34}S_{CRS}$ variations indicate alternating high-and low-CH_4 flux phases: seawater-like δ^{98}Mo (+2.3‰) and moderately depleted $\delta^{34}S_{CRS}$ mark shallow SMTZ and strong H_2S flux, whereas depleted δ^{98}Mo (-0.37 to +1.69‰) and highly negative $\delta^{34}S_{CRS}$ (-38 to -20‰) signify deeper SMTZ and Fe-Mn redox control. Each MoEZ represents a short-lived (0.1 - 4.1 kyr) methane pulse linked to tectonic reactivation of fluid pathways within over-pressured strata.

8.7. Mo-speciation

The Mo speciation study reveals two key findings. First, Fe-oxides show seawater-like δ^{98}Mo values (+2.23 to +2.38‰), unlike experimental predictions (+0.2 to +1.5‰), implying adsorption of thiomolybdate (MoS_4^{2-}) formed at the sulfidic sediment-water interface onto Fe-oxides via inner-sphere sulfur complexes, likely with goethite Xu et al. (2006) Second, vertical profiles show a marked decline in Fe-oxides-bound Mo and a corresponding increase in pyrite-bound Mo, coupled with positive δ^{98}Mo correlations between the two phases. This trend indicates progressive sulfidization of Fe-oxides during burial, accompanied by redistribution and isotopic fractionation of Mo from Fe-oxide to Fe-sulfide phases during diagenesis in the cold-seep sediments.

8.8 Scope of the future work

Integrating detailed geochronological frameworks alongside radiogenic strontium isotope ($^{87}Sr/^{86}Sr$) systematics will provide critical insights into the temporal evolution of authigenic carbonate structures and help precisely fingerprint deep advective fluid sources. Determining absolute precipitation rates via Uranium-Thorium (U-Th) dating is essential to delineate the direct impact of regional tectonic or structural adjustments on historical paleo-cold seep episodes.

Furthermore, a significant knowledge gap persists regarding phase-specific molybdenum (Mo) sequestration mechanisms in marine sediments, as most existing literature relies strictly on bulk-rock data. This study highlights the importance of tetrathiomolybdate complexation with reactive iron oxides, contrasting with traditional models. Future investigations should utilize sequential chemical extractions coupled with high-resolution multi-collector ICP-MS to track Mo isotopic fractionation and elemental redistribution at the mineral-speciation level. Explicitly decoupling the interlinked effects of boundary redox conditions and post-depositional diagenesis is critical, as downcore mineral transformations actively govern both Mo sequestration pathways and secondary isotopic fractionation. Examining these coupled mechanisms within cold-seep systems is vital, as they preserve a high-resolution geological record of localized redox fluctuations and the structural evolution of fault-controlled fluid pathways fueling anaerobic methane oxidation.

Appendix

Table 3.1. Location and recovery details of sediment cores collected during the SSD045 expedition

Station	Latitude	Longitude	Water depth (mbsl)	Recovery (m)
SSD045/4/G4	15°42.9232′ N	82°04.0193′ E	1756.5	6.0
SSD045/13/G1	15°23.4870′ N	81°00.7470′ E	1424	4.34

Table 3. 2. Radiocarbon Dating and Sedimentation Rates of Core SSD045/4/G4

Depth (cmbsf)	Age Kyr BP	Sedimentation rate cm^2/kyr
110	1.94	
140	3.44	20.0
180	4.46	39.2
210	6.47	14.9
310	11.71	19.1
340	13.16	20.8
380	18.38	7.7
410	21.45	9.8
480	23.25	39.0
510	24.47	24.6
552	30.57	6.9
580	34.19	7.7

Table 4. 1 . Pore fluid geochemistry data of cold seep core SSD045/4/G4.

Sr. No.	Depth (cmbsf)	H_2S (µM)	SO_4^{2-} (mM)	Cl^- (mM)	$100*SO_4^{2-}/Cl^-$	$\delta^{34}S$ H_2S (‰-VCDT)	$\delta^{34}S$ SO_4^{2-} (‰-VCDT)	$\Delta\delta^{34}S$-SO_4^{2-}-$\delta^{34}S$-H_2S	CH_4 (µM)	CH_4 (mM)	$\delta^{13}C_{CH4}$ (‰-VPDB)	C_2H_6 (µM)	C1/C2	SO_4^{2-}/CH_4
1	1	826	28.1	571.3	4.91	-27.78	22.20		bd	bd	bd			
2	5	bd	26.3	469.4	5.60	bd			bd	bd	bd			
3	10	bd	27.7	579.1	4.79	bd	22.92		bd	bd	bd			
4	15	163	26.8	567.2	4.72	bd	24.95		bd	bd	bd			
7	20	bd	24.1	479.1	5.03	bd	24.85		bd	bd	bd			
8	40	bd	23.5	458.7	5.12	-24.45	24.72	49.17	bd	bd	bd			
9	60	bd	25.1	497.8	5.05	-20.65	27.38	48.04	bd	bd	bd			
10	80	470	20.8	473.1	4.40	-23.06	30.72	53.79	15.20	0.02	-61.1			1371.0
11	100	bd	19.4	416.5	4.66	-20.50	nm		12.4	0.01	-56.7			1558.1
12	110	721	22.4	484.8	4.62	-20.93	28.97	49.91	bd	bd	bd			
13	120	2737	21.0	432.3	4.85	-18.43	32.86	51.29	258.7	0.26	-69.7			81.1
14	140	213	19.4	420.9	4.60	-19.64	27.33	46.97	63.9	0.06	-63.7			303.3
15	160	458	21.6	453.2	4.76	-17.22	27.63	44.85	20	0.02	-65.4			1078.7
16	180	487	19.3	408.2	4.73	-17.43	27.21	44.64	31.9	0.03	-70.4			605.0
17	200	214	20.6	435.5	4.73	-23.04	nm		49	0.05	-62.0			420.8
18	210	896	22.0	434.9	5.07	bd	25.70		nm	nm	nm			
19	220	158	23.2	447.5	5.18	-24.50	25.49	49.99	131.3	0.13	-72.1			176.4
20	240	36	24.7	478.4	5.17	-26.10	26.59	52.69	nm	nm	nm			
21	260	bd	22.5	445.1	5.07	-25.87	26.46	52.32	130.0	0.13	-69.3			173.4
22	280	755	22.8	463.0	4.93	-20.74	27.21	47.94	156.7	0.16	-65.1			145.6
23	300	1117	23.1	473.3	4.88	-18.40	27.05	45.45	210.7	0.21	-68.6			109.6
24	310	bd	22.8	450.5	5.05	-19.32	29.11	48.43	539.6	0.54	-68.4			42.2
25	320	1002	22.5	449.2	5.01	-20.85	nm		7847.0	7.85	-68.7			2.9

26	340	1976	19.7	450.3	4.37	-15.15	32.17	47.32	14078.8	14.08	-72.2	12.9	1083.30	1.4
27	360	2075	19.7	447.3	4.40	-17.09	32.94	50.03	6723.9	6.72	-72.8	6.3	1065.50	2.9
28	370	2194	19.4	430.7	4.50	-16.74	31.6	48.34	3869.0	3.87	-73.8			
29	380	906	23.0	569.2	4.03	bd	nm		4040.6	4.04	-73.6			5.9
30	400	3530	20.5	407.5	5.04	-8.22	35.73	43.95	14540.5	14.54	-73.8	3.8	3771.90	5.1
31	410	2455	15.1	422.3	3.57	-6.50	35.56	42.06	nm	nm	nm			1.0
32	420	bd	14.0	551.9	2.54	-10.22	nm		1502.6	1.50	-73.2			9.3
33	440	5981	4.9	353.1	1.39	-1.89	44.86	46.74	2306.3	2.31	-80.0			2.1
34	460	5645	5.0	491.0	1.01	5.32	62.58	57.26	4782.4	4.78	-90.2			1.0
35	471	9032	9.4	409.6	2.31	7.50	78.78	71.28	nm	nm	nm			
36	480	7328	1.3	362.2	0.36	11.64	76.30	64.66	1349.0	1.35	-94.7			1.0
37	491	5371	bd	nm		bd	nm		nm	nm	nm			
38	500	bd	1.3	nm		bd	nm		5648.8	5.65	-83.7			0.2
39	520	7270	4.8	514.8	0.93	16.23	nm		18162.7	18.16	-78.2			0.3
40	530	bd	bd	nm		bd	nm		7421.0	7.42	-77.9	6.3	1180.20	
41	534	6764	3.5	422.2	0.83	16.06	nm		nm	nm	nm			
42	552	5885	0.6	469.6	0.13	15.46	nm		nm	nm	nm			
43	560	4725	0.68	364.9	0.19	16.54	nm		3940.0	3.94	-76.1			0.2
44	580	bd	bd	528.7		bd	nm		7174.9	7.17	-75.8			
45	600	4437	1.7	nm		14.50	nm		7555.5	7.56	-75.8			
									nm					
	Minimum		0.6	353.1	0.1	-27.8	22.2	43.9	12.4	0.0	-94.7	3.8	1065.5	0.2
	Maximum		28.1	579.1	5.6	16.5	78.8	53.8	18162.7	18.2	-56.7	12.9	3771.9	1558.1
	Average		17.4	461.1	3.9	-11.0	33.6	48.6	4020.1	4.0	-72.6	7.3	1775.2	243.9

bd= below detection limit

nm= not measured

Table 5. 1. Locations of spade cores and the corresponding water depths

Sr. No	Station	Spade core	Latitude	Longitude	Water depth (mbsl)
1	4	Spade-1	15°42.9986' N	82°04.0154' E	1752.9
2	4	Spade-2	15°43.0058' N	82°04.0787' E	1756.5
3	4	Spade-3	15°43.0055' N	82°04.0791' E	1754.5
4	4	Spade-4	15°42.9115' N	82°03.9830' E	1753.7
5	4	Spade-5	15°43.0411' N	82°04.0599' E	1750.0
6	4	Spade-6	15°42.9090' N	82°04.0006' E	1754.0

Table 5. 2. Mineralogical, isotope ratio data and TOC content of HMC-tubes and arg-crust samples from SSD045/4 (methane seep sites off K-G basin)

Sr. No	Sample Number	Arg %	HMC%	LMC	$MgCO_3$ (mol%)	$\delta^{13}C_{TIC}$ (‰VPBD)	$\delta^{18}O$ (‰VPBD)	$\delta^{18}O_{mes\text{-}cal}$ (‰ VPDB)	$\delta^{13}C_{TOC}$ (‰VPBD)	TOC (wt%)
1	HMC-Tube-1	0.8	99.2	nd	14.7	-51.1	4.8	1.5	-28.1	0.27
2	HMC-Tube-2	nd	100.0	nd	16.7	-51.6	4.7	1.4	-35.6	0.35
3	HMC-Tube-3	nd	100.0	nd	16.7	-53.9	4.6	1.2	-26.5	0.28
4	HMC-Tube-4	nd	100.0	nd	17.3	-49.7	4.9	1.4	nm	nm
5	HMC-Tube-5	nd	100.0	nd	16.0	-50.9	4.8	1.5	-40.6	0.38
6	HMC-Tube-6	nd	100.0	nd	14.7	-54.5	4.7	1.5	-31.5	0.45
7	HMC-Tube-7	0.4	99.6	nd	14.7	-51.9	4.9	1.6	-31.3	0.27
8	HMC-Tube-8	0.1	99.9	nd	15.4	-46.2	5.4	2.1	-54.8	0.23
9	HMC-Tube-9	nd	100.0	nd	15.4	-48.9	5.6	2.3	-44.0	0.42
10	HMC-Tube-10	7.6	92.4	nd	14.7	-50.8	6.2	2.9	-40.5	0.69
11	HMC-Tube-11	6.4	93.6	nd	14.1	-48.9	5.6	2.4	-44.1	0.56
12	HMC-Tube-12	nd	100.0	nd	14.1	-49.7	4.9	1.6	-31.3	0.33
13	HMC-Tube-13	13.8	86.2	nd	15.4	-51.6	4.3	1.0	-42.5	0.50

14	HMC-Tube-14	nd	100.0	nd	15.4	-49.6	4.8	1.5	-33.9	0.56
15	HMC-Tube-15	2.4	97.6	nd	16.0	-50.6	4.6	1.2	-35.0	0.38
16	HMC-Tube-16	1.2	98.8	nd	15.4	-48.7	4.7	1.4	-24.4	0.41
17	HMC-Tube-17	2.1	97.9	nd	16.0	-50.8	5.1	1.7	-36.6	0.49
18	HMC-Tube-18	nd	100.0	nd	16.0	-50.4	4.8	1.4	-39.4	0.42
19	HMC-Tube-19	nd	100.0	nd	18.0	-51.9	4.5	1.0	-28.1	0.77
20	HMC-Tube-20	nd	100.0	nd	14.4	-50.8	4.8	1.5	-33.9	0.40
21	HMC-Tube-21	nd	100.0	nd	15.1	-48.9	5.0	1.7	nm	nm
22	HMC-Tube-22	18.3	81.7	nd	15.4	-52.0	4.8	1.5	-31.6	0.40
23	HMC-Tube-23	0.1	99.9	nd	14.7	-49.6	5.2	1.9	-36.5	0.30
24	HMC-Tube-24	0.2	99.8	nd	15.4	-52.9	5.8	2.5	-39.3	0.43
25	HMC-Tube-25	nd	100.0	nd	16.0	-50.9	4.8	1.5	-30.5	0.45
26	HMC-Tube-26	0.5	99.5	nd	16.0	-51.7	4.6	1.3	-32.0	0.17
27	HMC-Tube-27	9.6	90.4	nd	13.4	-51.9	4.8	1.6	-46.6	0.35
28	HMC-Tube-28	4.3	95.7	nd	13.4	-50.3	4.5	1.3	-31.8	0.42
29	HMC-Tube-29	1.6	98.4	nd	16.0	-54.3	4.4	1.1	nm	nm
30	HMC-Tube-30	0.5	99.5	nd	16.7	-51.9	4.6	1.2	-33.5	0.37
31	HMC-Tube-31	12.5	87.5	nd	15.4	-50.3	5.5	2.2	-52.0	0.49
32	HMC-Tube-32	0.2	99.8	nd	14.7	-51.9	5.4	2.1	-21.2	0.46
33	HMC-Tube-33	1.0	99.0	nd	14.7	-49.9	5.2	1.9	-33.1	0.38
34	HMC-Tube-34	0.1	99.9	nd	14.7	-51.6	5.0	1.7	-20.0	0.38
35	HMC-Tube-35	5.1	94.9	nd	13.4	-49.7	5.8	2.6	nm	nm
36	Arg-crust-1	>99%	nd	minor	0.00	-35.8	2.4	-1.5	nm	nm
37	Arg-crust-2	>99%	nd	minor	0.00	-34.8	2.5	-1.4	nm	nm
38	Arg-crust-3	>99%	nd	minor	0.00	-49.0	3.8	-0.1	nm	nm
39	Arg-crust-4	>99%	nd	minor	0.00	-47.9	2.6	-1.0	nm	nm
40	Arg-crust-5	>99%	nd	minor	0.00	-47.4	3.2	-0.4	nm	nm
41	Arg-crust-6	>99%	nd	minor	0.00	-46.4	1.8	-1.8	nm	nm
42	Arg-crust-7	>99%	nd	minor	0.00	-57.6	3.8	0.2	nm	nm
43	Arg-crust-8	>99%	nd	minor	0.00	-50.3	2.3	-1.3	nm	nm
44	Arg-crust-9	>99%	nd	minor	0.00	-49.1	4.3	0.7	nm	nm

nd= not detectable
minor = not quantified
nm = not measured

Table 5. 3. Major, and trace element composition of the HMC-tubes and arg-crust samples

Sr. No	Sample Number	IR (wt. %)	Mg (wt. %)	Sr (ppm)	Ba (ppm)	Al (wt. %)	Ca (wt. %)	Mn (wt. %)	Fe (wt. %)	Mg/Ca mmol/mole	Sr/Ca mmol/mol	Ba/Ca mmol/mol
1	HMC-tube-1	9.5	2.8	1294.0	124.4	0.0	22.3	0.0048	0.0204	207.8	2.7	0.16
2	HMC-tube-2	14.9	3.0	1162.7	157.6	0.0	22.6	0.0040	0.0366	216.1	2.4	0.20
3	HMC-tube-3	14.2	3.2	1197.7	66.8	0.0	24.2	0.0037	0.0439	216.7	2.3	0.08
4	HMC-Tube-6	5.2	2.8	1077.3	104.3	0.0	21.0	0.0121	0.0414	218.7	2.3	0.14
5	HMC-Tube-7	16.1	3.3	1492.9	171.3	0.0	26.3	0.0069	0.0676	206.3	2.6	0.19
6	HMC-tube-8	8.2	3.7	1627.4	468.8	0.0	25.2	0.0056	0.0301	241.7	2.9	0.54
7	HMC-tube-9	10.2	3.0	1222.9	108.2	0.0	22.6	0.0055	0.0450	220.3	2.5	0.14
8	HMC-tube-10	6.5	2.9	2168.5	263.5	0.0	19.6	0.0065	0.0339	244.3	5.1	0.39
9	HMC-tube-11	11.2	3.2	1810.6	209.9	0.0	28.6	0.0014	0.0270	185.5	2.9	0.21
10	HMC-tube-12	12.2	2.8	1241.1	214.8	0.0	24.9	0.0064	0.0401	186.3	2.3	0.25
11	HMC-Tube-13	9.5	2.8	3168.5	226.6	0.0	25.7	0.0031	0.0355	180.8	5.6	0.26
12	HMC-Tube-14	14.1	3.3	1175.8	145.4	0.0	24.5	0.0026	0.0498	219.7	2.2	0.17
13	HMC-Tube-15	8.6	3.3	1794.5	224.0	0.0	24.3	0.0047	0.0445	223.9	3.4	0.27
14	HMC-Tube-16	12.5	3.2	1482.7	186.2	0.0	24.6	0.0098	0.0464	212.0	2.8	0.22
15	HMC-Tube-17	14.7	3.3	1905.1	243.0	0.0	26.5	0.0242	0.0402	204.4	3.3	0.27
16	HMC-Tube-18	16.5	2.8	377.7	68.4	0.0	26.7	0.0047	0.0279	171.4	0.6	0.07
17	HMC-Tube-19	17.7	3.4	1047.9	20.0	0.1	26.7	0.0044	0.0616	207.9	1.8	0.02
18	HMC-Tube-22	13.8	2.4	3706.8	276.2	0.1	28.3	0.0035	0.0470	139.5	6.0	0.28
19	HMC-Tube-23	10.9	3.3	1413.9	184.2	0.0	27.4	0.0025	0.0521	201.1	2.4	0.20
20	HMC-Tube-24	16.1	3.0	1177.3	140.5	0.0	24.7	0.0343	0.0369	198.0	2.2	0.17

21	HMC-Tube-25	15.7	3.3	1052.0	105.4	0.0	27.4	0.0037	0.0399	197.0	1.8	0.11
22	HMC-Tube-26	16.2	3.2	1298.2	117.5	0.0	20.8	0.0168	0.0457	254.7	2.9	0.17
23	HMC-Tube-27	10.9	2.7	2248.6	140.9	0.0	26.8	0.0130	0.0307	165.7	3.8	0.15
24	HMC-Tube-28	15.4	3.1	1929.7	92.9	0.0	27.0	0.0165	0.0162	188.5	3.3	0.10
25	HMC-Tube-29	15.0	3.5	1644.3	86.3	0.1	27.9	0.0172	0.0146	205.0	2.7	0.09
26	HMC-Tube-30	6.4	3.4	1307.7	105.7	0.0	24.7	0.0143	0.0143	223.4	2.4	0.12
27	HMC-Tube-31	10.9	2.8	3492.4	282.8	0.0	29.8	0.0029	0.0370	157.2	5.4	0.28
28	HMC-Tube-32	15.2	3.3	1317.8	139.9	0.0	28.1	0.0068	0.0487	195.4	2.1	0.15
29	HMC-Tube-33	6.4	2.8	1451.8	149.9	0.0	22.6	0.0046	0.0326	205.7	2.9	0.19
30	HMC-Tube-34	16.5	3.6	1394.8	81.7	0.1	31.0	0.0064	0.0268	189.9	2.1	0.08
31	HMC-Tube-35	14.1	2.8	1955.3	78.2	0.0	29.7	0.0031	0.0210	154.7	3.0	0.08
32	Arg-crust-1	bd	0.4	9330.3	73.8	0.1	31.7	0.0080	0.0392	19.6	13.5	0.07
33	Arg-crust-2	bd	0.5	10312.3	109.6	0.1	31.0	0.0082	0.0340	27.3	15.2	0.10
34	Arg-crust-3	bd	1.1	8169.1	44.1	0.1	30.9	0.0082	0.0306	58.8	12.1	0.04
35	Arg-crust-4	bd	0.1	7822.0	11.6	0.0	31.1	0.0010	0.0179	6.7	11.5	0.011
36	Arg-crust-6	bd	0.1	7223.5	10.1	0.0	29.5	0.0009	0.0151	5.8	11.2	0.010
37	Arg-crust-7	bd	0.1	8974.2	9.2	0.0	30.1	0.0026	0.0083	3.5	13.6	0.009
38	Arg-crust-8	bd	0.1	7791.3	bd	0.0	33.6	0.0004	0.0044	4.3	10.6	
39	Arg-crust-9	bd	0.1	7448.2	7.0	0.0	32.1	0.0010	0.0237	4.6	10.6	0.006
40	Arg-crust-10	bd	0.1	7856.1	11.8	0.0	31.8	0.0004	0.0072	4.1	11.3	0.011
41	Arg-crust-11	bd	0.1	6980.3	bd	0.0	32.8	0.0106	0.0448	4.2	9.7	
42	Arg-crust-12	bd	0.1	8254.3	10.3	0.0	27.5	0.0009	0.0214	8.1	13.7	0.011
43	Arg-crust-13	bd	0.1	6777.2	8.2	0.0	21.9	0.0007	0.0190	9.4	14.1	0.011
44	Arg-crust-14	bd	0.1	8728.1	10.6	0.0	27.3	0.0015	0.0263	7.8	14.6	0.011
45	Arg-crust-15	bd	0.2	7391.4	9.7	0.0	23.2	0.0049	0.0187	14.8	14.6	0.012
46	Arg-crust-16	bd	0.2	8379.3	11.1	0.0	22.7	0.0023	0.0114	11.6	16.9	0.014

bd: below detection limit

Table 5. 4. REE composition of the HMC-tubes and arg-crust samples.

Sample Number	La (ppm)	Ce (ppm)	Pr (ppm)	Nd (ppm)	Sm (ppm)	Eu (ppm)	Gd (ppm)	Tb (ppm)	Dy (ppm)	Ho (ppm)	Er (ppm)	Tm (ppm)	Yb (ppm)	Lu (ppm)	Y (ppm)	Y/Ho (molar)
HMC-tube-1	2.8	8.3	0.63	3.6	0.76	0.25	0.79	0.12	0.91	0.19	0.58	0.10	0.65	0.12	6.4	62.4
HMC-tube-2	2.8	8.4	0.63	3.6	0.76	0.26	0.73	0.11	0.81	0.18	0.51	0.09	0.55	0.10	5.4	57.4
HMC-tube-3	3.0	8.6	0.64	3.6	0.73	0.21	0.75	0.11	0.78	0.16	0.47	0.08	0.52	0.09	5.2	60.1
HMC-Tube-6	3.0	8.7	0.68	3.9	0.84	0.27	0.90	0.14	1.10	0.23	0.69	0.12	0.76	0.13	7.8	61.8
HMC-Tube-7	4.7	13.6	1.01	5.7	1.20	0.37	1.25	0.19	1.43	0.30	0.92	0.16	1.07	0.19	10.2	62.4
HMC-tube-8	2.9	8.5	0.65	3.8	0.83	0.39	0.90	0.15	1.17	0.25	0.77	0.13	0.84	0.15	8.5	62.6
HMC-tube-9	3.5	10.4	0.77	4.3	0.88	0.26	0.91	0.13	0.95	0.20	0.58	0.10	0.65	0.11	6.5	60.8
HMC-tube-10	2.4	6.4	0.46	2.6	0.55	0.25	0.60	0.09	0.69	0.15	0.44	0.07	0.45	0.08	5.2	63.8
HMC-tube-11	2.6	7.3	0.55	3.2	0.70	0.26	0.74	0.11	0.89	0.19	0.56	0.09	0.59	0.10	6.4	63.7
HMC-tube-12	3.2	9.2	0.69	3.9	0.84	0.31	0.91	0.14	1.13	0.25	0.75	0.13	0.83	0.15	8.4	63.4
HMC-Tube-13	2.8	8.3	0.59	3.3	0.70	0.26	0.73	0.11	0.82	0.17	0.49	0.08	0.50	0.09	5.4	59.6
HMC-Tube-14	3.2	8.9	0.67	3.7	0.77	0.25	0.77	0.11	0.78	0.16	0.44	0.07	0.46	0.08	4.8	56.7
HMC-Tube-15	3.6	10.4	0.78	4.4	0.96	0.33	1.02	0.15	1.19	0.25	0.77	0.12	0.79	0.14	8.1	59.5
HMC-Tube-16	3.2	9.3	0.70	4.0	0.82	0.29	0.87	0.13	0.92	0.19	0.56	0.09	0.59	0.10	6.1	60.1
HMC-Tube-17	2.9	8.5	0.62	3.5	0.72	0.28	0.75	0.11	0.82	0.17	0.51	0.08	0.53	0.09	5.7	61.4
HMC-Tube-18	2.9	8.5	0.64	3.7	0.79	0.27	0.79	0.12	0.86	0.18	0.54	0.09	0.61	0.11	6.0	61.0
HMC-Tube-19	4.2	12.4	0.94	5.3	1.10	0.28	1.11	0.16	1.14	0.22	0.63	0.10	0.64	0.11	6.7	55.6
HMC-Tube-22	3.2	9.1	0.67	3.8	0.80	0.31	0.83	0.12	0.90	0.19	0.55	0.09	0.57	0.10	6.0	60.1
HMC-Tube-23	4.4	12.7	0.98	5.7	1.24	0.41	1.38	0.22	1.70	0.36	1.09	0.18	1.15	0.20	11.8	59.9
HMC-Tube-24	3.3	9.5	0.68	3.9	0.78	0.26	0.80	0.11	0.77	0.15	0.44	0.07	0.43	0.07	5.2	61.8
HMC-Tube-25	3.3	9.6	0.71	4.0	0.81	0.26	0.86	0.13	0.92	0.19	0.55	0.09	0.61	0.11	6.0	59.3
HMC-Tube-26	3.4	10.1	0.77	4.4	0.93	0.30	1.00	0.15	1.11	0.23	0.67	0.11	0.71	0.12	7.4	60.3
HMC-Tube-27	3.8	10.9	0.82	4.7	1.00	0.32	1.08	0.16	1.22	0.25	0.72	0.12	0.72	0.12	8.0	59.7
HMC-Tube-28	3.4	9.6	0.75	4.4	0.96	0.29	1.01	0.15	1.13	0.24	0.68	0.11	0.72	0.12	7.8	61.4
HMC-Tube-29	4.0	11.4	0.89	5.2	1.11	0.33	1.16	0.17	1.23	0.25	0.72	0.11	0.73	0.13	7.9	58.6
HMC-Tube-30	3.5	9.7	0.74	4.3	0.93	0.29	0.98	0.15	1.11	0.23	0.66	0.11	0.69	0.12	7.4	60.1
HMC-Tube-31	4.9	13.8	1.00	5.7	1.19	0.43	1.29	0.19	1.47	0.30	0.86	0.14	0.89	0.15	9.5	58.9

HMC-Tube-32	4.6	13.2	0.99	5.7	1.18	0.37	1.29	0.20	1.49	0.32	0.94	0.16	1.00	0.17	10.5	61.1
HMC-Tube-33	2.7	7.7	0.57	3.3	0.68	0.24	0.72	0.11	0.80	0.17	0.50	0.08	0.54	0.10	5.6	62.9
HMC-Tube-34	4.0	11.2	0.91	5.4	1.18	0.35	1.20	0.18	1.34	0.28	0.81	0.13	0.85	0.15	9.0	60.4
HMC-Tube-35	3.9	10.6	0.87	5.2	1.12	0.35	1.26	0.20	1.50	0.32	0.95	0.16	1.01	0.18	10.6	62.1
Arg-crust-1	3.8	8.0	0.72	4.1	0.79	0.22	0.74	0.10	0.61	0.11	0.29	0.04	0.27	0.04	3.6	59.5
Arg-crust-2	3.1	6.3	0.56	3.2	0.58	0.18	0.53	0.07	0.45	0.08	0.22	0.03	0.22	0.04	2.8	61.4
Arg-crust-3	2.3	6.2	0.47	2.6	0.55	0.15	0.53	0.07	0.47	0.09	0.23	0.04	0.22	0.04	2.6	57.3
Arg-crust-4	14.7	38.7	2.80	15.0	1.91	0.38	1.32	0.11	0.46	0.07	0.17	0.02	0.12	0.02	1.7	46.7
Arg-crust-6	6.0	16.7	1.07	6.0	0.82	0.18	0.66	0.06	0.30	0.04	0.12	0.01	0.09	0.01	1.3	52.8
Arg-crust-7	3.8	9.1	0.66	3.6	0.47	0.10	0.36	0.03	0.14	0.02	0.05	0.01	0.03	0.00	0.7	57.7
Arg-crust-8	9.3	23.6	1.68	9.2	1.27	0.28	1.11	0.09	0.43	0.07	0.17	0.02	0.11	0.02	1.7	47.6
Arg-crust-9	5.6	16.0	1.06	8.2	0.84	0.19	0.68	0.07	0.33	0.05	0.12	0.01	0.07	0.01	1.3	46.8
Arg-crust-10	8.4	21.1	1.40	7.0	1.00	0.22	0.75	0.07	0.31	0.05	0.11	0.01	0.07	0.01	1.3	51.6
Arg-crust-11	7.3	18.3	1.40	7.3	0.98	0.21	0.73	0.06	0.27	0.04	0.10	0.01	0.08	0.01	1.1	46.0
Arg-crust-12	2.1	4.6	0.37	1.9	0.35	0.09	0.30	0.04	0.21	0.03	0.09	0.01	0.08	0.01	1.1	61.4
Arg-crust-13	3.4	8.7	1.11	3.5	0.56	0.13	0.52	0.05	0.27	0.04	0.11	0.01	0.09	0.01	1.3	55.6
Arg-crust-14	3..0	8.3	0.56	3.0	0.47	0.12	0.42	0.04	0.22	0.04	0.08	0.01	0.06	0.01	1.0	52.2
Arg-crust-15	4.6	11.0	1.29	4.6	0.81	0.21	1.23	0.09	0.55	0.11	0.26	0.04	0.25	0.03	3.0	50.6
Arg-crust-16	4.5	9.3	0.70	4.1	0.72	0.19	0.68	0.08	0.47	0.08	0.19	0.02	0.15	0.02	2.2	52.4

bd: below detection limit

Sample Number	∑REE	∑LREE	∑MREE	∑HREE	ΣLREE/ΣHREE	Pr/Pr*	Ce/Ce*	Eu anomaly
HMC-tube-1	19.7	16.0	2.1	1.6	9.8	0.66	1.44	1.47
HMC-tube-2	19.5	16.1	1.9	1.4	11.4	0.66	1.44	1.61
HMC-tube-3	19.8	16.6	1.8	1.3	12.6	0.65	1.44	1.34
HMC-Tube-6	21.5	17.1	2.4	1.9	8.8	0.66	1.41	1.41
HMC-Tube-7	32.1	26.2	3.2	2.6	9.9	0.65	1.43	1.41
HMC-tube-8	21.4	16.7	2.6	2.1	7.8	0.66	1.41	2.10
HMC-tube-9	23.8	19.9	2.3	1.6	12.1	0.65	1.44	1.36
HMC-tube-10	15.2	12.4	1.6	1.2	10.4	0.64	1.40	2.03
HMC-tube-11	17.9	14.3	2.0	1.5	9.3	0.65	1.42	1.71
HMC-tube-12	22.5	17.9	2.5	2.1	8.5	0.65	1.42	1.62
HMC-Tube-13	19.0	15.7	1.9	1.3	11.8	0.64	1.47	1.68
HMC-Tube-14	20.2	17.1	1.9	1.2	14.2	0.66	1.44	1.52
HMC-Tube-15	24.8	20.1	2.7	2.1	9.6	0.65	1.44	1.55
HMC-Tube-16	21.7	18.0	2.2	1.5	11.7	0.66	1.42	1.57
HMC-Tube-17	19.6	16.2	2.0	1.4	11.7	0.65	1.46	1.74
HMC-Tube-18	20.1	16.5	2.0	1.5	10.8	0.65	1.44	1.60
HMC-Tube-19	28.3	23.9	2.7	1.7	14.1	0.66	1.44	1.18
HMC-Tube-22	21.2	17.5	2.2	1.5	11.7	0.65	1.43	1.78
HMC-Tube-23	31.7	25.0	3.7	3.0	8.4	0.66	1.41	1.44
HMC-Tube-24	21.3	18.2	1.9	1.7	15.7	0.63	1.47	1.53
HMC-Tube-25	22.1	18.4	2.2	1.5	11.9	0.65	1.44	1.42
HMC-Tube-26	24.0	19.6	2.5	1.8	10.7	0.66	1.43	1.43
HMC-Tube-27	26.0	21.3	2.8	1.9	11.0	0.65	1.41	1.42
HMC-Tube-28	23.6	19.1	2.6	1.9	10.2	0.65	1.38	1.39
HMC-Tube-29	27.4	22.5	2.9	1.9	11.6	0.66	1.38	1.36
HMC-Tube-30	23.6	19.3	2.5	1.8	10.7	0.65	1.38	1.42
HMC-Tube-31	32.3	26.6	3.4	2.3	11.4	0.64	1.43	1.58
HMC-Tube-32	31.7	25.7	3.3	2.6	9.9	0.65	1.42	1.39

HMC-Tube-33	18.2	15.0	1.9	1.4	10.8	0.65	1.41	1.57
HMC-Tube-34	28.0	22.7	3.1	2.2	10.2	0.67	1.35	1.37
HMC-Tube-35	27.6	21.7	3.3	2.6	8.3	0.66	1.33	1.37
Arg-crust-1	19.8	17.4	1.7	0.7	23.3	0.71	1.10	1.35
Arg-crust-2	15.5	13.6	1.2	0.6	22.9	0.71	1.09	1.52
Arg-crust-3	14.0	12.2	1.2	0.6	19.7	0.65	1.39	1.33
Arg-crust-4	75.7	73.0	2.3	0.4	184.8	0.66	1.38	1.10
Arg-crust-6	32.1	30.6	1.2	0.3	110.4	0.60	1.50	1.14
Arg-crust-7	18.4	17.6	0.6	0.1	151.0	0.65	1.31	1.19
Arg-crust-8	47.3	45.0	1.9	0.4	119.9	0.65	1.36	1.12
Arg-crust-9	33.3	31.8	1.3	0.3	123.0	0.52	1.50	1.20
Arg-crust-10	41.2	39.6	1.3	0.2	156.5	0.63	1.39	1.15
Arg-crust-11	36.9	35.4	1.3	0.2	139.6	0.69	1.31	1.14
Arg-crust-12	10.2	9.3	0.6	0.2	42.2	0.70	1.20	1.26
Arg-crust-13	18.5	17.3	1.0	0.3	63.1	1.14	1.02	1.16
Arg-crust-14	16.4	15.4	0.8	0.2	77.1	0.63	1.48	1.25
Arg-crust-15	25.1	22.3	2.1	0.7	32.5	1.03	1.03	0.94
Arg-crust-16	21.1	19.3	1.4	0.5	41.8	0.65	1.19	1.26

Table 6. 2. Bulk sediment elemental compositions and isotope ratios of SSD045/4/G4 core.

S.No	Depth (cmbsf)	TOC (wt%)	CRS (wt%)	$\delta^{34}S_{CRS}$ (‰ VCDT)	Fe_D (wt%)	Fe_{ox} (wt%)	Fe_{TR}	DOP
1	0.5	1.58	bd	-12.91				
2	2.5	1.16	bd	bd				
3	4.5		bd	bd				
4	6.5		bd	bd				
5	8.5	1.37	bd	bd				
6	11	0.94	bd	bd				
7	13		bd	bd				
8	15		bd	bd				
9	17	0.94	bd	bd				
10	19	1.11	bd	bd				
11	20	1.65	0.15	-9.7	0.27	0.22	0.62	0.21
12	22	1.59	0.84	-12.3				
13	24	1.62	1.03	-12.5				
14	26	1.66	0.36	-16.6				
15	28	1.09	0.69	-11.8			0.60	
16	32	1.41	0.90	-13.6	0.72	0.19	1.70	0.46
17	34	1.47	0.97	-10.8				
18	36	1.74	0.50	-13.7				
19	38		0.13	-13.1	0.21	0.19	0.51	0.22
20	40	0.87						
21	42	1.79	0.63	-10.7				
22	44	1.78	0.92	-10.0	0.92	0.04	1.77	0.45
23	46	1.81	0.28	-18.0				
24	48	1.73	1.01	-8.4	0.77	0.09	1.75	0.50

25	52	1.72	0.88	-8.2				
26	54	1.70	0.44	-8.8	0.25	0.20	0.83	0.46
27	56	1.76	1.02	-7.1				
28	58	1.82	0.49	-10.8				
29	62	1.64	0.95	-8.7	0.46	0.08	1.37	0.60
30	64	1.67	0.87	-8.2	0.41	0.18	1.35	0.56
31	66	1.67	0.30	-11.9	0.91	0.21	1.39	0.19
32	68		0.46	-14.4	0.22	0.11	0.74	0.55
33	72	1.85	0.68	-6.6				
34	74	1.85	0.83	-6.1				
35	76	1.91	0.64	-5.6	0.60	0.15	1.30	0.42
36	78		0.41	-4.0				
37	82		0.47	-10.1	0.70	0.23	1.33	0.31
38	84	1.95	0.77	0.6				
39	86	1.97	0.68	-0.6				
40	88	1.94	0.82	0.1				
41	92	2.02	0.95	0.6				
42	94		0.85	1.2	0.65	0.15	1.54	0.48
43	96	1.84	0.85	-1.1				
44	98	1.87	0.39	-14.3	0.96	0.14	1.44	0.23
45	102	1.85	0.49	-4.3				
46	104	1.87	0.88	-4.5				
47	106	1.79	0.49	-2.6				
48	108	1.83	1.17	-4.2	0.84	0.20	2.06	0.50
49	112	1.75	0.84	-6.9				
50	114	1.82	0.71	-10.3	0.66	0.21	1.48	0.42
51	116	1.74	0.67	-5.0				
52	118	1.76	0.45	-15.2				
53	122	1.83	0.89	-9.9	0.47	0.13	1.38	0.56
54	124	1.89	0.50	-14.3				
55	126	1.79	0.78	-15.2	0.55	0.23	1.46	0.46

56	128	1.84	0.77	-10.7				
57	132	1.83	0.81	-13.2				
58	134	1.85	1.03	-16.0				
59	136	1.80	0.96	-10.0				
60	138	1.73	0.66	-9.9				
61	142	1.89	0.71	-7.0	0.43	0.22	1.26	0.49
62	144		0.70	-6.6				
63	146	1.91	0.94	-7.0	0.34	0.17	1.33	0.62
64	148	1.94	0.62	-12.7				
65	152		0.85	-6.8	0.35	0.14	1.23	0.60
66	154		0.74	-6.3				
67	156	1.98	0.75	-6.0	0.72	0.11	1.49	0.44
68	158		0.81					
69	162	1.81	0.77	-5.9	0.14	0.18	0.98	0.68
70	164	0.98	0.73	-3.1	0.48	0.21	1.32	0.48
71	166	1.79	0.69					
72	168		0.70	-5.2				
73	172	1.75	0.64	-10.2	0.14	0.22	0.92	0.61
74	174		0.84	-12.1				
75	176	1.68	0.36	-11.4	0.14	0.25	0.70	0.44
76	178	1.66	0.27	-11.8				
77	182	1.64	0.78	-15.9	0.54		1.22	0.56
78	184		0.45	-18.1				
79	186		0.69	-13.5				
80	188	1.66	1.11	-13.5				
81	192	1.65	0.41	-24.1	0.33	0.24	0.93	0.38
82	194		1.03	-10.8				
83	196	1.22	0.50	-15.9	0.16	0.20	0.79	0.55
84	198		0.65	-12.6				
85	202	1.96	0.72	-12.9				
86	204		0.42	-11.3				

87	206	1.72	0.60	-19.5	0.69	0.17	1.38	0.38
88	208		0.33	-13.4				
89	212	1.68	0.56	-17.1	0.27	0.18	0.95	0.52
90	214		0.61	-18.7				
91	216	1.59	0.57	-8.0				
92	218		0.36	-17.9				
93	224	1.59	0.34	-13.5				
94	228	1.35	0.75	-6.8				
95	234	1.45	0.50	-10.2				
96	238	1.49	0.34	9.0	0.53	0.18	1.00	0.29
97	244	1.49	0.64	0.6	0.63	0.12	1.31	0.42
98	248	1.55	0.61	3.5				
99	254	1.40	0.70	-1.6	0.22	0.10	0.93	0.66
100	258		0.42	-0.7	0.38	0.23	0.98	0.37
101	264	1.38	0.57	-5.6	0.37	0.16	1.03	0.48
102	268	1.47	0.57	-1.5				
103	272	1.55						
104	274	1.47	0.45	-1.0				
105	278	1.36	0.59	-1.4				
106	282							
107	284	1.57	0.64	0.2	0.33	0.12	1.01	0.55
108	288	1.61	0.75	0.0				
109	294	1.55	0.68	-0.1	0.39	0.19	1.17	0.51
110	296	1.50	0.79	2.2				
111	298	1.60	0.24	-19.0				
112	304	1.60	0.47	2.8				
113	308	1.52	0.80	-3.6	0.56	0.14	1.39	0.50
114	312							
115	314	1.60	0.53	-3.5				
116	318	1.75	0.77	-4.7				
117	324	1.71	0.40	-6.5	0.32	0.19	0.85	0.41

118	328	1.48	0.64	-11.0	0.51	0.16	1.22	0.46
119	330	1.11	0.80	-15.2				
120	332	1.71			0.29	0.28	0.58	
121	334	1.35	1.28	-20.2	0.39	0.23	1.75	0.64
122	336	1.37			0.31	0.23	0.54	
123	338	1.79	1.23	-13.1				
124	342		0.86	-4.0	0.11	0.15	1.01	0.74
125	344	1.65	0.71	-6.4				
126	348	1.51	1.12	-9.1				
127	352	1.42		-11.8				
128	354	1.46	0.94	-3.2				
129	356		0.66	5.1				
130	358	1.39	0.38	-9.5	0.48	0.15	0.96	0.34
131	364	1.40	0.72	-1.6	0.35	0.17	1.16	0.54
132	368	1.36	0.92	4.2	0.64	0.27	1.71	0.47
133	370	0.93						
134	374	1.22	0.82	0.7				
135	378	1.22	0.75	0.9	0.19	0.14	0.99	0.66
136	384	1.31	0.56	2.6	0.21	0.17	0.87	0.56
137	388	1.26	0.45	7.6	0.18	0.23	0.80	0.49
138	390	1.33			0.13	0.19	0.32	
139	394	1.38	0.51	1.1	0.14	0.10	0.69	0.65
140	398	1.27	0.88	1.2				
141	404	1.42	0.92	-0.3	0.17	0.22	1.18	0.68
142	408		0.86	3.4				
143	410	1.51						
144	414	1.26	0.85	5.3				
145	418	1.42	0.89	5.6				
146	424	1.98	0.49	0.2	0.23	0.14	0.79	0.54
147	428	1.94	0.92	0.6				
148	434	1.69	1.33	1.4				

149	438	1.73	1.42	-1.7				
150	442	1.35						
151	444	1.57	1.36	-2.9	0.40	0.15	1.74	0.68
152	448	1.40	1.24	-6.5				
153	454	1.66	1.30	-7.1				
154	456	1.40	2.04	-12.5				
155	458	1.51	2.45	-8.3	0.46	0.46	3.05	0.70
156	462	1.57	1.46	-14.8	0.51	0.33	2.12	0.60
157	464		1.07	-20.2				
158	468	1.47	1.12	-23.3	0.32	0.42	1.72	0.57
159	470	1.34						
160	474	1.69	1.20	-23.9	0.68	0.33	2.06	0.51
161	476	1.66			0.42	0.36	0.78	
162	478	1.76	0.80		0.44	0.45	1.58	0.44
163	484	1.58	1.05	-27.3	0.26	0.32	1.49	0.61
164	488	1.60	1.44	-30.6	0.30	0.20	1.76	0.71
165	492	1.64						
166	494	1.68	1.06	-28.7	0.52	0.25	1.69	0.54
167	498	1.62	1.25	-29.4				
168	502	1.64						
169	504	1.66	1.33	-27.8	0.28	0.33	1.77	0.66
170	506	1.71						
171	508	1.80	1.11	-30.6				
172	512	1.37						
173	514	1.46	0.62	-32.7	0.23	0.23	1.01	0.54
174	516		0.83	-24.6				
175	518	1.35	2.20	-14.9	0.25	0.38	2.54	0.75
176	524	1.44	1.14	0.1	0.35	0.38	1.73	0.58
177	528	1.39	1.16	-23.4				
178	534	1.78	1.09	-16.9				
179	536	1.59						

180	538	1.29	0.85	-24.6	0.21	0.32	1.27	0.58
181	542	1.81						
182	544	2.04	1.00	-15.2				
183	548	2.08	0.84	-28.6				
184	554	1.88	0.45	-24.1				
185	556	1.84						
186	558	2.50	1.50	-30.2				
187	560	1.66						
188	562	1.59						
189	564	1.77	0.97	-28.7	0.39	0.17	1.41	0.60
190	568	1.44	1.48		0.32	0.20	1.80	0.71
191	572	1.60						
192	574	1.77	1.17	-25.3				
193	578	2.01	1.56	-31.1				
194	580							
195	582	1.96						
196	584	1.76	1.12	-32.8				
197	588	1.51	2.54	-38.0	0.24	0.29	2.74	0.81
198	594	1.72	1.09	-33.4	0.22	0.28	1.45	0.66
199	598	1.89	1.25	-34.8				
Minimum		0.87	0.13	-37.97	0.11	0.04	0.32	0.19
Maximum		2.50	2.54	9.01	0.96	0.46	3.05	0.81
Average		1.61	0.82	-10.42	0.41	0.21	1.29	0.52

bd=below detection limit

Table 6. 3. Bulk sediment elemental compositions and isotope ratios of SSD045/13/G1 core.

Depth (cmbsf)	TOC (wt%)	CRS (wt%)	Fe_D (wt%)	Fe_{OX} (wt%)	Fe_{TR} (wt%)	DOP	$\delta^{34}S_{CRS}$ (‰-VCDT)
1	0.98	0.001					-7.8
3		0.011					-10.4
5		0.006					-10.4
7		0.013					-10.0
9	0.87	0.006					-8.8
11		0.004					-9.0
13		0.006					-10.7
15		0.003					-8.9
17	0.99	0.003					-8.9
19		0.010					-9.5
21		0.004					-9.8
23		0.015					-13.1
25	0.98	0.001					-10.8
27		0.008					-8.4
29		0.008					-10.2
31		0.015					-9.7
33	0.74	0.025					-8.5
35		0.013					-6.6
37		0.006					-15.7
39	0.85	0.009					-11.2
40	0.96	0.0130	0.09	0.22	0.324	0.04	
44							
50	0.86						
54							

58							
60	1.04	0.0008					-21.9
64							
70	1.00						
74							
78							
80	0.91	0.0137					-28.8
84							
90	1.10						
94							
98							
100	1.16	0.0008					-32.9
104							
110	1.28						
114							
118							
120	1.25	0.0103					-37.3
124							
128							
134	1.36						
138	1.34						
140	1.33	0.0082	0.16	0.21	0.381	0.02	-35.5
144							
150	1.41						
154							
158							
160	1.41	0.0192					-38.4
164							

170	1.49						
174							
178							
180	1.48	0.0289					-38.3
184							
190	1.60						
194							
198							
200	1.51	0.0322					-38.4
204							
210	1.67						
214							
218							
220	1.66	0.0276					-39.4
224							
228							
234	1.64						
238	1.81						
240	1.77	0.0080	0.12	0.28	0.410	0.02	-35.1
244							
250	1.85						
254							
258							
260	1.94	0.0098					-38.6
264							
270	2.06						
274							
278							

280	2.05	0.0296					
284							
290	2.16						
294							
298							
300	2.12	0.0074					-39.6
304							
310	2.25						
314							
318							
320	2.18	0.0178					-40.7
324							
328	2.39						
334							
338	2.00						
340	2.18	0.0171	0.15	0.18	0.340	0.05	-43.7
344							
350	2.06						
354							
358							
360	2.08	0.0168					-43.0
364							
370	1.88						
374							
378							
380	2.06	0.0262					-43.4
384							
390	1.98						

394							
398							
400	2.16	0.0266					-43.9
404							
410	2.33						
414							
418							
420	2.13	0.0150					-44.6
424							
428	1.82						
434	1.30						
Minimum	0.74	0.00	0.09	0.18	0.27	0.003	-44.6
Maximum	2.39	0.03	0.16	0.28	0.41	0.05	-6.6
Average	1.59	0.01	0.13	0.22	0.36	0.03	-23.2

Table 7. 1. Major and trace element geochemical data of cold seep core SSD045/4/G4.

Depth (cmbsf)	Al (wt%)	Mn (ppm)	Fe (wt%)	Mo (ppm)	U (ppm)	Mn/Al (ppm/wt%)	Fe/Al (wt%/wt%)	Mo_{EF}	U_{EF}	δ^{98}Mo (‰)
0.5	10.2	736.6	8.9	1.3	1.8	72.3	0.9	0.8	0.6	0.71
2.5	8.9	655.8	8.2	1.5	2.3	73.3	0.9	1.1	0.8	
4.5	9.8	646.4	9.2	1.4	2.8	66.2	0.9	1.0	0.9	0.33
6.5	10.2	623.4	9.1	1.4	3.1	61.4	0.9	0.9	0.9	
8.5	10.1	616.6	8.8	1.6	3.1	61.0	0.9	1.0	1.0	
11	10.1	597.5	9.2	1.5	3.0	59.1	0.9	1.0	0.9	1.01
13	9.7	583.9	8.9	1.6	3.4	60.5	0.9	1.1	1.1	
15	9.7	588.2	8.8	1.8	3.5	60.4	0.9	1.2	1.1	1.83
17	10.0	586.5	9.2	1.6	3.6	58.9	0.9	1.1	1.1	
19	9.5	576.5	8.6	1.8	3.4	60.9	0.9	1.3	1.1	0.57
20	8.2	392.6	6.3	12.3	4.1	48.2	0.8	10.0	1.6	2.33
22										
24	7.8	432.3	6.4	16.0	5.1	55.4	0.8	13.6	2.1	1.30
26										
28	7.7	433.9	6.4	15.0	5.7	56.4	0.8	13.0	2.3	2.11
32	8.0	416.5	6.8	17.4	5.7	52.0	0.9	14.5	2.2	
34	8.0	393.8	5.5	11.6	4.8	49.4	0.7	9.7	1.9	2.16
36										
38	7.9	438.2	6.0	13.5	3.9	55.5	0.8	11.4	1.5	1.99
40	7.9	559.0	5.8	8.5	4.2	71.1	0.7	7.2	1.7	
42										
44	8.5	487.8	6.3	10.2	4.3	57.5	0.7	8.0	1.6	2.03
46										
48	8.2	378.0	6.3	5.6	4.3	46.1	0.8	4.6	1.6	

52										
54	8.3	353.5	6.2	5.3	4.0	42.3	0.7	4.3	1.5	
56										
58	8.2	370.5	6.1	10.6	4.1	45.1	0.7	8.6	1.6	1.86
62	8.3	507.7	6.4	2.9	3.5	60.9	0.8	2.3	1.3	2.62
64	8.3	356.7	6.3	2.6	3.6	43.1	0.8	2.1	1.4	
66	8.3	331.5	5.9	2.3	3.2	40.1	0.7	1.9	1.2	
68	8.8	336.4	5.9	4.2	3.5	38.2	0.7	3.2	1.2	
72										
74	7.9	366.8	6.0	4.9	4.2	46.4	0.8	4.1	1.7	2.02
76										
78	7.8	359.6	5.8	2.7	3.8	45.9	0.7	2.3	1.5	
82	8.6	381.1	6.0	2.2	2.8	44.1	0.7	1.7	1.0	1.66
84										
86										
88	8.1	372.0	6.0	1.2	2.8	46.0	0.7	1.0	1.1	0.28
92										
94	8.2	439.8	6.0	1.2	3.8	53.6	0.7	1.0	1.5	1.14
96										
98	8.1	361.6	5.7	1.1	3.0	44.6	0.7	0.9	1.2	
102										
104	7.5	380.7	5.6	1.3	3.6	50.5	0.7	1.1	1.5	1.09
106										
108	7.5	380.8	5.6	1.2	3.5	50.6	0.7	1.1	1.5	
112										
114	8.0	376.1	5.8	1.6	3.8	46.9	0.7	1.3	1.5	0.79
116										
118	8.3	396.5	5.7	2.3	3.4	47.9	0.7	1.8	1.3	2.38

122	7.8	391.4	5.8	1.6	4.7	50.2	0.7	1.4	1.9	1.22
124										
126	7.2	376.7	5.4	1.9	3.9	52.2	0.7	1.8	1.7	1.30
128										
132	6.7	350.1	4.7	2.1	3.9	52.5	0.7	2.1	1.8	
134										
136	6.5	335.9	4.4	2.5	4.3	51.4	0.7	2.5	2.1	1.25
138										
142	8.1	408.3	6.1	1.2	3.2	50.5	0.8	1.0	1.3	
144										
146	7.7	412.2	5.9	1.1	3.5	53.3	0.8	0.9	1.4	0.87
148										
152	7.7	412.1	5.8	1.0	3.5	53.5	0.7	0.9	1.4	
154										
156	8.0	476.5	5.9	1.1	3.7	59.5	0.7	0.9	1.5	1.19
158										
162	8.1	389.9	5.8	1.0	5.1	47.9	0.7	0.8	1.9	
164	7.8	381.0	5.7	1.6	3.1	49.1	0.7	1.4	1.2	
166	8.3	433.7	5.9	2.4	4.2	52.1	0.7	1.9	1.6	1.21
168										
172	8.0	387.6	6.3	2.1	3.3	48.4	0.8	1.7	1.3	
174										
176	7.7	450.4	5.5	5.4	3.8	58.3	0.7	4.7	1.5	2.11
178	7.1	416.2	4.9	3.6	3.6	58.8	0.7	3.4	1.6	1.52
182	8.5	438.7	5.7	6.0	4.7	51.6	0.7	4.7	1.7	1.48
184										
186	8.1	341.2	5.8	3.8	5.4	42.1	0.7	3.1	2.1	
188	8.1	473.0	6.1	7.5	5.2	58.6	0.7	6.2	2.0	1.94

192	8.3	394.9	5.5	1.0	2.9	47.5	0.7	0.8	1.1	
194										
196	8.0	430.8	5.4	2.5	4.3	53.8	0.7	2.1	1.7	1.98
198										
202	8.2	462.3	5.8	1.8	4.0	56.4	0.7	1.5	1.5	
204										
206	7.9	544.5	5.5	2.5	3.8	69.1	0.7	2.1	1.5	2.13
208										
212	7.8	621.1	5.6	2.3	3.1	79.4	0.7	1.9	1.2	
214										
216	8.0	413.2	5.3	1.4	3.8	51.6	0.7	1.2	1.5	1.66
218										
224	7.8	460.6	5.5	1.7	3.7	58.8	0.7	1.4	1.5	
228	8.0	529.8	5.9	3.3	3.5	66.6	0.7	2.7	1.4	2.15
234	8.1	432.0	5.5	2.4	4.0	53.3	0.7	1.9	1.5	
238	7.5	524.4	5.3	3.6	4.4	70.0	0.7	3.2	1.8	1.59
244	8.1	487.9	5.4	1.8	3.5	60.4	0.7	1.5	1.3	1.76
248	7.9	397.1	5.7	1.2	3.4	50.4	0.7	1.0	1.4	
254	8.0	463.8	5.5	2.6	2.6	58.3	0.7	2.2	1.0	2.04
258	8.1	372.5	5.4	1.0	3.7	46.1	0.7	0.8	1.4	
264	8.1	440.8	5.5	2.1	3.2	54.7	0.7	1.7	1.2	1.54
268	8.5	347.8	5.7	2.0	4.9	40.7	0.7	1.6	1.8	
272	8.1	358.0	5.4	2.6	4.6	44.3	0.7	2.1	1.8	1.10
274										
278										
282	9.0	418.1	6.2	3.2	3.9	46.6	0.7	2.4	1.4	1.24
284	7.8	402.4	5.4	2.8	3.0	51.9	0.7	2.4	1.2	1.15
288	9.9	374.6	6.8	1.3	3.3	37.7	0.7	0.9	1.0	

294	8.1	338.9	5.7	1.1	4.5	41.9	0.7	0.9	1.7	0.74
296	8.0	336.1	5.6	1.4	4.8	42.0	0.7	1.2	1.9	
298										
304	8.7	359.3	5.9	1.4	5.9	41.4	0.7	1.1	2.1	
308	8.1	399.7	5.6	3.2	3.8	49.5	0.7	2.6	1.5	0.89
312	7.8	353.9	5.8	2.4	4.5	45.3	0.7	2.0	1.8	
314	7.8	389.2	5.7	1.2	3.8	50.2	0.7	1.0	1.5	
318	8.7	485.1	6.4	1.7	3.6	56.0	0.7	1.3	1.3	1.19
324	7.5	413.8	5.8	1.4	3.9	55.4	0.8	1.2	1.6	
328	7.7	441.3	5.9	2.2	3.6	57.4	0.8	1.9	1.5	
330	7.4	429.0	6.0	4.0	4.7	58.0	0.8	3.6	2.0	1.42
332	7.6	434.3	5.7	3.0	4.5	57.1	0.7	2.6	1.9	
334	7.3	536.9	5.7	10.0	3.7	73.4	0.8	9.1	1.6	1.85
336	7.3	491.9	6.0	9.0	5.7	67.2	0.8	8.2	2.4	
338	7.9	505.4	6.3	4.6	4.9	64.2	0.8	3.9	1.9	1.91
342	7.9	459.3	5.7	3.2	6.3	58.2	0.7	2.7	2.5	1.26
344										
348	8.1	443.2	5.8	2.5	4.8	54.5	0.7	2.0	1.8	0.93
352	7.2	451.7	5.5	1.9	4.5	63.0	0.8	1.7	2.0	
354	7.6	449.3	6.0	1.4	4.2	59.1	0.8	1.2	1.7	
356										
358	8.1	449.9	6.0	1.4	3.5	55.2	0.7	1.1	1.3	
364	7.7	475.7	5.8	1.4	3.9	61.6	0.7	1.2	1.6	
368	7.4	464.9	5.4	1.0	3.6	63.1	0.7	0.9	1.5	
370	7.4	462.4	5.7	2.4	3.7	62.2	0.8	2.2	1.5	1.32
374	7.4	458.3	5.6	1.5	4.9	62.2	0.8	1.4	2.1	
378	7.7	491.1	5.7	1.0	4.1	63.7	0.7	0.9	1.6	0.97
384	7.6	436.5	5.7	1.0	4.6	57.5	0.7	0.9	1.9	

388	7.4	444.5	5.1	1.1	4.2	59.8	0.7	1.0	1.8	
390	7.4	455.5	5.4	1.1	5.1	61.4	0.7	1.0	2.1	
394	7.4	447.1	5.3	1.5	4.3	60.6	0.7	1.3	1.8	1.56
398	7.7	447.2	5.4	1.0	5.4	58.2	0.7	0.8	2.2	
404	7.7	470.4	5.4	1.7	5.5	61.4	0.7	1.5	2.2	1.25
408	8.0	478.4	5.4	1.3	5.5	59.6	0.7	1.1	2.2	
410	7.4	463.2	5.2	1.2	5.6	62.6	0.7	1.1	2.4	
414	7.3	426.7	5.2	1.0	5.4	58.2	0.7	0.9	2.3	
418	7.5	469.5	5.5	1.4	5.5	62.7	0.7	1.2	2.3	
424	7.8	403.0	5.4	1.3	6.4	51.6	0.7	1.1	2.6	1.30
428	7.6	382.1	5.6	1.1	4.7	50.1	0.7	1.0	1.9	
434	7.7	378.4	5.4	1.1	4.5	49.1	0.7	0.9	1.8	0.48
438	7.9	437.3	5.7	1.3	4.1	55.1	0.7	1.1	1.6	
442	7.3	441.4	5.5	1.5	3.6	60.1	0.7	1.3	1.5	
444	7.6	470.4	5.7	3.4	3.6	62.2	0.8	3.0	1.5	0.75
448	7.3	405.1	5.5	1.4	3.5	55.6	0.8	1.3	1.5	
454	7.9	486.5	5.8	2.7	3.1	62.0	0.7	2.3	1.2	
456										
458	7.6	859.1	7.2	4.4	4.8	112.9	0.9	3.9	2.0	0.07
462	7.2	580.8	5.5	3.7	5.1	81.1	0.8	3.4	2.2	
464										
468	7.6	426.5	5.8	7.1	4.6	56.1	0.8	6.2	1.9	0.72
470	8.3	500.5	6.7	10.1	4.7	60.5	0.8	8.1	1.8	-0.37
474	8.9	576.9	6.7	9.7	4.7	65.2	0.8	7.3	1.7	1.08
476	7.9	584.5	5.9	6.1	4.2	74.1	0.7	5.1	1.7	
478	7.3	570.7	5.5	2.6	4.1	78.3	0.8	2.4	1.8	
484	6.4	406.5	5.5	2.5	5.1	63.7	0.9	2.6	2.5	0.78
488	10.2	466.6	7.6	1.9	5.4	45.5	0.7	1.2	1.7	

492										
494	8.6	464.3	6.6	2.5	5.6	54.2	0.8	1.9	2.1	0.37
498	8.2	454.0	6.1	2.7	6.5	55.7	0.7	2.2	2.5	1.69
502										
504	7.6	528.6	6.2	4.5	4.8	69.4	0.8	3.9	2.0	0.55
506										
508	8.6	441.4	6.8	7.0	5.3	51.2	0.8	5.4	1.9	1.14
512										
514	7.2	341.8	5.3	3.4	3.8	47.4	0.7	3.1	1.7	
516										
518	9.0	515.8	7.3	5.8	4.2	57.1	0.8	4.3	1.5	0.66
524	7.4	461.5	5.8	1.8	4.5	62.1	0.8	1.6	1.9	0.63
528	8.0	437.1	5.8	1.9	3.6	54.4	0.7	1.6	1.4	
534	7.4	378.1	5.4	1.8	3.7	51.0	0.7	1.6	1.6	
536										
538	7.2	444.6	5.4	3.2	4.5	61.6	0.7	3.0	2.0	0.59
542										
544	7.2	461.4	5.8	1.6	5.1	63.9	0.8	1.5	2.2	
548	7.3	416.4	5.5	2.3	4.5	56.7	0.7	2.1	1.9	
554	7.4	382.9	5.6	1.9	4.3	51.8	0.8	1.7	1.8	
556										
558	7.8	408.9	6.1	4.4	4.7	52.5	0.8	3.8	1.9	0.72
560										
562										
564	6.9	361.3	5.4	1.5	3.6	52.2	0.8	1.4	1.6	
568	7.4	509.7	6.0	3.1	3.3	68.8	0.8	2.8	1.4	0.66
572										
574	7.0	416.8	6.2	3.4	3.4	59.7	0.9	3.3	1.5	

578	7.3	386.9	6.4	5.4	3.7	53.2	0.9	5.0	1.6	0.29
580										
582										
584	9.0	420.7	6.7	2.7	3.6	46.5	0.7	2.0	1.2	
588	7.6	572.4	6.4	5.4	4.0	75.1	0.8	4.8	1.7	0.43
594	8.8	484.8	7.2	2.1	4.0	55.1	0.8	1.6	1.4	
598	9.0	476.9	7.3	3.0	4.9	53.0	0.8	2.2	1.7	0.83
Minimum	6.4	331.5	4.4	1.0	1.8	37.7	0.7	0.8	0.6	-0.37
Maximum	10.2	859.1	9.2	17.4	6.5	112.9	0.9	14.5	2.6	+2.62
Average	8.0	449.4	6.0	3.3	4.1	56.3	0.8	2.7	1.6	+1.26

Table 7. 2. Major and trace element geochemical data of non-cold seep core SSD045/13/G1

S.No	**Depth**	**Al (wt%)**	**Mn (wt%)**	**Fe (wt%)**	**Mo (ppm)**	**U (ppm)**	**Mn/Al (ppm/wt%)**	**Fe/Al (wt%/wt%)**	**Mo_{EF}**	**U_{EF}**	**$\delta^{98}Mo$ (‰)**
1	1	9.7	690.9	8.8	1.2	1.5	71.3	0.91	0.8	0.5	
2	3										
3	5										
4	7										
5	9	10.3	646.2	9.0	0.9	1.5	62.8	0.88	0.6	0.4	
6	11										
7	13										
8	15										
9	17	9.6	593.4	8.5	1.1	1.5	62.0	0.89	0.7	0.5	
10	19										
11	21										

12	23										
13	25	10.5	530.6	9.2	1.1	1.7	50.5	0.87	0.7	0.5	
14	27										
15	29										
16	31										
17	33	9.4	663.3	8.8	1.1	1.4	70.2	0.93	0.8	0.5	
18	35										
19	37										
20	39	9.6	683.8	8.8	1.0	1.4	71.1	0.92	0.7	0.4	
21	40	9.7	497.1	8.7	1.4	1.4	51.5	0.90	1.0	0.5	1.22
22	44										
23	50	9.9	517.1	9.1	1.1	1.6	52.3	0.92	0.7	0.5	
24	54										
25	58										
26	60	10.7	489.8	9.0	1.3	1.9	45.8	0.85	0.8	0.5	
27	64										
28	70	9.7	473.4	8.7	1.1	1.7	48.7	0.89	0.8	0.5	
29	74										
30	78										
31	80	8.8	625.9	8.5	1.1	1.4	71.2	0.97	0.8	0.5	
32	84										
33	90	9.8	495.3	9.1	1.3	1.7	50.5	0.93	0.9	0.5	1.37
34	94										
35	98										
36	100	9.9	457.1	8.8	1.5	1.7	46.3	0.90	1.0	0.5	
37	104										
38	110	10.2	411.9	8.4	1.4	1.7	40.4	0.83	0.9	0.5	
39	114										
40	118										
41	120	10.4	450.3	8.8	1.4	1.6	43.1	0.85	0.9	0.5	
42	124										

43	128										
44	134	10.0	435.7	8.6	1.2	1.7	43.5	0.85	0.8	0.5	
45	138	10.3	433.0	9.1	1.1	1.7	42.0	0.89	0.7	0.5	
46	140	10.4	448.2	9.1	1.7	1.6	42.9	0.88	1.1	0.5	0.05
47	144										
48	150	10.0	435.6	8.4	1.3	1.8	43.6	0.84	0.8	0.6	
49	154										
50	158										
51	160	10.7	466.4	8.8	1.2	1.9	43.8	0.83	0.8	0.5	
52	164										
53	170	11.2	440.3	9.3	1.1	1.8	39.3	0.84	0.7	0.5	
54	174										
55	178										
56	180	10.0	466.7	8.8	1.3	1.7	46.8	0.88	0.8	0.5	
57	184										
58	190	10.4	435.1	8.7	1.2	1.8	41.7	0.84	0.8	0.5	0.54
59	194										
60	198										
61	200	9.1	374.3	7.3	1.2	1.7	41.2	0.80	0.8	0.6	
62	204										
63	210	10.3	407.7	8.3	1.4	1.9	39.7	0.81	0.9	0.6	
64	214										
65	218										
66	220	11.5	481.5	9.6	1.2	2.1	42.0	0.84	0.7	0.6	
67	224										
68	228										
69	234	11.0	598.1	9.2	1.8	2.0	54.2	0.83	1.1	0.6	
70	238	10.5	398.8	8.4	1.1	1.8	38.0	0.80	0.7	0.5	
71	240	10.9	381.8	8.9	1.1	1.9	35.1	0.82	0.7	0.5	1.03
72	244										
73	250	10.7	374.9	8.3	1.4	2.0	34.9	0.77	0.9	0.6	

74	254										
75	258										
76	260	11.2	378.1	8.8	1.2	2.0	33.7	0.79	0.7	0.6	
77	264										
78	270	11.1	361.2	8.3	1.4	2.3	32.5	0.74	0.9	0.6	
79	274										
80	278										
81	280	11.3	375.6	8.7	1.5	2.2	33.2	0.77	0.9	0.6	
82	284										
83	290	10.8	383.5	8.6	1.3	2.1	35.6	0.80	0.8	0.6	0.61
84	294										
85	298										
86	300	11.0	356.7	8.0	1.2	2.1	32.4	0.72	0.7	0.6	
87	304										
88	310	11.2	364.9	7.7	1.4	2.3	32.7	0.69	0.8	0.7	
89	314										
90	318										
91	320	11.1	343.9	7.8	1.2	2.2	31.0	0.70	0.7	0.6	
92	324										
93	328	10.8	378.8	8.5	1.3	2.1	35.0	0.79	0.8	0.6	
94	334										
95	338	10.9	352.4	7.4	1.1	2.2	32.2	0.68	0.6	0.6	
96	340	11.6	337.5	7.8	1.0	2.2	29.0	0.67	0.6	0.6	0.57
97	344										
98	350	10.9	355.9	7.4	1.4	2.4	32.8	0.68	0.9	0.7	
99	354										
100	358										
101	360	11.2	340.4	7.6	1.2	2.2	30.5	0.68	0.7	0.6	
102	364										
103	370	11.6	338.1	8.0	1.2	2.3	29.1	0.69	0.7	0.6	
104	374										

105	378										
106	380	11.3	321.3	7.6	1.7	2.0	28.5	0.67	1.0	0.6	
107	384										
108	390	11.0	325.9	7.7	1.9	2.3	29.6	0.70	1.1	0.6	0.98
109	394										
110	398										
111	400	11.1	332.1	7.9	1.4	2.1	29.9	0.71	0.8	0.6	
112	404										
113	410	10.5	382.1	7.9	1.3	2.3	36.3	0.75	0.8	0.7	
114	414										
115	418										
116	420	11.3	413.7	8.1	1.5	2.2	36.8	0.72	0.9	0.6	
117	424										
118	428	10.4	399.9	7.5	1.1	2.3	38.6	0.73	0.7	0.7	
119	434	10.4	431.5	8.0	0.9	2.1	41.4	0.77	0.6	0.6	0.77
Minimum		8.8	321.3	7.3	0.9	1.4	28.5	0.67	0.6	0.45	0.05
Maximum		11.6	690.9	9.6	1.9	2.4	71.3	0.97	1.1	0.71	1.37
Average		10.5	441.6	8.5	1.3	1.9	42.5	0.81	0.8	0.6	0.79

Table 7. 3. Molybdenum speciation data and isotope ratios of Mo associated with Fe-oxide and pyrite phases from the cold seep core SSD045/4/G4.

Depth (cmbsf)	Carb (ppm)	Fe (ppm)	Humic (ppm)	Pyrite (ppm)	Silicate (ppm)	Sum (ppm)	Total (ppm)	Recovery (%)	$\delta^{98}Mo_{bulk}$ (‰)	$\delta^{98}Mo_{Fe\text{-}Ox}$ (‰)	$\delta^{98}Mo_{FeS2}$ (‰)	$\Delta\delta^{98}Mo_{FeS2\text{-}FeOX}$
20	0.3	8.6	0.7	1.1	1.1	11.8	12.3	95.6	2.33	2.23	2.80	0.58
28	0.3	10.2	0.5	0.9	1.3	13.2	15.0	87.7	2.11			
34	0.8	4.1	0.8	2.1	1.4	9.2	11.6	79.5	2.16	2.39	2.50	0.10
44	0.2	8.1	0.5	0.1	0.3	9.2	10.2	89.9	2.03			
82	0.1	1.1	1.0	0.2	0.3	2.6	2.2	119.1	1.66			
176	0.3	1.2	0.4	1.4	1.6	4.9	5.4	90.2	2.11			
176	0.2	1.0	0.3	1.4	2.5	5.3	5.4	98.3	2.11			
188	0.1	1.6	0.2	2.0	2.5	6.5	7.5	87.7	1.94			
196	0.3	0.9	0.2	1.1	2.0	4.5	5.5	82.7	1.98			
228	0.3	0.9	0.5	0.4	1.2	3.2	3.3	99.7	2.15			
308	0.0	0.3	0.1	0.2	0.4	1.0	1.4	75.0	0.89	0.86	2.02	1.16
334	0.6	3.1	0.7	4.3	2.3	11.0	10.0	110.5	1.85	1.83	3.03	1.20
468	0.0	3.0	0.3	1.8	2.7	7.7	7.1	108.8	0.72			
470	0.3	0.7	0.2	5.4	2.5	9.0	10.1	89.2	-0.37	0.39	0.02	-0.37
476	0.2	1.1	0.3	1.4	2.7	5.6	6.1	92.9	nm			
508	0.3	0.7	0.3	2.9	2.3	6.5	7.0	92.4	1.14	0.28	0.90	0.62
558	0.1	0.5	0.1	1.2	2.0	3.9	5.4	72.7	0.72			
578	0.5	2.7	0.4	1.3	1.5	6.5	5.4	118.9	0.29			
Minimum	0.0	0.3	0.1	0.1	0.3	1.0	1.4	72.7	-0.37	0.28	0.02	-0.37
Maximum	0.8	10.2	1.0	5.4	2.7	13.2	15.0	119.1	2.33	2.39	3.03	1.20

nm = not measured

Mo speciation in %					
Depth (cmbsf)	**Carb (%)**	**Fe (%)**	**Humic (%)**	**FeS_2 (%)**	**Silicate (%)**
20	2.2	70.3	5.5	9.0	8.6
28	2.0	67.8	3.5	5.7	8.7
34	6.9	35.2	7.2	18.5	11.7
44	1.9	79.0	4.7	1.3	2.9
82	2.6	50.9	44.9	9.1	11.7
176	5.5	21.5	7.6	25.9	29.7
176	2.9	18.6	4.8	25.5	46.6
188	1.7	22.0	3.3	27.2	33.5
196	5.8	16.5	3.9	20.5	36.0
228	8.0	28.5	14.5	13.1	35.6
308	2.7	21.5	4.8	13.3	32.7
334	5.7	31.5	6.6	43.2	23.5
468	0.0	41.6	4.3	25.5	37.4
470	2.5	7.1	1.6	53.1	24.9
476	3.3	18.4	4.2	22.9	44.1
508	4.6	9.8	3.7	41.1	33.2
558	2.3	8.6	1.5	22.9	37.3
578	9.0	50.4	7.7	23.4	28.3
Minimum	0.0	7.1	1.5	1.3	2.9
Maximum	9.0	79.0	44.9	53.1	46.6

References

Adam, P., Schmid, J. C., Mycke, B., Strazielle, C., Connan, J., Huc, A., Riva, A., & Albrecht, P. (1993). Structural investigation of nonpolar sulfur cross-linked macromolecules in petroleum. *Geochimica et Cosmochimica Acta*, *57*(14), 3395-3419.

Aguilar Pérez, M. I., Zapata-Ramírez, P. A., & Micallef, A. (2024). A review of cold seeps in the Western Atlantic, focusing on Colombia and the Caribbean. *Frontiers in Marine Science*, *11*, 1430377.

Akam, S. A., Swanner, E. D., Yao, H., Hong, W.-L., & Peckmann, J. (2023). Methane-derived authigenic carbonates–A case for a globally relevant marine carbonate factory. *Earth-Science Reviews*, 104487.

Albarède F., & B., B. (2004). Analytical Methods for Non-Traditional Isotopes. In B. B. Johnson C.M., Albarède F. (Ed.), *Geochemistry of non-traditional stable isotopes. Reviews in Mineralogy and Geochemistry* (Vol. 55, pp. 113-152).

Algeo, T. J., & Lyons, T. W. (2006). Mo–total organic carbon covariation in modern anoxic marine environments: Implications for analysis of paleoredox and paleohydrographic conditions. *PALEOCEANOGRAPHY*, *21*(1). https://doi.org/https://doi.org/10.1029/2004PA001112

Algeo, T. J., & Tribovillard, N. (2009). Environmental analysis of paleoceanographic systems based on molybdenum–uranium covariation. *Chemical Geology*, *268*(3-4), 211-225. https://doi.org/doi:10.1016/j.chemgeo.2009.09.001

Aloisi, G., Bouloubassi, I., Heijs, S. K., Pancost, R. D., Pierre, C., Sinninghe Damsté, J. S., Gottschal, J. C., Forney, L. J., & Rouchy, J. M. (2002). CH4-consuming microorganisms and the formation of carbonate crusts at cold seeps. *Earth and Planetary Science Letters*, *203*(1), 195-203.

Aloisi, G., Pierre, C., Rouchy, J. M., Foucher, J. P., & Woodside, J. (2000). Methane-related authigenic carbonates of eastern Mediterranean Sea mud volcanoes and their possible relation to gas hydrate destabilisation. *Earth and Planetary Science Letters*, *184*(1), 321-338.

Alperin, M. J., Reeburgh, W. S., & Whiticar, M. J. (1988). Carbon and hydrogen isotope fractionation resulting from anaerobic methane oxidation. *Global Biogeochemical Cycles*, *2*(3), 279-288.

Andreae, M. O. (1990). Ocean-atmosphere interactions in the global biogeochemical sulfur cycle. *Marine Chemistry*, *30*, 1-29.

Antler, G., Turchyn, A. V., Herut, B., Davies, A., Rennie, V. C. F., & Sivan, O. (2014). Sulfur and oxygen isotope tracing of sulfate driven anaerobic methane oxidation in estuarine sediments. *Estuarine, Coastal and Shelf Science*, *142*, 4-11.

Archer, D., Buffett, B., & McGuire, P. (2012). A two-dimensional model of the passive coastal margin deep sedimentary carbon and methane cycles. *Biogeosciences*, *9*(8), 2859-2878.

Argentino, C., Johnson, J. E., Conti, S., Fioroni, C., & Fontana, D. (2020). Preservation of 34S-enriched sulfides in fossil sulfate-methane transition zones: new evidence from Miocene outcrops of the northern Apennines (Italy). *Geo-Marine Letters*, *40*(3), 379-390.

Arvidson, R. S., Morse, J. W., & Joye, S. B. (2004). The sulfur biogeochemistry of chemosynthetic cold seep communities, Gulf of Mexico, USA. *Marine Chemistry*, *87*(3-4), 97-119.

Ãstrom, E. K. L., Sen, A., Carroll, M. L., & Carroll, J. (2020). Cold seeps in a warming Arctic: Insights for benthic ecology. *Frontiers in Marine Science*, *7*, 244.

Bak, F., & Cypionka, H. (1987). A novel type of energy metabolism involving fermentation of inorganic sulphur compounds.

Bangs, N. L., Shipley, T. H., & Moore, G. F. (1996). Elevated fluid pressure and fault zone dilation inferred from seismic models of the northern Barbados Ridge decollement. *Journal of Geophysical Research: Solid Earth*, *101*(B1), 627-642.

Barling, J., & Anbar, A. (2004). Molybdenum isotope fractionation during adsorption by manganese oxides. *Earth Planetary Science Letters*, *217*(3-4), 315-329.

Bascomb, C. L. (1968). Distribution of pyrophosphateâ€• extractable iron and organic carbon in soils of various groups. *Journal of Soil Science*, *19*(2), 251-268.

Bastia, R. (2006). An overview of Indian sedimentary basins with special focus on emerging east coast deepwater frontiers. *The Leading Edge*, *25*(7), 818-829.
Bastia, R. (2007). *Geologic Settings and Petroleum Systems of India's East Coast Offshore Basins : Concepts and Applications*. TECHNOLOGY PUBLICATIONS.
Bastia, R., & Nayak, P. K. (2006). Tectonostratigraphy and depositional patterns in Krishna offshore basin, Bay of Bengal. *The Leading Edge*, *25*(7), 839-845.
Bastia, R., & Radhakrishna, M. (2012). *Basin evolution and petroleum prospectivity of the continental margins of India* (Vol. 59). Elsevier.
Bau, M., & Dulski, P. (1996). Distribution of yttrium and rare-earth elements in the Penge and Kuruman iron-formations, Transvaal Supergroup, South Africa. *Precambrian Research*, *79*(1-2), 37-55.
Bayon, G., Dupré, S., Ponzevera, E., Etoubleau, J., Chéron, S., Pierre, C., Mascle, J., Boetius, A., & De Lange, G. J. (2013). Formation of carbonate chimneys in the Mediterranean Sea linked to deep-water oxygen depletion. *Nature Geoscience*, *6*(9), 755-760.
Bayon, G., Henderson, G. M., & Bohn, M. (2009). U-Th stratigraphy of a cold seep carbonate crust. *Chemical Geology*, *260*(1-2), 47-56.
Bayon, G., Pierre, C., Etoubleau, J., Voisset, M., Cauquil, E., Marsset, T., Sultan, N., Le Drezen, E., & Fouquet, Y. (2007). Sr/Ca and Mg/Ca ratios in Niger Delta sediments: Implications for authigenic carbonate genesis in cold seep environments. *Marine Geology*, *241*(1-4), 93-109.
Bazzaro, M., Ogrinc, N., Relitti, F., Lucchi, R., Giani, M., Adami, G., Pavoni, E., & De Vittor, C. (2020). Geochemical signatures of intense episodic anaerobic oxidation of methane in near-surface sediments of a recently discovered cold seep (Kveithola trough, NW Barents Sea). *Marine Geology*, *425*, 106189.
Belshaw, N., Freedman, P., O'nions, R., Frank, M., & Guo, Y. (1998). A new variable dispersion double-focusing plasma mass spectrometer with performance illustrated for Pb isotopes. *International Journal of Mass Spectrometry*, *181*(1-3), 51-58.
Berg, J. S., Schwedt, A., Kreutzmann, A.-C., Kuypers, M. M. M., & Milucka, J. (2014). Polysulfides as Intermediates in the Oxidation of Sulfide to Sulfate by Beggiatoa spp. *Applied and Environmental Microbiology*, *80*(2), 629-636.
Bernardino, A. F., Levin, L. A., Thurber, A. R., & Smith, C. R. (2012). Comparative composition, diversity and trophic ecology of sediment macrofauna at vents, seeps and organic falls. *PLoS One*, *7*(4), e33515.
Berner, R. (1970). Sedimentary pyrite formation. *American Journal of Science*, *268*, 1-23.
Berner, R., & Westrich, J. (1985). Bioturbation and the early diagenesis of carbon and sulfur. *Am. J. Sci*, *285*, 193-206.
Bertine, K. K., & Turekian, K. K. (1973). Molybdenum in marine deposits. *Geochimica et Cosmochimica Acta*, *37*(6), 1415-1434.
Beulig, F., Roy, H., Glombitza, C., & Jorgensen, B. B. (2018). Control on rate and pathway of anaerobic organic carbon degradation in the seabed. *Proceedings of the National Academy of Sciences*, 201715789. https://doi.org/ https://doi.org/10.1073/pnas.1715789115
Beulig, F., Røy, H., McGlynn, S., & Jørgensen, B. (2019). Cryptic CH4 cycling in the sulfate–methane transition of marine sediments apparently mediated by ANME-1 archaea. *The ISME journal*, *13*(2), 250-262.
Beulig, F., Roy, H., McGlynn, S. E., & Jorgensen, B. B. (2018). Cryptic CH4 cycling in the sulfate-methane transition of marine sediments apparently mediated by ANME-1 archaea. *ISME J*, *296*(169), 10.1038.
Biksham, G., & Subramanian, V. (1988). Sediment transport of the Godavari River basin and its controlling factors. *Journal of Hydrology*, *101*(1-4), 275-290. https://doi.org/DOI:10.1016/0022-1694(88)90040-6
Blouet, J. P., Imbert, P., Ho, S., Wetzel, A., & Foubert, A. (2021). What makes seep carbonates ignore self-sealing and grow vertically: the role of burrowing decapod crustaceans. *Solid Earth*, *12*(10), 2439-2466. https://doi.org/10.5194/se-12-2439-2021
Boetius, A., Ravenschlag, K., Schubert, C. J., Rickert, D., Widdel, F., Giesecke, A., Amann, R., Jørgensen, B. B., Witte, U., Pfannkuche, O. (2000). A marine microbial consortium apparently

mediating anaerobic oxidation of methane. *Nature*, *407*, 623– 626. https://doi.org/doi:10.1038/35036572
Boetius, A., & Wenzhofer, F. (2013). Seafloor oxygen consumption fuelled by methane from cold seeps. *Nature Geoscience*, *6*(9), 725-734.
Bohrmann, G., Greinert, J., Suess, E., & Torres, M. (1998). Authigenic carbonates from the Cascadia subduction zone and their relation to gas hydrate stability. *Geology*, *26*(7), 647-650.
Bohrmann, G., Suess, E., Greinert, J., Teichert, B., & Naehr, T. (2002). Gas hydrate carbonates from Hydrate Ridge, Cascadia convergent margin: indicators of near-seafloor clathrate deposits. Proceedings of 4th International Conference of Gas Hydrates, Yokohama, Japan,
Boon, M., Rickard, W. D., Rohl, A. L., & Jones, F. (2020). Stabilization of aragonite: role of Mg2+ and other impurity ions. *Crystal growth & design*, *20*(8), 5006-5017.
Borowski, W., Paull, C., & Ussler III, W. (1996). Marine pore-water sulfate profiles indicate in situ methane flux from underlying gas hydrate. *Geology*, *24*(7), 655-658. https://doi.org/10.1130/0091-7613
Borowski, W. S., Paull, C. K., & Ussler III, W. (1999). Global and local variations of interstitial sulfate gradients in deep-water, continental margin sediments: Sensitivity to underlying methane and gas hydrates. *Marine Geology*, *159*(1-4), 131-154. https://doi.org/10.1016/S0025-3227(99)00004-3
Borowski, W. S., Rodriguez, N. M., Paull, C. K., & Ussler III, W. (2013). Are 34S-enriched authigenic sulfide minerals a proxy for elevated methane flux and gas hydrates in the geologic record? *Marine Petroleum Geology*, *43*, 381-395. https://doi.org/https://doi.org/10.1016/j.marpetgeo.2012.12.009
Bostick, B. C., Fendorf, S., & Helz, G. R. (2003). Differential adsorption of molybdate and tetrathiomolybdate on pyrite (FeS2). *Environmental Science Technology*, *37*(2), 285-291.
Bots, P., Benning, L. G., Rickaby, R., & Shaw, S. (2011). The role of SO4 in the switch from calcite to aragonite seas. *Geology*, *39*(4), 331-334.
Böttcher, M. E., & Thamdrup, B. (2001). Anaerobic sulfide oxidation and stable isotope fractionation associated with bacterial sulfur disproportionation in the presence of MnO2. *Geochimica et Cosmochimica Acta*, *65*(10), 1573-1581.
Bottrell, S. H., & Newton, R. J. (2006). Reconstruction of changes in global sulfur cycling from marine sulfate isotopes. *Earth-Science Reviews*, *75*(1-4), 59-83.
Bowles, M. W., Mogollon, J. M., Kasten, S., Zabel, M., & Hinrichs, K.-U. (2014). Global rates of marine sulfate reduction and implications for sub-sea-floor metabolic activities. *Science*, *344*(6186), 889-891. https://doi.org/10.1126/science.1249213
Braithwaite, A., & Smith, J. (2012). *Chromatographic methods*. Springer Science & Business Media.
Brassell, S., Lewis, C., De Leeuw, J., De Lange, F., & Damsté, J. (1986). Isoprenoid thiophenes: novel products of sediment diagenesis? *Nature*, *320*(6058), 160-162.
Bruchert, V. (2004). Physiological and ecological aspects of sulfur isotope fractionation during bacterial sulfate reduction. In Sulfur Biogeochemistry - Past and Present: GSA Special Paper; Amend, J., Edwards, K., Lyons, T., Eds., The Geological Society of America: Boulder, CO, 2004; Vol. 379, pp 1-16.
Brüchert, V. (1998). Early diagenesis of sulfur in estuarine sediments: The role of sedimentary humic and fulvic acids. *Geochimica et Cosmochimica Acta*, *62*(9), 1567-1586.
Brüchert, V., & Pratt, L. M. (1996). Contemporaneous early diagenetic formation of organic and inorganic sulfur in estuarine sediments from St. Andrew Bay, Florida, USA. *Geochimica et Cosmochimica Acta*, *60*(13), 2325-2332.
Buffett, B., & Archer, D. (2004). Global inventory of methane clathrate: sensitivity to changes in the deep ocean. *Earth and Planetary Science Letters*, *227*(3-4), 185-199.
Busenberg, E., & Plummer, L. N. (1985). Kinetic and thermodynamic factors controlling the distribution of SO32− and Na+ in calcites and selected aragonites. *Geochimica et Cosmochimica Acta*, *49*(3), 713-725.
Butler, I. B., Bottcher, M. E., Rickard, D., & Oldroyd, A. (2004). Sulfur isotope partitioning during experimental formation of pyrite via the polysulfide and hydrogen sulfide pathways:

implications for the interpretation of sedimentary and hydrothermal pyrite isotope records. *Earth and Planetary Science Letters*, *228*(3-4), 495-509.
Campbell, K. A. (2006). Hydrocarbon seep and hydrothermal vent paleoenvironments and paleontology: Past developments and future research directions. *Palaeogeography, Palaeoclimatology, Palaeoecology*, *232*(2-4), 362-407.
Canfield, D. (1989). Reactive iron in marine sediments. *Geochimica et Cosmochimica Acta*, *53*(3), 619-632.
Canfield, D., Kristensen, E., & Thamdrup, B. (2005). The sulfur cycle. *Advances in Marine Biology*, *48*, 313-381.
Canfield, D., Raiswell, R., & Bottrell, S. (1992). The reactivity of sedimentary iron minerals toward sulfide. *American Journal of Science*, *292*, 659-683.
Canfield, D., Raiswell, R., & Westrich, J. (1986). The use of chromium reduction in the analysis of reduced inorganic sulphur in sediments and shales. *Chemical Geology*, *54*, 149-155.
Canfield, D. E. (1989 b). Sulfate reduction and oxic respiration in marine sediments: implications for organic carbon preservation in euxinic environments. *Deep Sea Research Part A. Oceanographic Research Papers*, *36*(1), 121-138.
Canfield, D. E. (1994). Factors influencing organic carbon preservation in marine sediments. *Chemical Geology*, *114*(3-4), 315-329.
Canfield, D. E., Olesen, C. A. and Cox, R. P. (2006). Temperature and its control of isotope fractionation by a sulfate-reducing bacterium. *Geochemical Cosmochimica Acta*, *70*, 548-561.
Casagrande, D. J., Idowu, G., Friedman, A., Rickert, P., Siefert, K., & Schlenz, D. (1979). H2S incorporation in coal precursors: origins of organic sulphur in coal. *Nature*, *282*, 599-600.
Ceramicola, S., Dupre, S., Somoza, L., & Woodside, J. (2018). Cold seep systems. In *Submarine geomorphology* (pp. 367-387). Springer.
Chanton, J. P., & Martens, C. S. (1985). The effects of heat and stannous chloride addition on the active distillation of acid volatile sulfide from pyrite-rich marine sediment samples. *Biogeochemistry*, *1*(4), 375-382.
Chao, T. T. (1972). Selective dissolution of manganese oxides from soils and sediments with acidified hydroxylamine hydrochloride. *Soil Science Society of America Journal*, *36*(5), 764-768.
Chappaz, A., Lyons, T. W., Gregory, D. D., Reinhard, C. T., Gill, B. C., Li, C., & Large, R. R. (2014). Does pyrite act as an important host for molybdenum in modern and ancient euxinic sediments? *Geochimica et Cosmochimica Acta*, *126*, 112-122.
Chen, F., Hu, Y., Feng, D., Zhang, X., Cheng, S., Cao, J., Lu, H., & Chen, D. (2016). Evidence of intense methane seepages from molybdenum enrichments in gas hydrate-bearing sediments of the northern South China Sea. *Chemical Geology*, *443*, 173-181.
Chen, K., & Morris, J. (1972). Kinetics of oxidation of aqueous sulfide by oxygen. *Environmental Science & Technology*, *6*(6), 529-537.
Chen, S.-C., Li, X.-M., Battisti, N., Guan, G., Montoya, M. A., Osvatic, J., Pjevac, P., Pollak, S., Richter, A., & Schintlmeister, A. (2025). Microbial iron oxide respiration coupled to sulfide oxidation. *Nature*, 1-9.
Chen, Y., Zou, C., Mastalerz, M., Hu, S., Gasaway, C., & Tao, X. (2015). Applications of micro-fourier transform infrared spectroscopy (FTIR) in the geological sciences—a review. *International journal of molecular sciences*, *16*(12), 30223-30250.
Cheng, M., Li, C., Zhou, L., & Xie, S. (2015). Mo marine geochemistry and reconstruction of ancient ocean redox states. *Science China Earth Sciences*, *58*, 2123-2133.
Childress, J. J., & Girguis, P. R. (2011). The metabolic demands of endosymbiotic chemoautotrophic metabolism on host physiological capacities. *Journal of Experimental Biology*, *214*(2), 312-325.
Choudhuri, M., Guha, D., Dutta, A., Sinha, S., & Sinha, N. (2010). Spatiotemporal Variations and Kinematics of Shale Mobility in the Krishna-Godavari Basin, India. *Shale Tectonics: AAPG Memoir 93*, *93*(1), 91-109.
Choudhuri, M., Guha, D., Dutta, A., Sinha, S., & Sinha, N. (2011). Spatiotemporal Variations and Kinematics of Shale Mobility in the Krishna-Godavari Basin, India. *Shale Tectonics: AAPG Memoir 93*, *93*(1), 91-109.

Chuang, P.-C., Yang, T. F., Wallmann, K., Matsumoto, R., Hu, C.-Y., Chen, H.-W., Lin, S., Sun, C.-H., Li, H.-C., & Wang, Y. (2019). Carbon isotope exchange during anaerobic oxidation of methane (AOM) in sediments of the northeastern South China Sea. *Geochimica et Cosmochimica Acta*, *246*, 138-155.

Cline, J. D. (1969). Spectrophotometric determination of hydrogen sulfide in natural waters. *Limnology and Oceanography*, *14*(3), 454-458.

Collett, T., Riedel, M., Cochran, J. R., Boswell, R., Kumar, P., & Sathe, A. V. (2008). Indian continental margin gas hydrate prospects: results of the Indian National Gas Hydrate Program (NGHP) expedition 01.

Collier, R. W. (1985). Molybdenum in the northeast Pacific Ocean. *Limnology and Oceanography*, 1351-1354.

Compston, W., & Oversby, V. M. (1969). Lead isotopic analysis using a double spike. *Journal of Geophysical Research*, *74*(17), 4338-4348.

Cordes, E. E., Hourdez, S., & Roberts, H. H. (2010). Unusual habitats and organisms associated with the cold seeps of the Gulf of Mexico. *The Vent Seep Biota: Aspects from Microbes to Ecosystems*, 315-331.

Coskun, O. (2016). Separation techniques: chromatography. *Northern clinics of Istanbul*, *3*(2), 156.

Creech, J. B., & Paul, B. (2015). IsoSpike: Improved double‐spike inversion software. *Geostandards and Geoanalytical Research*, *39*(1), 7-15.

Cremiere, A., Bayon, G., Ponzevera, E., & Pierre, C. (2013). Paleo-environmental controls on cold seep carbonate authigenesis in the Sea of Marmara. *Earth and Planetary Science Letters*, *376*, 200-211.

Crémière, A., Lepland, A., Chand, S., Sahy, D., Condon, D. J., Noble, S. R., Martma, T., Thorsnes, T., Sauer, S., & Brunstad, H. (2016). Timescales of methane seepage on the Norwegian margin following collapse of the Scandinavian Ice Sheet. *Nature communications*, *7*(1), 11509.

Crémière, A., Lepland, A., Chand, S., Sahy, D., Kirsimäe, K., Bau, M., Whitehouse, M. J., Noble, S. R., Martma, T., & Thorsnes, T. (2016). Fluid source and methane-related diagenetic processes recorded in cold seep carbonates from the Alvheim channel, central North Sea. *Chemical Geology*, *432*, 16-33.

Cremiere, A., Strauss, H., Sebilo, M., Hong, W.-L., Gros, O., Schmidt, S., Tocny, J., Henry, F. o., Gontharet, S., & Laverman, A. M. (2017). Sulfur diagenesis under rapid accumulation of organic-rich sediments in a marine mangrove from Guadeloupe (French West Indies). *Chemical Geology*, *454*, 67-79.

Cuesta Mayorga, I., Astilleros, J. M., & Fernández-Díaz, L. (2019). Precipitation of CaCO3 polymorphs from aqueous solutions: The role of pH and sulphate groups. *Minerals*, *9*(3), 178.

Cypionka, H. (1995). Solute transport and cell energetics. *Sulfate-reducing bacteria*, *8*, 151–184.

Dahl, T. W., Anbar, A. D., Gordon, G. W., Rosing, M. T., Frei, R., & Canfield, D. E. (2010). The behavior of molybdenum and its isotopes across the chemocline and in the sediments of sulfidic Lake Cadagno, Switzerland. *Geochimica et Cosmochimica Acta*, *74*(1), 144-163.

Dahl, T. W., Chappaz, A., Fitts, J. P., & Lyons, T. W. (2013). Molybdenum reduction in a sulfidic lake: Evidence from X-ray absorption fine-structure spectroscopy and implications for the Mo paleoproxy. *Geochimica et Cosmochimica Acta*, *103*, 213-231.

De Choudens-Sanchez, V., & Gonzalez, L. A. (2009). Calcite and aragonite precipitation under controlled instantaneous supersaturation: elucidating the role of CaCO3 saturation state and Mg/Ca ratio on calcium carbonate polymorphism. *Journal of Sedimentary Research*, *79*(6), 363-376.

Deng, Y., Ren, J., Guo, Q., Cao, J., Wang, H., & Liu, C. (2017). Rare earth element geochemistry characteristics of seawater and porewater from deep sea in western Pacific. *Scientific Reports*, *7*(1), 16539.

Dewangan, P., Ramprasad, T., Ramana, M., Mazumdar, A., Desa, M., & Badesab, F. (2010). Seabed Morphology and Gas Venting Features in the Continental Slope Region of Krishna-Godavari Basin, Bay of Bengal: Implications in Gas-Hydrate Exploration. *Marine and Petroleum Geology*, *27*, 1628-1641.

Dewangan, P., Sriram, G., Kumar, A., Mazumdar, A., Peketi, A., Mahale, V., Reddy, S. S. C., & Babu, A. (2021). Widespread occurrence of methane seeps in deep-water regions of Krishna-Godavari basin, Bay of Bengal. *Marine and Petroleum Geology*, *124*, 104783. https://doi.org/https://doi.org/10.1016/j.marpetgeo.2020.104783

Dewangan, P., Sriram, G., Ramprasad, T., Ramana, M., & Jaiswal, P. (2011). Fault system and thermal regime in the vicinity of site NGHP-01-10, Krishna-Godavari basin, Bay of Bengal. *Marine and Petroleum Geology*, 1899-1914.

DFO. (2018). Assessment of Canadian Pacific Cold Seeps against Criteria for Determining Ecologically and Biologically Significant Areas. InDFO Canadian Science Advisory Secretariat Science 2018/002.

Dickens, G. (2001). Sulfate profiles and barium fronts in sediment on the Blake Ridge: Present and past methane fluxes through a large gas hydrate reservoir. *Geochimica et Cosmochimica Acta*, *65*(4), 529-543.

Dickson, A. J., Idiz, E., Porcelli, D., & van den Boorn, S. H. (2020). The influence of thermal maturity on the stable isotope compositions and concentrations of molybdenum, zinc and cadmium in organic-rich marine mudrocks. *Geochimica et Cosmochimica Acta*, *287*, 205-220.

Dinur, D., Spiro, B., & Aizenshtat, Z. (1981). The distribution and isotopic composition of sulfur in organic-rich sedimentary rocks. *Chemical Geology*, *31*, 37-51.

Dodson, M. (1963). A theoretical study of the use of internal standards for precise isotopic analysis by the surface ionization technique: Part I-General first-order algebraic solutions. *Journal of Scientific Instruments*, *40*(6), 289.

Dodson, M. H. (1970). Simplified equations for double-spiked isotopic analyses. *Geochimica et Cosmochimica Acta*, *34*(11), 1241-1244.

Donahue, M. A., Werne, J. P., Meile, C., & Lyons, T. W. (2008). Modeling sulfur isotope fractionation and differential diffusion during sulfate reduction in sediments of the Cariaco Basin. *Geochimica et Cosmochimica Acta*, *72*(9), 2287-2297.

Drobner, E., Huber, H., Wächtershäuser, G., Rose, D., & Stetter, K. (1990). Pyrite formation linked with hydrogen evolution under anaerobic conditions. *Nature*, *346*, 742-744.

Dufour, S. C., & Felbeck, H. (2003). Sulphide mining by the superextensile foot of symbiotic thyasirid bivalves. *Nature*, *426*(6962), 65-67.

Eckert, T., Brunner, B., Edwards, E. A., & Wortmann, U. G. (2011). Microbially mediated re-oxidation of sulfide during dissimilatory sulfate reduction by< i> Desulfobacter latus</i>. *Geochimica et Cosmochimica Acta*, *75*(12), 3469-3485.

Eilertsen, M. H., Georgieva, M. N., Kongsrud, J. A., Linse, K., Wiklund, H., Glover, A. G., & Rapp, H. T. (2018). Genetic connectivity from the Arctic to the Antarctic: Sclerolinum contortum and Nicomache lokii (Annelida) are both widespread in reducing environments. *Scientific Reports*, *8*(1), 1-12.

Elderfield, H., & Sholkovitz, E. R. t. (1987). Rare earth elements in the pore waters of reducing nearshore sediments. *Earth and Planetary Science Letters*, *82*(3-4), 280-288.

Erickson, B. E., & Helz, G. R. (2000). Molybdenum (VI) speciation in sulfidic waters:: stability and lability of thiomolybdates. *Geochimica et Cosmochimica Acta*, *64*(7), 1149-1158.

Eroglu, S., Scholz, F., Frank, M., & Siebert, C. (2020). Influence of particulate versus diffusive molybdenum supply mechanisms on the molybdenum isotope composition of continental margin sediments. *Geochimica et Cosmochimica Acta*, *273*, 51-69.

Eroglu, S., Scholz, F., Salvatteci, R., Siebert, C., Schneider, R., & Frank, M. (2021). The impact of postdepositional alteration on iron-and molybdenum-based redox proxies. *Geology*, *49*(12), 1411-1415.

Eymold, W. K., Frederick, J. M., Nole, M., Phrampus, B. J., & Wood, W. T. (2021). Prediction of gas hydrate formation at Blake Ridge using machine learning and probabilistic reservoir simulation. *Geochemistry, Geophysics, Geosystems*, *22*(4), e2020GC009574.

Feng, D., Qiu, J.-W., Hu, Y., Peckmann, J. r., Guan, H., Tong, H., Chen, C., Chen, J., Gong, S., & Li, N. (2018). Cold seep systems in the South China Sea: An overview. *Journal of Asian Earth Sciences*, *168*, 3-16.

Feng, J., Li, N., Luo, M., Liang, J., Yang, S., Wang, H., & Chen, D. (2020). A quantitative assessment of methane-derived carbon cycling at the cold seeps in the Northwestern South China Sea. *Minerals*, *10*(3), 256.

Feng, J., Yang, S., Liang, J., Fang, Y., He, Y., Luo, M., & Chen, D. (2018). Methane seepage inferred from the porewater geochemistry of shallow sediments in the Beikang Basin of the southern South China Sea. *Journal of Asian Earth Sciences*.

Fernandes, S., Mazumdar, A., Peketi, A., Anand, S. S., Rengarajan, R., Jose, A., Manaskanya, A., Carvalho, M. A., & Shetty, D. (2020). Sulfidization processes in seasonally hypoxic shelf sediments: a study off the West coast of India. *Marine and Petroleum Geology*, *117*, 104353.

Fernández-Díaz, L., Fernández-González, Á., & Prieto, M. (2010). The role of sulfate groups in controlling CaCO3 polymorphism. *Geochimica et Cosmochimica Acta*, *74*(21), 6064-6076.

Findlay, A. J., Boyko, V., Pellerin, A., Avetisyan, K., Guo, Q., Yang, X., & Kamyshny Jr, A. (2019). Sulfide oxidation affects the preservation of sulfur isotope signals. *Geology*, *47*(8), 739-743.

Findlay, A. J., Pellerin, A., Laufer, K., & Jørgensen, B. B. (2020). Quantification of sulphide oxidation rates in marine sediment. *Geochimica et Cosmochimica Acta*, *280*, 441-452.

Finster, K. (2008). Microbiological disproportionation of inorganic sulfur compounds. *Journal of Sulfur Chemistry*, *29*(3-4), 281-292.

Fischer, D., Mogollón, J. M., Strasser, M., Pape, T., Bohrmann, G., Fekete, N., Spiess, V., & Kasten, S. (2013). Subduction zone earthquake as potential trigger of submarine hydrocarbon seepage. *Nature Geoscience*, *6*(8), 647-651.

Formolo, M. J., Lyons, T. W., Zhang, C., Kelley, C., Sassen, R., Horita, J., & Cole, D. R. (2004). Quantifying carbon sources in the formation of authigenic carbonates at gas hydrate sites in the Gulf of Mexico. *Chemical Geology*, *205*(3-4), 253-264.

Forsberg, C., Solheim, A., Kvalstad, T., Vaidya, R., & Mohanty, S. (2007). Slope instability and mass transport deposits on the Godavari River Delta, east Indian margin from a regional geological perspective.

Fossing, H., & Jørgensen, B. (1990 a). Oxidation and reduction of radiolabeled inorganic sulfur compounds in an estuarine sediment, Kysing Fjord, Denmark. *Geochimica et Cosmochimica Acta*, *54*(10), 2731-2742.

Foucher, J.-P., WestbrooK, G. K., BoEtius, A., CeramicoLa, S., Dupre, S., Mascle, J., Mienert, J., Pfannkuche, O., Pierre, C., & Praeg, D. (2009). Structure and drivers of cold seep ecosystems. *Oceanography*, *22*(1), 92-109.

Francois, R. (1987). A study of sulphur enrichment in the humic fraction of marine sediments during early diagenesis. *Geochimica et Cosmochimica Acta*, *51*(1), 17-27.

Furukawa, Y., & Barnes, H. (1995). Reactions forming pyrite from precipitated amorphous ferrous sulfide.

Galer, S. J. G. (1999). Optimal double and triple spiking for high precision lead isotopic measurement. *Chemical Geology*, *157*(3), 255-274.

Galimov, E. (2006). Isotope organic geochemistry. *Organic Geochemistry*, *37*(10), 1200-1262.

Gao, Y., Wang, Y., Lee, H.-S., & Jin, P. (2022). Significance of anaerobic oxidation of methane (AOM) in mitigating methane emission from major natural and anthropogenic sources: a review of AOM rates in recent publications. *Environmental Science: Advances*, *1*(4), 401-425.

Goetschl, K. E., Purgstaller, B., Dietzel, M., & Mavromatis, V. (2019). Effect of sulfate on magnesium incorporation in low-magnesium calcite. *Geochimica et Cosmochimica Acta*, *265*, 505-519.

Goldberg, T., Archer, C., Vance, D., & Poulton, S. W. (2009). Mo isotope fractionation during adsorption to Fe (oxyhydr) oxides. *Geochimica et Cosmochimica Acta*, *73*(21), 6502-6516.

Goldberg, T., G. Gordon, G. Izon, C. Archer, C. R. Pearce, J. McManus, & Rehkamper, A. D. A. a. M. (2013). Resolution of inter-laboratory discrepancies in Mo

isotope data: an intercalibration. *J. Anal. At. Spectrom*, *28*, 724.

Goldhaber, M., & Kaplan, I. (1975). Controls and consequences of sulfate reduction rates in recent marine sediments. *Soil Science*, *119*(1), 42-55.

Goldsmith, J. R., Graf, D. L., & Heard, H. C. (1961). Lattice constants of the calcium magnesium carbonates. In: Mineralogical Society of America.

Gong, S., Hu, Y., Li, N., Feng, D., Liang, Q., Tong, H., Peng, Y., Tao, J., & Chen, D. (2018). Environmental controls on sulfur isotopic compositions of sulfide minerals in seep carbonates from the South China Sea. *Journal of Asian Earth Sciences*, *168*, 96-105.

Gontharet, S., Pierre, C., Blanc-Valleron, M. M., Rouchy, J.-M., Fouquet, Y., Bayon, G., Foucher, J.-P., Woodside, J., Mascle, J., & Party, T. N. S. (2007). Nature and origin of diagenetic carbonate crusts and concretions from mud volcanoes and pockmarks of the Nile deep-sea fan (eastern Mediterranean Sea). *Deep Sea Research Part II: Topical Studies in Oceanography*, *54*(11-13), 1292-1311.

Goto, S., Matsubayashi, O., & Nagakubo, S. (2016). Simulation of gas hydrate dissociation caused by repeated tectonic uplift events. *Journal of Geophysical Research: Solid Earth*, *121*(5), 3200-3219.

Graves, C. A., James, R. H., Sapart, C. J., Stott, A. W., Wright, I. C., Berndt, C., Westbrook, G. K., & Connelly, D. P. (2017). Methane in shallow subsurface sediments at the landward limit of the gas hydrate stability zone offshore western Svalbard. *Geochimica et Cosmochimica Acta*, *198*, 419-438.

Greinert, J., Bohrmann, G., & Suess, E. (2001). Gas hydrate-associated carbonates and methane-venting at Hydrate Ridge: classification, distribution and origin of authigenic lithologies. *GEOPHYSICAL MONOGRAPH-AMERICAN GEOPHYSICAL UNION*, *124*, 99-114.

Grossman, E. L., & Ku, T. L. (1986). Oxygen and carbon isotope fractionation in biogenic aragonite: temperature effects. *Chemical Geology: Isotope Geoscience Section*, *59*, 59-74.

Habicht, K., Canfield, D., & Rethmeier, J. (1998). Sulfur isotope fractionation during bacterial reduction and disproportionation of thiosulfate and sulfite. *Geochimica et Cosmochimica Acta*, *62*(15), 2585-2595.

Haley, B. A., Klinkhammer, G. P., & McManus, J. (2004). Rare earth elements in pore waters of marine sediments. *Geochimica et Cosmochimica Acta*, *68*(6), 1265-1279.

Hardy, R., & Tucker, M. (1988). X-ray powder diffraction of sediments. *Techniques in Sedimentology*, 191-228.

Helz, G., Miller, C., Charnock, J., Mosselmans, J., Pattrick, R., Garner, C., & Vaughan, D. (1996). Mechanism of molybdenum removal from the sea and its concentration in black shales: EXAFS evidence. *Geochimica et Cosmochimica Acta*, *60*(19), 3631-3642.

Helz, G. R., & Vorlicek, T. P. (2019). Precipitation of molybdenum from euxinic waters and the role of organic matter. *Chemical Geology*, *509*, 178-193.

Hensen, C., Zabel, M., Pfeifer, K., Schwenk, T., Kasten, S., Riedinger, N., Schulz, H., & Boetius, A. (2003). Control of sulfate pore-water profiles by sedimentary events and the significance of anaerobic oxidation of methane for the burial of sulfur in marine sediments. *Geochimica et Cosmochimica Acta*, *67*(14), 2631-2647.

Hesse, R., & Harrison, W. E. (1981). Gas hydrates (clathrates) causing pore-water freshening and oxygen isotope fractionation in deep-water sedimentary sections of terrigenous continental margins. *Earth and Planetary Science Letters*, *55*(3), 453-462.

Himmler, T., Bach, W., Bohrmann, G., & Peckmann, J. (2010). Rare earth elements in authigenic methane-seep carbonates as tracers for fluid composition during early diagenesis. *Chemical Geology*, *277*(1-2), 126-136.

Himmler, T., Haley, B. A., Torres, M. E., Klinkhammer, G. P., Bohrmann, G., & Peckmann, J. (2013). Rare earth element geochemistry in cold-seep pore waters of Hydrate Ridge, northeast Pacific Ocean. *Geo-Marine Letters*, *33*, 369-379.

Hinrichs, K.-U., & Boetius, A. (2002). The anaerobic oxidation of methane: new insights in microbial ecology and biogeochemistry. *Ocean margin systems*, 457-477.

Hinrichs, K. U., Hayes, J. M., Sylva, S. P., Brewer, P. G., & DeLong, E. F. (1999). Methane-consuming archaebacteria in marine sediments. *Nature*, *398*(6730), 802-805.

Hlohowskyj, S. R., Chappaz, Anthony, Dickson, Alexander J. (2021). *Molybdenum as a Paleoredox Proxy: Past, Present, and Future*. Cambridge University Press.

Hoehler, T., Alperin, M., Albert, D., & Martens, C. (1994). Field and laboratory studies of methane oxidation in an anoxic marine sediment: evidence for a methanogen-sulfate reducer consortium. *Global Biogeochemical Cycles*, *8*(4), 451-463.

Hofmann, A. (1971). Fractionation corrections for mixed-isotope spikes of Sr, K, and Pb. *Earth and Planetary Science Letters*, *10*(4), 397-402.

Hong, W.-L., Torres, M. E., Carroll, J., Cremiere, A., Panieri, G., Yao, H., & Serov, P. (2017). Seepage from an arctic shallow marine gas hydrate reservoir is insensitive to momentary ocean warming. *Nature communications*, *8*(1), 1-14.

Hong, W.-L., Torres, M. E., Kim, J.-H., Choi, J., & Bahk, J.-J. (2013). Carbon cycling within the sulfate-methane-transition-zone in marine sediments from the Ulleung Basin. *Biogeochemistry*, *115*(1-3), 129-148.

Hong, W.-L., Torres, M. E., Kim, J.-H., Choi, J., & Bahk, J.-J. (2014). Towards quantifying the reaction network around the sulfate-methane-transition-zone in the Ulleung Basin, East Sea, with a kinetic modeling approach. *Geochimica et Cosmochimica Acta*, *140*, 127-141.

Hu, C. Y., Yang, T. F., Burr, G. S., Chuang, P.-C., Chen, H.-W., Walia, M., Chen, N.-C., Huang, Y.-C., Lin, S., & Wang, Y. (2017). Biogeochemical cycles at the sulfate-methane transition zone (SMTZ) and geochemical characteristics of the pore fluids offshore southwestern Taiwan. *Journal of Asian Earth Sciences*, *149*, 172-183.

Hu, Y., Chen, L., Feng, D., Liang, Q., Xia, Z., & Chen, D. (2017). Geochemical record of methane seepage in authigenic carbonates and surrounding host sediments: A case study from the South China Sea. *Journal of Asian Earth Sciences*, *138*, 51-61.

Hu, Y., Feng, D., Liang, Q., Xia, Z., Chen, L., & Chen, D. (2015). Impact of anaerobic oxidation of methane on the geochemical cycle of redox-sensitive elements at cold-seep sites of the northern South China Sea. *Deep Sea Research Part II: Topical Studies in Oceanography*, *122*, 84-94. https://doi.org/http://dx.doi.org/10.1016/j.dsr2.2015.06.012

Hu, Y., Feng, D., Peckmann, J. r., Roberts, H. H., & Chen, D. (2014). New insights into cerium anomalies and mechanisms of trace metal enrichment in authigenic carbonate from hydrocarbon seeps. *Chemical Geology*, *381*, 55-66.

Huerta-Diaz, M. A., & Morse, J. W. (1990). A quantitative method for determination of trace metal concentrations in sedimentary pyrite. *Marine Chemistry*, *29*, 119-144.

Jiang, Q., Jing, H., Liu, H., & Du, M. (2022). Biogeographic distributions of microbial communities associated with anaerobic methane oxidation in the surface sediments of deep-sea cold seeps in the South China Sea. *Frontiers in Microbiology*, *13*, 1060206.

Jin, M., Chen, F., Li, N., Peckmann, J., Mathur, R., Godfrey, L., & Chen, D. (2024). Isotope evidence for the enrichment mechanism of molybdenum in methane-seep sediments: Implications for past seepage intensity. *Geochimica et Cosmochimica Acta*, *373*, 282-291.

Jin, M., Feng, D., Huang, K., Peckmann, J. r., Li, N., Huang, H., Liang, Q., & Chen, D. (2021). Behavior of Mg isotopes during precipitation of methane-derived carbonate: Evidence from tubular seep carbonates from the South China Sea. *Chemical Geology*, *567*, 120101.

Johnson, C. M., & Beard, B. L. (1999). Correction of instrumentally produced mass fractionation during isotopic analysis of Fe by thermal ionization mass spectrometry. *International Journal of Mass Spectrometry*, *193*(1), 87-99.

Jorgensen, B. (1979). A theoretical model of the stable sulfur isotope distribution in marine sediments. *Geochimica et Cosmochimica Acta*, *43*(3), 363-374.

Jørgensen, B. (1982). Mineralization of organic matter in the sea bed—the role of sulphate reduction. *Nature*, 643-645.

Jorgensen, B., Böttcher, M., Lüschen, H., Neretin, L., & Volkov, I. (2004). Anaerobic methane oxidation and a deep H2S sink generate isotopically heavy sulfides in Black Sea sediments. *Geochimica et Cosmochimica Acta*, *68*(9), 2095-2118.

Jørgensen, B., & Kasten, S. (2006). Sulfur cycling and methane oxidation. In *Marine geochemistry* (pp. 271-309). Springer.

Jørgensen, B. B. (2021). Sulfur biogeochemical cycle of marine sediments. *Geochemical Perspectives*, *10*(2), 145-146.

Jørgensen, B. B., Böttcher, M. E., Lüschen, H., Neretin, L. N., & Volkov, I. I. (2004). Anaerobic methane oxidation and a deep H2S sink generate isotopically heavy sulfides in Black Sea sediments. *Geochimica et Cosmochimica Acta*, *68*(9), 2095-2118. https://doi.org/doi:10.1016/j.gca.2003.07.017

Jorgensen, B. B., Findlay, A. J., & Pellerin, A. (2019). The Biogeochemical Sulfur Cycle of Marine Sediments. *Frontiers in Microbiology*, *10*.

Joseph, C., Campbell, K. A., Torres, M. E., Martin, R. A., Pohlman, J. W., Riedel, M., & Rose, K. (2013). Methane-derived authigenic carbonates from modern and paleoseeps on the Cascadia margin: Mechanisms of formation and diagenetic signals. *Palaeogeography, Palaeoclimatology, Palaeoecology*, *390*, 52-67.

Joshi, R. K., Mazumdar, A., Peketi, A., Ramamurty, P. B., Naik, B. G., Kocherla, M., Carvalho, M. A., Mahalakshmi, P., Dewangan, P., & Ramana, M. V. (2014). Gas hydrate destabilization and methane release events in the Krishna-Godavari Basin, Bay of Bengal. *Marine and Petroleum Geology*, *58*, 476-489.

Judd, A., & Hovland, M. (2009). *Seabed fluid flow: the impact on geology, biology and the marine environment*. Cambridge University Press.

Kashiwabara, T., Takahashi, Y., & Tanimizu, M. (2009). A XAFS study on the mechanism of isotopic fractionation of molybdenum during its adsorption on ferromanganese oxides. *Geochemical Journal*, *43*(6), e31-e36.

Kashiwabara, T., Takahashi, Y., Tanimizu, M., & Usui, A. (2011). Molecular-scale mechanisms of distribution and isotopic fractionation of molybdenum between seawater and ferromanganese oxides. *Geochimica et Cosmochimica Acta*, *75*(19), 5762-5784.

Kasten, S., & Jørgensen, B. B. (2000). Sulfate reduction in marine sediments. *In: HD Schulz, M. Zabel (eds.) Marine Geochemistry. Heidelberg; Springer*, 263-282.

Kendall, B., Dahl, T. W., & Anbar, A. D. (2017). The stable isotope geochemistry of molybdenum. *Reviews in Mineralogy Geochemistry*, *82*(1), 683-732.

Kim, J.-H., Torres, M. E., Haley, B. A., Kastner, M., Pohlman, J. W., Riedel, M., & Lee, Y.-J. (2012). The effect of diagenesis and fluid migration on rare earth element distribution in pore fluids of the northern Cascadia accretionary margin. *Chemical Geology*, *291*, 152-165.

Kim, S. T., & O'Neil, J. R. (1997). Equilibrium and nonequilibrium oxygen isotope effects in synthetic carbonates. *Geochimica et Cosmochimica Acta*, *61*(16), 3461-3475.

Klaver, M., & Coath, C. D. (2019). Obtaining accurate isotopic compositions with the double spike technique: Practical considerations. *Geostandards and Geoanalytical Research*, *43*(1), 5-22.

Knittel, K., & Boetius, A. (2009). Anaerobic oxidation of methane: progress with an unknown process. *Annual review of microbiology*, *63*, 311-334.

Knittel, K., & Boetius, A. (2010). Anaerobic methane oxidizers. *Handbook of Hydrocarbon and Lipid Microbiology, edited by: Timmis, KN*, 4699.

Knittel, K., Losekann, T., Boetius, A., Kort, R., & Amann, R. (2005). Diversity and distribution of methanotrophic archaea at cold seeps. *Applied and Environmental Microbiology*, *71*(1), 467.

Kohnen, M. E. L., Sinnighe-Damsté, J. S.; ten Haven, & H. L.; de Leeuw, J. W. (1989). Early incorporation of polysulfides in sedimentary organic matter. *Nature*, *341*, 640-641.

Komada, T., Burdige, D. J., Li, H.-L., Magen, C., Chanton, J. P., & Cada, A. K. (2016). Organic matter cycling across the sulfate-methane transition zone of the Santa Barbara Basin, California Borderland. *Geochimica et Cosmochimica Acta*, *176*, 259-278.

Kontrec, J., Kralj, D., Brečević, L., Falini, G., Fermani, S., Noethig‐Laslo, V., & Mirosavljević, K. (2004). Incorporation of inorganic anions in calcite. *European Journal of Inorganic Chemistry*, *2004*(23), 4579-4585.

Krause, S., Steeb, P., Hensen, C., Liebetrau, V., Dale, A. W., Nuzzo, M., & Treude, T. (2014). Microbial activity and carbonate isotope signatures as a tool for identification of spatial differences in methane advection: a case study at the Pacific Costa Rican margin. *Biogeosciences*, *11*(2), 507-523.

Kravchishina, M. D., Lein, A. Y., Flint, M. V., Baranov, B. V., Miroshnikov, A. Y., Dubinina, E. O., Dara, O. M., Boev, A. G., & Savvichev, A. S. (2021). Methane-derived authigenic carbonates on the seafloor of the Laptev Sea shelf. *Frontiers in Marine Science*, *8*, 690304.

Krishna, K. S., Ismaiel, M., Srinivas, K., Gopala Rao, D., Mishra, J., & Saha, D. (2016). Sediment pathways and emergence of Himalayan source material in the Bay of Bengal. *Current Science*, *110*(3), 363-372.

Kristensen, E. (2000). Organic matter diagenesis at the oxic/anoxic interface in coastal marine sediments, with emphasis on the role of burrowing animals. *Hydrobiologia*, *426*(1), 1-24.
Kumar, R., Singh, R., & Sharma, K. (2005). Water resources of India. *Current Science*, *89*(5), 794-811.
Kvenvolden, K. (1993). Gas hydrates—geological perspective and global change. *Rev. Geophys*, *31*(2), 173–187.
Kvenvolden, K. A., & Rogers, B. W. (2005). Gaia's breath—global methane exhalations. *Marine and Petroleum Geology*, *22*(4), 579-590.
Lapham, L. L., Lloyd, K. G., Fossing, H., Flury, S., Jensen, J. B., Alperin, M. J., Rehder, G., Holzhueter, W., Ferdelman, T., & Jørgensen, B. B. (2024). Methane leakage through the sulfate–methane transition zone of the Baltic seabed. *Nature Geoscience*, *17*(12), 1277-1283.
Lawal, M. A., Bialik, O. M., Lazar, M., Waldmann, N. D., Foubert, A., & Makovsky, Y. (2023). Modes of gas migration and seepage on the salt-rooted Palmahim Disturbance, southeastern Mediterranean. *Marine and Petroleum Geology*, *153*, 106256.
Le Bris, N., Arnaud-Haond, S., Beaulieu, S., Cordes, E., Hilario, A., Rogers, A., van de Gaever, S., & Watanabe, H. (2016). Hydrothermal vents and cold seeps. *UN Ed.) First Global Integrated Marine Assessment*, *18*.
Leventhal, J., & Taylor, C. (1990). Comparison of methods to determine degree of pyritization. *Geochimica et Cosmochimica Acta*, *54*(9), 2621-2625.
Levin, L. A. (2005). Ecology of cold seep sediments: interactions of fauna with flow, chemistry and microbes. In *Oceanography and marine biology* (pp. 11-56). CRC Press.
Levin, L. A., Baco, A. R., Bowden, D. A., Colaco, A., Cordes, E. E., Cunha, M. R., Demopoulos, A. W. J., Gobin, J., Grupe, B. M., & Le, J. (2016). Hydrothermal vents and methane seeps: rethinking the sphere of influence. *Frontiers in Marine Science*, *3*, 72.
Li, C., Chen, H., Bettencourt, R., Feng, D., Jing, H., Qiu, J.-W., Sun, J., & Wang, Y. (2023). *Deep-sea chemosynthetic ecosystems: Living in extreme environments* (Vol. 10).
Li, J., Peng, X., Bai, S., Chen, Z., & Van Nostrand, J. D. (2018). Biogeochemical processes controlling authigenic carbonate formation within the sediment column from the Okinawa Trough. *Geochimica et Cosmochimica Acta*, *222*, 363-382.
Li, J., Zhu, X. k., Tang, S. h., & Zhang, K. (2016). High‐precision measurement of molybdenum isotopic compositions of selected geochemical reference materials. *Geostandards Geoanalytical Research*, *40*(3), 405-415.
Li, N., Feng, D., Chen, L., Wang, H., & Chen, D. (2016). Using sediment geochemistry to infer temporal variation of methane flux at a cold seep in the South China Sea. *Marine Petroleum Geology*, *77*, 835-845.
Liang, Q., Huang, H., Sun, Y., Gong, S., Wang, X., Xiao, X., Dong, Y., Feng, J., & Feng, D. (2022). New insights into the archives of redox conditions in seep carbonates from the northern South China Sea. *Frontiers in Marine Science*, *9*, 945908.
Lim, Y. C., Lin, S., Yang, T. F., Chen, Y. G., & Liu, C. S. (2011). Variations of methane induced pyrite formation in the accretionary wedge sediments offshore southwestern Taiwan. *Marine and Petroleum Geology*.
Lin, Q., Wang, J., Taladay, K., Lu, H., Hu, G., Sun, F., & Lin, R. (2016). Coupled pyrite concentration and sulfur isotopic insight into the paleo sulfate-methane transition zone (SMTZ) in the northern South China Sea. *Journal of Asian Earth Sciences*, *115*, 547-556.
Lin, Z., Sun, X., Lu, Y., Strauss, H., Xu, L., Gong, J., Teichert, B. M. A., Lu, R., Lu, H., & Sun, W. (2016). The enrichment of heavy iron isotopes in authigenic pyrite as a possible indicator of sulfate-driven anaerobic oxidation of methane: Insights from the South China Sea. *Chemical Geology*.
Lin, Z., Sun, X., Peckmann, J., Lu, Y., Xu, L., Strauss, H., Zhou, H., Gong, J., Lu, H., & Teichert, B. M. A. (2016). How sulfate-driven anaerobic oxidation of methane affects the sulfur isotopic composition of pyrite: A SIMS study from the South China Sea. *Chemical Geology*, *440*, 26-41.
Lin, Z., Sun, X., Strauss, H., Eroglu, S., Bottcher, M. E., Lu, Y., Liang, J., Li, J., & Peckmann, J. (2021). Molybdenum isotope composition of seep carbonates-Constraints on sediment biogeochemistry in seepage environments. *Geochimica et Cosmochimica Acta*.

Liu, L. (2025). Formation mechanisms of pyrite in Earth's diverse geological systems. *Earth-Science Reviews*, 105234.

Liu, W., Wu, Z., Xu, S., Wei, J., Peng, X., Li, J., & Wang, Y. (2020). Pore-water dissolved inorganic carbon sources and cycling in the shallow sediments of the Haima cold seeps, South China Sea. *Journal of Asian Earth Sciences*, *201*, 104495.

Lu, Y., Sun, X., Xu, H., KoniSHi, H., Lin, Z., Xu, L., CHen, T., Hao, X., Lu, H., & PeCKmann, J. (2018). Formation of dolomite catalyzed by sulfate-driven anaerobic oxidation of methane: Mineralogical and geochemical evidence from the northern South China Sea. *American Mineralogist*, *103*(5), 720-734.

LÜ, Z., Liu, C., Liu, J., & Zhao, Z. (2003). Carbon, oxygen and boron isotopic studies of Huangbai-shuwan witherite deposit at Ziyang and Wenyuhe witherite deposit at Zhushan. *Science in China Series D: Earth Sciences*, *46*, 1273-1291.

Lu, Z., Zhu, J.-M., Tan, D., Johnson, T. M., & Wang, X. (2023). Double spike-standard addition technique and its application in measuring isotopes. *Analytical Chemistry*, *95*(4), 2253-2259.

Luff, R., & Wallmann, K. (2003). Fluid flow, methane fluxes, carbonate precipitation and biogeochemical turnover in gas hydrate-bearing sediments at Hydrate Ridge, Cascadia Margin: numerical modeling and mass balances. *Geochimica et Cosmochimica Acta*, *67*(18), 3403-3421.

Luff, R., Wallmann, K., & Aloisi, G. (2004). Numerical modeling of carbonate crust formation at cold vent sites: significance for fluid and methane budgets and chemosynthetic biological communities. *Earth and Planetary Science Letters*, *221*(1), 337-353.

Luo, Y.-R., & Byrne, R. H. (2004). Carbonate complexation of yttrium and the rare earth elements in natural waters. *Geochimica et Cosmochimica Acta*, *68*(4), 691-699.

Luther III, G. (1991). Pyrite synthesis via polysulfide compounds. *Geochimica et Cosmochimica Acta*, *55*(10), 2839-2849.

Madigan, M., Martinko, J., & Parker, J. (2000). *Biology of Microorganisms*.

Magalhães, V. H., Pinheiro, L. M., Ivanov, M. K., Kozlova, E., Blinova, V., Kolganova, J., Vasconcelos, C., McKenzie, J. A., Bernasconi, S. M., & Kopf, A. J. (2012). Formation processes of methane-derived authigenic carbonates from the Gulf of Cadiz. *Sedimentary Geology*, *243*, 155-168.

Malinverno, A., & Pohlman, J. W. (2011). Modeling sulfate reduction in methane hydrate-bearing continental margin sediments: Does a sulfate-methane transition require anaerobic oxidation of methane? *Geochemistry Geophysics Geosystems*, *12*(7), Q07006.

Mandal, R., Dewangan, P., Ramprasad, T., Kumar, B. J. P., & Vishwanath, K. (2014). Effect of thermal non-equilibrium, seafloor topography and fluid advection on BSR-derived geothermal gradient. *Marine and Petroleum Geology*.

Mansor, M., Duverger, A., Pasquier, V., Gorlas, A., Guyot, F., Berg, J. S., Marin-Carbonne, J., Cosmidis, J., & Picard, A. (2025). Biogenic pyrite and metastable iron sulfides: Emerging formation pathways and geological and societal relevance. *Geo-bio interfaces*, *2*, e6.

Marlow, J. J., Hoer, D., Jungbluth, S. P., Reynard, L. M., Gartman, A., Chavez, M. S., El-Naggar, M. Y., Tuross, N., Orphan, V. J., & Girguis, P. R. (2021). Carbonate-hosted microbial communities are prolific and pervasive methane oxidizers at geologically diverse marine methane seep sites. *Proceedings of the National Academy of Sciences*, *118*(25), e2006857118.

Mavromatis, V., Goetschl, K., Grengg, C., Konrad, F., Purgstaller, B., & Dietzel, M. (2018). Barium partitioning in calcite and aragonite as a function of growth rate. *Geochimica et Cosmochimica Acta*, *237*, 65-78.

Mazumdar, A., Dewangan, P., Joäo, H., Peketi, A., Khosla, V., Kocherla, M., Badesab, F., Joshi, R., Roxanne, P., & Ramamurty, P. (2009). Evidence of paleo–cold seep activity from the Bay of Bengal, offshore India. *Geochemistry, Geophysics, Geosystems*, *10*(6).

Mazumdar, A., Dewangan, P., Peketi, A., Badesaab, F., Sadique, M., Sivan, K., Mathai, J., Ghosh, A., Zatale, A., & Pillutla, S. P. K. (2021). The first record of the genus Lamellibrachia (Siboglinidae) tubeworm along with associated organisms in a chemosynthetic ecosystem from the Indian Ocean: A report from the Cauvery-Mannar Basin. *Journal of Earth System Science*, *130*(2), 1-10.

Mazumdar, A., Dewangan, P., Peketi, A., Gullapalli, S., Kalpana, M., Naik, G., Shetty, D., Pujari, S., Pillutla, S. P. K., & Gaikwad, V. (2019). The first record of active methane (cold) seep ecosystem associated with shallow methane hydrate from the Indian EEZ. *Journal of Earth System Science*, *128*, 1-8.

Mazumdar, A., Joao, H. M., Peketi, A., Dewangan, P., Kocherla, M., Joshi, R. K., & Ramprasad, T. (2012). Geochemical and geological constraints on the composition of marine sediment pore fluid: Possible link to gas hydrate deposits. *Marine and Petroleum Geology*, *38*(1), 35-52.

Mazumdar, A., Joshi, R. K., Peketi, A., & Kocherla, M. (2011). Occurrence of faecal pellet-filled simple and composite burrows in cold seep carbonates: a glimpse of a complex benthic ecosystem. *Marine Geology*, *289*(1-4), 117-121.

Mazumdar, A., Kocherla, M., Carvalho, M. A., Peketi, A., Joshi, R. K., Mahalaxmi, P., Joao, H. M., & Jisha, R. (2015). Geochemical characterization of the Krishna-Godavari and Mahanadi offshore basin (Bay of Bengal) sediments: a comparative study of provenance. *Marine and Petroleum Geology*, *60*, 18-33.

Mazumdar, A., Peketi, A., Dewangan, P., Badesab, F., Ramprasad, T., Ramana, M. V., Patil, D. J., & Dayal, A. (2009). Shallow gas charged sediments off the Indian west coast: Genesis and distribution. *Marine Geology*, *267*(1-2), 71-85.

Mazumdar, A., Peketi, A., Joao, H., Dewangan, P., Borole, D., & Kocherla, M. (2012). Sulfidization in a shallow coastal depositional setting: Diagenetic and palaeoclimatic implications. *Chemical Geology*, *322*, 68-78.

Mazumdar, A., Peketi, A., Joao, H., Dewangan, P., & Ramprasad, T. (2014). Pore-water chemistry of sediment cores off Mahanadi Basin, Bay of Bengal: Possible link to deep seated methane hydrate deposit. *Marine and Petroleum Geology*, *49*, 162-175.

Mazzini, A., Svensen, H., Hovland, M., & Planke, S. (2006). Comparison and implications from strikingly different authigenic carbonates in a Nyegga complex pockmark, G11, Norwegian Sea. *Marine Geology*, *231*(1), 89-102.

McGlynn, S. E., Chadwick, G. L., Kempes, C. P., & Orphan, V. J. (2015). Single cell activity reveals direct electron transfer in methanotrophic consortia. *Nature*, *526*(7574), 531-535.

McManus, J., Berelson, W. M., Severmann, S., Poulson, R. L., Hammond, D. E., Klinkhammer, G. P., & Holm, C. (2006). Molybdenum and uranium geochemistry in continental margin sediments: paleoproxy potential. *Geochimica et Cosmochimica Acta*, *70*(18), 4643-4662.

McManus, J., NÃ¤gler, T. F., Siebert, C., Wheat, C. G., & Hammond, D. E. (2002). Oceanic molybdenum isotope fractionation: Diagenesis and hydrothermal ridge-flank alteration. *Geochemistry, Geophysics, Geosystems*, *3*(12), 1-9.

Mehra, O., & Jackson, M. (1960). Iron oxide removal from soils and clays by a dithionite-citrate system buffered with sodium bicarbonate [Iron oxide removal from soils and clays by a dithionate-citrate system buffered with sodium bicarbonate, p. 317-327 in Swineford, A., Editor, Clays and clay minerals, proceedings of the Seventh National Conference: London, Pergamon Press, 369 p.]. *Clays and Clay Minerals*, *7*, 317-327.

Miao, X., Feng, X., Li, J., & Lin, L. (2021). Tracing the paleo-methane seepage activity over the past 20,000 years in the sediments of Qiongdongnan Basin, northwestern South China Sea. *Chemical Geology*, *559*, 119956.

Miao, X., Oppo, D., Wei, J., Li, J., Li, J., Du, M., Guan, H., Liu, X., Li, J., & Wu, T. (2025). Environmental sulfidation and Mo source jointly control Mo isotopic composition in sediments under methane seepage. *Geological Society of America Bulletin*.

Miao, X., Wei, J., Li, J., Liu, X., Wang, D., Li, J., & Feng, X. (2024). Isotopically light Mo in sediments of methane seepage controlled by the benthic Fe–Mn redox shuttle process. *Global and Planetary Change*, *239*, 104512.

Miller, C. A., Peucker-Ehrenbrink, B., Walker, B. D., & Marcantonio, F. (2011). Re-assessing the surface cycling of molybdenum and rhenium. *Geochimica et Cosmochimica Acta*, *75*(22), 7146-7179.

Milliman, J., MÃ¼ller, G., & FÃ¶rstner, F. (1974). *Recent sedimentary carbonates: Part 1 marine carbonates*. Springer Science & Business Media.

Milucka, J., Ferdelman, T. G., Polerecky, L., Franzke, D., Wegener, G., Schmid, M., Lieberwirth, I., Wagner, M., Widdel, F., & Kuypers, M. M. (2012). Zero-valent sulphur is a key intermediate in marine methane oxidation. *Nature*, *491*(7425), 541-546.

Moran, J. J., Beal, E. J., Vrentas, J. M., Orphan, V. J., Freeman, K. H., & House, C. H. (2008). Methyl sulfides as intermediates in the anaerobic oxidation of methane. *Environmental Microbiology*, *10*(1), 162-173.

Mossmann, J., Aplin, A., Curtis, C., & Coleman, M. (1991). Geochemistry of inorganic and organic sulphur in organic-rich sediments from the Peru Margin. *Geochimica et Cosmochimica Acta*, *55*(12), 3581-3595.

Mucci, A., & Morse, J. W. (1983). The incorporation of Mg2+ and Sr2+ into calcite overgrowths: influences of growth rate and solution composition. *Geochimica et Cosmochimica Acta*, *47*(2), 217-233.

Murthy, K., & Rao, T. (1990). Acoustic wipeouts over the continental margins off Krishna, Godavari and Mahanadi river basins, East coast of India. *J Geol Soc India*, *35*, 559-568.

Naehr, T. H., Eichhubl, P., Orphan, V. J., Hovland, M., Paull, C. K., Ussler III, W., Lorenson, T. D., & Greene, H. G. (2007). Authigenic carbonate formation at hydrocarbon seeps in continental margin sediments: a comparative study. *Deep Sea Research Part II: Topical Studies in Oceanography*, *54*(11-13), 1268-1291.

Nägler, T., Neubert, N., Böttcher, M., Dellwig, O., & Schnetger, B. (2011). Molybdenum isotope fractionation in pelagic euxinia: Evidence from the modern Black and Baltic Seas. *Chemical Geology*, *289*(1-2), 1-11.

Nägler, T. F., Anbar, A. D., Archer, C., Goldberg, T., Gordon, G. W., Greber, N. D., Siebert, C., Sohrin, Y., & Vance, D. (2014). Proposal for an international molybdenum isotope measurement standard and data representation. *Geostandards Geoanalytical Research*, *38*(2), 149-151.

Nakagawa, Y., Takano, S., Firdaus, M. L., Norisuye, K., Hirata, T., Vance, D., & Sohrin, Y. (2012). The molybdenum isotopic composition of the modern ocean. *Geochemical Journal*, *46*(2), 131-141.

Nan, J., Tsang, M. Y., Li, J., Köster, M., Henkel, S., Lin, F., & Yao, W. (2023). Postdepositional behavior of molybdenum in deep sediments and implications for paleoredox reconstruction. *Geophysical Research Letters*, *50*(21), e2023GL104706.

Nanajkar, M., De, K., Desai, A., Mote, S., & Sautya, S. (2022). Ecology of Cold Seep Habitats. *Systems Biogeochemistry of Major Marine Biomes*, 263-283.

Neretin, L., Böttcher, M., Jørgensen, B., Volkov, I., Lüschen, H., & Hilgenfeldt, K. (2004). Pyritization processes and greigite formation in the advancing sulfidization front in the upper Pleistocene sediments of the Black Sea 1. *Geochimica et Cosmochimica Acta*, *68*(9), 2081-2093.

Nielsen, L. P., Risgaard-Petersen, N., Fossing, H., Christensen, P. B., & Sayama, M. (2010). Electric currents couple spatially separated biogeochemical processes in marine sediment. *Nature*, *463*(7284), 1071-1074.

Niemann, H., Fischer, D., Graffe, D., Knittel, K., Montiel, A., Heilmeyer, O., Nathen, K., Pape, T., Kasten, S., & Bohrmann, G. (2009). Biogeochemistry of a low-activity cold seep in the Larsen B area, western Weddell Sea, Antarctica. *Biogeosciences*, *6*.

Niewöhner, C., Hensen, C., Kasten, S., Zabel, M., & Schulz, H. (1998). Deep sulfate reduction completely mediated by anaerobic methane oxidation in sediments of the upwelling area off Namibia. *Geochimica et Cosmochimica Acta*, *62*(3), 455-464.

Nöthen, K., & Kasten, S. (2011). Reconstructing changes in seep activity by means of pore water and solid phase Sr/Ca and Mg/Ca ratios in pockmark sediments of the Northern Congo Fan. *Marine Geology*, *287*, 1-13.

Ohta, A., & Kawabe, I. (2001). REE (III) adsorption onto Mn dioxide (Î´-MnO2) and Fe oxyhydroxide: Ce (III) oxidation by Î´-MnO2. *Geochimica et Cosmochimica Acta*, *65*(5), 695-703.

Oppo, D., Capozzi, R., Picotti, V., & Ponza, A. (2015). A genetic model of hydrocarbon-derived carbonate chimneys in shelfal fine-grained sediments: The Enza River field, Northern Apennines (Italy). *Marine and Petroleum Geology*, *66*, 555-565.

Orphan, V. J., House, C. H., Hinrichs, K. U., McKeegan, K. D., & DeLong, E. F. (2001). Methane-consuming archaea revealed by directly coupled isotopic and phylogenetic analysis. *Science*, *293*, 484– 487.

Patrick Meister, Bo Liu, Timothy G. Ferdelman, Bo Barker Jørgensen, & Khalili, A. (2013). Control of sulphate and methane distributions in marine sediments by organic matter reactivity. *Geochimica et Cosmochimica Acta*, *104*, 183-193.

Paull, C., Hecker, B., Commeau, R., Freeman-Lynde, R., Neumann, C., Corso, W., Golubic, S., Hook, J., Sikes, E., & Curray, J. (1984). Biological communities at the Florida Escarpment resemble hydrothermal vent taxa. *Science*, *226*(4677), 965-967.

Pearce, C. R., Cohen, A. S., & Parkinson, I. (2009). Quantitative separation of molybdenum and rhenium from geological materials for isotopic determination by MC‐ICP‐MS. *Geostandards Geoanalytical Research*, *33*(2), 219-229.

Pecher, I. A., Minshull, T. A., Singh, S. C., & von Huene, R. (1996). Velocity structure of a bottom simulating reflector offshore Peru: Results from full waveform inversion. *Earth and Planetary Science Letters*, *139*(3-4), 459-469.

Peckmann, J., Reimer, A., Luth, U., Luth, C., Hansen, B., Heinicke, C., Hoefs, J., & Reitner, J. (2001). Methane-derived carbonates and authigenic pyrite from the northwestern Black Sea. *Marine Geology*, *177*(1-2), 129-150.

Peckmann, J., & Thiel, V. (2004). Carbon cycling at ancient methane-seeps. *Chemical Geology*, *205*(3-4), 443-467.

Peketi, A. (2012). *Marine sedimentary Sulfur-Carbon-Iron systematics: A study from Krishna Godavari Basin, Bay of Bengal* Andhra University]. Visakhapatnam.

Peketi, A., Mazumdar, A., Joao, H. M., Patil, D. J., Usapkar, A., & Dewangan, P. (2015). Coupled C-S-Fe geochemistry in a rapidly accumulating marine sedimentary system: diagenetic and depositional implications. *Geochemistry, Geophysics, Geosystems*, *16*(9), 2865-2883.

Peketi, A., Mazumdar, A., Joshi, R., Patil, D., Srinivas, P., & Dayal, A. (2012). Tracing the Paleo sulfate‐methane transition zones and H2S seepage events in marine sediments: An application of C‐S‐Mo systematics. *Geochemistry, Geophysics, Geosystems*, *13*(10).

Peketi, A., Mazumdar, A., Pillutla, S. P. K., Rai, V., Sawant, B., & Chaitanya, A. (2020). Monsoon rainfall and contrasting source rocks influenced sediment composition of peninsular basins along the east coast of India (western Bay of Bengal). *Marine Petroleum Geology*, *118*, 104433.

Peketi, A., Mazumdar, A., Sawant, B., Manaskanya, A., & Zatale, A. (2022). Biogeochemistry and trophic structure of a cold seep ecosystem, offshore Krishna-Godavari basin (east coast of India). *Marine Petroleum Geology*, *138*, 105542.

Pellerin, A., Antler, G., Holm, S. A., Findlay, A. J., Crockford, P. W., Turchyn, A. V., JÃ¸rgensen, B. B., & Finster, K. (2019). Large sulfur isotope fractionation by bacterial sulfide oxidation. *Science Advances*, *5*(7), eaaw1480.

Pellerin, A., Antler, G., RÃ¸y, H., Findlay, A., Beulig, F., Scholze, C., Turchyn, A. V., & JÃ¸rgensen, B. B. (2018). The sulfur cycle below the sulfate-methane transition of marine sediments. *Geochimica et Cosmochimica Acta*, *239*, 74-89.

Pellerin, A., Bui, T. H., Rough, M., Mucci, A., Canfield, D. E., & Wing, B. A. (2015). Mass-dependent sulfur isotope fractionation during reoxidative sulfur cycling: a case study from Mangrove Lake, Bermuda. *Geochimica et Cosmochimica Acta*, *149*, 152-164.

Pi, D.-H., Jiang, S.-Y., Luo, L., Yang, J.-H., & Ling, H.-F. (2014). Depositional environments for stratiform witherite deposits in the Lower Cambrian black shale sequence of the Yangtze Platform, southern Qinling region, SW China: Evidence from redox-sensitive trace element geochemistry. *Palaeogeography, Palaeoclimatology, Palaeoecology*, *398*, 125-131.

Pierre, C., & Fouquet, Y. (2007). Authigenic carbonates from methane seeps of the Congo deep-sea fan. *Geo-Marine Letters*, *27*(2), 249-257.

Pillutla, S., Peketi, A., Mazumdar, A., Sadique, M., Sivan, K., Zatale, A., Mishra, S., & Verma, S. (2024). Biogeochemical reconstruction of authigenic carbonate deposits at methane seep site off Krishna‐Godavari (K‐G) basin, Bay of Bengal. *Geochemistry, Geophysics, Geosystems*, *25*(10), e2024GC011801.

Pop Ristova, P., Wenzhofer, F., Ramette, A., Zabel, M., Fischer, D., Kasten, S., & Boetius, A. (2012). Bacterial diversity and biogeochemistry of different chemosynthetic habitats of the REGAB cold seep (West African margin, 3160 m water depth). *Biogeosciences*, *9*(12), 5031-5048.

Portail, M., Olu, K., Escobar-Briones, E., Caprais, J.-C., Menot, L., Waeles, M., Cruaud, P., Sarradin, P.-M., Godfroy, A., & Sarrazin, J. (2015). Comparative study of vent and seep macrofaunal communities in the Guaymas Basin. *Biogeosciences*, *12*(18), 5455-5479.

Poulson Brucker, R. L., McManus, J., Severmann, S., & Berelson, W. M. (2009). Molybdenum behavior during early diagenesis: Insights from Mo isotopes. *Geochemistry, Geophysics, Geosystems*, *10*(6).

Poulson, R. L., Siebert, Christopher, McManus, James Berelson, William M (2006). Authigenic molybdenum isotope signatures in marine sediments. *Geology*, *34*(8), 617-620.

Poulton, S., & Canfield, D. (2005). Development of a sequential extraction procedure for iron: implications for iron partitioning in continentally derived particulates. *Chemical Geology*, *214*(3-4), 209-221. https://doi.org/https://doi.org/10.1016/j.chemgeo.2004.09.003

Prabhakar, K., & Zutshi, P. (1993). Evolution of southern part of Indian east coast basins. *Geological Society of India*, *41*, 215-215.

Prakash, L. S., Ray, D., Paropkari, A. L., Mudholkar, A. V., Satyanarayanan, M., Sreenivas, B., Chandrasekharam, D., Kota, D., Raju, K. K., & Kaisary, S. (2012). Distribution of REEs and yttrium among major geochemical phases of marine Fe–Mn-oxides: Comparative study between hydrogenous and hydrothermal deposits. *Chemical Geology*, *312*, 127-137.

Price, F., & Shieh, Y. (1979). Fractionation of sulfur isotopes during laboratory synthesis of pyrite at low temperatures. *Chemical Geology*, *27*(3), 245-253.

Qin, S. S., Zhu, M. X., Sun, Z., Li, T., Zhang, X., Geng, W., Cao, H., Xu, C., Zhai, B., & Chen, Y. (2023). Diagenetic geochemistry of iron, sulfur, and molybdenum in sediments of the middle Okinawa Trough impacted by hydrothermal plumes and/or cold seeps. *Earth and Space Science*, *10*(3), e2022EA002709.

Rabus, R., Hansen, T. H., & Widdel, F. (2006). *Dissimilatory sulfate- and sulfur-reducing prokaryotes. In: Dworkin M (ed) The prokaryotes. A handbook of the biology of bacteria: symbiotic associations, Biotechnology, Applied Microbiology, 3rd edn. Springer, New York, 2:659–76*.

Raiswell, R., & Canfield, D. E. (2012). The iron biogeochemical cycle past and present. *Geochemical Perspectives*, *1*(1), 1-2.

Ramana, M., & Ramprasad, T. (2010). Gas hydrate occurrence in the Krishna-Godavari offshore basin off the east coast of India. 22-28.

Ramesh, R., & Subramanian, V. (1988). Temporal, spatial and size variation in the sediment transport in the Krishna River basin, India. *Journal of Hydrology*, *98*(1-2), 53-65.

Ramprasad, T., Dewangan, P., Ramana, M. V., Mazumdar, A., Karisiddaiah, S. M., Ramya, E. R., & Sriram, G. (2011). Evidence of slumping/sliding in Krishna-Godavari offshore basin due to gas/fluid movements. *Marine and Petroleum Geology*, *28*(10), 1806-1816.

Rao, A. M., Malkin, S. Y., Hidalgo-Martinez, S., & Meysman, F. J. (2016). The impact of electrogenic sulfide oxidation on elemental cycling and solute fluxes in coastal sediment. *Geochimica et Cosmochimica Acta*, *172*, 265-286.

Rao, G. (2001). Sedimentation, stratigraphy, and petroleum potential of Krishna-Godavari basin, East Coast of India. *AAPG Bulletin*, *85*(9), 1623-1643.

Rao, G., & Mani, K. (1993). A study on generation of abnormal pressures in Krishna Godavari basin. *India: Indian Journal of Petroleum Geology*, *2*(1), 20-30.

Rathore, C., Saha, M., Gupta, P., Kumar, M., Naik, A., & de Boer, J. (2023). Standardization of micro-FTIR methods and applicability for the detection and identification of microplastics in environmental matrices. *Science of The Total Environment*, *888*, 164157.

Raven, M. R., Sessions, A. L., Adkins, J. F., & Thunell, R. C. (2016). Rapid organic matter sulfurization in sinking particles from the Cariaco Basin water column. *Geochimica et Cosmochimica Acta*, *190*, 175-190.

Reeburgh, W., & and Alperin, M. J. (1988). Studies on anaerobic methane oxidation. . *SCOPE/UNEP*, *66*, 367-375.

Reeburgh, W. S. (2007). Oceanic methane biogeochemistry. *Chemical reviews*, *107*(2), 486-513.

Rickard, D. (1995). Kinetics of FeS precipitation: Part 1. Competing reaction mechanisms. *Geochimica et Cosmochimica Acta*, *59*(21), 4367-4379.
Rickard, D., & Luther III, G. W. (2007). Chemistry of iron sulfides. *Chemical reviews*, *107*(2), 514-562.
Rickard, D., & Morse, J. W. (2005). Acid volatile sulfide (AVS). *Marine Chemistry*, *97*(3-4), 141-197.
Rickard, D., Mussmann, M., & Steadman, J. (2017). Sedimentary sulfides. Elements 13 (2): 117–122. In.
Roberts, H. H., & Feng, D. (2013). Carbonate precipitation at Gulf of Mexico hydrocarbon seeps: An overview.
Roberts, H. H., Feng, D., & Joye, S. B. (2010). Cold-seep carbonates of the middle and lower continental slope, northern Gulf of Mexico. *Deep Sea Research Part II: Topical Studies in Oceanography*, *57*(21-23), 2040-2054.
Rongemaille, E., Bayon, G., Pierre, C., Bollinger, C., Chu, N. C., Fouquet, Y., Riboulot, V., & Voisset, M. (2011). Rare earth elements in cold seep carbonates from the Niger delta. *Chemical Geology*, *286*(3-4), 196-206.
Ruban, A., Rudmin, M., Mazurov, A., Chernykh, D., Dudarev, O., & Semiletov, I. (2022). Cold-seep carbonates of the Laptev Sea continental slope: Constraints from fluid sources and environment of formation. *Chemical Geology*, *610*, 121103.
Rudge, J. F., Reynolds, B. C., & Bourdon, B. (2009). The double spike toolbox. *Chemical Geology*, *265*(3-4), 420-431.
Rudge, J. F., Reynolds, B. C., & Bourdon, B. (2009). The double spike toolbox. *Chemical Geology*, *265*(3), 420-431.
Ruppel, C. D., & Waite, W. F. (2020). Grand Challenge: Timescales and Processes of Methane Hydrate Formation and Breakdown, with Application to Geologic Systems. *Journal of Geophysical Research: Solid Earth*, e2018JB016459.
Russell, W. A., Papanastassiou, D. A., & Tombrello, T. A. (1978). Ca isotope fractionation on the Earth and other solar system materials. *Geochimica et Cosmochimica Acta*, *42*(8), 1075-1090.
Sahling, H., Rickert, D., Lee, R. W., Linke, P., & Suess, E. (2002). Macrofaunal community structure and sulfide flux at gas hydrate deposits from the Cascadia convergent margin, NE Pacific. *MARINE ECOLOGY PROGRESS SERIES*, *231*, 121-138.
Sauer, S., Hong, W.-L., Yao, H., Lepland, A., Klug, M., Eichinger, F., Himmler, T., Crémière, A., Panieri, G., & Schubert, C. J. (2021). Methane transport and sources in an Arctic deep-water cold seep offshore NW Svalbard (Vestnesa Ridge, 79 N). *Deep Sea Research Part I: Oceanographic Research Papers*, *167*, 103430.
Savard, M. M., Beauchamp, B., & Veizer, J. (1996). Significance of aragonite cements around Cretaceous marine methane seeps. *Journal of Sedimentary Research*, *66*(3), 430-438.
Scheller, S., Ermler, U., & Shima, S. (2017). Catabolic Pathways and Enzymes Involved in Anaerobic Methane Oxidation. *Anaerobic Utilization of Hydrocarbons, Oils, and Lipids*, 1-29.
Scheller, S., Yu, H., Chadwick, G. L., McGlynn, S. E., & Orphan, V. J. (2016). Artificial electron acceptors decouple archaeal methane oxidation from sulfate reduction. *Science*, *351*(6274), 703-707.
Scheller, S., Yu, H., Chadwick, G. L., McGlynn, S. E., & Orphan, V. J. (2017). Artificial electron acceptors decouple archaeal methane oxidation from sulfate reduction. *Science*, *351*(6274), 703-707.
Scholz, F., Siebert, C., Dale, A. W., & Frank, M. (2017). Intense molybdenum accumulation in sediments underneath a nitrogenous water column and implications for the reconstruction of paleo-redox conditions based on molybdenum isotopes. *Geochimica et Cosmochimica Acta*, *213*, 400-417.
Schoonen, M., & Barnes, H. (1991 (b)). Reactions forming pyrite and marcasite from solution: II. Via FeS precursors below 100 C. *Geochimica et Cosmochimica Acta*, *55*(6), 1505-1514.
Schoonen, M., & Barnes, H. (1991(a)). Reactions forming pyrite and marcasite from solution: I. Nucleation of FeS2 below 100 C. *Geochimica et Cosmochimica Acta*, *55*(6), 1495-1504.
Schoonen, M. A. A. (2004). Mechanisms of sedimentary pyrite formation. *Sulfur biogeochemistry—Past and present*, 117–134.

Scott, C., & Lyons, T. W. (2012). Contrasting molybdenum cycling and isotopic properties in euxinic versus non-euxinic sediments and sedimentary rocks: Refining the paleoproxies. *Chemical Geology*, *324*, 19-27.
Seike, K., Jenkins, R. G., Watanabe, H., Nomaki, H., & Sato, K. (2012). Novel use of burrow casting as a research tool in deep-sea ecology. *Biology Letters*, *8*(4), 648-651.
Sekerci, F., Fischer, S., Joshi, P., Peiffer, S., Kappler, A., & Mansor, M. (2025). Sulfur microenvironments as hotspots for biogenic pyrite formation. *Scientific Reports*, *15*(1), 20148.
Shen, Z., Liu, Y., Brown, P. E., Szlufarska, I., & Xu, H. (2014). Modeling the effect of dissolved hydrogen sulfide on Mg2+-water complex on dolomite {104} surfaces. *The Journal of Physical Chemistry C*, *118*(29), 15716-15722.
Shields, G., & Stille, P. (2001). Diagenetic constraints on the use of cerium anomalies as palaeoseawater redox proxies: an isotopic and REE study of Cambrian phosphorites. *Chemical Geology*, *175*(1), 29-48.
Sholkovitz, E. R., Landing, W. M., & Lewis, B. L. (1994). Ocean particle chemistry: the fractionation of rare earth elements between suspended particles and seawater. *Geochimica et Cosmochimica Acta*, *58*(6), 1567-1579.
Sholkovitz, E. R., Shaw, T. J., & Schneider, D. L. (1992). The geochemistry of rare earth elements in the seasonally anoxic water column and porewaters of Chesapeake Bay. *Geochimica et Cosmochimica Acta*, *56*(9), 3389-3402.
Sibuet, M., & Olu-Le Roy, K. (2002). Cold seep communities on continental margins: structure and quantitative distribution relative to geological and fluid venting patterns. In *Ocean margin systems* (pp. 235-251). Springer.
Siebert, C. (2001). Nagler TF, Kramers J D. Determination of molybdenum isotope fractionation by double-spike multi-collector inductively coupled plasma mass spectrometry. *Geochemistry Geophysics Geosystems*, *2*, 2000GC000124.
Siebert, C., McManus, J., Bice, A., Poulson, R., & Berelson, W. M. (2006). Molybdenum isotope signatures in continental margin marine sediments. *Earth Planetary Science Letters*, *241*(3-4), 723-733.
Siebert, C., Nägler, T. F., & Kramers, J. D. (2001). Determination of molybdenum isotope fractionation by double-spike multicollector inductively coupled plasma mass spectrometry. *Geochem. Geophys. Geosyst*, *2*(7), 1032.
Siebert, C., Nägler, T. F., von Blanckenburg, F., & Kramers, J. D. (2003). Molybdenum isotope records as a potential new proxy for paleoceanography. *Earth Planetary Science Letters*, *211*(1-2), 159-171.
Singha, D. K., & Chatterjee, R. (2014). Detection of overpressure zones and a statistical model for pore pressure estimation from well logs in the Krishnaâ€• Godavari Basin, India. *Geochemistry, Geophysics, Geosystems*, *15*(4), 1009-1020.
Sinninghe Damsté, J., Eglinton, T., Rijpstra, W., & Leeuw, J. (1990). Characterisation of organically-bound sulfur, in high-molecular-weight sedimentary organic matter using flash-pyrolysis and Raney Ni desulfurisation. *Relation*, *97*, 6156.
Sinninghe Damsté, J., Leeuw, J., Kock, A., Zeeuw, M., Lange, F. D., Rijpstra, W., & Schenck, P. (1987). The occurence and identification of series of organic sulphur compounds in oils and sediment extracts. I. A study of Rozel Point Oil (USA).
Sinninghe Damsté, J., Ten Haven, H., De Leeuw, J., & Schenck, P. (1986). Organic geochemical studies of a Messinian evaporitic basin, northern Apennines (Italy)--II Isoprenoid and n-alkyl thiophenes and thiolanes*. *Organic Geochemistry*, *10*(4-6), 791-805.
Sivan, K., Mazumdar, A., Peketi, A., Sudheer, A., Pillutla, S., & Mishra, S. (2025). Pyritization may archive the influence of Sulfate-AOM and bioturbation activities in marine sulfidic shelf sediments. *Continental Shelf Research*, 105591.
Skierszkan, E., Amini, M., & Weis, D. (2015). A practical guide for the design and implementation of the double-spike technique for precise determination of molybdenum isotope compositions of environmental samples. *Analytical and bioanalytical chemistry*, *407*(7), 1925-1935.
Sloan, E. (1998). *Clathrate hydrates of natural gases*. CRC Press.
Sloan, E., & Koh, C. (2008). *Clathrate hydrates of natural gases*. CRC.

Smedley, P. L., & Kinniburgh, D. G. (2017). Molybdenum in natural waters: A review of occurrence, distributions and controls. *Applied Geochemistry*, *84*, 387-432.
Smrzka, D., Zwicker, J., Bach, W., Feng, D., Himmler, T., Chen, D., & Peckmann, J. (2019). The behavior of trace elements in seawater, sedimentary pore water, and their incorporation into carbonate minerals: a review. *Facies*, *65*, 1-47.
Smrzka, D., Zwicker, J., Lu, Y., Sun, Y., Feng, D., Monien, P., Bohrmann, G., & Peckmann, J. r. (2021). Trace element distribution in methane-seep carbonates: The role of mineralogy and dissolved sulfide. *Chemical Geology*, *580*, 120357.
Solongo, T., Fukushi, K., Altansukh, O., Takahashi, Y., Akehi, A., Baasansuren, G., Ariuntungalag, Y., Enkhjin, O., Davaajargal, B., & Davaadorj, D. (2018). Distribution and chemical speciation of molybdenum in river and pond sediments affected by mining activity in Erdenet City, Mongolia. *Minerals*, *8*(7), 288.
Stakes, D. S., Orange, D., Paduan, J. B., Salamy, K. A., & Maher, N. (1999). Cold-seeps and authigenic carbonate formation in Monterey Bay, California. *Marine Geology*, *159*(1-4), 93-109.
Subramanian, V. (1993). Sediment load of Indian rivers. *Current Science*, 928-930.
Suess, E. (2014). Marine cold seeps and their manifestations: geological control, biogeochemical criteria and environmental conditions. *International Journal of Earth Sciences*, *103*(7), 1889-1916.
Suess, E. (2018). Marine cold seeps: background and recent advances. *Hydrocarbons, Oils and Lipids: Diversity, Origin, Chemistry and Fate. Handbook of Hydrocarbon and Lipid Microbiology*, 1-21.
Suess, E. (2020). Marine cold seeps: background and recent advances. *Hydrocarbons, oils and lipids: diversity, origin, chemistry and fate*, 747-767.
Sultan, N., Garziglia, S. b., & Ruffine, L. (2016). New insights into the transport processes controlling the sulfate-methane-transition-zone near methane vents. *Scientific Reports*, *6*.
Sun, T., Yin, P., Cao, K., Duan, X., & Zhang, X. (2024). Geochemical and mineralogical features as indicators of sulfate-methane transition zones in shallow gas-bearing offshore sediments from Zhoushan. *Marine and Petroleum Geology*, *165*, 106863.
Sun, Y., Peckmann, J., Hu, Y., Wang, X., Gong, S., Peng, Y., Chen, D., & Feng, D. (2020a). Formation of tubular carbonates within the seabed of the northern South China Sea. *Minerals*, *10*(9), 768.
Sun, Y., Peckmann, J. r., Hu, Y., Wang, X., Gong, S., Peng, Y., Chen, D., & Feng, D. (2020b). Formation of tubular carbonates within the seabed of the northern South China Sea. *Minerals*, *10*(9), 768.
Sunagawa, I., Takahashi, Y., & Imai, H. (2007). Strontium and aragonite-calcite precipitation. *Journal of Mineralogical and Petrological Sciences*, *102*(3), 174-181.
Sundby, B., Anschutz, P., Lecroart, P., & Mucci, A. (2021). Ideas and perspectives: Sea-level change, anaerobic methane oxidation, and the glacial-interglacial phosphorus cycle. *Biogeosciences Discussions*, *2021*, 1-24.
Syrbu, N., Kholmogorov, A., Maltseva, E., & Venikova, A. (2024). Cold seeps and heat flow: gas hydrate provinces offshore Sakhalin Island. *Water*, *16*(2), 213.
Syrbu, N., Snyder, G., Shakirov, R., Kholmogorov, A., Zharkov, R., & Tsunogai, U. (2022). Geochemical distribution of helium, hydrogen, carbon dioxide, and methane in Sakhalin Island mud volcanoes, hot springs, and cold seeps. *Journal of Volcanology and Geothermal Research*, *431*, 107667.
Tanaka, M., Ariga, D., Kashiwabara, T., & Takahashi, Y. (2018). Adsorption mechanism of molybdenum (VI) on manganese oxides causing a large isotope fractionation. *ACS Earth Space Chemistry*, *2*(11), 1187-1195.
Tarutani, T., Clayton, R. N., & Mayeda, T. K. (1969). The effect of polymorphism and magnesium substitution on oxygen isotope fractionation between calcium carbonate and water. *Geochimica et Cosmochimica Acta*, *33*(8), 987-996.
Teichert, B. M., Bohrmann, G., & Suess, E. (2005). Chemoherms on Hydrate Ridge—Unique microbially-mediated carbonate build-ups growing into the water column. *Palaeogeography, Palaeoclimatology, Palaeoecology*, *227*(1-3), 67-85.

Teichert, B. M., Gussone, N., Eisenhauer, A., & Bohrmann, G. (2005a). Clathrites: archives of near-seafloor pore-fluid evolution (δ44/40Ca, δ13C, δ18O) in gas hydrate environments. *Geology*, *33*(3), 213-216.

Thamdrup, B., Fossing, H., & Jorgensen, B. B. (1994). Manganese, iron and sulfur cycling in a coastal marine sediment, Aarhus Bay, Denmark. *Geochimica et Cosmochimica Acta*, *58*(23), 5115-5129.

Theberge, S. M., & Luther III, G. W. (1997). Determination of the electrochemical properties of a soluble aqueous FeS species present in sulfidic solutions. *Aquatic Geochemistry*, *3*(3), 191-211.

Thiel, J., Byrne, J. M., Kappler, A., Schink, B., & Pester, M. (2019). Pyrite formation from FeS and H2S is mediated through microbial redox activity. *Proceedings of the National Academy of Sciences*, *116*(14), 6897-6902.

Tomaru, H., Torres, M. E., Matsumoto, R., & Borowski, W. S. (2006). Effect of massive gas hydrate formation on the water isotopic fractionation of the gas hydrate system at Hydrate Ridge, Cascadia margin, offshore Oregon. *Geochemistry, Geophysics, Geosystems*, *7*(10).

Torres, M., Brumsack, H., Bohrmann, G., & Emeis, K. (1996 a). Barite fronts in continental margin sediments: A new look at barium remobilization in the zone of sulfate reduction and formation of heavy barites in diagenetic fronts. *Chemical Geology*, *127*(1-3), 125-139.

Tossell, J. (2005). Calculating the partitioning of the isotopes of Mo between oxidic and sulfidic species in aqueous solution. *Geochimica et Cosmochimica Acta*, *69*(12), 2981-2993.

Tribovillard, N., Riboulleau, A., Lyons, T., & Baudin, F. (2004). Enhanced trapping of molybdenum by sulfurized marine organic matter of marine origin in Mesozoic limestones and shales. *Chemical Geology*, *213*(4), 385-401.

Tunnicliffe, V., Juniper, S. K., & Sibuet, M. (2003). Reducing environments of the deep-sea floor. *Ecosystems of the World*, 81-110.

Ussler III, W., & Paull, C. K. (2008). Rates of anaerobic oxidation of methane and authigenic carbonate mineralization in methane-rich deep-sea sediments inferred from models and geochemical profiles. *Earth and Planetary Science Letters*, *266*(3-4), 271-287.

Ussler, W., & Paull, C. (1995). Effects of ion exclusion and isotopic fractionation on pore water geochemistry during gas hydrate formation and decomposition. *Geo-Marine Letters*, *15*(1), 37-44.

Vairavamurthy, A., Zhou, W., Eglinton, T., & Manowitz, B. (1994). Sulfonates: a novel class of organic sulfur compounds in marine sediments. *Geochimica et Cosmochimica Acta*, *58*(21), 4681-4687.

Vanneste, H., Kastner, M., James, R. H., Connelly, D. P., Fisher, R. E., Kelly-Gerreyn, B. A., Heeschen, K., Haeckel, M., & Mills, R. A. (2012). Authigenic carbonates from the Darwin Mud Volcano, Gulf of Cadiz: A record of palaeo-seepage of hydrocarbon bearing fluids. *Chemical Geology*, *300*, 24-39.

Vanreusel, A., Andersen, A. C., Boetius, A., Connelly, D., Cunha, M. R., Decker, C., Hilario, A., Kormas, K. A., Maignien, L., & Olu, K. (2009). Biodiversity of cold seep ecosystems along the European margins. *Oceanography*, *22*(1), 110-127.

Venkatarathnam, K., & Biscaye, P. (1973). Clay mineralogy and sedimentation in the eastern Indian Ocean.

Vogel, A., & Bassett, J. (1987). *Vogel's textbook of quantitative inorganic analysis: Including elementary instrumental analysis*. Longman Scientific & Technical.

Vorlicek, T. P., Helz, G. R., Chappaz, A., Vue, P., Vezina, A., & Hunter, W. (2018). Molybdenum burial mechanism in sulfidic sediments: iron-sulfide pathway. *ACS Earth Space Chemistry*, *2*(6), 565-576.

Wagner, M., Chappaz, A., & Lyons, T. W. (2017). Molybdenum speciation and burial pathway in weakly sulfidic environments: Insights from XAFS. *Geochimica et Cosmochimica Acta*, *206*, 18-29.

Walker, J. C. G. (1986). Global geochemical cycles of carbon, sulfur and oxygen. *Marine Geology*, *70*(1-2), 159-174.

Wallmann, K., Pinero, E., Burwicz, E., Haeckel, M., Hensen, C., Dale, A., & Ruepke, L. (2012). The global inventory of methane hydrate in marine sediments: A theoretical approach. *Energies*, *5*(7), 2449-2498.

Wang, H., Wang, X., Cao, L., Zhong, Z., Luan, Z., & Li, C. (2023). Macrofauna community of the cold seep area at Site F, South China Sea. *Frontiers in Marine Science*, *10*, 1068916.

Wang, J., Wu, S., Sun, J., Feng, W., & Li, Q. (2021). Influence of seafloor topography on gas hydrate occurrence across a submarine canyon-incised continental slope in the northern margin of the south china sea. *Marine and Petroleum Geology*, 105279.

Wang, L., Sun, Z., Cao, H., Li, H.-C., Wang, X., Liu, Y., Xiao, J., & Ma, Z. (2021). A new method for the U–Th dating of a carbonate chimney deposited during the last glaciation in the northern Okinawa Trough, East China Sea. *Quaternary Geochronology*, *66*, 101199.

Wang, X., Guan, H., Qiu, J.-W., Xu, T., Peckmann, J., Chen, D., & Feng, D. (2022). Macro-ecology of cold seeps in the South China Sea. *Geosystems and Geoenvironment*, 100081.

Wang, X., Zhao, D., Yu, T., Zhu, Y., Jiang, M., Liu, Y., Hu, S., Luo, Y., Xiang, H., & Zheng, Y. (2025). Biological nitrogen fixation driven by methane anaerobic oxidation supports the complex biological communities in cold-seep habitat. *Environmental Technology & Innovation*, *37*, 103938.

Wasylenki, L. E., Rolfe, B. A., Weeks, C. L., Spiro, T. G., & Anbar, A. D. (2008). Experimental investigation of the effects of temperature and ionic strength on Mo isotope fractionation during adsorption to manganese oxides. *Geochimica et Cosmochimica Acta*, *72*(24), 5997-6005.

Wasylenki, L. E., Weeks, C. L., Bargar, J. R., Spiro, T. G., Hein, J. R., & Anbar, A. D. (2011). The molecular mechanism of Mo isotope fractionation during adsorption to birnessite. *Geochimica et Cosmochimica Acta*, *75*(17), 5019-5031.

Wegener, G., Krukenberg, V., Riedel, D., Tegetmeyer, H. E., & Boetius, A. (2015). Intercellular wiring enables electron transfer between methanotrophic archaea and bacteria. *Nature*, *526*(7574), 587-590.

Wehrmann, L. M., Titschack, J., Böttcher, M. E., & Ferdelman, T. G. (2015). Linking sedimentary sulfur and iron biogeochemistry to growth patterns of a cold‐water coral mound in the Porcupine Basin, SW Ireland (IODP Expedition 307). *Geobiology*, *13*(5), 424-442.

Weidlich, R., Bialik, O., Rüggeberg, A., Grobéty, B., Vennemann, T., Neuman, A., Makovsky, Y., & Foubert, A. (2023). Occurrence and Genesis of Cold‐Seep Authigenic Carbonates from the South‐Eastern Mediterranean Sea. *The Depositional Record*, *9*(4), 844-870.

Werne, J., Hollander, D., Behrens, A., Schaeffer, P., Albrecht, P., & Sinninghe Damste, J. (2000). Timing of early diagenetic sulfurization of organic matter: a precursor-product relationship in Holocene sediments of the anoxic Cariaco Basin, Venezuela. *Geochimica et Cosmochimica Acta*, *64*(10), 1741-1752.

Werne, J., Lyons, T., Hollander, D., Formolo, M., & Sinninghe Damsté, J. (2003). Reduced sulfur in euxinic sediments of the Cariaco Basin: sulfur isotope constraints on organic sulfur formation. *Chemical Geology*, *195*(1-4), 159-179.

Werne, J. P., Hollander, D. J., Lyons, T. W., & Damste, J. S. S. (2004). Organic sulfur biogeochemistry: recent advances and future research directions. *Sulfur Biogeochemistry: Past and Present*, 135.

Westrich, J., & Berner, R. (1988). The effect of temperature on rates of sulfate reduction in marine sediments. *Geomicrobiology Journal*, *6*(2), 99-117.

Whiticar, M. J. (1999). Carbon and hydrogen isotope systematics of bacterial formation and oxidation of methane. *Chemical Geology*, *161*(1-3), 291-314.

Whiticar, M. J., Faber, E., & Schoell, M. (1986). Biogenic methane formation in marine and freshwater environments: CO2 reduction vs. acetate fermentation--isotope evidence. *Geochimica et Cosmochimica Acta*, *50*(5), 693-709.

Wilkin, R., & Barnes, H. (1996). Pyrite formation by reactions of iron monosulfides with dissolved inorganic and organic sulfur species. *Geochimica et Cosmochimica Acta*, *60*(21), 4167-4179.

Wirsig, C., Kowsmann, R. O., Miller, D. J., de Oliveira Godoy, J. M., & Mangini, A. (2012). U/Th-dating and post-depositional alteration of a cold seep carbonate chimney from the Campos Basin offshore Brazil. *Marine Geology*, *329*, 24-33.

Xiao, K.-Q., Beulig, F., Kjeldsen, K. U., Jorgensen, B. B., & Risgaard-Petersen, N. (2017). Concurrent Methane Production and Oxidation in Surface Sediment from Aarhus Bay, Denmark [Original Research]. *Frontiers in Microbiology*, *8*(1198). https://doi.org/10.3389/fmicb.2017.01198

Xu, H., Peng, X., Chen, S., Li, J., Dasgupta, S., Ta, K., & Du, M. (2018). Macrofaunal burrowing enhances deep-sea carbonate lithification on the Southwest Indian Ridge. *Biogeosciences*, *15*(21), 6387-6397.

Xu, N., Christodoulatos, C., & Braida, W. (2006). Adsorption of molybdate and tetrathiomolybdate onto pyrite and goethite: effect of pH and competitive anions. *Chemosphere*, *62*(10), 1726-1735.

Xu, T., Chai, X., Chen, C., Watanabe, H. K., Sun, J., Xiao, Y., Wang, Y., Chen, J., Qiu, J. W., & Qian, P. Y. (2024). Genetic divergence and migration patterns of a galatheoid squat lobster highlight the need for deep‐sea conservation. *Molecular ecology*, *33*(1), e17200.

Yang, J., Torres, M., McManus, J., Algeo, T. J., Hakala, J. A., & Verba, C. (2017). Controls on rare earth element distributions in ancient organic-rich sedimentary sequences: Role of post-depositional diagenesis of phosphorus phases. *Chemical Geology*, *466*, 533-544.

Yao, H., Panieri, G., Lehmann, M. F., Himmler, T., & Niemann, H. (2021). Biomarker and isotopic composition of seep carbonates record environmental conditions in two Arctic methane seeps. *Frontiers in Earth Science*, *8*, 755.

Yao, W., & Millero, F. (1993). The rate of sulfide oxidation by [delta] MnO2 in seawater. *Geochimica et Cosmochimica Acta*, *57*(14), 3359-3365.

Yao, W., & Millero, F. H. (1995). Oxidation of hydrogen sulfide by Mn (IV) and Fe (III)(hydr) oxides in seawater. In. ACS Publications.

Ye, T., Jin, G., Wu, D., & Liu, L. (2019). Experimental and numerical simulation of the formation of cold seep carbonates in marine sediments. *International Journal of Environmental Research and Public Health*, *16*(8), 1433.

Yu, H., Skennerton, C. T., Chadwick, G. L., Leu, A. O., Aoki, M., Tyson, G. W., & Orphan, V. J. (2022). Sulfate differentially stimulates but is not respired by diverse anaerobic methanotrophic archaea. *The ISME journal*, *16*(1), 168-177.

Yu, Z., Colin, C., Douville, E., Meynadier, L., Duchampâ€• Alphonse, S. p., Sepulcre, S., Wan, S., Song, L., Wu, Q., & Xu, Z. (2017). Yttrium and rare earth element partitioning in seawaters from the Bay of Bengal. *Geochemistry, Geophysics, Geosystems*, *18*(4), 1388-1403.

Yucel, M., Sommer, S., Dale, A. W., & Pfannkuche, O. (2017). Microbial Sulfide Filter along a Benthic Redox Gradient in the Eastern Gotland Basin, Baltic Sea. *Frontiers in Microbiology*, *8*.

Zehnder A.J.B., & S.H., Z. (1980). *The sulfur cycle. In The Handbook of Environmental Chemistry. O Hutzinger (ed) Springer Verlag, Heidelberg, pp 105-145*.

Zhang, F., Xu, H., Konishi, H., Kemp, J. M., Roden, E. E., & Shen, Z. (2012). Dissolved sulfide-catalyzed precipitation of disordered dolomite: Implications for the formation mechanism of sedimentary dolomite. *Geochimica et Cosmochimica Acta*, *97*, 148-165.

Zhang, F., Yan, C., Teng, H. H., Roden, E. E., & Xu, H. (2013). In situ AFM observations of Ca–Mg carbonate crystallization catalyzed by dissolved sulfide: Implications for sedimentary dolomite formation. *Geochimica et Cosmochimica Acta*, *105*, 44-55.

Zhang, L., Li, J., Xu, Y.-G., & Ren, Z.-Y. (2018). The influence of the double spike proportion effect on stable isotope (Zn, Mo, Cd, and Sn) measurements by multicollector-inductively coupled plasma-mass spectrometry (MC-ICP-MS). *Journal of Analytical Atomic Spectrometry*, *33*(4), 555-562.

Zhang, M., Konishi, H., Xu, H., Sun, X., Lu, H., Wu, D., & Wu, N. (2014). Morphology and formation mechanism of pyrite induced by the anaerobic oxidation of methane from the continental slope of the NE South China Sea. *Journal of Asian Earth Sciences*, *92*, 293-301.

Zhang, W., Chen, C., Su, P., Wan, Z., Huang, W., Shang, J., Liang, J., Feng, J., Zhou, W., & Zhong, L. (2023). Formation and implication of cold-seep carbonates in the southern South China Sea. *Journal of Asian Earth Sciences*, *241*, 105485.

Zhao, Y., Liu, Y., Cao, S., Hao, Q., Liu, C., & Li, Y. (2024). Anaerobic oxidation of methane driven by different electron acceptors: A review. *Science of The Total Environment*, *946*, 174287.

Zheng, Y., Anderson, R. F., Van Geen, A., & Kuwabara, J. (2000). Authigenic molybdenum formation in marine sediments: a link to pore water sulfide in the Santa Barbara Basin. *Geochimica et Cosmochimica Acta*, *64*(24), 4165-4178.

Zhou, Z., Tran, P. Q., Cowley, E. S., Trembath-Reichert, E., & Anantharaman, K. (2025). Diversity and ecology of microbial sulfur metabolism. *Nature Reviews Microbiology*, *23*(2), 122-140.

Zhu, Y., & Itoh, A. (2021). Pseudo isotope dilution (PID) as an approach for correcting barium-related spectral interferences on the measurement of europium by inductively coupled plasma mass spectrometry (ICP-MS). *Analytica Chimica Acta*, *1180*, 338854.

Zopfi, J., Ferdelman, T., & Fossing, H. (2004). Distribution and fate of sulfur intermediates–sulfite, tetrathionate, thiosulfate, and elemental sulfur–in marine sediments. *Sulfur Biogeochemistry–Past and Present*, 97–116.

Zwicker, J., Smrzka, D., Gier, S., Goedert, J. L., & Peckmann, J. (2015). Mineralized conduits are part of the uppermost plumbing system of Oligocene methane-seep deposits, Washington State (USA). *Marine and Petroleum Geology*, *66*, 616-630.

Zwicker, J., Smrzka, D., Himmler, T., Monien, P., Gier, S., Goedert, J. L., & Peckmann, J. (2018). Rare earth elements as tracers for microbial activity and early diagenesis: a new perspective from carbonate cements of ancient methane-seep deposits. *Chemical Geology*, *501*, 77-85.